Applications of Ionic Liquids towards the Nuclear Industry.

David Sanders

A thesis presented for the degree of

Doctor of Philosophy

The University of Edinburgh

2004.

Abstract.

Ionic liquids have been highlighted as possible replacements of their relatives, high-temperature molten salts, in the electrorefining of U (and Pu) from irradiated nuclear fuel. The reasons for this are their far lower operating temperatures (room temperature up to 200°C) and less corrosive nature. This investigation is concerned with determining the electrochemistry of solute species in the chloride and bis(trifluoromethanesulfonyl)amide ionic liquids and their transport properties in these novel solvents, namely their diffusion coefficients, in order to assess their suitability as replacements for high temperature molten salts.

The electrochemistry of solute species in ionic liquids is investigated by use of cyclic voltammetry. The cyclic voltammetry of transition metals of varying oxidation states are presented as well as the electrochemistry of uranium as both a solute and a metallic electrode in a variety of ionic liquids and comparisons are made between their behaviour.

Transport properties of the solute species have been determined by the use of an electrochemical technique known as chronocoulometry. This involves the application of a potential step and the subsequent observation of the charge passed as a function of time to determine the diffusion coefficient of the solute. Diffusion data is collected at a variety of temperatures in order to obtain an Arrhenius plot, and thus obtain activation energies for diffusion for each solute species, and data have been compared and contrasted for the ionic liquids and solutes employed.

Structural analysis of the ionic liquids has also been performed by utilising single crystal x-ray crystallography to study the interaction between both the anion and cation of the ionic liquid, and between solute species and the anion and cation of the ionic liquid. The crystal structure of 1-ethyl-3-methylimidazolium chloride that offers a significant improvement over previously published data is presented along with the crystal structure of a new ionic liquid, 1-ethyl-3-methylimidazolium dichloroargentate. Powder x-ray diffraction and Raman spectroscopy data are also presented as part of the structural analysis of these ionic liquid systems.

Acknowledgements.

Many thanks are due for the help and support I have received from so many people throughout my PhD. My particular thanks to;

My supervisors, Dr Andy Mount and Dr Colin Pulham, without their help, support and enthusiasm, completion of this research would not have been possible, you can unlock your doors now!

My supervisors at BNFL, Dr Robert Thied, Dr Robert Lewin and Melissa Hetherington. Thanks for the enthusiasm, the funding and the warm welcome we always received on our regular trips to sunny Sellafield.

The X-ray crystallographers, Dr Simon Parsons, Dr Andy Parkin and especially Iain Oswald (I'm sure you will never forget the crystal structure of [Emim][$AgCl_2$]!).

Colleagues at both the Centre for Radiochemistry Research and the QUILL labs at Queens University of Belfast for sample preparation and fruitful discussions.

The departmental services for their hard work, especially Stuart Johnson for all the lovely Schlenk tubes he made, which I then broke!

Thanks must go to all the wonderful people I have met through university life, who were as varied as they were entertaining, and to the bar staff at KBH for all the free food and good chat.

A big thank you to the inhabitants of 20 Mayfield Rd past and present, you all know why, I am lucky to have such good friends.

Finally, thanks to my family who have been supportive both emotionally and financially to the end, I just can't thank you enough, and you can now stop asking if it's finished……no really, it's finished!

Contents.

Abbreviations.

[Emim][Cl]	1-ethyl-3-methylimidazolium chloride
[Hmim][Cl]	1-hexyl-3-methylimidazolium chloride
$[Emim][N(Tf)_2]$	1-ethyl-3-methylimidazolium bis(trifluoromethanesulfonyl)imide
$[Emim][AgCl_2]$	1-ethyl-3-methylimidazolium dichloro-argentate
$[Emim][CuCl_2]$	1-ethyl-3-methylimidazolium dichloro-cuprate
$[Phos][N(Tf)_2]$	trihexyl(hexamethyl)phosphonium bis(trifluoromethanesulfonyl)imide
$[Pyr][N(Tf)_2]$	*N*-butyl-*N*-methylpyrrolidinium bis(trifluoromethanesulfonyl)imide
$[TMA]_2[UCl_6]$	bis (tetramethylammonium) hexachlorouranate(IV)
$[BuPy]^+$	N-*n*-Butyl-Pyridinium cation
C.V.	cyclic Voltammetry
C.A.	Chronoamperometry
v	scan rate (Vs^{-1})
D	diffusion coefficient (cm^2s^{-1})
E_d	activation energy for self diffusion ($kJmol^{-1}$)
i^a_p	peak oxidation current (A)
i^c_p	peak reduction current (A)
$E^{o'}$	formal potential, $= (E^a_p - E^c_p)/2$ (V)
E	measured potential (V)
ΔE_p	peak potential separation for a cyclic voltammogram, $\Delta E_p = E^a_p - E^c_p$
E^a_p	peak oxidation potential (V)
E^c_p	peak reduction potential (V)
$E^a_{p/2}$	potential at half peak oxidation current (V)
$E^c_{p/2}$	potential at half peak reduction current (V)
Ru	uncompensated resistance (Ohms)
m/z	mass per unit charge
M	molarity ($mol\ dm^{-3}$)
M.P.	melting point
Esd	estimated standard deviation

1 Introduction

1.1 Nuclear Fuel

Uranium is the heaviest naturally occurring element, and is usually found as an oxide, nitrate, acetate or other compound. The element contains 92 protons and between 138 and 147 neutrons, giving naturally occurring isotopes of uranium from ^{230}U through to ^{239}U, all of which are radioactive. Other isotopes are possible, but have a very short half-life. In its natural composition uranium has the isotopic composition, ^{238}U (99.27%), ^{235}U (0.72%) and a small amount of ^{234}U (0.0055%). The other isotopes of uranium have to be produced by bombarding elements (thorium, uranium, etc) with protons, neutrons or other particles.

Throughout its brief history, nuclear fuel has been produced in a variety of forms.[1] Nuclear fuel occurs as uranium metal, uranium oxides, and mixtures of oxides (MOX) of uranium and plutonium. It may contain uranium in the isotopic ratio found in nature, or it may be enriched with one of the isotopes, normally fissile ^{235}U. MOX fuels have the advantage of using up stores of weapons-grade plutonium, with ^{239}Pu replacing ^{235}U as the fissile material. Countries with large thorium deposits (e.g. India) thorium based reactor systems have been designed . Neutron capture followed by two β-decay processes results in the formation of fissile ^{233}U from ^{232}Th.

1.2 Why reprocess nuclear fuel?

After about four years of operation in nuclear power stations, nuclear fuel pins contain around 96% uranium, 3% fission products (F.P) and 1% plutonium, causing the fission of uranium to be less efficient. Fission products are produced by the fissile element ^{235}U absorbing a 'thermal' neutron ('fast' neutrons moderated by graphite), this extra neutron destabilises the ^{235}U and causes nuclear fission. The fission process involves the splitting of the uranium atom into two daughter elements and up to 3 fast neutrons, thus causing the chain reaction in nuclear reactors. This is shown in simplified form in figure 1.1. ^{239}Pu is produced by ^{238}U absorbing 'fast' neutrons and then undergoing transmutation through a series of beta decays, this is shown in equation (1).

$$^{238}_{92}U \xrightarrow{n} {}^{239}_{92}U \xrightarrow{-\beta^-} {}^{239}_{93}Np \xrightarrow{-\beta^-} {}^{239}_{94}Pu \qquad (1)$$

When ^{235}U undergoes nuclear fission, two or more daughter nuclei are formed, these can also be radioactive and undergo further fission themselves. Typical products of ^{235}U fission are strontium, iodine and xenon, but there are many other possibilities. Since the fission products can themselves undergo fission, the eventual mixture of elements can be rather complex.

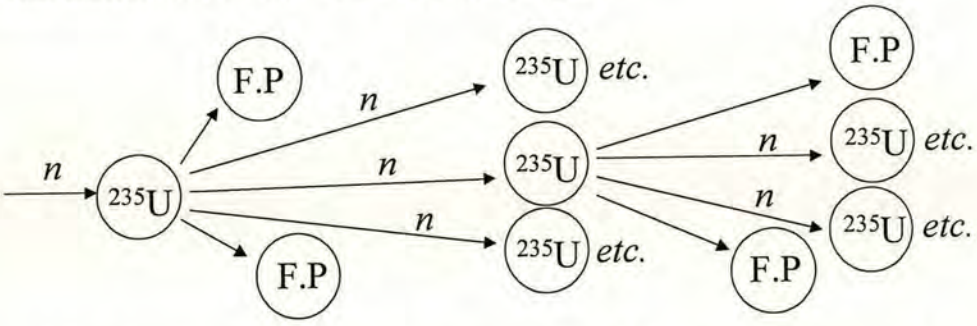

Figure 1.1: Schematic diagram of nuclear fission of ^{235}U in a nuclear reactor to produce a nuclear chain reaction.

By separating the fission products from the uranium and plutonium, it is possible to recover valuable fuel, reduce the volume of radioactive waste, eliminate the need to mine new supplies of uranium and extend the lifetime of resources.

1.3 Current methods of nuclear fuel reprocessing

Spent nuclear fuel consists of 97% uranium and plutonium by metal. Rather than direct disposal of these materials, reprocessing offers the chance to reuse these materials as fuel. Current methods of reprocessing involve solvent extraction,[2] although other means of reprocessing are being investigated.[3,4]

1.3.1 The PUREX process

The Plutonium-Uranium Extraction (PUREX) process was developed during the 1950's and is the basis for the reprocessing of metallic and oxide fuel.[2] The Thermal Oxide Reprocessing Process (THORP) facility run by British Nuclear Fuels Limited (BNFL) in Sellafield, Cumbria, is based on the PUREX process, and separates the spent fuel into uranium, plutonium and fission products. The recovered uranium and plutonium is fabricated into new fuel pins while the fission products are vitrified and prepared for long-term storage.

At the THORP facility, the first step in reprocessing is the removal of the fuel cladding (the housing used to hold the fuel pellets together and prevent release of volatile fission products) by a mechanical chopper to expose the oxide fuel. The oxide fuel is then dissolved in concentrated nitric acid and the aqueous stream is then contacted with a solution of tributylphosphate in odourless kerosene (TBP/OK). This is done using a pulsed column with the aqueous inlet at the top, aqueous outlet at the bottom, TBP/OK inlet at the bottom and TBP/OK outlet at the top as shown in figure 1.2.

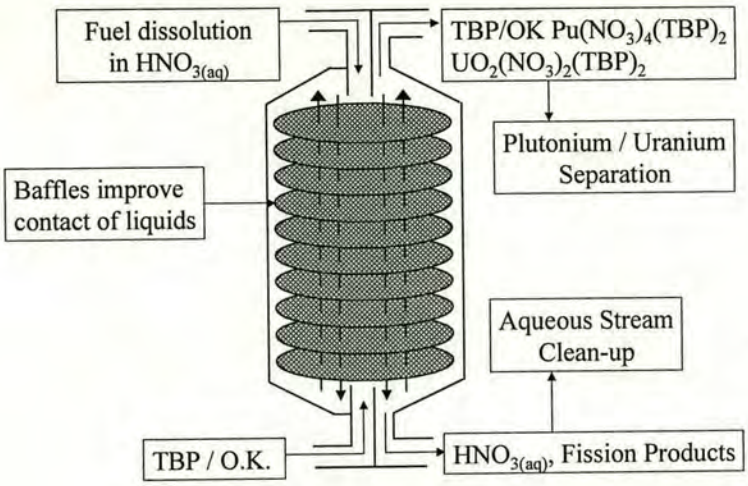

Figure 1.2: Schematic of the solvent extraction stage of the PUREX process showing the inlets and outlets of the pulsed column.

The UO_2^{2+} and Pu(IV) present in the nitrate solution are complexed as $UO_2(NO_3)_2(TBP)_2$ and $Pu(NO_3)_4(TBP)_2$ and are extracted from the aqueous layer into the organic phase. The plutonium is then separated from the uranium by contacting the TBP/OK with a fresh aqueous stream and selectively reducing the Pu(IV) to Pu(III) with hydrazine, which is extracted into a fresh aqueous stream and then precipitated using oxalate. The plutonium and uranium are then worked up to their oxides and either stored or returned to the fuel cycle. This process is outlined schematically in figure 1.3.

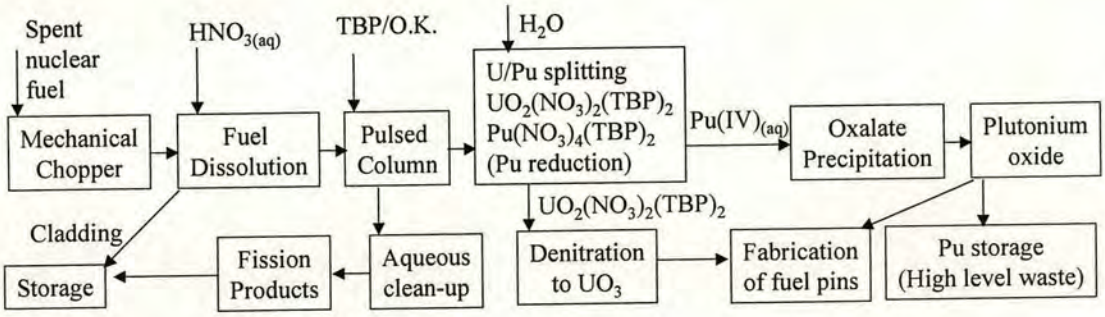

Figure 1.3: The PUREX process at the THORP facility in Sellafield, Cumbria.

1.3.2 Pyrochemical processing

Pyrochemical processes involve the use of molten salts as a solvent and are carried out at elevated temperatures, usually above 973K. Molten salts are inorganic salts such as NaCl, $KAlCl_4$ or $SrCl_2$ heated to temperatures above their respective melting points. Alternatively, two salts may be mixed to reduce the melting point of the mixture, such as NaCl / KCl, these melt at a temperature lower than the lowest melting component and are referred to as eutectic melts at the composition corresponding to the lowest melting point. Molten salts are highly corrosive media, require handling under dry atmospheres and the use of expensive materials for reactors such as Hastalloy (an alloy mainly composed of Mo and Cr, but also containing Fe, W, Co, Mn, C, Si, V and Ni). An industrial example of a molten salt process is the Hall-Heroult process, where molten cryolite (Na_3AlF_6) is the electrolytic medium and alumina is the feedstock in the electrochemical recovery of aluminium.

The desire to eliminate volatile organic solvents (for environmental and safety concerns) and reduce aqueous streams (decontamination of aqueous stream before release to effluent is technically challenging) has led to the investigation of new systems for the reprocessing of spent nuclear fuel. In the 1970's, the United States government decided to halt PUREX reprocessing of spent nuclear fuel to minimise the generation of waste products and to limit the availability of weapons grade plutonium, a product of the PUREX process.[3]

1.4 Ionic liquids

1.4.1 Introduction

Ionic liquids are often referred to as room temperature molten salts, that is they are similar to the high temperature molten salt systems described above, but are generally liquids at temperatures below 373K or at room temperature. In order to obtain this lowered melting point with respect to molten salts, large bulky organic cations are used in place of metal cations. This lower melting point can be explained by the Kapustinskii equation, equation (2), the best known general method for estimating lattice energies. As can be seen, the lattice energy is inversely proportional to the sum of the ionic radii, and a lowering in the lattice energy results in a reduced melting point.

$$\Delta U(0\ K) = kv\ |z_+||z_-| / (r_+ + r_-) \qquad (2)$$

Where ΔU is lattice energy ($kJmol^{-1}$), k is a constant ($1.07 \times 10^5 kJÅmol^{-1}$), v is the number of ions in the molecular formula of the salt, z_+ and z_- are the charge numbers on the cation and anion and r_+ and r_- are the ionic radius (Å) of the cation and anion respectively. The cations are usually based on bulky asymmetric organic cations, such as the *N,N*-dialkylimidazolium and *N*-alkylpyridinium cations, and an organic or inorganic anion, such as lactate or chloride respectively. Examples include 1-ethyl-3-methyl-imidazolium chloride, [Emim][Cl], **1**, 1-butyl-3-methyl-imidazolium tetrafluoroborate, [Bmim][BF_4], **2**, and *tetra*-butylammonium trifluoroacetate,[TBA][Tf], **3**. The structures of these compounds are shown in figure 1.5. Excellent reviews of the properties and uses of ionic liquids are available[7].

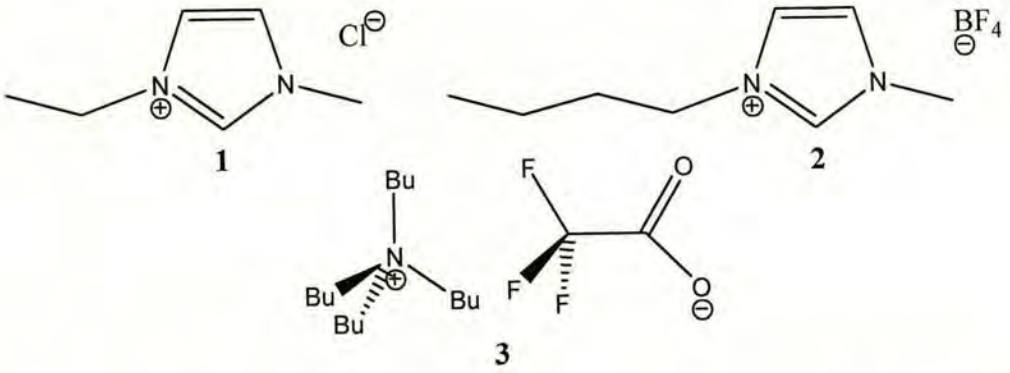

Figure 1.5: Structures of commonly used ionic liquids, **1**: 1-ethyl-3-methylimidazolium chloride, **2**: 1-butyl-3-methylimidazolium tetrafluoroborate, **3**: *tetra*-butylammonium trifluoroacetate.

Early work using ionic liquids focussed on the chloroaluminate systems, these systems were widely used due to their low viscosity, low melting point and adjustable Lewis acidity. By mixing varying compositions of $AlCl_3$ and chloride ionic liquids, one can obtain Lewis basic, neutral or acidic melts. For compositions up to 50 mole % $AlCl_3$, the melt contains $[AlCl_4]^-$ and $[Cl]^-$, and it is the free $[Cl]^-$ that makes this melt Lewis basic. The Lewis neutral melt is obtained when the melt is composed of 50 mole % $AlCl_3$, with $[AlCl_4]^-$ present as the only anionic species. Lewis acidic melts are produced from melts that contain more than 50 mole % $AlCl_3$, giving $[AlCl_4]^-$ and $[Al_2Cl_7]^-$ as the main anionic species, although for very acidic melts (mole % $AlCl_3$ = 67 - 75%) the $[Al_3Cl_{10}]^-$ anion has been observed.[8]

Ionic liquids have possible advantages over high temperature molten salts in that they melt at a much reduced temperature, thus lowering operating temperature, operating costs and allowing the possibility of adding materials such as organic complexing agents without them being destroyed by the high temperatures involved in molten salt systems. Operating at lower temperatures would also give much greater control over the reactions, leading to higher yields and product purity. The number of possible organic cations available allows for fine-tuning of the cathodic limit of the electrochemical window (the potential at which the cation is reduced) whereas in the high temperature systems there are a limited number of metal cations

used. The choice of anion generally determines if the ionic liquid is hydrophobic or hydrophilic, and will also determine the coordination environment of dissolved transition metal species. The use of ionic liquids also allows for possible recycle of solvent,[9] leading to significantly less waste generation.

1.4.1 Actinide and Lanthanide chemistry in ionic liquids

To date the majority of work on actinides and lanthanides in ionic liquids has been carried out in Lewis acidic or basic chloroaluminate systems. As far back as far as 1982, DeWaele *et al.*[10] demonstrated that uranium (IV) chloride was soluble in the Lewis acidic *N*-butylpyridinium chloroaluminate ionic liquid and could be electrochemically reduced to U(III) or oxidised to U(V), which in turn could be oxidised to U(VI). Schoebrechts and Gilbert[11] demonstrated that in Lewis acidic *N*-butylpyridinium chloroaluminate melts, the Np(IV)/(III) redox couple is similar in terms of complexation and electron-transfer properties to its actinide neighbour U(IV)/(III), this was attributed to similar ionic radii. Studies in the Lewis acidic $AlCl_3$/[Emim][Cl] melt found that the uranyl species, $[UO_2]^{2+}$, could be reduced to the U(V), U(IV) and U(III) species, but was unstable and lost it's '-yl'-oxygens to form a chloride complex.[12] Dissolution of uranium dioxide was achieved under oxidative conditions in the Lewis basic $AlCl_3$/[Emim][Cl] ionic liquids, where electrolysis produced the U(IV) species and also led to deoxygenation of the uranium species.[13] In Lewis basic $AlCl_3$/*N*-butylpyridinium chloride melts, U(III) was found to be an unstable oxidation state and was oxidised by the *N*-butylpyridinium cation, $[BuPy]^+$. The absorption spectrum of the resulting solution showed the combined spectrum of $[UCl_6]^{2-}$ and the 1,1`-dibutyl-4,4`-bipyridinium radical cation, a product of the primary pyridinyl radical coupling.[14]

Studies by S. Dai *et al.* at Oak Ridge National Laboratories (ORNL) have also demonstrated the spontaneous reduction of the U(V) hexachloride complex to the U(IV) hexachloride complex when the solvent is moved from a Lewis acidic composition to a Lewis basic composition.[15] Other work at ORNL has demonstrated the dependence of the solubility of uranium oxide complexes upon the organic cation

of the ionic liquid[16] showing increasing solubility with increasing hydrogen-bonding ability of the cation.

In joint work carried out between the Department of Chemistry at Florida State University, ORNL and Los Alamos National Laboratories (LANL), the spontaneous conversion of $[UO_2]^{2+}$ to U(V) was observed in an acidic chloroaluminate ionic liquid.[17] A three-step mechanism was proposed by Choppin *et al.* whereby oxygen is removed and the U(VI) is reduced by the solvent, eqn (3)-(5). Reaction (4) was determined to be the rate-limiting step.

$$[UO_2]^{2+} + [Al_2Cl_7]^- \leftrightarrow [UO]^{4+} + [AlCl_4]^- + [AlOCl_3]^{2-} \quad (3)$$

$$[UO]^{4+} + [Al_2Cl_7]^- \leftrightarrow U^{6+} + [AlCl_4]^- + [AlOCl_3]^{2-} \quad (4)$$

$$U^{6+} + 2[AlCl_4]^- \leftrightarrow U^{5+} + [Al_2Cl_7]^- + {}^1\!/_2Cl_{2(g)} \quad (5)$$

Recent work at ORNL[18] has demonstrated the extraction of strontium nitrate from an aqueous media, using a crown-ether dissolved in the hydrophobic 1-butyl-3-methylimidazolium hexafluorophosphate, [Bmim][PF_6], ionic liquid. This is extremely relevant to the direct solvent replacement in a PUREX type process, with the [Bmim][PF_6] replacing the organic solvent phase.

Interest in ionic liquids for the purification of actinides and actinide waste forms at LANL is highlighted in a recent publication by D.A. Costa *et al.*[19] Electrochemical studies of $PuCl_3$ and $Cs_2PuO_2Cl_2$ dissolved in Lewis basic $AlCl_3$/[Emim][Cl] show a pseudo-reversible Pu(IV)/(III) couple, and neither Pu(IV) or Pu(III) are soluble in the Lewis acidic $AlCl_3$/[Emim][Cl] melt. More recent work from D.A. Costa *et al*[20] has focussed on developing ionic liquids with increased electrochemical stability, air and water stability, water immiscibility, lowest possible viscosity, highest possible conductivity and high actinide solubility to allow for electrodeposition of the electropositive actinides. To achieve this they focussed upon ionic liquids where the anion was the bis(trifluoromethanesulfonyl)imide anion,

$[N(SO_2CF_3)_2]^-$, abbreviated to $[N(Tf)_2]^-$. The cations used were of the imidazolium, quaternary ammonium and pyrrolidinium type. It was found that $UO_2(NO_3)_2(OH_2)_2$, $UI_3(thf)_4$ and $UBr_4(NCMe)_3$ were soluble in all the $[N(Tf)_2]^-$ ionic liquids tested, however UCl_4 was found to be only slightly soluble at ambient temperatures. By adopting a common strategy of synthesising the $[UCl_6]^{2-}$ salt, solubility was greatly increased, (6).

$$2[\text{cation}][Cl] + UCl_4 \longrightarrow [\text{cation}]_2[UCl_6] \qquad (6)$$

Electrochemical studies have been carried out using the $[N(Tf)_2]^-$ salt with the *N*-methyl-*N*-(2-methoxyethyl)pyrrolidinium cation, and two redox couples are observed, although no formal assignments have been made to these peaks. Similar results have been obtained using the imidazolium cation. Additional research[21] by the same group has demonstrated the reversible deposition and stripping of the electropositive metals sodium and potassium from the salts $[K][N(Tf)_2]$ or $[Na][N(Tf)_2]$ dissolved in $[NMe_2(i\text{-}Pr)(n\text{-}Pr)][N(Tf)_2]$, **4**, both of which have reduction potentials more negative than all the actinides, showing the potential applicability of these ionic liquids for the electrodeposition of actinide elements. Further work from LANL[22] focuses on the coordination of uranyl dichloride in ionic liquids. It was found that treatment of $UO_2Cl_2(thf)_3$ in THF with two equivalents of 1,3-dimesitylimidazole-2-ylidene (IMes) or 1,3-dimesityl-4,5-imidazole-2-ylidene ($IMesCl_2$) results in the formation of novel monomeric uranyl *N*-heterocyclic carbenes (NHC's), representing the first case of actinyl carbon bonds. As it is thought these carbene complexes can be formed in ionic liquids through control of pH, this work shows potential as novel separation technology based on imidazolium-cation/NHC interconversion.

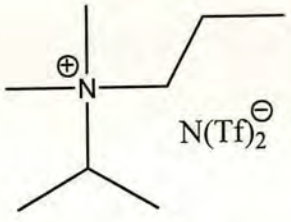

4

Investigators at the Centre for Radiochemistry Research at the University of Manchester[23] have also focussed on extending the electrochemical stability of ionic liquids for the electrodeposition of electropositive metals. The strategy was to prepare group 15 quaternary alkyl bis(trifluoromethanesulfonyl)imide salts and investigate the electrochemistry of lithium and europium in these melts. The ionic liquids prepared were $[(Me)_4X][N(Tf)_2]$, where X = N, P or As, and the cathodic stability was observed to follow the order $[As(Me)_4]^+ > [P(Me)_4]^+ > [N(Me)_4]^+$. Lithium stripping/plating at a glassy carbon electrode was observed just before the cathodic limit in the $[(Me)_4P][N(Tf)_2]$ melt at 463K. To further demonstrate the applicability of these melts for the deposition of U or Pu, cyclic voltammetry of $Eu[N(Tf)_2]_3$ in $[(Me)_4P][N(Tf)_2]$ was carried out and the Eu(III)/(II) and Eu(II)/(0) couples were both observed. The standard reduction potential of Eu(II)/(0) is -2.81V, which is more negative than that of Pu(III)/Pu, -2.01V, showing the possible applicability of these melts in the nuclear fuel cycle. Preliminary investigations of other Ln(III) ions have shown the electrodeposition of La and Sm.

Other groups investigating the chemical and electrochemical properties of lanthanides in ionic liquids include I. Wen Sun at the National Cheng Kung University in Taiwan. Studies of Ytterbium in $AlCl_3$/[Emim][Cl] system[24] showed that in the Lewis basic $AlCl_3$/[Emim][Cl] (44.4 mol% $AlCl_3$), Yb (III) is present as $[YbCl_6]^{3-}$ and can be reduced to a Yb (II) species by a quasi-reversible one electron charge-transfer process. It is suggested that Yb (II) is present as $[YbCl_5]^{3-}$, due to the dependency of the formal potential, $E^{o'}$, of this redox reaction on the $p[Cl]^-$ of the basic melt. Yb(II) was unstable in the basic melt as it was observed to be slowly oxidised by some components of the melt. In acidic melts the Yb(III)/(II) redox couple is a reversible one electron charge-transfer process, but occurs at around 2.5V more positive, indicating a significant change in the coordination sphere from that in the basic melts. The electrochemistry of Eu(III)/(II) in $AlCl_3$/[Emim][Cl][25] melts is similar to Yb(III)/(II), except Eu(II) is stable in the Lewis basic melt and is believed to be complexed as $[EuCl_4]^{2-}$.

1.4.2 Electrodeposition from ionic liquids

As with most electrochemical studies in ionic liquids, the vast majority of the literature on electrodeposition using ionic liquids is in the chloroaluminate melts. This is presumably due to the adjustable Lewis acid/base properties of these melts, wide electrochemical windows and low viscosities. An important feature of solvents for deposition of metals is the electrochemical window that they posses, and is quite simply the potential range that can be accessed without significant currents due to solvent or electrolyte breakdown. As has been mentioned earlier, the anionic species in chloroaluminate melts depends on the mole ratio of $AlCl_3$. This variation of anion results in electrochemical windows ranging from 2-4V depending upon the composition of the melt. An example of the electrochemical windows observed in the chloroaluminate melts is demonstrated by the $AlCl_3$/[Emim][Cl][26] melt as shown in Figure 1.6.

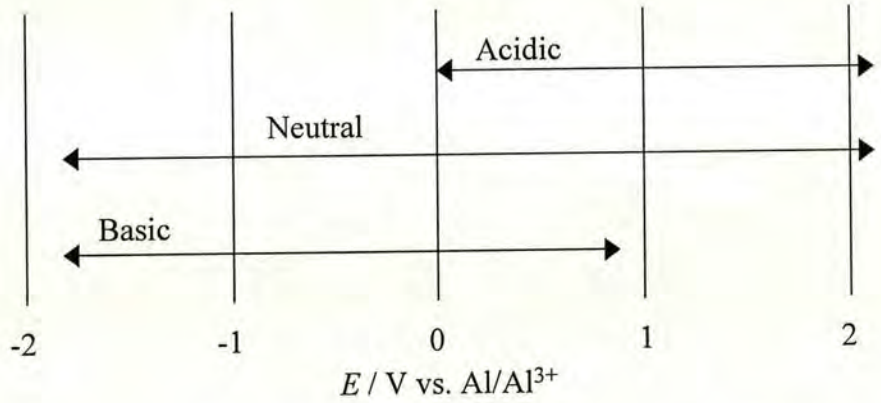

Figure 1.6: Electrochemical windows of $AlCl_3$/[Emim][Cl] depending upon the composition of the melt.

In the Lewis acidic and Lewis neutral regimes, oxidation is limited by formation of chlorine from chloroaluminate complexes, in the Lewis basic melts it is limited by chlorine formation from the chloride anion. In Lewis acidic chloroaluminates the cathodic limit is determined by aluminium deposition from $[Al_2Cl_7]^-$, in Lewis basic and neutral melts it is limited by the reduction of the cation.

Obviously the choice of cation is important in electrochemistry, not only in terms of lowering the melting point as mentioned earlier, but also to increase the cathodic stability of the ionic liquid if required. Aluminium electrodeposition is only possible from Lewis acidic ambient temperature chloroaluminate melts since in the neutral and basic melts reduction of the organic cation takes place before reduction of $[AlCl_4]^-$.

The possibility of using room temperature chloroaluminate melts for the electrodeposition of aluminium was first realised by Hurley and Wier as far back as 1948[27] where they proposed using *N*-alkylpyridinium chloride (or bromide) mixed with $AlCl_3$ in the presence of benzene or its derivatives as a co-solvent. As an example they cited (66.6:33.3 mole %) $AlCl_3$/*N*-ethyl pyridinium chloride with toluene added until it formed a layer on top. Current densities of 0.5 - 1 Adm^{-2} and aluminium electrodes were employed. Hurley[28] also submitted a patent the same year outlining the potential use of pure (63.0:37.0 mole %) $AlCl_3$/*N*-ethylpyridinium chloride (or bromide) at 398K for the electrodeposition of aluminium employing similar current densities and electrodes as above. Studies have shown that the aluminium deposits obtained from acidic chloroaluminate ionic liquids[29,30] show superior deposits compared to those obtained from organic solutions. Addition of benzene to chloroaluminate melts was found to result in mirror bright deposits of aluminium upon electrodeposition.[31]

Studies of copper in (67:33 mole %) $AlCl_3$/*N*-methylpyridinium chloride[32] found that the Cu(II)/(I) redox couple was reversible at both glassy carbon and tungsten electrodes. It was also found to be possible to deposit copper from Cu(I) containing solutions at these electrodes, obeying criteria for instantaneous three dimensional nucleation followed by hemispherical growth of the nuclei. At Pt electrodes the deposition of copper was preceded by nucleation but was considerably faster than for the other two electrode materials and this required a smaller overpotential. Using a closely related molten salt, (66:34 mole %) $AlCl_3$/[Bmim][Cl], containing $CuCl_2$, Cu(II) was reversibly reduced to Cu(I) and

copper was electrodeposited from Cu(I) onto an Au(111) surface and highly oriented pyrolytic graphite (HOPG).[33] Several underpotential deposition processes were observed on an Au(111) surface and by reducing the potential further 3-D nucleation became more pronounced. At overpotentials of -5-10mV columnar growth of copper was observed. In contrast, only overpotential deposition was observed on HOPG, with overpotentials of -100mV resulting in nucleation of copper preferentially occurring on the basal planes of HOPG, the transient being consistent with instantaneous nucleation. At overpotentials larger than -100mV the mechanism changed from instantaneous to progressive nucleation at a limited number of sites. Copper electrodeposition has also been observed in basic melts[34] at the nitrogen-incorporated tetrahedral amorphous (taC:N), platinum and glassy carbon electrodes. Using a (47.5:52.5 mole %) $AlCl_3$/1-ethyl-3-methylimidazolium chloride melt at 308-313K containing Cu(I) introduced through controlled coulometric anodisation of copper mesh, it was observed that copper deposition showed a higher nucleation overpotential for deposition on a taC:N electrode than that observed on platinum or glassy carbon electrodes. The electrodeposition of copper from Cu(I) at taC:N and its anodisation showed an unusual delayed stripping behaviour where most of the deposit was removed only when the potential reached that of Cu(I) oxidation. The deposition of copper on taC:N agreed with the model of progressive nucleation with three-dimensional growth with slight deviation from ideal behaviour at very high overpotentials, attributed to the low density of active nucleation sites.

Similar electrochemical studies[35] were performed using Co(II) in the (67:33 mole %) $AlCl_3$/*N*-n-butylpyridinium chloride melt. Cobalt deposition and stripping was observed at a glassy carbon electrode although in the more Lewis acidic melts (67 mole % $AlCl_3$) co-deposition of aluminium from the melt was observed. However, by decreasing the melt acidity (53.3 mole % $AlCl_3$) it was possible to obtain a deposition/stripping voltammogram that appeared to involve only one redox species.

The electrodeposition of lead[36] at a glassy carbon electrode from solutions of $PbCl_2$ or electrogenerated Pb(II) in (66.7:33.3 mole %) $AlCl_3$/[Emim][Cl] exhibited progressive three-dimensional nucleation with diffusion controlled growth of the nuclei. Stripping of lead from this electrode occurred with 100% efficiency. In similar studies from the same research group, the deposition/stripping of silver[37] was investigated using the same chloroaluminate melt at four different electrodes: polycrystalline gold, platinum, tungsten and glassy carbon. Large overpotentials were required to deposit silver at glassy carbon and tungsten electrodes. Deposition at tungsten was found to involve progressive three-dimensional nucleation, whereas deposition at glassy carbon involved instantaneous three-dimensional nucleation. Both electrodes displayed hemispherical diffusion-controlled growth of the nuclei. In contrast, multiple deposition waves were observed at a gold electrode, resulting from underpotential deposition of more than one monolayer, but less than two monolayers of silver. At platinum electrodes, the silver deposition/stripping process appeared to be less complicated with no obvious signs of nucleation kinetics or underpotential deposition phenomena. Bulk plating/stripping at all four electrodes showed virtually 100% efficiency. The electrodeposition of silver on HOPG[38] from (55:45 mole %) $AlCl_3$/[Bmim][Cl] containing AgCl was found to require an overpotential of -300mV to -350mV. With rising overpotential the deposition mechanism changed from progressive three-dimensional nucleation at a finite number of active sites to instantaneous three-dimensional nucleation. In the far overpotential range deposition was found to occur mainly at steps and defects between different basal planes of graphite and to a lesser extent on the basal planes themselves as evidenced by STM studies. Silver deposited on flame annealed Au(111) films from (66.6:33.3 mole %) $AlCl_3$/[Bmim][Cl][39] resulted in diffusion controlled growth in the overpotential deposition regime and the current transients showed no sign of the typical 3-D nucleation and growth observed on HOPG.[38]

The desire to develop practical secondary batteries using room temperature chloroaluminates as electrolytes has led to research on the plating/stripping of lithium and sodium from $AlCl_3$/[Emim][Cl] melts.[40] The reduction of lithium was observed at the cathodic limit of the Lewis neutral melt buffered with LiCl but no re-oxidation was observed. Sodium reduction occurs beyond the cathodic limit of the NaCl buffered Lewis neutral $AlCl_3$/[Emim][Cl] melt. Addition of a proton source, triethanolamine hydrogen chloride, extended the cathodic limit of the melt by *ca.* 0.3V. No explanation was given for the extension of the cathodic limit through the addition of a proton source. This resolved the lithium deposition process from the cathodic limit of the solvent and the reverse wave was observed at least for a short time. This increased cathodic stability allowed for the electroplating of sodium to be observed within the electrochemical window of the melt, although it was not completely resolved from the reduction of the solvent. Careful choice of reversal potential was required for the stripping peak to be observed as scanning beyond the reduction peak led to passivation of the electrode.

The electrochemistry of indium[41] in (44.4:55.6 mole %) $AlCl_3$/1,2-dimethyl-3-propylimidazolium chloride ($AlCl_3$/[DMPim][Cl]), thallium[42] in (44.4:55.6 mole %) $AlCl_3$/[Emim][Cl] and tellurium[43] in (44.4:55.6 mole %) $AlCl_3$/[Emim][Cl] showed the possibility of depositing *p*-block elements from ionic liquids. Electrodeposition of indium on glassy carbon, tungsten and nickel electrodes proceed by a three electron reduction of $[InCl_5]^{2-}$ to indium with large overpotentials being necessary. The deposition of indium on nickel electrodes involved progressive three-dimensional nucleation with diffusion controlled growth of the nuclei, whereas on carbon and tungsten electrodes, deposition involved progressive three-dimensional nucleation on a limited number of active sites followed by diffusion controlled growth. Thallium exists in the Lewis basic melt as $[TlCl_6]^{3-}$ and can be electrochemically reduced to a Tl(I) species, with the electrode reaction exhibiting slow charge-transfer kinetics and the formal potential of the couple being dependent on chloride ion concentration. The Tl(I) species, thought to be $[TlCl_4]^{3-}$ can be further reduced to give thallium metal at nickel and tungsten electrodes. The

electrodeposition process involved instantaneous three-dimensional nucleation with diffusion controlled growth of the nuclei. Tellurium existed in basic melts as $[TeCl_6]^{2-}$ which could be reduced to tellurium metal at a glassy carbon electrode by a four electron charge-transfer process, and involved nucleation under kinetic control.

Chloroaluminate ionic liquids show promise for use as electrolytes, although they do have disadvantages, among them are their high sensitivity to moisture (which leads to the breakdown of the melt) and contamination of deposits with aluminium. As a result of this, non-chloroaluminate ionic liquids have also been used for the study of electrodeposition of metals and main group elements. One such study is the electrodeposition of copper from the Lewis basic [Emim][Cl]/[Emim][BF_4] ionic liquid.[44] Copper could be deposited from a Cu(I) solution on both a platinum and glassy carbon electrode. Underpotential deposition was observed at the Pt electrode whereas overpotential deposition was observed at the glassy carbon electrode. The chemical and electrochemical behaviour of Cu(I) in [Emim][Cl]/[Emim][BF_4] was very similar to that observed in the Lewis basic $AlCl_3$/[Emim][Cl] melts.

The electrochemical behaviour of cadmium was also studied in this melt, at platinum, tungsten and glassy carbon electrodes.[45] Sufficient chloride ion concentrations were required for the electrodissolution of the deposited cadmium to produce the soluble $[CdCl_4]^{2-}$ ion. Cadmium was found to deposit at all three electrodes from the [Emim][Cl]/[Emim][BF_4] ionic liquid, with the platinum electrode showing the highest nucleation overpotential. Chronoamperometry experiments revealed the electrodeposition of cadmium on all three electrodes involved three-dimensional progressive nucleation with diffusion controlled growth. The cadmium deposit adhered well to the tungsten electrode and was shown to be free from halide impurities by energy dispersive spectroscopy, EDS.

The electrochemistry of silver was studied in the pure [Emim][BF_4] ionic liquid and it was possible to introduce Ag(I) into solution using the $AgBF_4$ salt. The electrodeposition/stripping of silver at a platinum electrode was found to be electrochemically irreversible. From diffusion coefficient measurements the

solvodynamic radius of the Ag(I) species was determined, and from this was suggested to exist essentially as a "bare" cation in [Emim][BF_4].

The electrodeposition of thin films of germanium[46] on gold substrates from GeI_4 dissolved in [Bmim][PF_6] has been reported. No re-oxidation of the deposited films were observed on the reverse scan and this was attributed to chemical attack of the films by GeI_4 in solution. This was evidenced by the deposit disappearing when the electrode current control was turned off. The maximum thickness of germanium film obtained was around 20nm. In an effort to improve upon the deposition of Ge films, the same workers investigated using $GeBr_4$[47] and $GeCl_4$[48] as sources of Ge in [Bmim][PF_6]. From $GeBr_4$ a thin layer with rather metallic behaviour formed on Au(III) before bulk deposition of Ge was observed. The bulk growth begins with formation of nanoclusters and layers with thickness of roughly 5 μm can be prepared. Scanning electron microscopy, SEM, showed the deposits are like nano-sized wires of Ge growing from the electrode surface. Again, no re-oxidation of the deposited Ge was observed in the cyclic voltammogram, this was attributed to chemical attack of the deposit by $GeBr_4$. Electrochemical studies using $GeCl_4$ as the germanium source was found to give the most chemically reversible electroplating/stripping behaviour of the germanium halides studied by the fact a re-oxidation wave was observed after deposition of Ge. Underpotential deposition was observed, giving Ge islands with apparent heights of 150 pm (measured by STEM) which can be reversibly stripped from the surface. Before bulk Ge deposition occurred, a rough but completely closed layer with a maximum thickness of 300 pm was formed, this was attributed to alloying between Ge and Au due to the metallic nature of the layer.

Numerous studies have also focussed on the deposition of alloys from ionic liquids, mostly concerning the electrodeposition of a metal solute with aluminium from a chloroaluminate melt, many examples of which are given in a recent review.[49]

1.4.4 Diffusion coefficients in ionic liquids

The diffusion coefficient of a solute species is the rate at which the species and its solvation shell move through the solution it is dissolved in, and is governed by the Stokes–Einstein equation, (7).

$$D = {}^{(kT)}/_{(6\pi\eta r)} \qquad (7)$$

Where D is the diffusion coefficient (m^2s^{-1}), k is the Boltzmann constant ($1.38065 \times 10^{-23}/JK^{-1}$), η is the viscosity ($kgms^{-2}$) and r is the Stokes radius , also known as the solvodynamic radius (m). Examples of diffusion coefficient values[50] of different species in different solvents are given in table 1.1.

Molecules in liquids				**Ions in water**			
I_2 in hexane	4.05	**N_2 in $CCl_{4(l)}$**	3.42	**H^+**	9.31	**F^-**	1.46
Sucrose in H_2O	0.52	**O_2 in $CCl_{4(l)}$**	3.82	**Na^+**	1.33	**Cl^-**	2.03
H_2 in $CCl_{4(l)}$	9.75	**Ar in $CCl_{4(l)}$**	3.63	**K^+**	1.96	**Br^-**	2.08

Table1.1: Diffusion coefficients at 298K, $D/(10^{-9}\ m^2s^{-1})$ or $(10^{-5}\ cm^2s^{-1})$.

Generally speaking, the smaller the diffusing species (molecule/ion and solvation sphere) the larger the diffusion coefficient. Small ions give rise to stronger electric fields than larger ions since the electric field at the surface of a sphere of radius r is proportional to ze/r^2. Small ions thus tend to have large solvation spheres, and their effective (solvodynamic) radius tends to be larger than that of larger ions. That is why in table 1.1, Na^+ has a smaller D value than K^+, because its solvation shell is larger than that of K^+ and thus its solvodynamic radius is also larger, resulting in a lower diffusion coefficient.

An interesting question arises when considering the diffusion of ionic species in an ionic environment, and that is do these ionic species diffuse as bare or "naked" ions, or do they diffuse with components of the ionic liquid solvent, i.e. with a solvation sphere. Much information on diffusion coefficients have been obtained from ionic liquids, due in part to the study of electrodeposition and speciation of metals in ionic liquids, and also as a direct study of diffusion in these novel solvents. There have been diffusion coefficient studies of many different species in ionic liquids ranging from transition metal complexes,[51] lanthanides,[24,25,52] actinides,[10,11,13,14,53] organometallic complexes[54] and organic molecules.[55] It is generally true that diffusion coefficients are lower in ionic liquids than in molecular solvents due to their inherently higher viscosities.

1.5 Conclusions

If ionic liquids are to be used in the nuclear fuel cycle as a replacement for high temperature molten salts, i.e, the LiF/NaF/KF (FLINAK) eutectic salt, they must approach or surpass the advantages that molten salts bring to the industry. These advantages have been highlighted as low vapour pressure, large electrochemical window, large liquid range and inherently high conductivities. Preliminary investigations[56] of the 1,3-dialkylimidazolium ionic liquids of the nitrate and chloride anions, show the stability of ionic liquids to alpha and gamma radiation doses encountered in the reprocessing of spent nuclear fuel. Results suggest the stability of the ionic liquids are comparable to that of benzene under similar conditions, and there is no significant decomposition of the organic cation.

As has been stated previously, the majority of electrochemistry in ionic liquids has been undertaken in the haloaluminate systems. The suitability of the chloride based ionic liquids for use in electrochemistry will be investigated, as well as the more recently developed bis(trifluoromethanesulfonyl)imide ionic liquids. The use of cations other than the commonly used 1,3-dialkylimidazolium cation shall also be investigated. Cyclic voltammetry (CV) will be employed to investigate the electrochemistry of the ionic liquids as electrolytes, and the electrochemistry of solutes in ionic liquids. Potential step experiments will be undertaken to ascertain transport properties of solutes in ionic liquids, and these shall be compared to that of solute species in high temperature molten salts.

There is still paucity in the data with regards to structural information of ionic liquids in the solid state. This is due to many of the ionic liquids forming glasses on transition into the solid state, resulting in difficulties in obtaining crystals of suitable quality for x-ray crystallographic structure determination. The interactions between the anion and cation in the solid state shall be investigated to ascertain the interactions that occur, giving an insight into the interactions that may occur in the liquid state. This technique is also used to determine the solute-solute and solute-

solvent interactions in the solid state, again giving insight into the interactions between the solute and ionic liquids in the molten state.

---

[1] Wilson, P.D. (1996) Basic Principles, in P.D. Wilson (ed.), *The Nuclear Fuel Cycle*, Oxford University Press, Oxford.

[2] Stoller, S.M. and Richards, R.B. (1961) *Reactor Handbook,* Interscience Publishers, Inc., New York.

[3] J.J. Laidler, J.E. Battles, W.E. Miller, J.P. Ackerman and E.L. Carls, *Progress in Nuclear Energy*, 1997, **31**, 131-140.

[4] O.V. Skiba, Y.P. Savochkin, A.V. Bychkov, P.T. Porodnov, L.G. Babikov and S.K. Vavilov, *GLOBAL*, 1993, **2**, 1344-1350.

[5] J.P. Ackermann, T.R. Johnson, L.S.H. Chow, E.L. Carls, W.H. Hannum and J.J. Laidler, *Progress in Nuclear Energy*, 1997, **31**, 141-154.

[6] V.A. Volkovich, T.R. Griffiths, R.C. Thied, *Journal of Nuclear Materials*, 2003, **323(1)**, 49-56.

[7] **(a)** J.D. Holbrey and K.R. Seddon, *Clean Products and Processes*, 1999, **1**, 223-236. **(b)** T. Welton, *ChemicalReviews*, 1999, **99**, 2071-2083.

[8] A.K. Abdul-Sada, A.M. Greenway, K.R. Seddon and T. Welton, *Org. Mass. Spectrom.*, 1989, **24**, 917-18.

[9] A.J. Jeapes, R.C. Thied, K.R. Seddon, W.R. Pitner, D.W. Rooney, J.E. Hatter, T. Welton, 2001, WO 2001015175 A2 20010301

[10] R. De Waele, L. Heerman and W. D'Olieslager, *J. Electroanal. Chem.,* 1982, **142,** 137-146.

[11] J.P. Schoebrechts and B. Gilbert, *Inorg. Chem.*, 1985, **24**, 2105-2110.

[12] P.B. Hitchcock, T.J. Mohammed, K.R. Seddon, J.A. Zora, C.L. Hussey and E.H. Ward, *Inorg. Chim. Acta.* 1986, **113**, L25-L26.

[13] C.J. Anderson, M.R. Deakin, G.R. Choppin, W. D'Olieslager and L. Heerman, *Inorg. Chem.*, 1991, **30**, 4013-4016.

[14] L. Heerman, R. De Waele and W. D'Olieslager, *J. Electroanal. Chem.,* 1985, **193**, 289-294.

[15] S. Dai, L.M. Toth, G.R. Hayes, and J.R. Peterson, *Inorg. Chim. Acta.,* 1997, **256,** 143-145.

[16] S. Dai, Y.S. Shin, L.M. Toth and C.E. Barnes, *Inorg. Chem.*,1997, **36**, 4900-4902.

[17] C.J. Anderson, G.R. Choppin, D.J. Pruett, D. Costa and W. Smith, *Radiochimica Acta.*, 1999, **84**, 31-36.

[18] S. Dai, Y.H. Ju and C.E. Barnes, *J. Chem. Soc., Dalton Trans.*, 1999, **8**, 1201-1202.

[19] D.A. Costa, W.H. Smith and H.J. Dewey, *Electrochemical society proceedings*, 2000, **99**(41), 80-99.

[20] K. Abney, E. Bluhm, E. Garcia, W. Smith, M. Barr, W. Oldham, D. Costa, D. Morris and D. Tait, FY000 yearly report, ADAPT program, Modern Pyroprocessing project. LA-UR-00-5043. http://lib-www.lanl.gov/la-pubs/00393792.pdf

[21] Oldham, W.J., Costa, D.A. and Smith, W.H. Development of room temperature ionic liquids for applications in actinide chemistry, *LANL internal yearly report*, LA-UR-01-2279,

http://lib-www.lanl.gov/la-pubs/00818127.pdf

[22] W.J. Oldham, S.M. Oldham, B.L. Scott, K.D. Abney, W.H. Smith and D.A. Costa, *Chem. Comm.*, 2001, **15**, 1348-1349.

[23] A. Bhatt, I. May, V. Volkovich, M.E. Hetherington, B. Lewin, R.C. Thied and N. Ertock, *Dalton.*, 2002, **24**, 4532-4534.

[24] W.J. Gau and I.W. Sun, *J. Electrochem. Soc.*, 1996, **143**, 170-174.

[25] W.J. Gau and I.W. Sun, *J. Electrochem. Soc.*, 1996, **143**, 914-919.

[26] C. Hussey, Chemistry of Nonaqueous Solutions Current Progress, 1994, (Eds. Mamantov, G. and Popov, A. I.), VCH, New York, p227.

[27] F.H. Hurley and T.P. Wier, 1948, U.S. Patent, US 2446349.

[28] F.H. Hurley, 1948, U.S. Patent, US 2446331.

[29] P.K. Lai and M. Skyllas-Kazacos, *J. Electroanal. Chem.*, 1988, **248**, 431-440.

[30] Y. Zhao and T.J. Vandernoot, *Electrochim. Acta.*, 1997, **42**, 1639-1643.

[31] Q. Liao, W.R. Pitner, G. Stewart and C.L. Hussey, *J. Electrochem. Soc.*, 1997, **144**, 936-943.

[32] C.L. Hussey, L.A. King and R.A. Carpio, *J. Electrochem. Soc.*, 1979, **126**, 1029-1034.

[33] F. Endres and A. Schweizer, *Phys. Chem. Chem. Phys.*, 2000, **2**, 5455-5462.

[34] J.J Lee, B. Miller, X. Shi, R. Kalish and K.A. Wheeler, *J. Electrochem. Soc.*, 2001, **148**, C183-C190.

[35] C.L. Hussey and T.M. Laher, *Inorg. Chem.*, 1981, **20**, 4206-4212.

[36] C.L. Hussey and X.H. Xu, *J. Electrochem. Soc.*, 1991, **138**, 1886-1890.

[37] X.H. Xu and C.L. Hussey, *J. Electrochem. Soc.*, 1992, **139**, 1295-1300.

[38] F. Endres and W. Freyland, *J. Phys. Chem. B.*, 1998, **102**, 10229-10233.

[39] C.A. Zell, F. Endres and W. Freyland, *Phys. Chem. Chem. Phys.*, 1999, **1**, 697-704.

[40] J.P. Piersma, D.M. Ryan, E.R. Schumacher and T.L. Riechel, *J. Electrochem. Soc.*, 1996, **143**, 908-913.

[41] S.Y.L. Liu and I.W. Sun, *J. Electrochem. Soc.*, 1997, **144**, 140-145.

[42] E.G.S. Jeng and I.W. Sun, *J. Electrochem. Soc.*, 1998, **145**, 1196-1201.

[43] E.G.S. Jeng and I.W. Sun, *J. Electrochem. Soc.*, 1997, **144**, 2369-2374.

[44] P.Y. Chen and I.W. Sun, *Electrochim. Acta.*, 1999, **45**, 441-450.

[45] P.Y. Chen and I.W. Sun, *Electrochim. Acta.*, 2000, **45**, 3163-3170.

[46] F. Endres, *Phys. Chem. Chem. Phys.*, 2001, **3**, 3165-3174.

[47] F. Endres and S.Z. El Abedin, *Phys. Chem. Chem. Phys.*, 2002, **4**, 1640-1648.

[48] F. Endres and S.Z. El Abedin, *Phys. Chem. Chem. Phys.*, 2002, **4**, 1649-1657.

[49] F. Endres, *Chem. Phys. Chem.*, 2002, **3**, 144–154.

[50] Atkins, P.W., Paula J.D. p1104 ,(2002) Physical Chemistry, 7th Ed. Oxford University Press

[51] C.L. Hussey, I.W. Sun, S.K.D. Strubinger and P.A. Barnard, *J. Electrochem. Soc.*, 1990, **137**, 2515-2516.

[52] J.P. Schoebrechts, B.P. Gilbert and G. Duyckaerts, *J. Electroanal. Chem.*, 1983, **145**, 127-138.

[53] K.G. Ray, Postdoctoral Thesis, University of Mississippi, 1985.

[54](**a**)V.M. Hultgren, A.W.A. Mariotti, A.M. Bond and A.G. Wedd, *Anal. Chem.*, 2002, **74**, 3151-3156.

(**b**)Z.J. Karpinski, C. Nanjundiah and R.A. Osteryoung, *Inorg. Chem.*, 1984, **23**, 3358-3364.

(**c**)B.K. Sweeny and D.G. Peters, *Electrochem. Comm.*, 2001, **3**, 712-715.

[55] C. Lagrost, D. Carrié, M. Vaultier, and P. Hapiot, *J. Phys. Chem.*, 2003, **107**, 745-752.

[56] D. Allen , G. Baston , A.E. Bradley , T. Gorman , A. Haile , I. Hamblett , J.E. Hatter , M.J.F. Healey, B. Hodgson , R. Lewin , K.V. Lovell , B. Newton , W.R. Pitner , D.W. Rooney , D. Sanders , K.R. Seddon , H.E. Sims and R.C. Thied., *Green Chem.*, 2002, **4**(2), 152-158.

2 Theory

2.1 Introduction

The techniques used in this research were mainly electrochemical, however other complementary techniques such as spectroscopic methods were also used. This chapter will give a brief introduction to each technique and recommend text for further reading on each subject for the interested reader.

2.2 Electrochemistry

Electrochemistry is the study of electron transfer reactions, usually occurring across the interface between an electrode and a redox active solute species in an electrolyte (solution with ionic species present). The electrode can be a metal (e.g. platinum, tungsten) or a non-metal (e.g. glassy carbon, GC) as long as it is an electrical conductor. The most commonly used electrochemical cell set-up is that consisting of three electrodes (working, counter and reference electrodes) immersed in an electrolyte (e.g. aqueous $NaClO_4$) or molten fused salt (e.g. $KCl/NaCl_{(l)}$) which contains ionic species that are responsible for carrying charge through solution. The operation of the cell is controlled by a potentiostat. There are two common modes of operating the potentiostat. When the potential of the working electrode is controlled with respect to a reference electrode and the current between working and counter electrode measured in response to the potential change, the experiment is said to be under potentiostatic control. If however the current that is allowed to pass between the working and counter electrode is controlled and the potential between the working and reference electrode required for such a current to flow is observed, then the experiment is said to be under galvanostatic control.

The electron transfer reaction of interest is studied at the working electrode (WE) through careful control of its potential. The electrode can be metallic or semiconducting, liquid or solid, but is normally constructed of a non-reactive material and can be thought of as an inert site at which electron transfer occurs. Platinum and GC are commonly used materials for working electrodes. The choice of electrode material is sometimes dictated by the experimental conditions, for example, in acidic aqueous solutions, underpotential formation of hydrogen and oxygen gas occurs when platinum is used as an electrode material, thus shortening the useful potential range of the solvent. It is also important to know the surface area of the electrode, as this is an important factor in determining the current in electrochemical processes. The larger the surface area of the electrode the more electrons can be transferred across the electrode/electrolyte interface.

The counter electrode (CE) is necessary for completion of the electrochemical circuit. If for example an oxidation reaction is performed at the working electrode, then there is a net flow of electrons, and these electrons flow to the counter electrode to perform a reduction reaction. This is shown schematically in figure 2.1, where there are oxidised species, O, and reduced species, R, present in bulk solution which are related by equation (1);

$$R \leftrightarrow O + ne^- \qquad (1)$$

Where n is the number of electrons involved in the redox reaction. It can be seen that for every oxidation electron produced there must be an accompanying reduction electron to preserve charge balance. The electrons accepted from the solution at the anode travel through the external electronics and are then supplied to the cathode where they are transferred to solution in a reduction reaction. The charged species moving through solution between the electrodes complete the electrochemical cell. Background electrolyte or a molten salt system ensures that the redox species do not have to travel from the WE to the CE for this, as the large number of ions in solution are available to carry the current. Indeed it is only true for

an electrotransport experiment that the same redox reaction occurs at the working and counter electrode as outlined in figure 2.1.

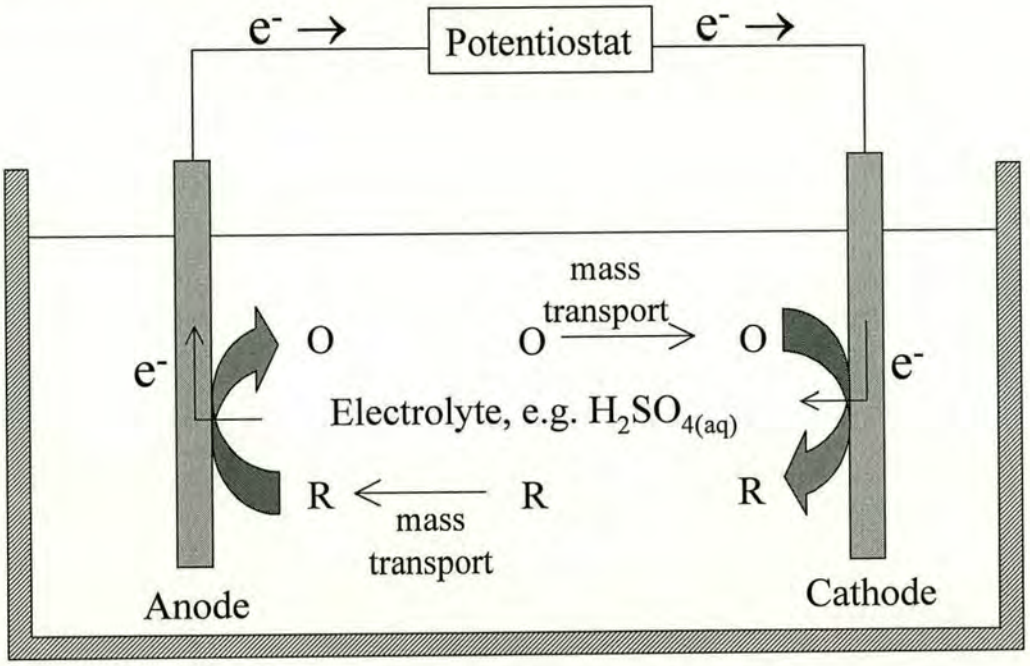

Note. reference electrode omitted for clarity

Figure 2.1: Schematic of electron flow in a complete electrochemical circuit for an electrotransport experiment.

The counter electrode is usually constructed of platinum and has a surface area larger than that of the working electrode so that it can easily pass equal and opposite current to the working electrode. Along with the control electronics, which ensure sufficient voltage is supplied to the counter electrode, this ensures that any electron transfer process is limited by the reaction of study occurring at the working electrode, and hence ensures current is a direct measure of the rate of the working electrode reaction. In order to achieve a large surface area, gauze or coiled wires are typically used. Both of these arrangements give the counter electrode a high surface area to volume ratio.

The final electrode to complete the cell is the reference electrode (RE) and is employed as the name suggests, to hold a constant potential to which the potential at the WE can be referred. A reference electrode should have a stable electrochemical potential as long as no (or experimentally small) currents flow through it. The

reference electrode that is used for quoting standard reduction potentials, E^{θ}, against is the Standard Hydrogen Electrode (SHE) and is by definition 0V, and all other standard potentials are quoted relative the SHE. The SHE electrode consists of a piece of Pt immersed in an a=1 (where a = activity) solution of a strong acid (source of $H^{+}_{(aq)}$), over which $H_{2(g)}$ is bubbled at 1 atm. Experimentally, using hydrogen gas is not practical and is also dangerous, so other reference electrodes are used, such as the saturated calomel electrode, SCE ($Hg/Hg_2Cl_2/KCl_{(sat'd\ in\ water)}$) which holds a constant potential of 0.242V versus SHE because of the following equilibrium, equation (2).

$$Hg_2Cl_{2(s)} + 2e^{-} \leftrightarrow 2Hg_{(l)} + 2Cl^{-}_{(aq)} \qquad (2)$$

The potential of the wire (energy of e^{-}) is fixed by the above equilibrium since large amounts of each reagent are present, so small currents do not change the equilibrium position. This gives a constant potential, E, at the reference electrode so when a voltage is applied between the WE and RE only the potential of the WE changes. In certain cases a suitable reference electrode may not be available and in such cases a pseudoreference electrode is employed. However they are generally not as stable and their potential is not as well defined and may be affected by redox active species in solution, so should be avoided if possible. A pseudoreference electrode may be as simple as a length of silver wire dipping into the test solution, but must be calibrated against a well-behaved redox couple such as ferrocene/ferrocenium in small concentrations in the test solution if potentials are to be quoted with reference to a standard reduction potential or reference electrode.

2.3 Cyclic voltammetry

In modern electrochemistry, the first electrochemical experiment to be performed on a sample is usually cyclic voltammetry. This technique involves sweeping the potential at a constant rate from the starting potential, E_1, normally a potential where there is no current flow, to an end potential, E_2, where the potential sweep is reversed at the same rate back to the starting potential, E_1. A typical potential/time profile is shown in figure 2.2(a).

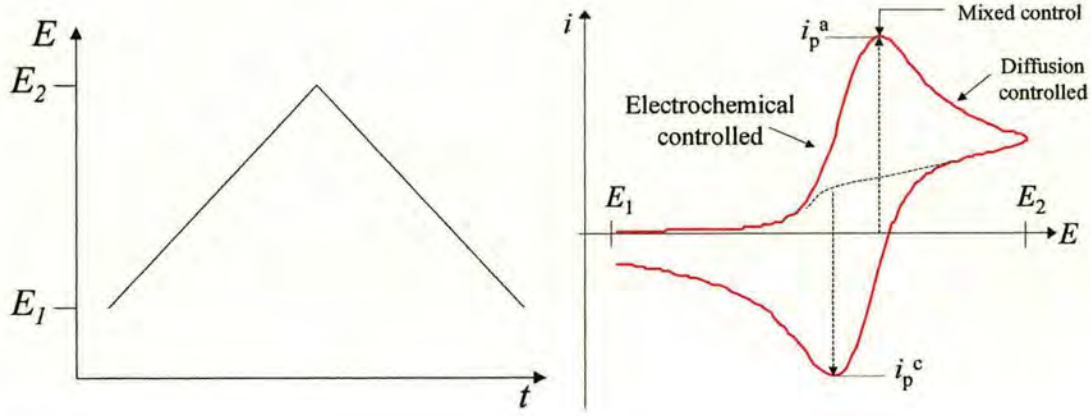

(a) (b)

Figure 2.2: (a) Example of potential variation with time, (b) A typical CV response.

The experiment is performed in a stagnant solution and thus the transport of material to the electrode surface is controlled by diffusion (with practically some uncontrolled convection through density and thermal gradients, and vibration which should ideally be minimised). In cyclic voltammetry, the change in current is measured in response to the potential sweep, the resulting graph of current versus potential is called a cyclic voltammogram and will be referred to as a CV hereafter. A typical CV of an electrochemically reversible system is presented in figure 2.2(b). The peak current i_{pc} and i_{pa} are the cathodic and anodic peak currents respectively and the potentials at which they occur are E_p^c and E_p^a respectively. The regimes where the electrode reaction is governed by thermodynamic contol (electrochemical),

and diffusion (mass transport) control are highlighted in figure 2.2(b). At potentials where the current starts to drop after i_p, the current is controlled by diffusion of the electroactive species from the bulk solution to the electrode surface. This is due to a steadily increasing depletion zone forming between the bulk solution and the electrode/solution interface as the electroactive species is consumed (mass transport control). $E^{\circ\prime}$ is the *formal potential* ($E^{\circ\prime} = (E_p^a + E_p^c) / 2$) and is the *measured* potential (against a reference electrode such as the SCE) of the redox reaction when O and R are present at equal activity. In electrochemistry, one frequently relies on the Nernst equation,[1] equation (3), to provide a linkage between the electrode potential, E, and the concentration of the redox species, O and R.

$$E = E^{O\prime} + \frac{RT}{nF} \ln \frac{[O]_0}{[R]_0} \tag{3}$$

Where E is the applied potential, $E^{\circ\prime}$ the formal potential (where O and R are at equilibrium concentrations), n the number of electrons transferred, R is the gas constant, F is Faradays constant and $[O]_0$ and $[R]_0$ are the concentration of the oxidised and reduced species at the electrode surface. Strictly speaking, the activities of the oxidised and reduced species, a_O and a_R respectively, should be employed when dealing with the Nernst equation, giving equation (4)

$$E = E^{O} + \frac{RT}{nF} \ln \frac{a_O}{a_R} \tag{4}$$

Where E° is the standard reduction potential (measured against the SHE). However, generally speaking this is impractical since the activities of the redox species are not usually known. The activities of the oxidised and reduced species, a_O and a_R, are related to the concentration of the oxidised and reduced species, $[O]$ and $[R]$ respectively through equation (5).

$$\frac{a_O}{a_R} = \frac{\gamma_O[O]}{\gamma_R[R]} \approx \frac{[O]}{[R]} \tag{5}$$

Where γ is the activity coefficient, a proportionality factor between activity and concentration and its value varies with concentration. When large amounts of ions are present such as in molten salts or background electrolyte the ionic strength, I, is constant and so activity coefficients are fixed. In this case, we can use equation (3) when performing thermodynamic equations in electrochemistry and we can use the formal potential, $E^{o'}$ in subsequent calculations, rather than the experimentally inconvenient standard reduction potential, E^{o}.

Information such as the electrochemical reversibility of the redox reaction can be deduced by employing cyclic voltammetry as an experimental technique. For diffusional systems, the peak current, i_p, in amperes is related to scan rate, v, in Vs^{-1} through the Randles-Sevcik[2] equation, equation (6).

$$i_p = 0.4663AFD^{1/2}v^{1/2}[A]_{bulk}(F/RT)^{1/2} \tag{6}$$

Where A is the electrode area (cm^2), D the diffusion coefficient (cm^2s^{-1}), and $[A]_{bulk}$ the bulk solution concentration ($molcm^{-3}$), all other symbols have their usual meaning. From equation (6), it follows that if the scan rate is increased, the peak current will respond in a manner that is consistent with $i_p \propto v^{1/2}$. E_p however, is independent of the scan rate, v. This is because at the electrode, equilibrium is always established and the surface concentrations, $[O]_0$ and $[R]_0$, are given by the Nernst equation, equation (3). The theoretical peak separation[1], ΔE_p, for a reversible system is given by equation (7),

$$\left|E_p^{ox} - E_p^{red}\right| = 2.218(RT/nF) \tag{7}$$

and the separation between the peak potential, E_p, and the potential at half peak current, $E_{P/2}$, is given by equation (8).

$$\left|E_P - E_{P/2}\right| = 2.2(RT/nF) \tag{8}$$

For a chemically reversible system, the ratio of the peak anodic current, i_p^a and peak cathodic current, i_p^c should be unity, equation (9).

$$\left|i_p^a / i_p^c\right| = -1 \tag{9}$$

This indicates that all of the redox species produced by the electrochemical reaction is available for the reverse redox reaction, and when the scan is reversed, the entire product is converted back to the initial redox species. This is only applicable as long as the scan rates employed are not sufficiently slow as to allow the redox species to diffuse away from the electrode surface into bulk solution.

We can summarise the diagnostics for cyclic voltammograms of reversible reactions; when $i_p \propto v^{1/2}$, E_P is independent of v, and equations (7) to (9) are satisfied, then the system being studied can be said to be reversible (or Nernstian).

For electrochemically irreversible systems, $i_p \propto v^{1/2}$, through equation (10).[1]

$$i_p = \left(2.99\times10^5\right)n(\alpha n_a)^{1/2} A C_O^* D_O^{1/2} v^{1/2} \tag{10}$$

Where the units are the same as equation (6), α is the electrochemical transfer coefficient and is a measure of the nature of the transition state ($0<\alpha<1$) and C^*_o is the bulk concentration of the redox species (molcm^{-3}). However, E_p varies with v through equation (11).

$$E_p = E^{\circ\prime} - \frac{RT}{\alpha n_a F}\left[0.780 + \ln\left(\frac{D_O^{1/2}}{k^\circ}\right) + \ln\left(\frac{\alpha n_a F v}{RT}\right)^{1/2}\right] \tag{11}$$

Thus, for a totally irreversible wave, i_p is also proportional to C_O^* and $v^{1/2}$, but E_P is a function of scan rate, shifting in a negative direction for a reduction reaction by an amount $1.15RT/\alpha n_a F$ for each tenfold increase in v.

For quasi-reversible systems,[3] as a general conclusion, the extent of irreversibility increases with increase in sweep rate, while at the same time there is a decrease in the peak current relative to that of a reversible system and the peak separation between anodic and cathodic peaks increases. For a quasi-reversible reaction, i_p is not proportional to $v^{1/2}$.

Care must exercised when performing CV experiments since the electrolyte is resistive to the flow of current. The magnitude of the resistance depends on the geometry of the electrochemical cell, and on the concentration and nature of the electrolyte used. When a cathodic current flows through the cell the true cell potential will be less negative than the potential measured by the chart recorder by an amount iR_u, where R_u is the uncompensated resistance (ohms) between the reference electrode and working electrode. The potential experienced at the electrode surface is $E' = E + iR_u$, where E' is the surface potential and E is the applied potential. By inspection of this simple relation, it can be seen that the difference between the applied potential and the surface potential is dependent on the current. The result of this is during CV experiments, the potential scan rate will no longer be linear and the peak potentials will be shifted from their real value. Care must therefore be taken when interpreting CVs without compensated resistance, as the increased peak separation may be misinterpreted as the redox couple being quasi-reversible or irreversible rather than reversible.

2.4 Potential Step (Chronoamperometric) Experiments

In potential sweep experiments, as has already been highlighted, the voltage scan rate is an important parameter. The extreme case of this being the case where the potential is stepped instantaneously from E_1 to E_2 where E_1 corresponds to a potential where no Faradaic current passes, and E_2 corresponds to a potential where diffusion controlled electrochemical reaction occurs at time, t_0, when the current response to this potential step is then measured as a function of time, this type of experiment is referred to as *chronoamperometry* and the resulting data as a chronoamperometric (or current-time) transient. This is shown schematically in figure 2.3 (a).

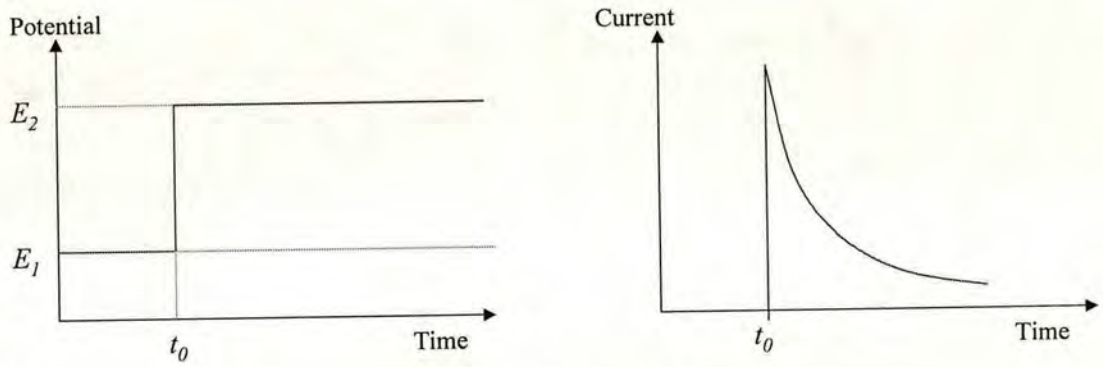

(a) (b)

Figure 2.3 (a) Potential/time profile for a potential step experiment (b) Current/time response to an applied potential step.

As the potential is stepped from a value where no current is flowing to one where an electrochemical reaction takes place, the current will rise suddenly to a current that is initially large due to the concentration of the reactant at the electrode surface being that of bulk solution. In a stagnant solution, the current will decrease with $(t-t_o)^{-1/2}$ as the concentration of reactant at the electrode surface becomes depleted according to the Cottrell equation,[4] equation (12).

$$i = nFAD^{1/2}C^{*}/\pi^{1/2}(t-t_o)^{1/2} \tag{12}$$

Where i is the current (A), n is number of electrons, F is Faradays constant ($Cmol^{-1}$), A is the electrode surface area (cm^2), D the diffusion coefficient of the redox species (cm^2s^{-1}) and C^* is the bulk concentration ($molcm^{-3}$) of the redox species.

Instead of studying the variation of current with time, we can study the variation of charge with time, this is known as chronocoulometry. By integration of equation (11) we obtain the integrated form of the Cottrell equation, equation (13).

$$Q = \left(-2nFAD^{1/2}C^{*}(t-t_o)^{1/2}\right)/\pi^{1/2} \tag{13}$$

Where Q is the charge passed (Coulombs). The diffusion coefficient of the electroactive species can then be ascertained from the gradient of the graph obtained by plotting Q against $(t\text{-}t_o)^{1/2}$. This graph will be a straight line if Cottrell behaviour is being observed, i.e, the electrochemical reaction is diffusion limited. There are a few advantages[1] to be gained by analysing chronocoulometry rather than chronoamperometry. Firstly, the signal usually increases with time, facilitating measurements towards the end of the transient when the current is almost zero. Secondly, integration is effective in reducing signal noise. Thirdly, when a potential is applied to an electrode, capacitive currents initially flow to build up the electrical double layer at the electrode surface, these currents occur on a short time scale but are emphasised on a $1/(t\text{-}t_o)^{1/2}$ graph. Thus by plotting Q vs $(t\text{-}t_o)^{1/2}$ rather than i vs $1/(t\text{-}t_o)^{1/2}$ these points on the graph are concentrated at the beginning of the plot. This allows the separation of the capacitive charge from the Faradaic charge and thus the gaining of a better estimate of the diffusion coefficient of the redox species.

2.5 X-ray crystallography

The most powerful method for structural analysis of solid structures is single crystal x-ray crystallography. This has been somewhat of a problem for analysis of ionic liquids since one of their attractive features is their low melting point. Thus the main problem is growing a single crystal that is of suitable quality for x-ray diffraction, this is further compounded by the tendency of ionic liquids to form glassy phases rather than crystalline solids.

In this technique, a single crystal of suitable quality is bombarded by electromagnetic radiation of a fixed wavelength in the X-ray region. The radiation interacts with the electron density of the atoms within the crystal and is diffracted. A detector is used to collect the diffracted radiation, giving a diffraction pattern of constructive and destructive interference according to Bragg's Law, equation (14).

$$n\lambda = 2d\sin\theta \tag{14}$$

Where λ is the wavelength of electromagnetic radiation, n is the number of wavelengths, d is the distance between planes of atoms and θ is the glancing angle. This is shown in figure 2.4, where it can be seen that when the difference in path-length of the two beams, (AB + BC) equals $n\lambda$, where n is an integer, then constructive interference occurs due to the two waves being in-phase. In the modern form of the Bragg Law n is absorbed into d and to regard the nth order reflections as occurring from the $\{nh, nk, nl\}$ planes.

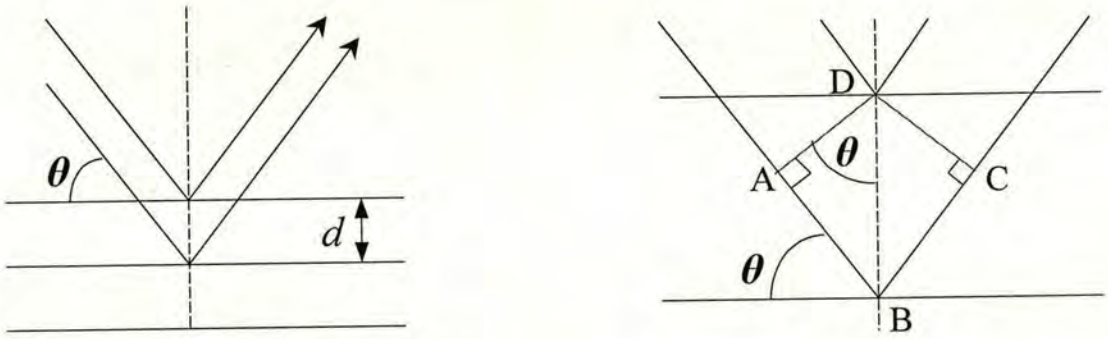

Figure 2.4: Common derivation of constructive interference for Braggs Law.

By using Fourier-transform techniques on the diffraction pattern it is possible to obtain a map of electron density within the sample, and thus the position of atoms within the sample can be deduced. From these atomic positions, geometrical data including bond lengths and angles can be obtained, allowing inference to the inter- and intra-molecular interactions that are occurring within the crystal. A drawback of using single crystal x-ray diffraction is that it is not possible to place hydrogen atoms precisely within the structure due to their low electron density and thus poor scattering ability. This problem is compounded if the material also contains heavy atoms that diffract strongly (e.g. transition metals).

2.6 Powder x-ray diffraction

If it is not possible to obtain a single crystal of suitable quality for x-ray analysis, some information about the crystal (unit cell dimensions, space group) can be obtained using x-ray diffraction from a powdered sample. In a typical experiment x-rays are scanned across the powdered sample and each crystallite within the powder diffracts the beam. The diffraction peaks in X-ray diffraction patterns are called reflections, even though this is factually incorrect in terms of the process, the terminology is so widely used that it is the accepted notation. Since the crystallites are all in random orientations relative to the incident beam, the Bragg reflections are detected as cones of varying intensities. Thus each reflection is represented by an angle and intensity and a plot of intensity versus diffraction angle (2θ) results in a

powder diffraction pattern. The diffraction pattern can serve as a "fingerprint" for a sample as the pattern will be unique to that sample, as well as giving structural information, or help identify unknown samples. The powder patterns were recorded using a Philips Diffractometer over a 2θ range of 10° to 70° using Cu-Kα radiation. The data was collected using Pc-Apd and Pc-Identify Philips software and was converted to MS Excel for further analysis. The finely ground samples were loaded onto aluminium slides that were mounted within an airtight sample holder fitted with a Mylar window under a nitrogen atmosphere.

2.7 Raman Spectroscopy

Raman spectroscopy is a technique used to explore molecular energy levels by examining the frequencies of scattered radiation from the sample, and is based on the Raman effect, which is the inelastic scattering of photons by molecules. The Indian physicist C.V. Raman discovered the effect in 1928. The sample can be a gas, liquid, solid, solution or suspension.

Raman scattering is very weak, generally 1 in 10^7 incident photons interact with molecules to produce Raman scattering, and thus lasers are needed as an intense incident radiation source. The highly monochromatic radiation produced from lasers is also desirable since the shift in frequency of the scattered radiation is very small. The incident photon can interact with the molecule and give up some of its energy to the molecule to produce Stokes radiation, or accept some energy from the molecule (in a vibrationally excited state) to produce Anti-Stokes radiation, figure 2.5.

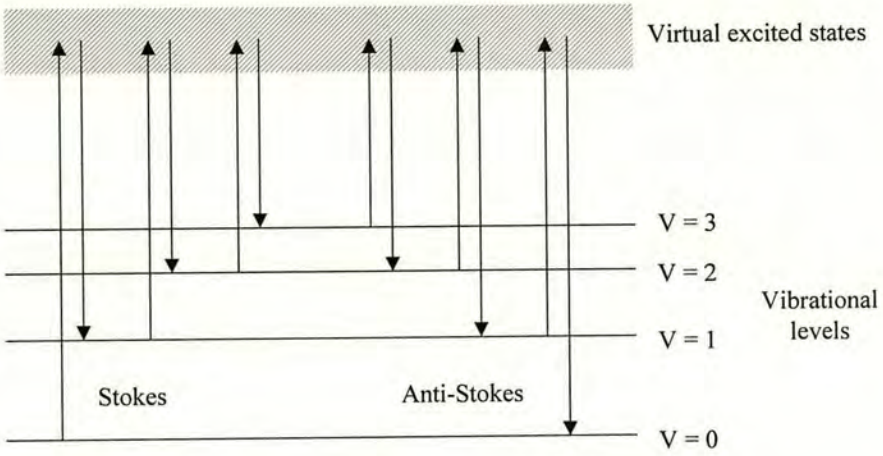

Figure 2.5: Schematic of how Stokes and Anti-Stokes radiation are produced in Raman scattering.

Stokes radiation is more intense since more molecules are likely to be in the ground state according to the Boltzmann distribution, equation (15).

$$N_v/N_o = \exp(-(E_v - E_o)/kT) \tag{15}$$

Where N_v and N_o is the number of molecules in the excited and ground state respectively, and E_v and E_o is the energy of the excited state and ground state respectively.

The wavenumber of the Stokes and Anti-Stokes lines are a direct measure of the vibrational energies of the molecule since the energy increase or decrease from the excitation is related to the vibrational energy spacing in the ground electronic state of the molecule. A typical Raman spectrum[5] is shown in figure 2.6.

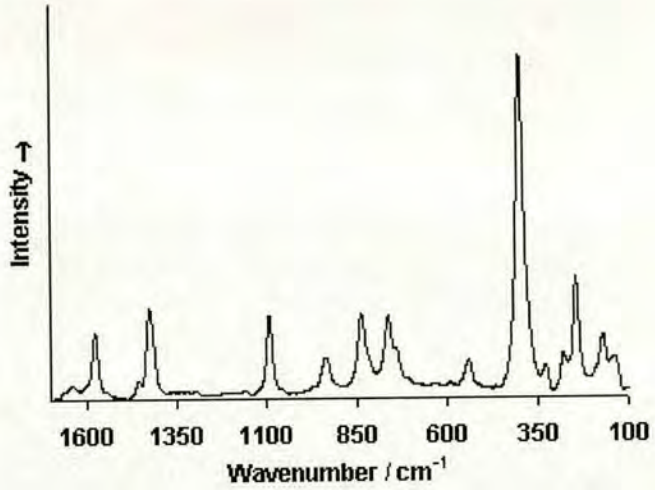

Figure 2.6: Raman spectrum of the mineral, azurite.

For samples with a fluorescent component, Raman scattering is more difficult to observe since the fluorescence emission from the sample is often more intense than the Raman signal, and much broader. If the fluorescence is inherent in the material, very little can be done except changing the excitation wavelength of the laser to reduce the effect. If the fluorescence is from an impurity, it can usually be dealt with by purification or photobleaching (exposing the sample to the laser beam for some time).

If two compounds have the same component, i.e. two salts with the same anion, then the frequency at which Raman scattering occurs for the anion will be similar for both salts. Raman experiments can thus be used with comparison to known spectra to infer the likely structure of certain components within a compound.

A modification[6] of the basic Raman effect involves using incident laser radiation of wavelength close to that of the maximum of an intense electronic absorption band. This technique is then called resonance Raman spectroscopy, and in contrast to Raman spectroscopy, the incident radiation has a frequency that coincides with a molecular transition, resulting in the excitation of the molecule to a real excited state. Use of this technique can lead to Raman scattering being enhanced by several orders of magnitude.

[1] A.J. Bard and L.R. Faulkner, *Electrochemical Methods, Fundamentals and Applications,* J. Wiley & sons.

[2] J.E.B. Randles, *Trans. Farady Soc.*, 1948, **44**, 327.

[3] H. Matsuda and Y. Ayabe, *Z. Elektrochem.*, 1955, **59**, 494.

[4] A.C. Fischer, *Electrode Dynamics*, 1996, Oxford University Press.

[5] http://www.chem.ucl.ac.uk/resources/raman/pigfiles/azurite.html.

[6] P. Atkins and J. de Paula, *Physical Chemistry*, 7th edition, 2002, Oxford University Press.

3 Experimental

3.1 Schlenk Techniques

Ionic liquids such as haloaluminate ionic liquids are reactive toward moisture, resulting in the formation of oxidic and protonic impurities in the ionic liquid. Ionic liquids tend to absorb moisture from their surroundings, especially if the anion is a halogen (e.g. 1-ethyl-3-methylimidazolium chloride) and even in the case of the so-called 'hydrophobic' ionic liquids, those containing the hexafluorophosphate $[PF_6]^-$ or bis(trifluoromethanesulfonyl)imide $[N(Tf_2)]^-$ anions. The halogen ionic liquids are an extreme example of the hygroscopic nature of ionic liquids. When for example a chloride ionic liquid is left in contact with ambient atmospheric conditions it absorbs so much water it eventually becomes an aqueous solution. Even small amounts of water can effect physical properties such as viscosity and density[1] thus these solvents must be treated as moisture-sensitive and handled under a dry inert atmosphere, e.g. N_2 or Argon. This was achieved using standard Schlenk line techniques using a dry, oxygen free nitrogen (BOC gases) atmosphere. Ionic liquids were dried by heating to 423K at a reduced pressure of 0.13 Pa using an oil-filled rotary pump. On some experiments the ionic liquid was further dried by stirring with 4A molecular sieves that were dried by heating to 473K at 0.13 Pa. The ionic liquids were decanted from the sieves before use. A glass syringe fitted with a wide bore stainless steel needle was used for transferring and measuring out the ionic liquids (A wide bore needle was required due to the high viscosity of the ionic liquids). All solvents were dried prior to use using dried 4A molecular sieves. Unless otherwise stated all chemicals were used as received.

3.2 Electrochemistry

3.2.1 Cyclic Voltammetry

Electrochemical experiments were carried out using a 5 - 15 ml cell (MF-1082) and a teflon cell top (ER-8946) both purchased from Bioanalytical Systems (BAS). The working electrode was a platinum flag with a geometric area of 1.42cm^2 and was made in-house by spot welding the platinum plate to a piece of platinum wire. The counter electrode was a coiled 23cm platinum wire, 0.5mm diameter, with gold-plated brass connector (MW-1033, BAS).

When analysing a chloride ionic liquid the reference electrode was constructed of a silver wire immersed in a 0.1M solution of AgCl in [emim][Cl] in a fritted Vycor tube. When analysing each $[N(Tf)_2]^-$ based ionic liquid the reference electrode was constructed of a silver wire immersed in a 0.1M solution of AgOTf (silver triflate) in the desired $[N(Tf)_2]^-$ ionic liquid in a fritted Vycor tube. An alternative pseudo-reference electrode was also employed under certain conditions, which was a platinum wire dipping into the electrochemical solution being studied. The pseudoreference electrode was placed as far away from the working and counter electrodes as possible to ensure it's potential wasn't affected by the products of the electrode reactions.

The volume of electrolyte in the electrochemical cell was generally 7ml and this was stirred between experiments using a Teflon coated magnetic stirrer bar, and heated using a sand-bath with the temperature controlled by a hotplate. Temperatures were recorded using a mercury filled thermometer, which was inserted through the Teflon cell cap via a hole of the same diameter and immersed in the ionic liquid solution under investigation. The electrochemical set-up was housed in a Gallenkamp desktop manipulator and maintained under an argon (Pureshield, BOC gases) atmosphere. Electrical connections between the potentiostat and

electrochemical cell were maintained by a sealed BNC bulkhead socket fitted to the wall of the manipulator which was further sealed by silicone sealant, with the coaxial cables terminating in crocodile clips for connection to the electrodes. The potential of the working electrode was controlled using an Oxford Electrodes modular potentiostat, with current and voltage data collected on a PC using in-house software written in Visual Designer version 4.0 (Burr-Brown).

3.2.2 Electrolysis

Electrolysis experiments were carried out in a manner similar to the cyclic voltammetry set-up. For bulk electrolysis experiments where redox products from the counter electrode needed to be isolated from the working electrode, a fritted glass tube (MR-1196, BAS) containing the counter electrode filled with the ionic liquid under study was used as the auxiliary electrode chamber. The working electrode used was typically a piece of the metal to be electrodissolved into solution unless otherwise stated.

3.3 Elemental analysis

CHN elemental analysis involves complete combustion of a known weight of a sample in oxygen. The combustion products are CO_2, H_2O, N_2 and nitrogen oxides. The combustion products are passed over copper using helium as a carrier gas to remove any excess oxygen and reduce nitrogen oxides to elemental nitrogen, other elements are removed by the use of specialised combustion reagents and then the gases are passed to a chromatographic column. The gases are eluted in the order N_2-CO_2-H_2O and measured by a thermal conductivity detector. The instrument is calibrated using an organic compound of known composition such as acetamide, CH_3CONH_2.

This technique was used as a guide to the purity of the ionic liquid and can be performed on either solid or liquid samples. The result of the elemental analysis gives the percentage weight of carbon, hydrogen and nitrogen in the sample and is thus usually abbreviated to CHN analysis. Any discrepancy between the experimental and the calculated percentage weights of C, H and N indicates the presence of impurities. An example would be the presence of water, which as eluded to earlier, can be absorbed by the ionic liquid, this would result in the experimental H content being greater, and the C and N content being lower than that predicted. In the case of moisture sensitive compounds, the loading of the cell for CHN analysis is performed under nitrogen to prevent the uptake of moisture by the sample.

A drawback of using CHN analysis for the detection of water is that the accuracy of CHN is *ca.* 0.3%, this makes detection of small quantities of water impurities difficult with CHN. Cyclic voltammetry will be examined as a technique for the detection of water in ionic liquids.

Elemental analysis was performed by the departmental service using a Perkin Elmer 2400 CHN Elemental Analyser, samples were loaded into the sample vial under a stream of dry nitrogen.

3.4 Powder X-ray Diffraction

Powder patterns were recorded using a Philips Diffractometer over a 2θ range of 10° to 70° using Cu-Kα radiation. The data was collected using Pc-Apd and Pc-Identify Philips software and was converted to MS Excel for further analysis. The finely ground samples were loaded onto aluminium slides that were mounted within an airtight sample holder fitted with a Mylar window under a nitrogen atmosphere.

---

[1] K.R. Seddon, A. Stark and M.J. Torres, *Pure and Applied chemistry*, 2000, **12**, 2275-2287.

4 Chemicals

4.1 Synthesis of Ionic Liquids

4.1.1 Synthesis of dialkylimidazolium chloride ionic liquids

The synthesis of dialkylimidazolium chlorides such as 1-ethyl-3-methylimidazolium chloride [Emim][Cl] is well established.[1] Early methods of synthesis involved condensing chloroethane gas (fourfold excess) into a glass pressure vessel containing 1-methylimidazole, before being heated to 348K with magnetic stirring for 2 days.[2] Excess chloroethane was boiled off after the reaction was complete and the off white solid remaining was recrystallised from acetonitrile/ethyl acetate.

Generally in this work these salts have been produced at the Quill (Queens University Ionic Liquids Laboratories) Centre at Queens University of Belfast using an autoclave dedicated solely to this task. For example, [Emim][Cl] is produced from the reaction of *N*-methylimidazole with excess chloroethane under an atmosphere of nitrogen in an autoclave at 6 atm. High pressures are used due to chloroethane being gaseous at atmospheric pressure. Once the reaction is completed the excess chloroethane is boiled off. The preparation of [Emim][Cl] is outlined in figure 4.1.

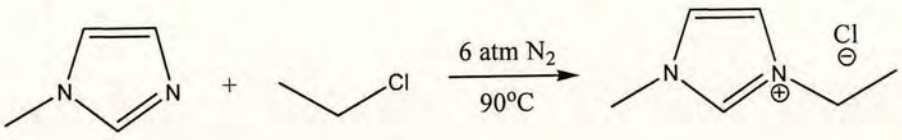

Figure 4.1: Reaction scheme for synthesis of [Emim][Cl] in an autoclave.

[Emim][Cl] was recrystallised by dissolving in dry acetonitrile, followed by slow addition of dry ethyl acetate to produce a two-phase system. Crystallisation occurred at the interface of the two phases and crystals were removed by filtration under a nitrogen atmosphere and dried at 5.33 Pa at 373K. This process was repeated several times before [Emim][Cl] was used.

The dialkylimidazolium chlorides with shorter alkyl chains (i.e. [Emim][Cl] to [Bmim][Cl]) are solids at room temperature and are very hygroscopic, however the use of longer alkyl chains (i.e. 1-hexyl-3-methylimidazolium chloride [Hmim][Cl]) yield highly viscous liquids at room temperature which are less hygroscopic. The synthesis of longer chain salts can be performed at atmospheric pressure due to the lower volatility of the longer chain chloroalkanes. Refluxing methylimidazole with the appropriate chloroalkane will yield the corresponding 1-alkyl-3-methylimidazolium chloride. The chloroalkane is used in excess since it is the most volatile of the reactants, and thus when the reaction is complete any unreacted chloroalkane is removed from the reaction mixture under reduced pressure, 5.33 Pa, at 373K.

4.1.2 Synthesis of [Emim][N(Tf)$_2$]

The preparation of the [Emim][N(Tf)$_2$] was performed by the metathesis of [Emim][Cl] with Li[N(Tf)$_2$] in a 1:1 molar ratio in aqueous media, the resulting hydrophobic ionic liquid, [Emim][N(Tf)$_2$] separates out as a separate liquid phase as shown in figure 4.2.

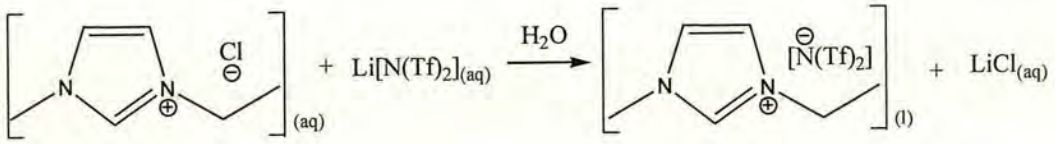

Figure 4.2: Synthesis of [Emim][N(Tf)$_2$] by metathesis of [Emim][Cl] with Li[N(Tf)$_2$]

[Emim][$N(Tf)_2$] was prepared at the Centre for Radiochemical Research (CRR) and was dried prior to use by heating to 423K under reduced pressure, 5.33 Pa, for 10 hours on a Schlenk line.

The other bis(trifluoromethanesulfonate)imide ionic liquids were made by similar methods using the appropriate chloride ionic liquid as a starting material. These were also all prepared at CRR and dried prior to use by heating to 423K under reduced pressure, 5.33 Pa, for 10 hours on a Schlenk line.

4.1.3 Synthesis of [Bmim][$LABSO_3$]

[Bmim][Cl] (5.09g, 0.029 moles) and linear alkylbenzenesulphonic acid ($LABSO_3H$) (9.40g, 0.029 moles) were dissolved separately in acetonitrile (50ml) and the $LABSO_3H$ solution was added to the [Bmim][Cl] solution with stirring. After 2.5 hours the acetonitrile was removed by rotovaporator at 333K. Litmus paper held at the neck of the reaction flask turned red, which suggested HCl was being liberated. The reaction mix was then heated at 333K under reduced pressure for 3 hours.

^{1}H NMR results (ppm):

[Bmim][$LABSO_3$] ($CDCl_3$, 500MHz); 9.75 (1H, br s), 7.88 (2H, d), 7.41 (1H, s), 7.30 (1H, s), 7.15 (2H, m), 4.21 (2H, s), 4.01, (3H, s), 2.68 (<1H, m), 2.41 (<1H, m), 1.80 (2H, s), 1.52 (3H, m), 1.20 (15H, m), 0.89 (8H, m).

$LABSO_3H$ ($CDCl_3$, 300MHz); 7.78 (2H, br s), 7.22 (2H, br s), 2.70(<1H, m), 2.52 (<1H, m), 1.53 (4H, m), 1.22 (13H, m), 0.85 (5H, m).

^{13}C NMR results (ppm):

[Bmim][$LABSO_3$] ($CDCl_3$, 300MHz); 150.77, 149.26, 148.96, 142.56, 137.81, 128.72, 128.43, 127.95, 127.87, 124.34, 122.71, 78.03, 77.60, 77.18, 50.08, 48.00, 46.16, 40.10, 38.58, 36.99, 32.41, 32.22, 32.18, 30.03, 29.99, 29.92, 29.91, 29.88, 29.67, 29.63, 27.97, 27.87, 23.03, 22.98, 22.95, 22.87, 22.55, 19.74, 14.43, 14.41, 13.75.

LABSO$_3$H ($CDCl_3$, 300MHz); 153.73, 152.41, 152.09, 137.06, 129.16, 128.54, 126.87, 48.28, 46.49, 46.21, 40.35, 38.52, 37.07, 32.26, 32.23, 32.08, 30.05, 29.99, 29.93, 29.84, 29.69, 29.55, 27.99, 27.91, 27.85, 27.55, 23.05, 23.02, 23.00, 22.88, 14.47, 14.43, 14.32, 12.44.

Cl analysis: Expected 0%, Found 2.44%

4.1.4 Synthesis of [Bmim][BuSO$_3$]

[Bmim]Cl (5.410g, 0.031moles) and sodium butyl-sulphonate ($NaBuSO_3$) (4.961g, 0.031moles) were dissolved separately in methanol (20ml, and 50ml respectively). The two solutions were added together and stirred for 3 hours. The methanol was removed by rotary evaporation and acetone (~50ml) was added, a white precipitate formed and was removed by filtration. The acetone was removed by rotary evaporation.

4.1.5 Synthesis of [Bmim][dimethyldithiocarbamate]

[Bmim][Cl] (5.254g, 0.0295moles) and sodium dimethyldithiocarbamate (4.225g, 0.0295moles) dissolved separately in methanol (15ml and 25ml respectively) were added together and stirred for 4 hours. The solution was filtered to remove NaCl that had precipitated and the methanol was removed by rotary evaporation at 333K. Acetone was added to the resulting liquid to precipitate any dissolved NaCl, and filtered again. Acetone was removed by rotary evaporation and dried at 333K under reduced pressure for 6 hours. The product was a viscous yellow liquid.

4.1.6 Synthesis of [Bmim][toluenesulfinate]

[Bmim][Cl] (5.166g, 0.0295moles) and sodium *p*-toluene sulfinate, $[Na][CH_3C_6H_4SO_2]$ (5.256g, 0.0295moles), dissolved separately in methanol (20ml and 40ml respectively), were added together and stirred for 3 hours. Methanol was removed by rotary evaporation at 333K, followed by addition of acetone to precipitate any residual NaCl. A white precipitate was removed by filtration, and the acetone was removed by rotary evaporation at 333K, and then dried under reduced pressure at 363K for 4 hours. The resulting product was a light brown solid.

4.1.7 Mixtures of [Emim][Cl]/[Hmim][Cl]

Attempts were made to lower the melting point of [Emim][Cl], the ionic liquid of choice to investigate the electrochemistry of plutonium at AEA (Atomic Energy Association), Harwell. The problem with [Emim][Cl] is that it is a solid at room temperature. Melting the crystals is easy, but when it cools down it produces a glass that requires longer times to melt. It was thought that by mixing [Hmim][Cl] with [Emim][Cl], the mix would stay liquid at room temperature, so extensive heating would not be required each time electrochemistry was to be performed. Mixtures were made up with [Emim][Cl]:[Hmim][Cl] ratios of 20:80, 40:60, 60:40 and 80:20 and heated under an atmosphere of dry nitrogen at 353K for 5 hours, and then allowed to cool. All of the mixtures solidified except for the 80:20 mixture, which remained a highly viscous liquid. This did not appear to be a promising solution to the problem and no further investigations were carried out.

4.2 Uranium compounds

4.2.1 Synthesis of uranium tetrachloride

All parts of this experiment were performed under an atmosphere of dry dinitrogen using standard Schlenk techniques. Uranium trioxide (4.183g, 0.015mol) was heated under reflux (438K) with hexachloropropene (22cm^3, 0.15 mol) for 14 hours, equation (3).

$$UO_{3(s)} + 3CCl_3CCl{=}CCl_{2(l)} \longrightarrow UCl_{4(s)} + 3CCl_2{=}CClCOCl_{(l)} + Cl_{2(g)} \qquad (3)$$

The resulting solution was reddish with a green precipitate, UCl_4, which was isolated from the solution by filtration and then washed with 20ml of dry carbon tetrachloride (distilled from P_2O_5). The solid was dried under high vacuum for a few hours at room temperature and then at 433K for 6 hours to give a yield of 4.942g of UCl_4 (89% yield based on UO_3). The trichloroacryloyl chloride produced from the reaction is extremely toxic and is distilled from the reaction mixture and quenched with water to give the less harmful 2,3,3-trichloropropenoic acid. Chloride analysis of the product gave a chloride content of 30.08%, which is less than the theoretical value, 38.34%. This could be a result of oxidation in air, either during transfer to the apparatus for Cl analysis or in the sample tube when waiting to be analysed, to give uranium oxychlorides with the liberation of chlorine gas. EXAFS conducted at Daresbury Laboratories on the UCl_4 dissolved in [Hmim][Cl] indicated that no oxides were present[3] as the radial distribution curve for UCl_4 in [Hmim][Cl] was fitted best to a model of the hexachloro species, $[UCl_6]^{2-}$.

4.2.2 Synthesis of $[TMA]_2[UCl_6]$

$[TMA]_2[UCl_6]$ was prepared at the Centre for Radiochemistry Research by Dr. Vladimir Volkovich by the reaction of two equivalents of [TMA][Cl] with one equivalent of UCl_4.

Elemental analysis:

$[TMA]_2[UCl_6]$ Expected: C: 16.04%, H: 4.04%, N: 4.68%, Cl: 35.51%, U: 39.73%.

Found: C: 15.84%, H: 3.92%, N: 4.51%, Cl: 32.51%, U: 40.71%.

4.2.3 Uranium metal

Metallic uranium (Depleted in ^{235}U) was used as received from BNFL, Sellafield. The uranium was a sheet of approximately 3 x 6cm and had a black coating indicating some oxidation of the surface had occurred. This material was used to manufacture the uranium working electrodes by cutting to size with tinsnips and electrical connection to the potentiostat was maintained via a crocodile clip.

---

[1] T. Welton, *Chem. Rev.* 1999, **99**, 2071-2083.

[2] J.S. Wilkes, J.A. Levisky, R.A. Wilson and C.L. Hussey, *Inorg. Chem.*, 1982, **21**, 1263-1264.

[3] A. Bradley, BNFL internal report, 1999.

5 Structural analysis

5.1 Introduction

The relationship between the structure and the physical properties of ionic liquids remains an ongoing area of research. By their very nature, ionic liquids tend to be non-crystalline under normal conditions and on cooling frequently form glassy phases. Thus it is often difficult to obtain high quality crystals suitable for single crystal x-ray diffraction. Nevertheless, from the limited number of structures that have been studied, hydrogen bonding is thought to make a major contribution to the interactions within the solid and liquid state of those ionic liquids based on the imidazolium cation. The presence of hydrogen bonding in the liquid state between the anion and the hydrogen atom at the 2-position of the imidazolium cation has been suggested from NMR[1] and IR[2,3] evidence. For a clear understanding of the manner in which a solute species diffuses in ionic liquids, it is necessary to study the nature of the interactions between anion and cation, and between solute and ions. Although it is difficult to obtain information about the structure of the liquids directly, some insight can be gained by study of the structures in the solid state. X-ray crystallography is an important tool in determining the solid-state structure of ionic liquids, and information about the interactions between ions within the solid state structure can be gained.

5.2 X-ray crystallography

5.2.1 Crystal structure of [Emim][Cl]

The 1-alkyl-3-methylimidazolium halide ionic liquids are important systems, both as reaction media[4] and as synthetic starting materials on the route to other ionic liquids.[5] 1-ethyl-3-methylimidazolium chloride, [Emim][Cl], is one such example of this class of ionic liquids, although it is not used as a reaction medium as frequently as other ionic liquids due to its rather high melting point of 360K. However, this high melting point makes it easier to obtain a crystal of suitable quality for X-ray diffraction than for those melts with lower melting points.

The crystal structure of [Emim][Cl] recorded at 298K has already been published by Dymeck *et al.*[6] although the quality of the refinement was relatively poor (*R*-factor >10%), presumably as a result of the data being collected at room temperature. The lattice consists of a layered structure in which the imidazolium ions are stacked in a staggered top-to-tail arrangement. The chloride ions are spaced unevenly between the imidazolium ions. This was interpreted as evidence of chloride ions interacting specifically with imidazolium ions through hydrogen bonding. The authors reported the presence of hydrogen bonding from all three of the ring hydrogen atoms to chloride ions. The unit cell was composed of four unique chloride ions and four unique imidazolium ions, one of which showed disorder at the ethyl group. Each chloride ion displayed interactions with three imidazolium ions and each imidazolium ion displayed interactions with three chloride ions.

Due to the poor quality of the data obtained by Dymeck *et. al.* it was not possible to infer directly the presence of hydrogen bonding in the crystal structure. In the present study, X-ray diffraction measurement for [Emim][Cl] were made at 190K in order to obtain better quality data that would allow greater insight into the interactions within the crystal structure of [Emim][Cl]. A colourless, needle shaped crystal measuring 0.66 x 0.20 x 0.20 mm was grown by recrystallisation of

[Emim][Cl] from an acetonitrile/ethyl acetate (40:60 vol.%) mixture at room-temperature. The needle was removed from the mother liquor under nitrogen and single-crystal X-ray diffraction was performed using an Oxford Cryosystems Cryostream operating at 190K. The compound crystallises in the orthorhombic crystal system, with space group $P2_12_12_1$ which was also observed by Dymeck *et.al.* The unit cell dimensions are similar to those obtained by Dymeck *et. al.* although two of the cell lengths are slightly shorter, in line with the lower temperature of the present data collection. Comparisons between the structure obtained in this study and that obtained by Dymeck *et. al.* are presented in table 5.1.

Cell Parameter	**Previous †[Emim][Cl][6]**	**Presented ‡[Emim][Cl]**
***a* (Å)**	10.087(1)	10.095(1)
***b* (Å)**	11.179(1)	11.059(1)
***c* (Å)**	28.733(4)	28.587(4)
Volume (Å^3)	3240.0*	3191.6(7)
Density (gcm^{-3})	1.204	1.221
Z	16	16
***R*-factor**	> 10%	4.2%

Table 5.1: Comparison of published and presented crystal structures of [Emim][Cl]
† Data collected at room temperature, ‡ Data collected at 190(2)K. *esd not quoted.

In the study by Dymeck *et. al.* Hydrogen atoms were calculated and added to structure factor calculations, but their positions were not refined. Due to the uncertainty in the atomic co-ordinates of hydrogen atoms, it was not possible to draw any meaningful conclusions about H-bonding directly, and thus C···Cl$^-$ distances were used to infer H-bonding within the structure. The improvement in the quality of structural data in the present study allows for the direct investigation of C-H···Cl$^-$ interactions, and gives greater insight into the interactions between ions within the ionic liquid. Hydrogen atoms were placed in ideal geometries and refined isotropically using the riding model[7].

The numbering scheme for [Emim][Cl] is as displayed in figure 5.1. Hydrogen atoms will be referred to by the number of the carbon they are attached to, followed by the ring of the asymmetric unit to which the hydrogen belongs, followed by the *n*th hydrogen on the carbon if there are more than one hydrogen atoms, i.e. H7A1. Imidazolium units that have a close contact between a hydrogen and chloride ion (< sum of van der Waals radii, 2.95Å) are referred to as a nearest neighbour. The criteria used for the presence of hydrogen bonding (D-H···A)[8] are that the H···A distance must be less than the sum of the van der Waals radii of H and A by 0.12Å, and the D-H···A angle must be greater than 90°.

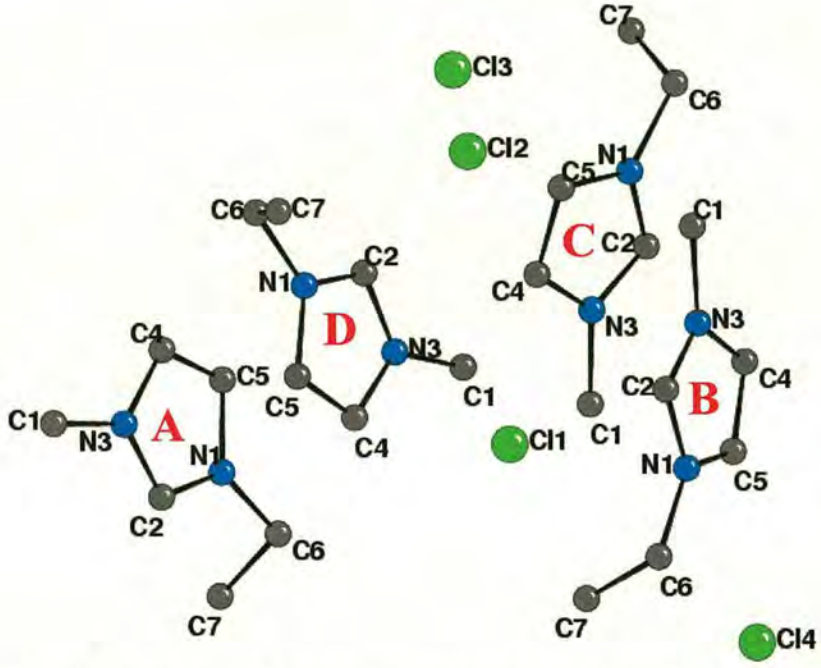

Figure 5.1: Numbering scheme for asymmetric unit of [Emim][Cl], hydrogen atoms have been omitted for clarity.

The number of nearest neighbour cations surrounding each chloride ion varies from four to six; four for Cl2, five for Cl1 and Cl4, and six for Cl3. The number of hydrogen bonds to each chloride ion also varies; Cl1, Cl3 and Cl4 have five hydrogen bonds, whereas Cl2 has only four hydrogen bonds. This differs from *Dymeck's* structure, in which it was determined that each cation is surrounded by three anions, and each anion by three cations. The five cations surrounding each Cl4

within the crystal structure of 1-ethyl-3-methylimidazolium chloride are shown in figure 5.2. The hydrogen bonds of the type C-H···Cl for all of the chloride ions are shown in table 5.2.

The contacts listed in table 5.2 are all less than the sum of the van der Waals radii by 0.12Å (2.95-0.12Å = 2.83Å) and can be regarded as hydrogen bonding between the hydrogens on the imidazolium cation and the chloride anion. The shortest contact is between the chloride ion, Cl3, and H2D, indicating the strongest hydrogen bonding present at this position. This was expected as it has been observed previously in a number of imidazolium based ionic liquids.[6,9,10]

D-H···A	D-H / Å	H···A / Å	D···A / Å	D-H-A / °
C2D-H2D···Cl3	0.95	2.45	3.380(3)	166
C2A-H2A···Cl4	0.95	2.49	3.373(2)	155
C2C-H2C···Cl3	0.96	2.52	3.391(3)	153
C2B-H2B···Cl1	0.95	2.62	3.459(4)	147
C5B-H5B···Cl4	0.95	2.63	3.541(3)	161
C4A-H4A···Cl3	0.95	2.64	3.511(3)	153
C5D-H5D···Cl4	0.95	2.68	3.555(3)	153
C1C-H1C1···Cl1	0.98	2.69	3.657(2)	168
C1B-H1B1···Cl2	0.98	2.71	3.665(2)	166
C1D-H1D3···Cl3	0.98	2.72	3.678(3)	165
C5A-H5A···Cl2	0.95	2.74	3.585(2)	148
C4D-H4D···Cl1	0.95	2.74	3.598(3)	151
C1B-H1B3···Cl3	0.98	2.75	3.724(2)	171
C1C-H1C3···Cl4	0.98	2.75	3.693(3)	161
C1C-H1C2···Cl1	0.98	2.76	3.702(3)	162
C6A-H6A1···Cl1	0.99	2.76	3.724(2)	164
C1A-H1A3···Cl4	0.98	2.79	3.723(3)	160
C1B-H1B2···Cl2	0.98	2.80	3.730(2)	158
C5C-H5C···Cl2	0.95	2.81	3.653(3)	148

Table 5.2: H-bonds of the type D-H···A in [Emim][Cl] at 190(2)K, esds in brackets.

From table 5.2, it is clear to see that hydrogen bonding is present at all imidazolium ring hydrogens, as was reported by *Dymeck*. However, it is also clear that there is significant hydrogen bonding between hydrogen atoms on the alkyl substituents and chloride ions, this was not observed in the previous study, presumably on account of the poorer quality of data. Hydrogen bonding has been observed between hydrogen atoms on alkyl substituents on the imidazolium cation and the anion previously.[11]

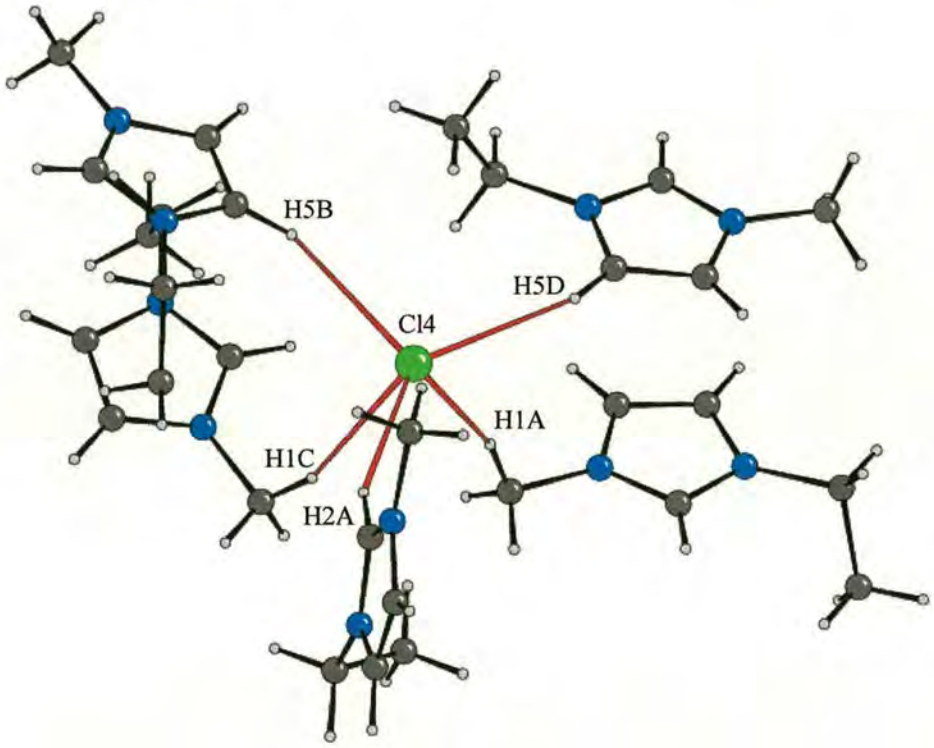

Figure 5.2: Diagram showing close contacts between the chloride ion and the five surrounding imidazolium ions.

Figure 5.3 shows the crystal structure of [Emim][Cl] along the *c* axis, with the layering of the imidazolium units and chloride ions. The chloride ions form layers between the rows of imidazolium cations. The interlayer hydrogen-bond interactions are more extensive than *Dymeck* reported previously due to the greater number of hydrogen bonds present.

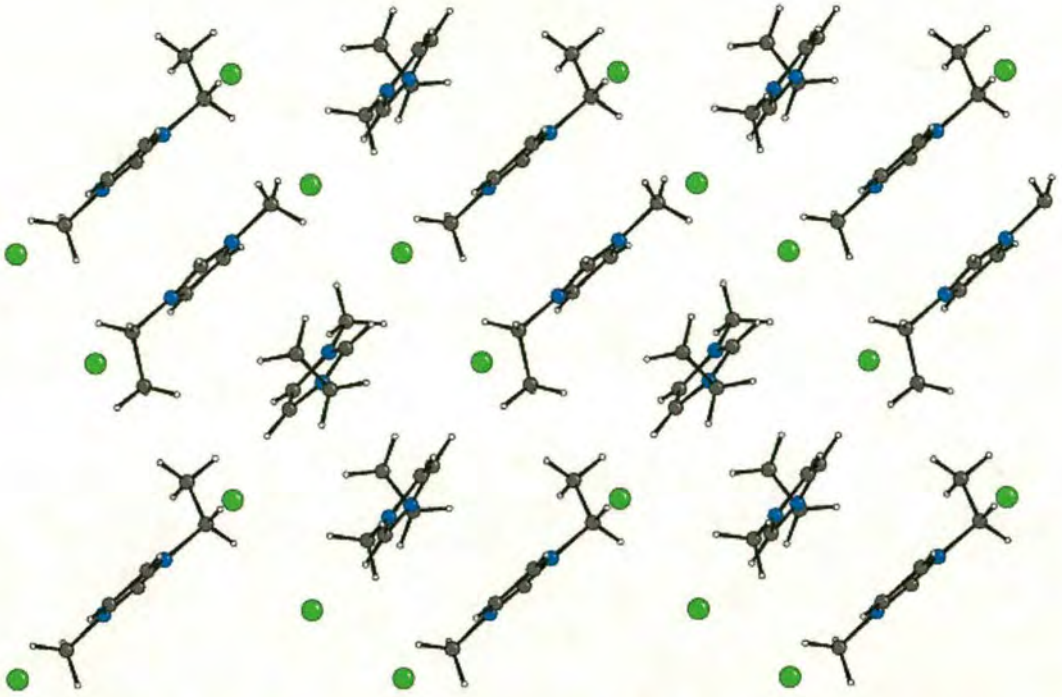

Figure 5.3: The crystal structure of [Emim][Cl] viewed along the *c*-axis

One of the imidazolium cations in the unit cell is disordered around the ring and the ethyl group, with disorder occurring at N1, C2, C6 and C7, with all associated hydrogens being disordered as well. The disorder in imidazolium unit B is displayed in figure 5.4, where atoms labelled B are part of the imidazolium unit that has 80% occupancy, and atoms labelled BB are part of the imidazolium unit that has 20% occupancy. Atoms that are common to both units within standard deviations are labelled B/BB. The atoms of imidazolium unit BB are shown as individual atoms rather than part of the bonded structure using the same numbering scheme as outlined earlier.

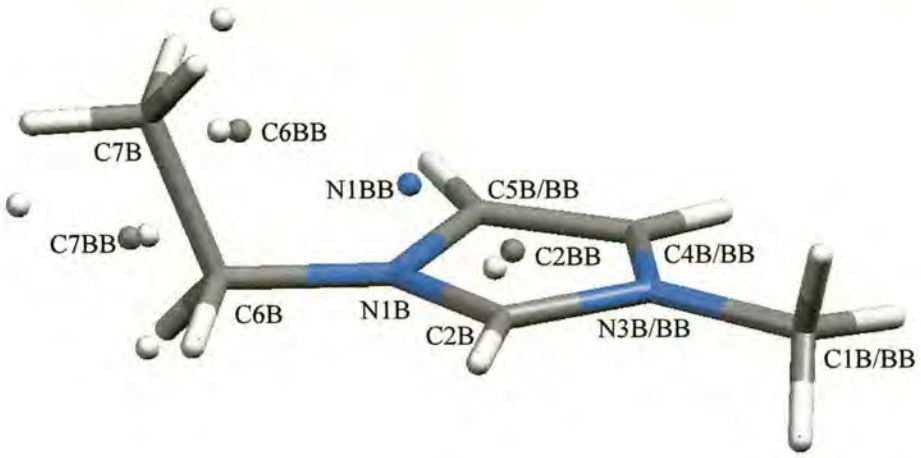

Figure 5.4: Disorder of the imidazolium cation in the unit cell of [Emim][Cl]

The disordered imidazolium ring is distorted from planarity, with the ring referred to as B being less distorted than the ring BB. The occupancy of the imidazolium ring B/BB is 0.8/0.2 and thus BB has been removed from diagrams for clarity. Torsion angles for both of the imidazolium rings in the disordered unit are shown in table 5.3. The disorder in this structure differs from that previously published.[6] *Dymeck et al.* observed that the disorder was only present at the C6 and C7 atoms of the imidazolium ion, with the ethyl group alternating between projecting above or below the imidazolium ring. In this structure the disorder is more extensive, with C2, N3 and H2 being disordered as well as C6 and C7. Identification of this extra disorder may be a contributing factor to the improved *R*-factor over previous data.

Atoms in ring B	**Torsion angle °**	**Atoms in ring BB**	**Torsion angle °**
C2-N3-C4-C5	5.8	C2-N3-C4-C5	-21.6
N3-C4-C5-N1	-6.4	N3-C4-C5-N1	26.6
C4-C5-N1-C2	4.7	C4-C5-N1-C2	-23.5
C5-N1-C2-N3	-1.1	C5-N1-C2-N3	10.7
N1-C2-N3-C4	-2.8	N1-C2-N3-C4	5.6

Table 5.3: Torsion angles of the disordered imidazolium ring in [Emim][Cl].

The distortion exhibited by the $[Emim]^+$ ring B/BB in [Emim][Cl] is not observed in the other three $[Emim]^+$ rings. Torsion angles range from -0.28° to 0.26° for ring A, -0.14° to 0.20° for ring C and -0.39° to 0.34° for ring D. There is also distortion of bond lengths for the disordered imidazolium unit B/BB with reference to the other three imidazolium cations as shown in table 5.4.

Bond	Bond lengths in imidazolium unit / Å				
	A	B	BB	C	D
C1-N3	1.472(3)	1.463(3)	1.463(3)	1.474(3)	1.468(3)
N3-C4	1.372(3)	1.370(4)	1.370(4)	1.368(3)	1.358(3)
C4-C5	1.340(3)	1.340(4)	1.340(4)	1.343(4)	1.349(4)
C5-N1	1.371(3)	1.391(4)	1.496(12)	1.361(3)	1.370(3)
N1-C2	1.326(3)	1.317(4)	1.327(17)	1.318(3)	1.316(3)
C2-N3	1.324(3)	1.334(4)	1.384(15)	1.310(3)	1.311(3)
N1-C6	1.475(3)	1.468(4)	1.51(2)	1.477(3)	1.480(4)
C6-C7	1.511(4)	1.487(6)	1.42(3)	1.485(4)	1.470(5)

Table 5.4: Bond lengths for imidazolium units in [Emim][Cl], where the numbers in brackets represents standard deviations in the last decimal place.

As can be seen in table 5.4, the main bond length distortion in imidazolium BB occurs in the ring with the C5-N1 bond being markedly longer than for the other imidazolium ions in the asymmetric unit. Other less pronounced distortions can also be seen with the C2-N3 and C6-C7 bonds and to a lesser extent with the N1-C6 bond.

By examination of published data from the Cambridge Structural Database, the internal geometry of the imidazolium cation generally remains largely unaffected by changing the anion in imidazolium salts.[12] The imidazolium units (A, C and D) that are not disordered have geometries that are consistent with previously published results. It therefore seems likely that these discrepancies are artefacts associated with the disorder.

Hydrogen bonding between the hydrogens on the imidazolium ring and chloride ions dominates the crystal structure of [Emim][Cl], with H2 showing the shortest contact and thus strongest interaction. The hydrogens on the ethyl and methyl groups also display hydrogen bonding to chloride ions, and though to a lesser extent than the ring hydrogens (there are 12 ring hydrogens and 32 alkyl hydrogens in the asymmetric unit, of these all 12 ring hydrogens display hydrogen bonding, and only 7 alkyl hydrogens display hydrogen bonding), the interactions are still significant.

5.1.2 Crystal structure of [Emim][$AgCl_2$]

[Emim][Cl] (1.00g, 0.0068moles) was dissolved in 5ml of dry acetonitrile and added to AgCl (0.974g, 0.0068moles) via a glass syringe. A reflux condenser was fitted to the Schlenk tube and the mixture was refluxed for 3h, resulting in the formation of two liquid phases. The upper-layer was a colourless liquid and the lower-layer a pale yellow liquid, there was no precipitate present. The reaction mixture was stored at 269K overnight resulting in the formation of a white precipitate in a pale yellow solution. The reaction mix was removed by canular filtration and the solid washed with cold acetonitrile, which was again removed by canular filtration. The white precipitate was dried *in vacuo* at 100°C for 10h to yield a white solid with a melting point of 324K.

Elemental analysis: [Emim][$AgCl_2$] Expected: C: 24.85%, H: 3.82%, N: 9.66%.
Found: C: 25.27%, H: 4.01%, N: 10.79%.

X-ray powder diffraction was used to determine whether this colourless solid was a new compound or if the solid was simply a mixture of AgCl and [Emim][Cl]. Powder X-ray diffraction patterns were therefore recorded for AgCl, [Emim][Cl] and the new solid.

It can clearly be seen from figure 5.5 that the powder pattern of the colourless solid is not a mixture of AgCl and [Emim][Cl]. Given the initial ratios of the starting materials, 1:1 AgCl:[Emim][Cl], it seemed likely that this colourless solid was therefore [Emim][$AgCl_2$]. CHN analysis supported the formation of [Emim][$AgCl_2$] with the experimental results correlating reasonably with the theoretical values calculated for [Emim][$AgCl_2$].

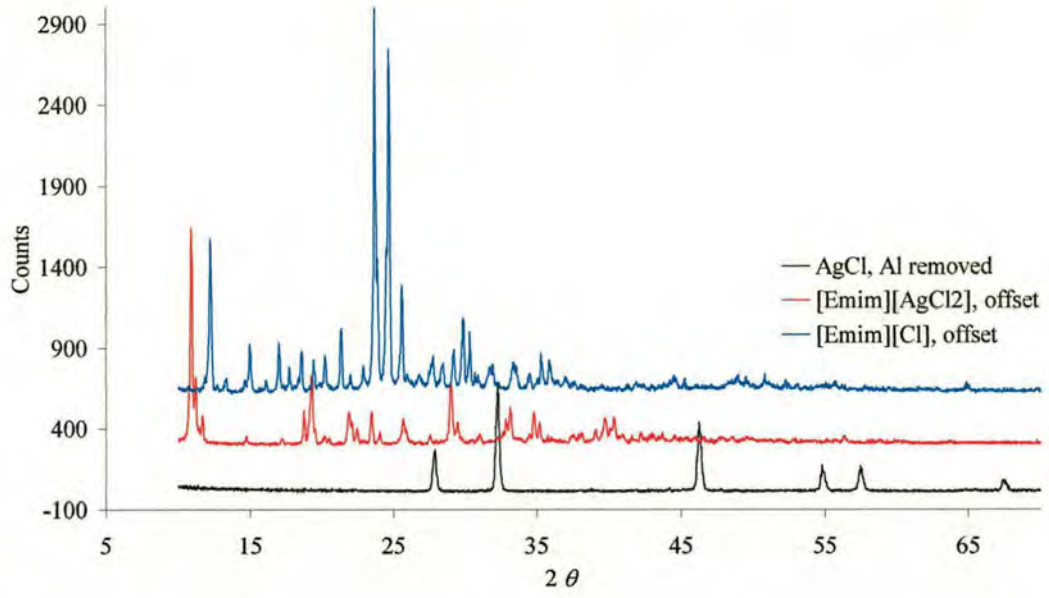

Figure 5.5: Powder X-ray diffraction data for AgCl, [Emim][Cl] and [Emim][$AgCl_2$]

A colourless crystal (0.54 x 0.42 x 0.40 mm) of sufficient quality to perform single crystal X-ray diffraction was obtained from the reaction mixture used to synthesise the [Emim][$AgCl_2$]. Data were collected at 190(2)K.

[Emim][$AgCl_2$] crystallises in the monoclinic crystal system, with space group C2/c. Unit cell parameters are $\underline{a}$ = 15.4284(10) Å, $\underline{b}$ = 10.9030(10) Å, $\underline{c}$ = 17.3246(12) Å, β = 103.872(2)°. The structure was refined by full-matrix least-squares on F^2 with SHELXL97,[13] giving a final *R*-factor of 3.7%. The unit cell volume was 2829.3(4) $Å^3$ with Z = 12, giving a calculated density of 2.04 g cm^{-3}. The repeat unit is shown in figure 5.6. The unit cell is generated by a 2-fold rotation round the y-axis, followed by a translation along the z-axis. The structure is made up of chains of $[AgCl_2]^-$ units oriented along the *c*-axis, with imidazolium units forming layers between the chains. The structure is an infinite polymeric anion accompanied by two discrete cations, one of which displays disorder around the rotation axis used to generate the structure. The polymeric anions may be considered as chains of edge sharing tetrahedra of $AgCl_4$ units. The $AgCl_4$ units are distorted away from ideal tetrahedral geometry. Imidazolium unit BB is generated by the symmetry operation

around the rotation axis with 50% B / 50% BB occupancy, the ethyl and methyl groups are interchanged in this disorder.

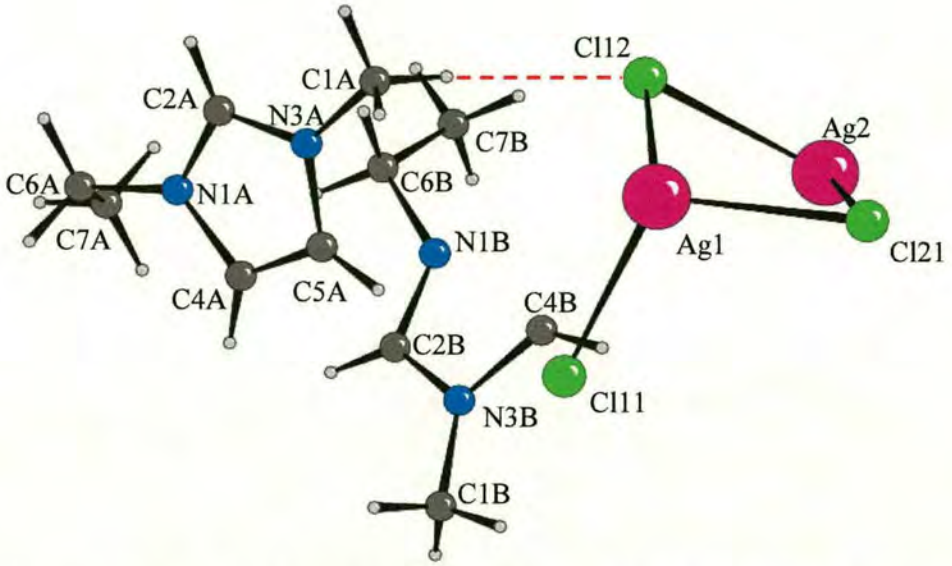

Figure 5.6: Numbering scheme for [Emim][$AgCl_2$], the disordered imidazolium group B is generated by a symmetry operation. (---) Denotes the shortest contact of the type C-H···Cl.

Hydrogen atoms are referred to by the number of the carbon atom they are attached to, followed by the ring unit to which the hydrogen is attached, followed by the *n*th hydrogen if there is more than one present on the same carbon. i.e., H7B3 is the third hydrogen on carbon 7 of imidazolium unit B. The disorder of the imidazolium unit B along with numbering scheme is shown in figure 5.7.

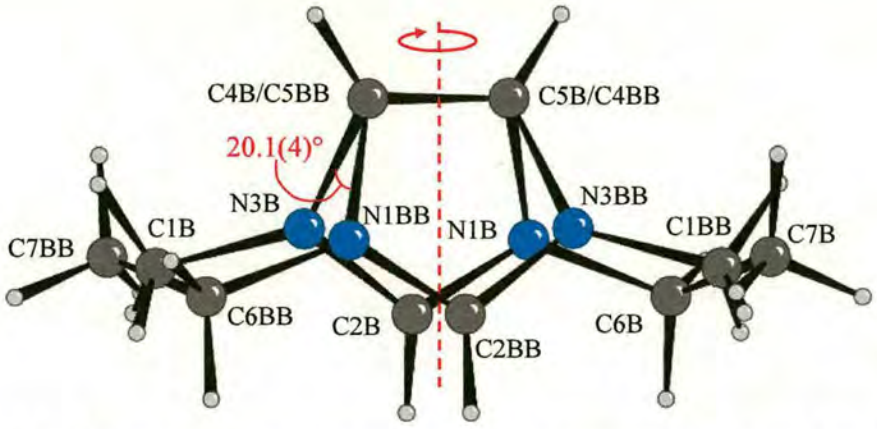

Figure 5.7: Disorder of imidazolium unit B, showing ethyl and methyl group interchange by the 2-fold rotation operation around the 2-fold axis (---).

The disorder of the imidazolium group in [Emim][$AgCl_2$] involves interchange of the ethyl and methyl groups with the imidazolium ring geometry unchanged. The imidazolium ring of unit BB is elevated from unit B by an angle of 20.1(4)° from the C4B—C5B axis (· N1BB—C4B—N3B) as shown in figure 5.8. The geometry of the imidazolium units are displayed in table 5.5.

Atoms in ring	**Angle °**		
	A	**B**	**BB**
C2-N1-C5	109.0(4)	114.6(7)	114.6(7)
C2-N1-C6	126.0(4)	125.6(8)	125.6(8)
C5-N1-C6	125.1(4)	119.7(8)	119.7(8)
N1-C6-C7	111.5(4)	112.4(8)	112.4(8)
N1-C2-N3	108.2(4)	108.8(7)	108.8(7)
C2-N3-C4	109.4(4)	102.9(7)	102.9(7)
C2-N3-C1	126.1(4)	126.3(8)	126.3(8)
C4-N3-C1	124.6(4)	130.6(8)	130.6(8)
C5-C4-N3	106.4(4)	115.5(5)	115.5(5)
C4-C5-N1	107.1(4)	98.1(3)	98.1(3)

Table 5.5:Geometry of the imidazolium rings in [Emim][$AgCl_2$]. Esds in parenthesis

As can be seen from table 5.5 the imidazolium rings B and BB only display distorted geometry from imidazolium ring A when either C4B/BB or C5B/BB are involved in the angle. The bond lengths of the imidazolium units are also displayed in table 5.6.

Bond	Bond length in Imidazolium unit / Å		
	A	B	BB
C1-N3	1.465(5)	1.482(14)	1.482(14)
N3-C4	1.377(5)	1.392(10)	1.392(10)
C4-C5	1.356(7)	1.354(11)	1.354(11)
C5-N1	1.378(6)	1.379(10)	1.379(10)
N1-C2	1.324(5)	1.321(12)	1.321(12)
C2-N3	1.327(5)	1.324(11)	1.324(11)
N1-C6	1.473(6)	1.488(12)	1.488(12)
C6-C7	1.499(8)	1.498(13)	1.498(13)

Table 5.6: Table of bond lengths for imidazolium units in [Emim][$AgCl_2$]. esds in brackets

As can be seen from table 5.6, the bonding within the imidazolium ring does not vary significantly for A, B and BB. The crystal packing along the *b* and *c* axis of the unit cell is shown in figures 5.8 and 5.9 respectively.

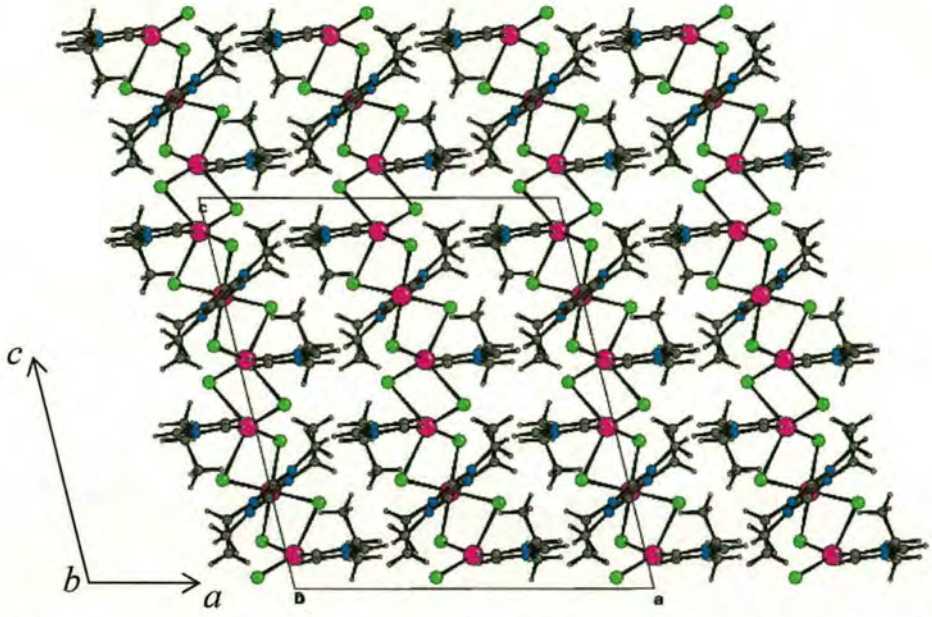

Figure 5.8: The crystal structure of [Emim][$AgCl_2$] viewed along the *b* axis of the unit cell.

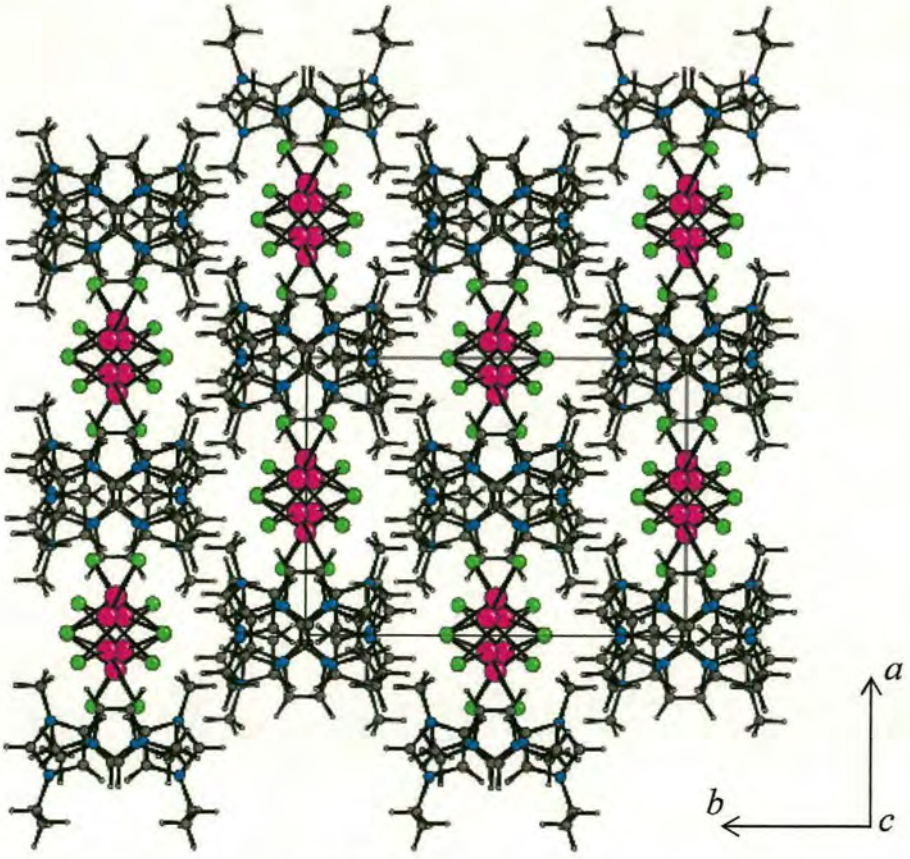

Figure 5.9: The crystal structure of [Emim][$AgCl_2$] viewed along the *c* axis of the unit cell.

Hydrogen bonds of the type D-H···A (where D-H = C-H and H···A = H···Cl) are listed in table 5.7.

D-H···A	D-H / Å	H···A / Å	D···A / Å	D-H-A / °
C2B-H2B···Cl21	0.95	2.71	3.513(7)	143
C5A-H5A···Cl21	0.95	2.81	3.709(5)	157
C1A-H1A1···Cl21	0.98	2.74	3.694(5)	164
C6B-H6B2···Cl21	0.99	2.81	3.593(9)	137
C7A-H7A1···Cl12	0.98	2.72	3.518(6)	139
C7A-H7A2···Cl12	0.98	2.83	3.579(6)	134
C1A-H1A2···Cl12	0.99	2.64	3.621(5)	175
C4B-H4B···Cl12	0.95	2.75	3.529(6)	139

Table 5.7: H-bonds of the type C-H···Cl in [Emim][$AgCl_2$], with d(H···A) < radius (H) + radius (A) - 0.12 Å as limit for hydrogen bonding[8]. Esds in paranthesis

Figure 5.10 shows an example of the interactions between the anion and cation.

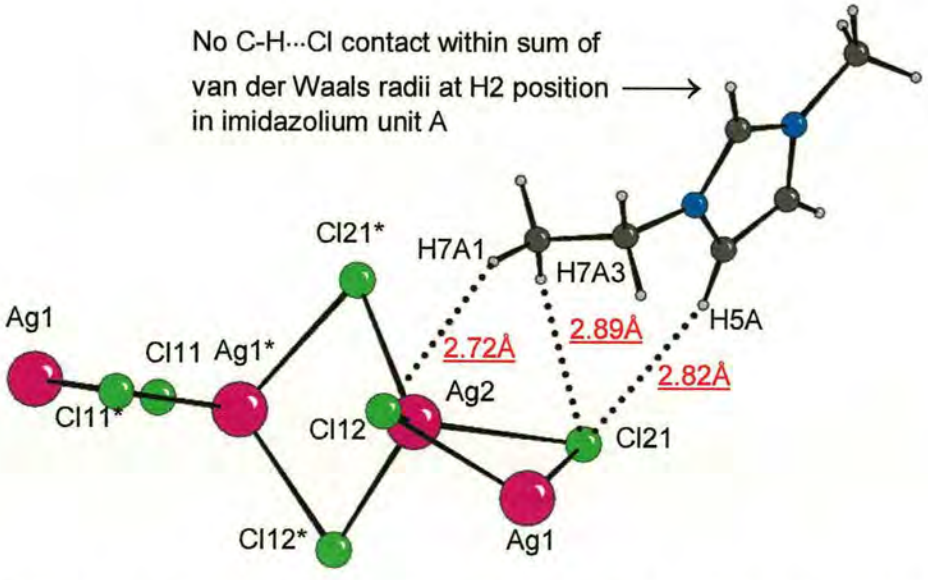

Figure 5.10: Close-contacts (····) between the cation and anion in [Emim][$AgCl_2$]. All hydrogens display close contacts to other chain units except H2A.

A surprising feature of the structure is that the strongest hydrogen-bonding interaction appears to involve H1A2. Evidence for this comes from the shortest H···Cl distance being 2.64Å and the C1A-H1A2···Cl12 angle being 175°. In all other crystal structures of imidazolium derivatives in which there is an available hydrogen atom attached to the C2 position, it is this H2 atom that is involved in the shortest D-H···A contact. The extensive hydrogen bonding that occurs within this structure could be a reason for the shortest contact not occurring at the H2 position, with the greater number of hydrogen bonds compensating for the loss of the strongest interaction at the C2 position. It would appear that the polymeric anions dictate the packing of the imidazolium cations, and that the alkyl hydrogens display a greater degree of hydrogen because of this packing arrangement. This is in contrast to crystal structures observed with simple monomeric anions where the imidazolium hydrogens display the most significant hydrogen bonding, this suggests that hydrogen bonding might not be as important to the crystal packing as it is currently thought to be. It is also interesting to note the C-H···Cl angle for the shortest contact is closest to 180° in this structure, giving another possible reason for the strongest interaction occurring at this position. To the best of the authors knowledge, this is the first example of an $[Emim]^+$ based crystal exhibiting the shortest D-H···A contact at this position when the H2 position is available for hydrogen bonding. In contrast to the [Emim][Cl] crystal structure, the alkyl hydrogens display the greater number of hydrogen bonds to the polymeric $[AgCl_2]^-$ anion. It is also interesting to note that the only hydrogen bonding to H2 is present at imidazolium rings B and BB. This could account for the disorder and distortion in imidazolium unit B/BB.

The anionic chains exhibit a helical structure with Ag-Ag-Ag angles varying from 150.74(2)° for ·Ag(1)*-Ag(2)-Ag(1) to 160.03(2)° for ·Ag(2)-Ag(1)-Ag(1)*. In addition Ag-Ag contacts vary from 3.0306(4)Å for Ag(2)-Ag(1) and 3.1900(7)Å for Ag(1)-Ag(1)*. The most pronounced view of this helical structure is looking along the unit cells *a*-axis, this is shown in figure 5.11 for which the $[Emim]^+$ units have been removed for clarity. The displacement of Ag1 and Ag1* along the *b*-axis of the

unit cell from the Ag(2) plane is observed best by the view along the *c*-axis of the unit cell.

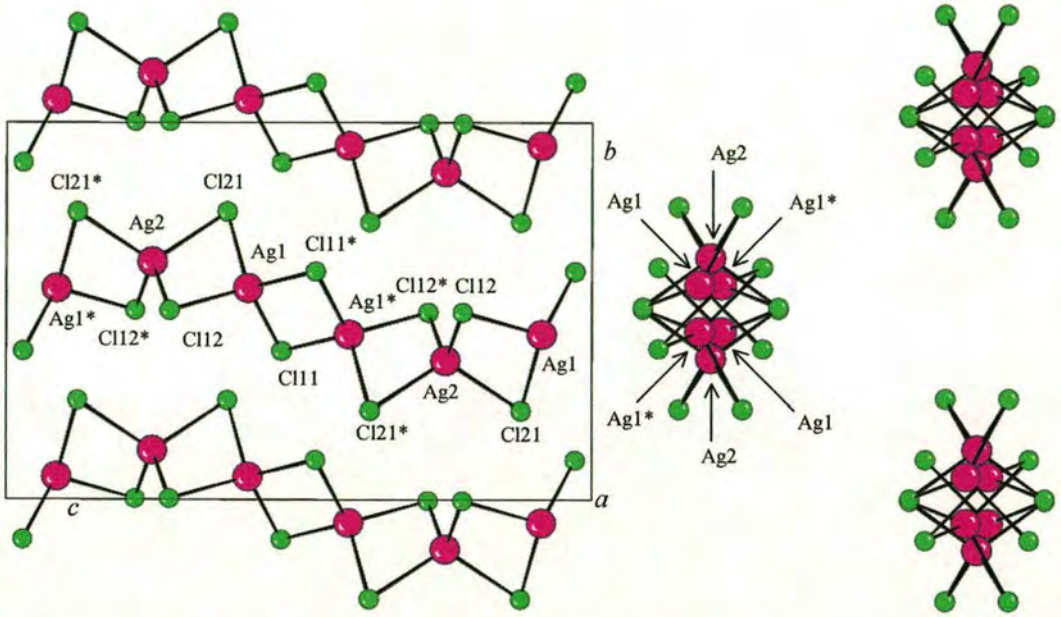

Figure 5.11: View of the infinite polymeric $[AgCl_2]^-$ anions along the *a*-axis (left view, unit cell included) and *c*-axis (right view) of the unit cell.

A selection of bond lengths and angles for the infinite polymeric $[AgCl_2]^-$ anion are presented in table 5.8. It should be noted that Ag1*, Cl(21)*, Cl(12)* and Cl(11)* are generated by the 2-fold rotation when the unit cell is being constructed. The repeat unit of the $[AgCl_2]^-$ chain is the Ag1-Ag2-Ag1* with its associated chloride ions, the rotation and translation of this repeat unit builds up the polymeric chain.

Atoms	Bond Length / Å	Atoms	Bond Angle / °
Ag(1)-Cl(12)	2.5889(11)	**Ag(2)-Ag(1)-Ag(1)***	160.03(2)
Ag(2)-Cl(12)	2.5603(10)	**Ag(1)-Ag(2)-Ag(1)***	150.74(2)
Ag(1)-Cl(21)	2.6720(10)	**Cl(12)-Ag(2)-Cl(12)***	113.56(3)
Ag(2)-Cl(21)	2.6246(10)	**Cl(21)-Ag(2)-Cl(21)***	113.43(5)
Ag(1)-Cl(11)	2.6006(12)	**Cl(21)-Ag(2)-Cl(12)**	105.15(3)
Ag(I)-Cl(11)*	2.5985(12)	**Cl(21)-Ag(1)-Cl(12)**	103.01(3)
Ag(1)-Ag(1)*	3.1900(7)	**Cl(12)-Ag(2)-Cl(21)***	109.88(3)
Ag(1)-Ag(2)	3.0306(4)	**Cl(11)-Ag(1)-Cl(11)***	104.30(3)
—	—	**Ag(2)-Cl(21)-Ag(1)**	69.80(3)
—	—	**Ag(2)-Cl(12)-Ag(1)**	72.11(3)
—	—	**Ag(1)*-Cl(11)-Ag(1)**	75.70(3)

Table 5.8: A selection of bond lengths and angles for the infinite polymeric $[AgCl_2]^-$ anion.

The most interesting feature from table 5.8 is the large difference in angles between Ag(1)-Ag(2)-Ag(1)* and Ag(2)-Ag(1)-Ag(1)*, giving rise to the helical structure and this would suggest that the weakest point in the polymeric anion as Ag(1)-Ag(2)-Ag(1)*. A possible reason for this is that if silver were to adopt its preferred tetrahedral geometry with the two bridging chlorides, the angle between three adjacent silver atoms would require to be as close to 180° as possible. At 150.74(2)° this is a large deviation from 180° and would suggest that this is where bonds are initially broken on melting the crystal. There is also a large variance in the Ag-Cl distances with values ranging from 2.56 to 2.67 Å. The longest Ag-Cl bonds occur when Cl(21) is involved, and the shortest Ag-Cl bonds occur when Cl12 is involved. These two bridging chlorides, Cl(12) and Cl(21), are involved in the bridging at Ag(1)-Ag(2)-Ag(1)*. The are 4 hydrogen bonds to both Cl(12) and Cl(21), with the strongest interaction occurring at Cl(12) which would suggest that the Ag-Cl bond for Cl(12) should be longer than that obtained for Ag-Cl(21). However, if we take into account close contacts between hydrogen atoms and the anion, we find that there are four close contacts to Cl(12), but there are 6 close

contacts to Cl(21), leading to the weakening of the Ag-Cl(21) bonds relative to the Ag-Cl(12) bonds. Thus it would seem reasonable to suggest that the polymeric anion is distorted into a helical structure by the different degrees of close contacts between the asymmetric imidazolium cations and each of the chlorides of the anion.

Examples of infinite polymeric chains[14,15] of $[AgCl_2]^-$ in the literature display near regular tetrahedral geometry extending parallel to the *c*-axis[14] for tetramethylammonium catena-di-μ-chloroargentate(I) or parallel to the *a*-axis[15] for bis(piperidine)gold(I) dichloroargentate(I). Other examples of silver geometry in published crystal structures are the infinite polymeric $[AgCl_3]^{2-}$ chain of corner-sharing $AgCl_4$ tetrahedra[16] and infinite double chains of $[Ag_2Cl_3]^-$ edge sharing $AgCl_4$ tetrahedra.[17] Examples of discrete anions include the chloride bridged $[Ag_2Cl_5]^{3-}$ anion,[18] the dimeric $[Ag_2Cl_4]^{2-}$ anion,[19] and the discrete $[AgCl_2]^-$ anion.[20,21] The melting points of the polymeric anions ranged from 479K[17] to 566K.[14,16]

An interesting feature of the $[Emim][AgCl_2]$ system was observed when conducting the crystallographic study. A glass capillary containing $[Emim][AgCl_2]$ sealed under an atmosphere of dry nitrogen using a bunsen burner was later found to be imperfectly sealed during preparation. As a result, slow diffusion of moisture from the atmosphere into the solid sample of dry $[Emim][AgCl_2]$ yielded a small 'Christmas-tree' shaped series of single crystals in the glass capillary, and the rest of the sample formed a pale yellow liquid. The solid was examined by X-ray diffraction by rotating the crystal to give a pseudo-powder diffraction pattern that corresponded to that of AgCl.[22] An aqueous solution of [Emim][Cl] had presumably been formed due to ingress of moisture from the atmosphere into the chloride ionic liquid and could possibly be produced as outlined in reaction (2).

$$[Emim][AgCl_2]_{(s)} + H_2O_{(l)} \longrightarrow [Emim][Cl]_{(aq)} + AgCl_{(s)} \qquad (2)$$

Due to the sparing solubility of silver chloride in common solvent systems, it is commonly recrystallised from molten silver chloride near its melting point, 457°C.

As has been evidenced by this study, AgCl can form 1:1 compounds with [Emim][Cl] allowing for an appreciable concentration of AgCl to be dissolved in these compounds, and as a result, present themselves as possible ambient temperature alternatives for the recrystallisation of silver chloride.

Thus [Emim][$AgCl_2$] is the first example of a crystal structure exhibiting such distortions in an infinite polymeric chain of edge sharing tetrahedra of $[AgCl_2]^-$. In addition to this, it represents the first example of an $[Emim]^+$ based ionic liquid exhibiting the shortest D-H···A contact at the methyl hydrogen in the crystal structure when the H2 position is available for hydrogen bonding. In combination, these may be the reason for the unusually low melting point (324K) of [Emim][$AgCl_2$] compared to other crystal structures containing infinite polymeric chains of silver chloride anions.

5.2 Raman spectroscopy

5.2.1 Raman spectroscopy of [Emim][$CuCl_2$]

[Emim][Cl] (0.500g, 0.0034moles) was dissolved in 5ml of dry acetonitrile and added to CuCl (0.338g, 0.0034moles) via a glass syringe. Upon addition of the colourless [Emim][Cl] solution to the solid CuCl, a white precipitate appeared on the bottom of the Schlenk tube. A reflux condenser was fitted to the Schlenk tube and the mixture was refluxed for 3h, resulting in a very pale yellow solution with no precipitate. On cooling the reaction mix, the solution became orange with a fine brown/black precipitate. The orange solution was removed from the precipitate by canular filtration and the solvent was removed *in vacuo* to leave a green liquid, which was dried by heating at 333K *in vacuo* for 10h.

Elemental analysis: [Emim][$CuCl_2$] Expected: C: 29.34%, H: 4.51%, N: 11.41%.
Found: C: 30.56%, H: 4.93%, N: 12.28%.

The same liquid could be formed through the mixing of equimolar amounts of [Emim][Cl] and CuCl at 353K for a few hours resulting in a highly viscous green liquid at room temperature. Cooling this liquid results in the formation of a glass rather than a crystalline solid as evidenced by observing the solid under plane polarised light. The [Emim][$CuCl_2$] ionic liquids instantaneously turn brown in colour when contacted with ambient air highlighting the care needed in handling this air sensitive material. On cooling to ~197 K with dri-ice, [Emim][$CuCl_2$] forms a glassy phase.

The viscosity of CuCl/[Emim][Cl] melts reached a minimum when the composition is 50 mol% CuCl, with the dominant copper containing species in composition likely to be the $[CuCl_2]^-$ anion.[23]

In order to obtain insight into the anionic species present in the room temperature ionic liquid, [Emim][$CuCl_2$], a Raman spectrum was obtained at room temperature using the 632.8nm line of a HeNe laser, the resulting spectra is shown in figure 5.12.

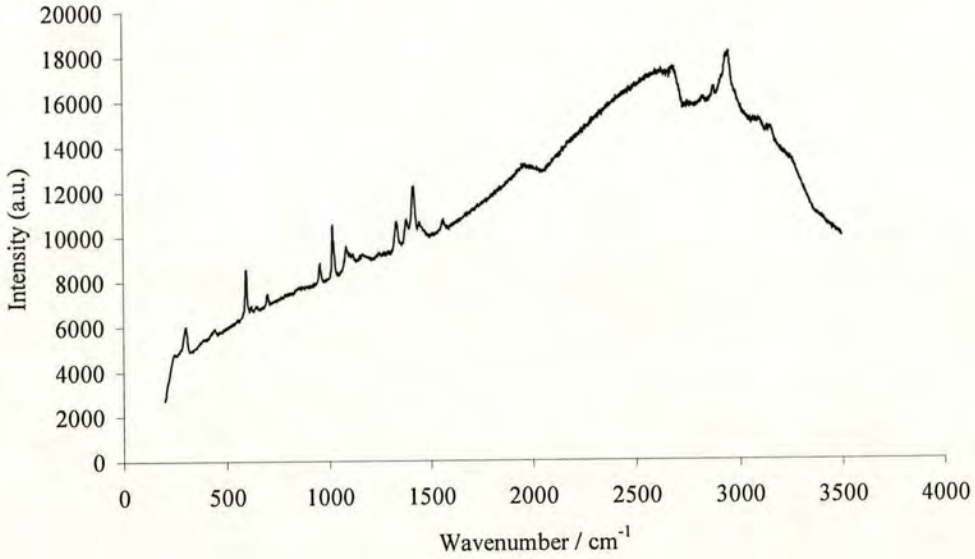

Figure 5.12: Raman scattering spectrum for [Emim][$CuCl_2$] in a N_2-filled glass capillary at room temperature.

Peaks at 596, 699 and from 1000 to 3000 cm^{-1} in figure 5.11 can be ascribed to the imidazolium cation.[24] Most peaks are present in the 200 to 2000 cm^{-1} region of the Raman spectrum and this region has been expanded for clarity and labelled with peak positions in figure 5.13.

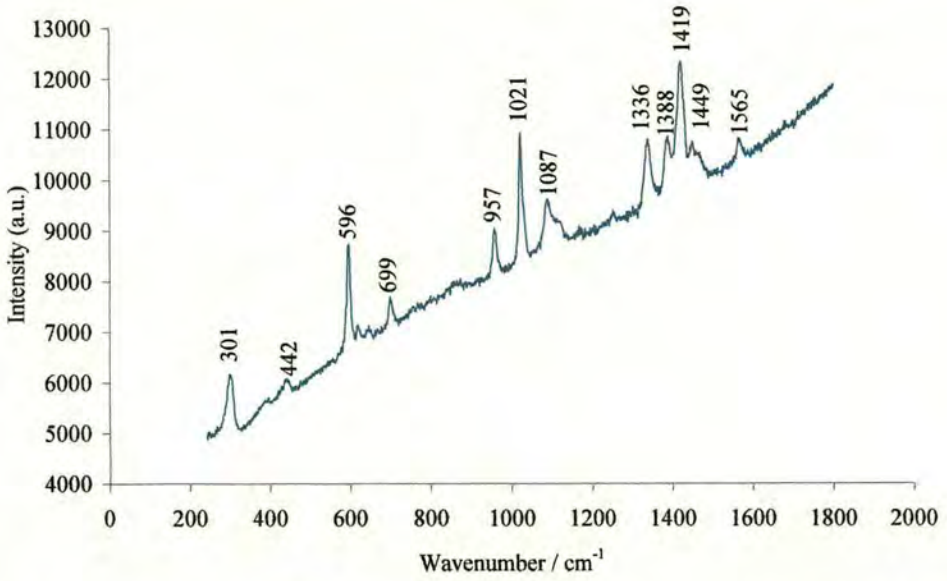

Figure 5.13: Raman spectrum of [Emim][$CuCl_2$] with peak wavenumbers labelled.

From figure 5.13 it can be seen that there are two peaks that do not correspond to the imidazolium cation, these occur at 302 cm^{-1} and 442 cm^{-1}. It has been found that liquids containing the $[CuCl_2]^-$ anion exhibit a strong sharp Raman absorption[25] at *ca* 300cm^{-1} corresponding to the symmetric Cu-Cl stretch, ν_1. This is observed as a peak at 302 cm^{-1} in [Emim][$CuCl_2$] in the present study. The presence of the peak at 442 cm^{-1} in conjunction with the broad peak at 302 cm^{-1} has been observed for melts of the composition $[Cu_2Cl_3]^-$ in equilibrium with $[CuCl_2]^-$ and CuCl according to equation (1).

$$[CuCl_2]^- + CuCl \leftrightarrow [Cu_2Cl_3]^- \quad (1)$$

This suggests that at room temperature the anion in the ionic liquid [Emim][$CuCl_2$] may exist as a mixture of CuCl and [Emim][$CuCl_2$]. This is the case for 50 mol % CuCl in [Emim][Cl], and it would seem logical to assume that in lower concentrations of CuCl the equilibrium in equation (1) would be shifted to the left..

5.2.2 Raman spectroscopy of [Emim][$AgCl_2$]

Raman spectroscopy was attempted on [Emim][$AgCl_2$] using the 632.8 nm line of a HeNe laser, but the very high level of fluorescence from the sample precluded the collection of useful data. It would have been useful to examine the Raman spectra of [Emim][$AgCl_2$] in both the crystalline and liquid phase in order to compare the species present in [Emim][$AgCl_2$] and [Emim][$CuCl_2$] in the liquid phase. This may have provided some insight into why [Emim][$CuCl_2$] forms a glass rather than a crystalline solid and why the melting point is so much lower in the chlorocuprate derivative.

5.3 Conclusions

A crystal structure determination of [Emim][Cl] has been presented which offers a significant improvement over previously reported structures. The improvement has been obtained by the collection of diffraction data at 190 K as opposed to the data previously collected at 298 K. An improved refinement of the structure has been achieved by introducing a greater degree of disorder involving the ethyl group and C2 and N1 on the imidazolium ring. In combination, these improvements have provided a better location of hydrogen-atom positions, which has given a more reliable insight into the degree of hydrogen bonding of the type C-H···Cl^- within the crystal structure. The structure displays a much greater degree of hydrogen bonding than observed in previous studies. Hydrogen bonding was observed not only between hydrogen atoms on the ring and chloride ions as was reported previously, but was also significant between hydrogen atoms on the alkyl substituents and chloride ions. The strongest C-H···Cl^- interaction was observed between H2D on the imidazolium ring and Cl3. The extent of the C-H···Cl^- interactions within the crystal structure of [Emim][Cl] highlights that hydrogen bonding contributes significantly to the ordering in the solid state structure. It can be anticipated that hydrogen bonding will also be a contributing factor to local ordering in the liquid state.

A new ionic liquid, [Emim][$AgCl_2$], with a melting point of 324 K has been formed and characterised by single crystal X-ray diffraction. The anion is an infinite polymeric chain of edge sharing tetrahedra of $[AgCl_2]^-$ units extending along the *c*-axis of the unit cell. The $[AgCl_2]^-$ chain displayed a helical structure, presumably as a result of distortions induced by the extensive hydrogen bonding to the asymmetric [Emim] cation. The Ag-Cl bond lengths observed in [Emim][$AgCl_2$] are comparable to those found in the infinite polymeric $[AgCl_2]^-$ chain of edge sharing tetrahedra in $[N(CH_3)_4][AgCl_2]$ which do not display a helical motif. As was observed with the [Emim][Cl] crystal structure, there was significant hydrogen bonding interactions of the type C-H···Cl between the anion and the hydrogen atoms on the alkyl groups as

well as the hydrogens on the imidazolium ring. The strongest of the C-H···Cl interactions was observed to occur, rather surprisingly, between H1A2 of the methyl substituent and Cl(12) on the anion. This is in contrast to the majority of ionic liquid structures, which invariably exhibit the strongest D-H···A interactions at the H2 position of the imidazolium ring, and suggests that hydrogen bonds are dictated by the packing of the crystal.

From the two crystal system studied it can be concluded that hydrogen bonding between the hydrogens on the imidazolium cations and the anions occurs at both the imidazolium and alkyl hydrogens and that hydrogen bonding is likely to be present within the liquid state on a localised scale once the solids are melted.

The Raman spectra of [Emim][$CuCl_2$] indicate that more species than the expected $[CuCl_2]^-$ species are present as the anionic species in the liquid state. Indeed it has already been postulated that (50:50 mol %) [Emim][$CuCl_2$] is composed of multiple anionic species linked through equilibria such as that observed in equation (1) previously and equations (3) and (4).

$$[Cu_2Cl_3]^- + Cl^- \leftrightarrow 2[CuCl_2]^- \quad (3)$$

$$[CuCl_2]^- + Cl^- \leftrightarrow [CuCl_3]^{2-} \quad (4)$$

This has been suggested as a possible explanation for the depression in melting point of the chlorocuprate melts at the 50:50 mol % composition, though the predominant species is expected to be $[CuCl_2]^-$ due to physical properties such as viscosity and conductivity displaying a minimum at this composition.[23]

---

[1]J.F. Huang, P.Y. Chen, I.W. Sun and S.P. Wang, *Inorg. Chim. Acta.*, 2001, **320**, 7-11.

[2]S. Dai, Y.S. Shin, L.M. Toth and C.E. Barnes, *Inorg. Chem.*, 1997, **36**, 4900-4902.

[3]S. Tait and R.A. Osteryoung, *Inorg. Chem.*, 1984, **23**, 4352-60.

[4] **(a)** F. Shi, Y. Deng, T SiMa, J. Peng, Y. Gu, and B. Qiao, *Angewandte. Chemie, Int. Ed.*, 2003, **42(28)**, 3257-3260. **(b)** J.X. Wu, B. Beck and R.X. Ren, *Tet. Lett.*, 2002, **43**, 387-389.

[5] **(a)** D. Zhao, M. Wu, Y. Kou and E. Min, *Catalysis Today*, 2002, **74**, 157-189. **(b)** H. Olivier-Bourbigou and L. Magna, *Journal of Molecular Catalysts A: Chemical*, 2002, **182-183**, 419-437.

[6]C.J. Dymeck Jr., D.A. Grossie, A.V. Fratini and W.W. Adams, *J. Mol. Chem.*, 1989, **213**, 25-34.

[7] Sheldrick. G.M. *SHELXL97, Hydrogen atom constraints*, University of Göttingen, Germany, 1997.

[8] Th. Steiner, *Cryst. Rev.*, 1996, **6**, 1-57.

[9] A. Abdul –Sada, A.M. Greenway, P.B. Hitchcock, T.J. Mohammed, K.R. Seddon and J.A. Zora, *J.Chem. Soc., Chem Commun.*, 1986, 1753-1754.

[10] J.S. Wilkes and M.J. Zaworotko, *J.Chem. Soc., Chem. Commun.*, 1992, 965-967.

[11] **(a)** S. Saha, S. Hayashi, A. Kobayashi and H. Hamaguchi, *Chem. Lett.*, 2003, **32**, 740-741. **(b)** J.D. Holbrey, W.M. Reichert, M. Nieuwenhuyzen, S. Johnston, K.R. Seddon and R.D. Rogers, *Chem. Commun.*, 2003, 1636-1637. **(c)** M.F. Ortwerth, M.J. Wyzlic and R.G. Baughman, *Acta. Cryst.*, 1998, **C54**, 1594-1596. **(d)** K. Matsumoto, T. Tsuda, T. Nohira, R. Hagiwara, Y. Ito and O. Tamada, *Acta. Cryst.*, 2002, **C58**, m186-m187.

[12]J. Pringle, *Postdoctoral Thesis*, The University of Edinburgh, 2001, p197-205.

[13] Sheldrick, G.M., *SHELXL97*, University of Göttingen, Germany, 1997.

[14] G. Helgesson, M. Josefsson and S. Jagner, *Acta. Cryst.*, 1998, C**44**, 1729-1731.

[15] B. Ahrens, S. Friedrichs, R. Herbst-Irmer and P.G. Jones, *Eur. J. Inorg. Chem.*, 2000, 2017-2029.

[16] C. Hasselgren and S. Jagner, *Acta. Cryst.*, 1999, C**55**, 1208-1210.

[17] G. Helgesson and S. Jagner, *Acta Cryst.*, 1988, C**44**, 2059-2062.

[18] J.C. Bowles and D. Hall, *Acta. Cryst.*, 1975, B**31**, 2149-2151.

[19] G. Helgesson and S. Jagner, *J. Chem .Soc. Dalton Trans.*, 1988, 2117-2120.

[20] G. Helgesson and S. Jagner, *Inorg. Chem.*, 1991, **30**, 2574-2577.

[21] G. Exarchos, S.C. Nyburg and S.D. Robinson, *Polyhedron*, 1998, **17**(8), 1257-1266.

[22] Private communication, Dr. A. Parkin, Departmental crystallography service, The University of Edinburgh.

[23] S.A. Bolkan and J.T. Yoke, *J. Chem. Eng. Data.*, 1986, **31**, 194-197.

[24] K. Matsumoto, R. Hagiwara and Y. Ito, *J. Fluorine Chem.*, 2002, **115**(2), 133-135.

[25] D.D. Axtell, B.W. Good, W.W. Porterfield and J.T. Yoke, *J. Am. Chem. Soc.*, 1973, 4555-4559.

6 Electrochemistry

6.1 Cyclic Voltammetry.

In the scientific literature to date, the vast majority of ionic liquid electrochemistry has been performed in imidazolium based ionic liquids. This is due to a combination of electrochemical stability, good electrical conductivity, relatively low viscosities and a large volume of published data on electrochemical investigations in these melts. A typical cyclic voltammogram of [Emim][Cl] is shown in figure 6.1. The anodic limit (1.19V) is attributed to the oxidation of the chloride anion, and the cathodic limit (-1.02V) is attributed to the reduction of the imidazolium cation.[1] This gives a usable potential range (electrochemical window) of 2.21V within which redox reactions can be studied. The reduction peak at *ca.* 0.55V is only observed after excursion into the oxidation limit of the melt and is due to reduction of chlorine absorbed on the surface of the platinum electrode.

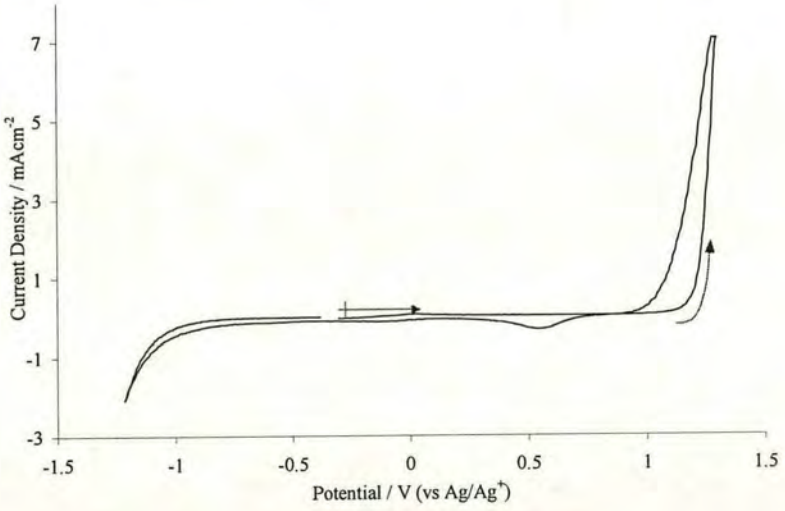

Figure 6.1: Electrochemical window of [Emim][Cl] at a platinum electrode, 50mVs^{-1}. Potentials are vs Ag/Ag^{+} (Silver wire in 0.01M silver chloride in [Emim][Cl]),

In addition to using a chloride ionic liquid, the ionic liquid 1-ethyl-3-methylimidazolium bis(trifluoromethanesulfonyl)imide, [Emim][$N(Tf)_2$], was also used. The advantages of using [Emim][$N(Tf)_2$] over the [Emim][Cl] are its lower melting point, its relatively hydrophobic nature (which reduces its propensity to water absorption, making the ionic liquid easier to handle) and its increased anodic stability. A typical cyclic voltammogram of [Emim][$N(Tf)_2$] is shown in figure 6.2.

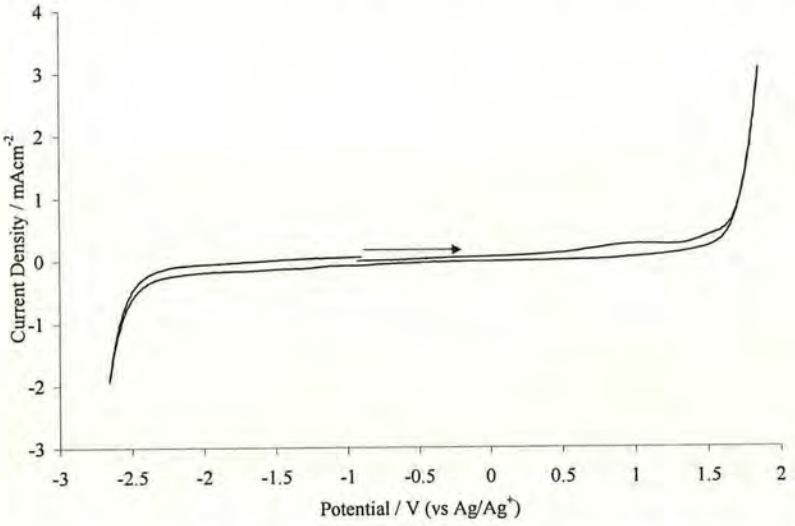

Figure 6.2: Electrochemical window of [Emim][$N(Tf)_2$] at a platinum electrode at 423.15K, 50mVs^{-1}. Potentials are vs Ag/Ag^+ (Silver wire in 0.01M silver triflate in [Emim][$N(Tf)_2$]),.

As can be seen from figure 6.2, the cathodic limit has shifted in comparison to that observed in figure 6.1. This is due to the use of a different reference electrode. The cathodic reaction is still the reduction of $[Emim]^+$, though the thermodynamics of reduction are different. In the case of the $[N(Tf)_2]^-$ melt, the observed potential for the cation reduction corresponds to the overall cell reaction, equation (3):

$$Ag_{(s)} \longrightarrow Ag^{+}_{(solv)} + e^{-} \quad (1)$$

$$[Emim]^{+}_{(solv)} + e^{-} \longrightarrow [Emim]^{\bullet}_{(solv)} \quad (2)$$

$$[Emim]^{+}_{(solv)} + Ag_{(s)} \longrightarrow Ag^{+}_{(solv)} + [Emim]^{\bullet}_{(solv)} \quad (3)$$

Equations (1) & (2) are the half-cell reactions for the reference electrode and the reduction of $[Emim]^{+}_{(solv)}$ respectively, and reaction (3) is the overall cell reaction. It should be noted that $[Emim]^{\bullet}_{(solv)}$ denotes the product of $[Emim]^{+}_{(solv)}$ reduction and therefore that solvation of these species also determines the overall thermodynamics of the half-cell reactions (The identity of $[Emim]^{\bullet}_{(solv)}$ is as of yet unknown, i.e., it is not known where the radical is situated on the $[Emim]^{\bullet}$, what the lifetime of the radical species is, or if undergoes further chemical reaction after the reduction reaction). For the chloride melt, the following reactions determine the thermodynamics of the cell reactions:

$$Ag_{(s)} + pCl^{-}_{(solv)} \longrightarrow AgCl_p^{(p-1)-}{}_{(solv)} + e^{-} \quad (4)$$

$$[Emim]^{+}_{(solv)} + e^{-} \longrightarrow [Emim]^{\bullet}_{(solv)} \quad (5)$$

$$[Emim]^{+}_{(solv)} + Ag_{(s)} + pCl^{-}_{(solv)} \longrightarrow AgCl_p^{(p-1)-}{}_{(solv)} + [Emim]^{\bullet}_{(solv)} \quad (6)$$

Equations (4) & (5) are the half-cell reactions for the reference electrode and the reduction of $[Emim]^{+}_{(solv)}$ respectively, and reaction (6) is the overall cell reaction. The cell potential, E_{cell}, is related to the Gibbs free energy, G, through the equation $\Delta G = -nFE_{cell}$, where n is the number of electrons and F is the Faraday constant (96485.3 $Cmol^{-1}$). The solvation of the reactants and products in an electrochemical reaction determines the ΔG of the reaction, clearly the solvation will be different for the $[Cl]^{-}$ and $[N(Tf)_2]^{-}$ melts. From the cyclic voltammogram of $[Emim][[N(Tf)_2]$, we can see the cathodic limit is -2.57V and the anodic limit is 1.72V, giving an electrochemical window of 4.29V, this is *ca.* 2V larger than that of

[Emim][Cl]. The $[Emim]^+$ reduction potential is more negative in the $[N(Tf)_2]^-$ melt due to the thermodynamics of eqns (3) and (6). In eqn (6), the $Ag/AgCl_p^{(p-1)-}{}_{(solv)}$ reduction potential is most likely to be more negative than the $Ag/Ag^+{}_{(solv)}$ reduction potential, reaction (1), due to the thermodynamic stability of $AgCl_p^{(p-1)-}{}_{(solv)}$ relative to that of $Ag^+{}_{(solv)}$. The increased anodic stability (and hence increased solvent window) is most likely due to the increased stability of the $[N(Tf)_2]^-$ anion to electrochemical oxidation compared to $[Cl]^-$. When comparing the oxidation or reduction limit of ionic liquids with common anions or cations, it is more useful for us to compare overall electrochemical stability, i.e, the electrochemical window. Electrochemical windows of the imidazolium ionic liquids, [Emim][$[N(Tf)_2]$ and [Emim][Cl] are summarised in table 6.1.

Ionic Liquid	Cathodic limit/V	Anodic limit/V	Electrochemical Window/V
[Emim][Cl]	-1.02†	1.19†	2.21
[Emim][$N(Tf)_2$]	-2.57‡	1.72‡	4.29

Table 6.1: Electrochemical windows of $[Emim]^+$ ionic liquids at a Pt electrode.

† Potential vs silver wire dipping in [Emim][Cl] with 0.01M AgCl.

‡ Potential vs silver wire dipping in [Emim][$N(Tf)_2$] with 0.01M $AgCF_3SO_3$.

6.1.1 Electrochemistry of silver in ionic liquids.

6.1.1.1 Introduction

It has been reported[2] that silver can be electrochemically deposited on a platinum electrode from N-ethyl pyridinium bromide at 408K by applying voltages between 6 and 12 volts. From Potentiometric titration experiments[3] silver was found to form very stable mononuclear complexes of the type $AgCl_p^{1-p}$ ($2 \leq p \leq 4$) in chloride ion rich (Lewis basic) $AlCl_3$/[Emim][Cl] and $AlCl_3$/[*N*-Butyl pyridinium][Cl] melts. However, silver chloride was found to be insoluble in the Lewis neutral melts and to re-dissolve on moving to Lewis acidic (> 50 mole % $AlCl_3$) melts. From potentiometric titration curves, the coordinatively saturated $[AgCl_4]^{3-}$ was inferred to be the predominant species in basic melts at 313K with some $[AgCl_2]^-$ also present. $[AgCl_3]^{2-}$ was present in small amounts at 313K but the relative concentration increased when measured at 333K, at the expense of $[AgCl_4]^{3-}$ and $[AgCl_2]^-$. This was interpreted as the equilibrium in equation (7) moving to the right as the temperature was increased. The tetrahedral $[AgCl_4]^{3-}$ species is still thought to be the predominant species at 333K.

$$[AgCl_2]^-_{(solv)} + [AgCl_4]^{3-}_{(solv)} \leftrightarrow 2[AgCl_3]^{2-}_{(solv)} \quad (7)$$

The electrochemistry of silver has also been studied in the Lewis acidic chloroaluminate melts where there are no free chloride ions for coordination of Ag(I). The electrodeposition of silver from (66.7-33.3 mole %) $AlCl_3$/[Emim][Cl] was studied on metallic and non-metallic electrodes.[4] Of the electrodes tested, platinum showed the most classical voltammogram, suggesting the silver deposition/stripping process was reasonably well behaved. Close scrutiny of Ag(I) reduction as a function of scan rate shows the current function $i_{p(red)} / v^{1/2}$ decreased, and the peak potential – half peak potential separation, $[E_P - E_{P/2}]$ increased with scan rate. From this it was suggested that some indistinct kinetic limitation of the phase

formation process or quasi-reversibility of the Ag(I)/Ag charge transfer reaction was responsible for the deviation. The diffusion coefficient of Ag(I) was calculated at a platinum rotating disc electrode (RDE) by plotting the limiting current, i_l, as a function of disc rotation speed. From the slope of these plots, the average diffusion coefficient for Ag(I) was found to be $(1.2 \pm 0.1) \times 10^{-6}$ cm^2s^{-1} (at 313K). Potential step experiments for silver electrodeposition on a platinum electrode were also performed and the diffusion coefficient of Ag(I) was calculated as $(1.4 \pm 0.2) \times 10^{-6}$ cm^2s^{-1} (at 313K) from a plot of $i_{(t)}$ vs $t^{-½}$. Underpotential deposition (UPD) of silver was observed on a gold electrode before bulk deposition of silver occurred. The UPD deposition and stripping charges were calculated and it was found that more than one and less than two close packed monolayers were formed during deposition, but the stripping charge was less than the deposition charge. The explanation given for this was alloy formation between the deposited silver and the gold electrode, with the kinetics for alloyed silver being sufficiently slow so as not to be observed on the reverse scan. At tungsten and glassy carbon (GC) electrodes, silver deposition exhibited a nucleation loop. This occurred since a considerable excess potential was required for silver to deposit on these substrates; when the scan was reversed the current continued to rise because silver was now deposited onto silver rather than the original substrate. The bulk deposition/stripping efficiency at all four electrodes was found to be virtually 100%.

Electrochemistry of Ag(I) in 55/45 mole % $AlCl_3$/[Bmim][Cl] at highly oriented pyrolytic graphite (HOPG)[5] showed the deposition of silver required an overpotential of *ca.* -300mV. The growth of silver clusters occurred mainly at the steps and defects between different basal planes of graphite as evidenced by *in-situ* electrochemical scanning tunnelling microscopy, EC-STM. Similar studies of Ag(I) in 66.7/33.3 mole % $AlCl_3$/[Bmim][Cl] on a Au(111)[6] electrode showed similar electrochemistry to that observed in aqueous solutions. From cyclic voltammetry absorption controlled UPD and diffusion controlled overpotential deposition (OPD) was observed and from current time transients, the UPD was consistent with a Langmuir absorption model. In another study of silver in the closely related 66.7/33.3 mole % $AlCl_3$/[Emim][Cl] at platinum and tungsten electrodes[7] it was

observed that Ag(I) absorbs strongly on the platinum and tungsten surfaces preceding bulk Ag(I) reduction or if the electrode was in contact with a concentrated Ag(I) solution. Addition of benzene to the melt inhibited the absorption of the silver on the electrodes. Ag-Al alloys could be electrodeposited on both electrode materials from this melt.

The air/moisture stable ionic liquid [Emim][BF_4][8] has also been employed to study the electrochemistry of Ag(I), dissolved as $AgBF_4$. The Ag(I)/Ag couple was found to be irreversible at a platinum electrode due to E_p for Ag(I) reduction shifting cathodic with increasing scan rate. The electron transfer coefficient, α, was estimated to be 0.7 from the gradient of a plot of ln j_p vs ($E_p - E^{o\prime}$) (Gradient = $\alpha nF/RT$). The diffusion coefficient of Ag(I) was calculated as 6 x 10^{-7} cm^2s^{-1} at room temperature from a plot of peak current density against the square root of the scan rate.

6.1.1.2 Present Work

In this work, the ionic liquid [Emim][Cl] was investigated as a solvent for the electrochemical plating and stripping of silver at a platinum electrode. This is because the electrochemistry of silver in this chloride ionic liquid may be very different to that found in the Lewis basic chloroaluminate melts, and since no aluminium is present, alloy formation with silver is impossible. Silver was introduced to [Emim][Cl] as AgCl and cyclic voltammetry was performed to ascertain if plating and stripping was observed. A typical cyclic voltammogram is shown in figure 6.3.

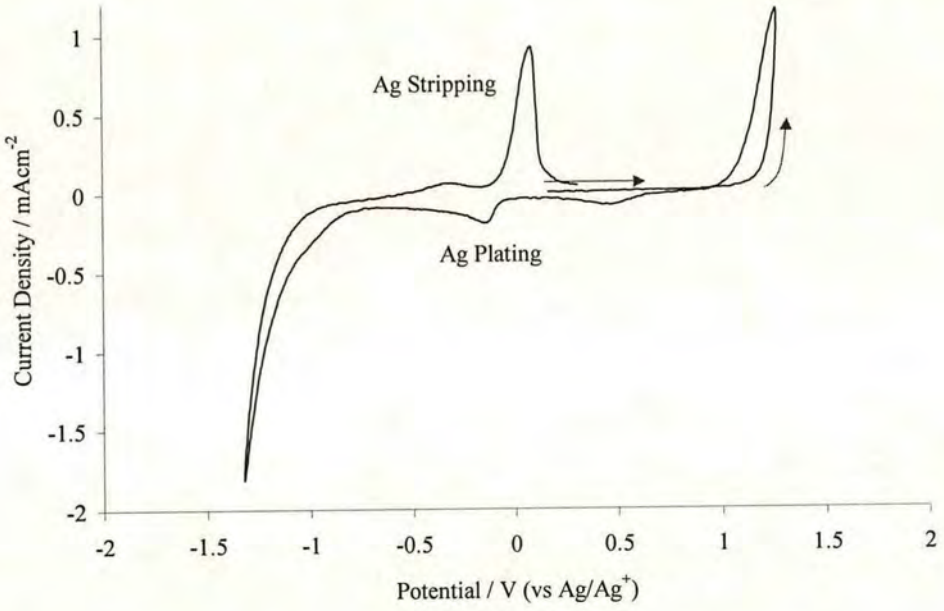

Figure 6.3: Typical CV of silver chloride (0.01M) in [Emim][Cl] at a platinum electrode, 50mVs^{-1}.

The reduction peak, $E_{p(red)}$ at -0.13V corresponds to the deposition (plating) of silver onto the platinum electrode. The reduction current is not limited by diffusion at potentials negative of $E_{p(red)}$ as the current does not vary linearly with $t^{1/2}$ as predicted by equation (4), chapter 1. The oxidation peak at +0.08V is a stripping peak, typical of a metal being oxidised from an electrode surface. The current rises

as the potential is increased until all the metal has been removed from the surface of the electrode, where the current drops sharply. Cyclic voltammetry of a silver electrode in [Emim][Cl] containing AgCl has also been recorded and a typical voltammogram can be seen in figure 6.4.

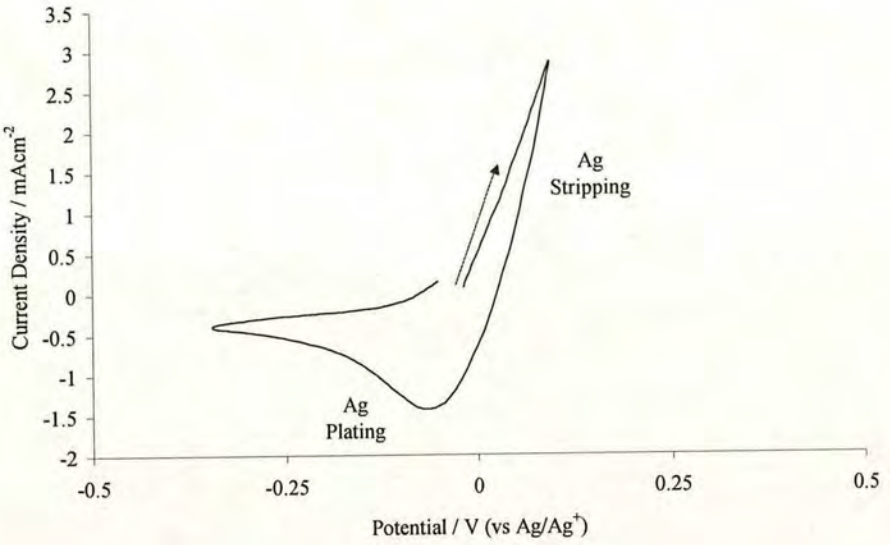

Figure 6.4: Typical CV of a silver electrode in [Emim][Cl] containing AgCl (0.01M), $50mVs^{-1}$, 388K.

As can be seen from figure 6.4, starting at zero current and sweeping the potential anodically, a rising current is observed corresponding to silver being oxidised as Ag(I) and stripping into solution. On reversing the potential sweep the current drops until a diffusion controlled reduction current flows, corresponding to the deposition of silver from Ag(I) in solution. The oxidation current rises linearly with potential as can be seen in figure 6.5.

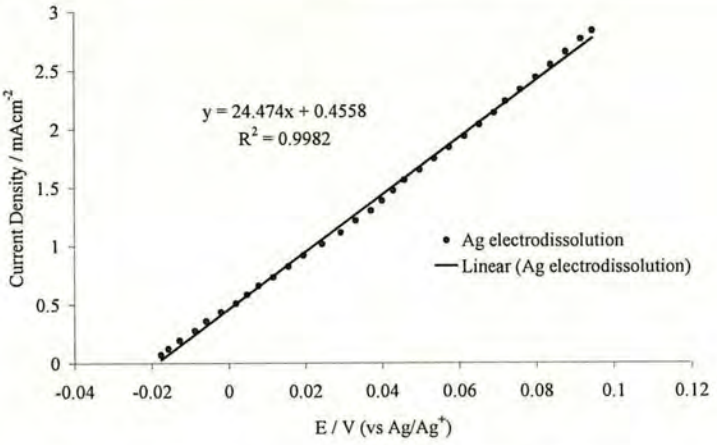

Figure 6.5: Plot of current density vs potential for 0.01M AgCl in [Emim][Cl] at a silver electrode, 388K, $50mVs^{-1}$

The current for oxidation of silver into solution should rise exponentially with potential if the electrochemical reaction is thermodynamically controlled, however the current rises linearly, as seen in figure 6.5. This can be attributed to the uncompensated *iR* drop between the working and reference electrodes in solution (maximum solution $R_u = 41\ \Omega cm^2$).

The behaviour of silver in the $[N(Tf)_2]^-$ salts is similar. When silver trifluoromethanesulfate (AgOTf) is added to $[Emim][N(Tf)_2]$, a similar CV as observed in [Emim][Cl] is obtained, figure 6.6.

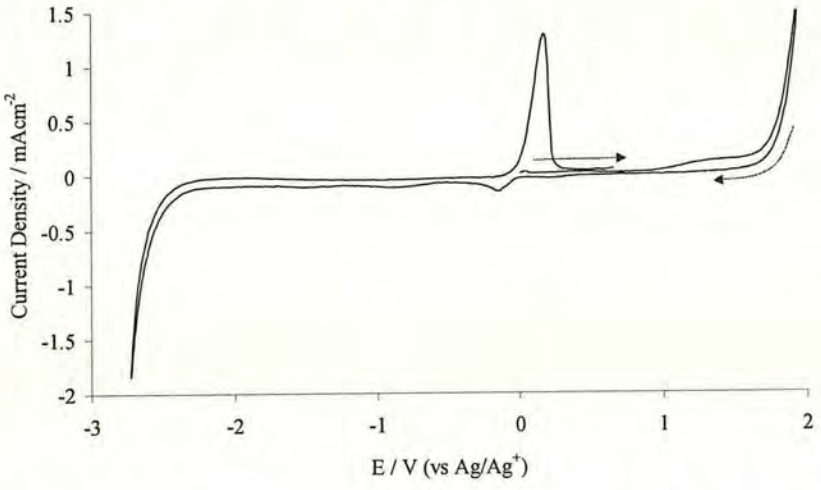

Figure 6.6: Typical CV of AgOTf (0.014M) in $[Emim][N(Tf)_2]$ at a platinum electrode, 348K, $50mVs^{-1}$.

It can be seen from figure 6.6 that the plating and stripping of silver is observed, again centred around 0V, as was observed in [Emim][Cl]. Given that the reference electrode is Ag/Ag^+ in each case, this is to be expected if there is little alloying of silver with platinum. The deposition of silver can be seen to occur at E_p = -0.14V and the peak stripping potential is +0.18V. The deposition current of silver is diffusion limited as observed in [Emim][Cl] and the stripping peak is of a similar shape to that observed in [Emim][Cl]. The separation of the reduction and oxidation peaks in $[Emim][N(Tf)_2]$ is *ca.* 0.1V larger than observed in [Emim][Cl], the decreased electrode kinetics are consistent with the fact that $[N(Tf)_2]^-$ will not stabilise the electron transfer transition state as well as chloride. The stripping and plating of silver in $[Emim][N(Tf)_2]$ at a silver electrode was recorded and the resulting CV is shown in figure 6.7.

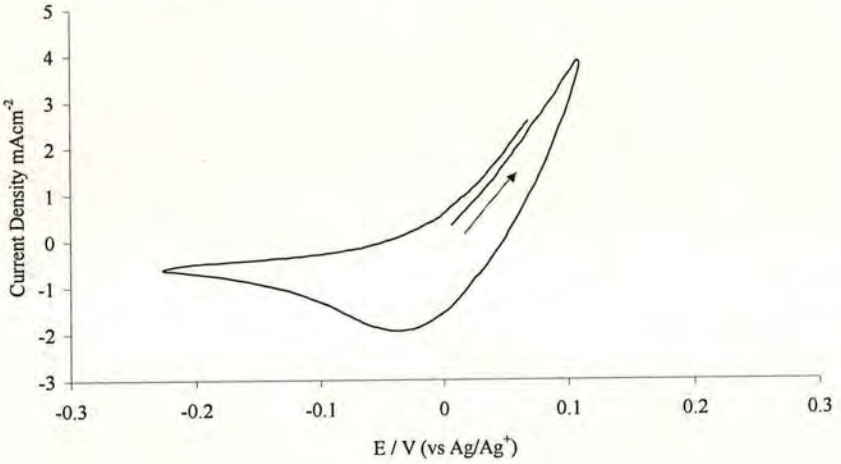

Figure 6.7: CV of AgOTf in $[Emim][N(Tf)_2]$ at a silver electrode, 348K, $50mVs^{-1}$.

The electrochemical behaviour of Ag(I) in $[Emim][N(Tf)_2]$ is similar to that observed in [Emim][Cl]. The current rises linearly with potential for the oxidation of silver into solution and a linear fit on this oxidation current is shown in figure 6.8.

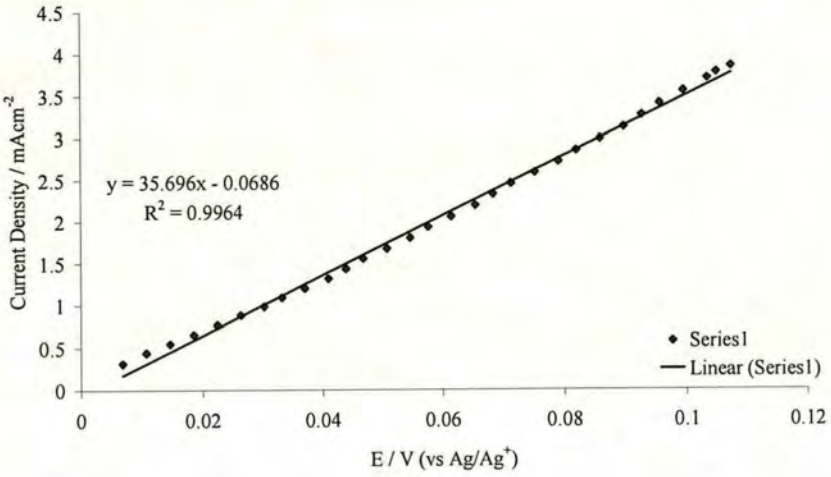

Figure 6.8: Plot of current density vs potential for 0.014M AgOTf in [Emim][$N(Tf)_2$] at a silver electrode, 348K, $50mVs^{-1}$.

From figure 6.8, the gradient of the graph gives the *iR* drop between the working and reference electrode (maximum solution R_u = 28 Ωcm^2), this value is lower than the solution resistance observed in [Emim][Cl].

A limitation of the imidazolium ionic liquids is that there is doubt concerning the chemical and electrochemical stability of the cation because of possible reactions at the C(2) position. As a result, the imidazolium ionic liquids are sometimes not stable enough to observe species that have a reduction potential close to or more negative than the imidazolium ion. Other cations have been investigated as possible ionic liquid forming alternatives to the imidazolium cation. Such an example is the *N*-butyl-*N*-methylpyrrolidinium cation and it was first reported as a room temperature ionic liquid[9] in combination with the bis(trifluoromethanesulfonyl)imide anion by MacFarlane *et. al.* This ionic liquid was chosen as an ionic liquid for study of metal ions with reduction potentials greater than the imidazolium cation, and silver was also studied in [Pyr][$N(Tf)_2$] to allow comparison with the imidazolium type ionic liquids. A cyclic voltammogram of AgOTf in [Pyr][$N(Tf)_2$] can be seen in figure 6.9.

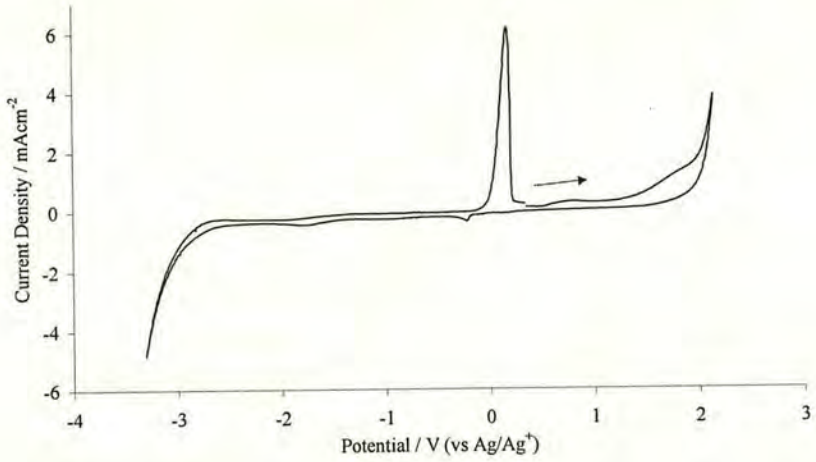

Figure 6.9: CV of 0.01M AgOTf in [Pyr][N(Tf)$_2$] at a Pt electrode, 50mVs^{-1}, 343K.

As can be seen from figure 6.9 the plating and stripping of silver is again observed at a platinum electrode near 0V. The anodic and cathodic limits of the CV can be attributed to the oxidation of the anion and the reduction of the cation respectively, the products of which have not been identified. The solvent oxidation limit is similar to that observed in [Emim][N(Tf)$_2$] as expected because both have been attributed to the oxidation of the [N(Tf)$_2$]$^-$ anion. The cathodic limit is shifted *ca.* 1V more negative than [Emim][N(Tf)$_2$], this is consistent with the cathodic reduction being of [Pyr]$^+$ to [Pyr]$^\cdot$ as this cation is expected to be more stable to reduction. It is interesting that the potential window observed is *ca.* 1V smaller than previously reported.[9] A glassy carbon electrode was used in recording the CV previously, whereas in this case a platinum electrode was used, platinum must therefore be catalytic for the oxidation of [N(Tf)$_2$]$^-$, the reduction of [Pyr]$^+$ or both. Previous studies[10] have shown that both the reduction and oxidation limits of 1-butyl-3-methylimidazolium trifluoroacetate are lowered when using a platinum electrode in comparison to a vitreous glass carbon electrode. The reduction peak at –0.21V is much smaller than the associated oxidation peak at 0.18V. This is due to the reduction peak corresponding to the electrodeposition of silver being controlled by the diffusion of Ag(I) to the electrode surface, whereas the oxidation peak corresponds to the oxidation of deposited silver from the electrode surface. The

stripping and plating of silver on a silver electrode in [Pyr][N(Tf)$_2$] has also been recorded using cyclic voltammetry and is shown in figure 6.10.

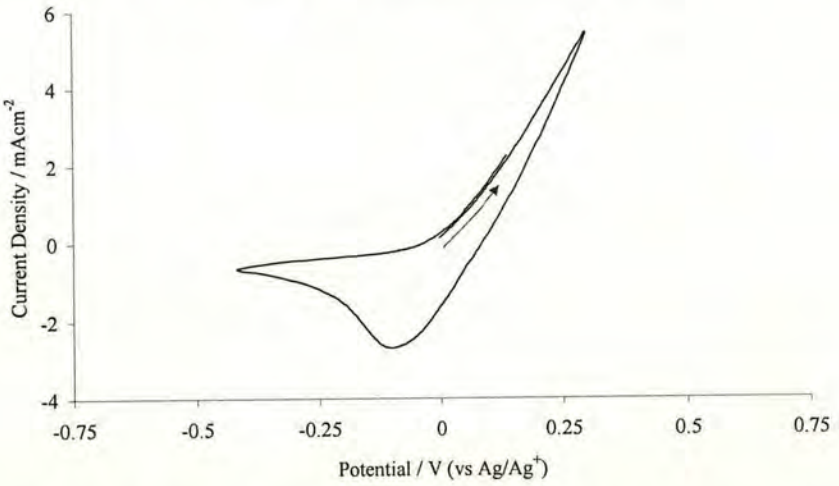

Figure 6.10: CV of 0.01M AgOTf in [Pyr][N(Tf)$_2$] at a silver electrode, 50mVs^{-1}, 343K.

As with the other ionic liquids tested, the electrochemistry of AgOTf at a silver electrode in the pyrrolidinium salt displays a linear rise in oxidation current with potential, and diffusion controlled reduction peak. A plot of the oxidation current versus potential was plotted in order to estimate the resistance of the solution and is shown in figure 6.11.

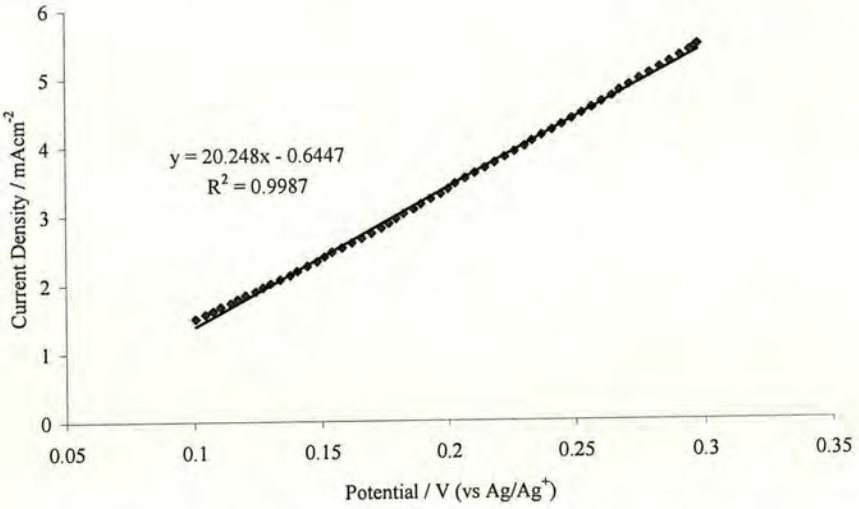

Figure 6.11: Plot of current density vs potential for 0.01M AgOTf in [Pyr][N(Tf)$_2$] at a silver electrode, 50mVs^{-1}, 343K.

From the slope of the graph in figure 6.11, the gradient of the graph gives the iR drop between the working and reference electrode (maximum solution R_u = 49 Ωcm^2). A comparison of the stripping/plating of silver onto silver or platinum electrodes in the ionic liquids [Emim][Cl], [Emim][N(Tf)$_2$] and [Pyr][N(Tf)$_2$] is shown in figure 6.12.

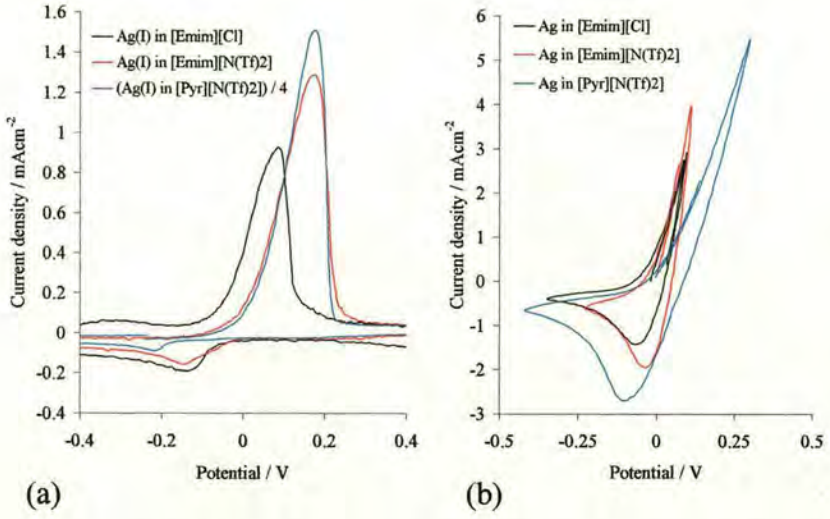

Figure 6.12: Stripping/plating of Ag(I) in [Emim][Cl] (——), [Emim][N(Tf)$_2$] (——) and [Pyr][N(Tf)$_2$] (——) at (a) a platinum electrode, and (b) a silver electrode.

From figure 6.12(a), the plating of silver on a platinum electrode is thermodynamically similar for both the imidazolium ionic liquids, [Emim][Cl] and [Emim][N(Tf)$_2$], and occurs at more negative potentials for [Pyr][N(Tf)$_2$]. The stripping of silver from a platinum electrode is thermodynamically similar for the bis(trifluoromethanesulfonyl)imide ionic liquids, [Emim][N(Tf)$_2$] and [Pyr][N(Tf)$_2$], and occurs at less positive potentials for [Emim][Cl]. This observation is expected as the chloride ion would be expected to stabilise the transition-state for the stripping and plating of silver. Similar behaviour is observed when comparing the deposition and stripping of silver from a silver electrode in [Emim][Cl], [Emim][N(Tf)$_2$] and [Pyr][N(Tf)$_2$], figure 6.12(b). The deposition of silver onto silver occurred at less negative potentials compared to silver on platinum for [Emim][Cl], [Emim][N(Tf)$_2$] and [Pyr][N(Tf)$_2$] indicating the deposition of silver onto a silver substrate is thermodynamically easier than for the deposition of silver onto a platinum substrate.

The onset of oxidation for silver stripping from silver or platinum was similar for each electrode studied, suggesting the removal of silver from the electrode surface is more dependant on the nature of the ionic liquid than the substrate.

6.1.2 Electrochemistry of copper in [Emim][Cl]

6.1.2.1 Introduction

There have been few studies on the electrochemistry of copper in ionic liquids to date. Examples in the literature are in pure halide[2] ionic liquid, basic[11,12] or acidic[13,14] chloroaluminate melts, basic (chloride containing) tetrafluoroborate melt[15] and trimethyl-n-hexylammonium bis(trifuoromethanesulfonyl)amide.[16]

A mixture of ethyl pyridinium bromide[2] with anhydrous cupric chloride at *ca.* 408K was found to be a suitable solvent for the electrolytic deposition of copper at a platinum cathode. In the same study, benzyl pyridinium bromide was also used as an ionic liquid, which when combined with low concentrations of cupric chloride gave a clean deposit of metallic copper at the cathode, but in high concentration exhibited a very low electrical conductivity and produced no deposit. From this result and similar observations with cadmium chloride, it was suggested that non-ionic complex compounds might be formed by the reaction between some metallic chlorides and the *N*-substituted pyridinium halides.

Potentiometric titration experiments and absorption spectroscopy was used to study Cu(I) and Cu(II) chloro complex formation in the $AlCl_3$/[Emim][Cl] ionic liquid.[11] The potential of the Cu(I)/Cu couple was measured as a function of mole % $AlCl_3$ at 313, 333 and 373K, and a large negative shift in cell potential was observed during the titration experiments when the melt composition was changed to below 50 mole % in $AlCl_3$. This observation was attributed to stable chloro-complex formation and was similar to that observed for silver,[3] though the magnitude of potential change was slightly larger for the Cu(I)/Cu system. Cu(I) precipitated as CuCl on going from Lewis acidic melt to Lewis neutral melt, and redissolved on going from Lewis neutral melt to Lewis basic melt as was observed with Ag(I) in similar experiments.[3] Using similar techniques employed in calculating chloro-

complex formation for Ag(I) (see section 6.1.1.1), Cu(I) was calculated to mainly be the mononuclear complexes $[CuCl_2]^-$ and $[CuCl_4]^{3-}$ at 313K. As the temperature was raised to 373K, the relative fractions of these species decreased in favour of $[CuCl_3]^{2-}$ as a result of the shift in the equilibrium shown in equation (8).

$$[CuCl_2]^-_{(solv)} + [CuCl_4]^{3-}_{(solv)} \leftrightarrow 2[CuCl_3]^{2-}_{(solv)} \quad (8)$$

Potentiometric titration experiments involving the Cu(II)/Cu(I) couple were attempted but the resulting data was irreproducible and could not be analysed in a meaningful way. However, absorption spectroscopy of Cu(II) in a Lewis basic melt exhibited a maxima at 407nm, with the molar absorptivity comparing favourably with that of Cu(II) in DMF with LiCl as a chloride source. The peak at 407nm is characteristic of unsolvated $[CuCl_4]^{2-}$, as previously observed[17] by *Elleb. et. al.*, by observing the UV-vis spectra of Cu(II) with varying Cl:Cu(II) ratios in propylene carbonate and dimethylsulfoxide.

Studies of electrogenerated Cu(I) in the Lewis basic (47.5/52.5 mole %) $AlCl_3$/[Emim][Cl] melt exhibited underpotential deposition of *ca.* one monolayer of copper followed by bulk deposition of copper at a platinum electrode[12]. On reversal of the potential, bulk stripping of copper was observed. Stripping of the copper monolayer occurred if the potential was reversed before bulk deposition of copper. Significantly higher potentials than those required on platinum were required for the deposition of copper on GC or taC:N (nitrogen-incorporated tetrahedral amorphous carbon) electrodes as was observed for aluminium deposition.[18]

In the Lewis acidic (67/33 mole %) $AlCl_3$/*N*-Methylpyridinium chloride melt containing Cu(II),[13] the Cu(II)/(I) couple was reversible at both glassy carbon and tungsten electrodes. Copper could be deposited from Cu(I) solutions at glassy carbon and tungsten electrodes. Bulk deposition was preceded by nucleation and both electrode materials required greater potentials than required for deposition on platinum. Deposition of copper on platinum was also preceded by nucleation but the process was considerably faster than the other two electrode materials. In a similar

study to that performed on Ag(I)[6] the electrodeposition of copper on Au(III) was investigated in the Lewis acidic (66/34 mole %) $AlCl_3$/[Bmim][Cl] melt.[14] The Cu(II)/(I) redox couple could not be observed because it was slightly positive of the step oxidation of Au(III). Several underpotential deposition processes were observed on Au(III) before bulk deposition of copper at a slight overpotential. In the same study, only overpotential deposition of copper was observed on a HOPG electrode.

The electrochemistry of copper was also studied in the air and moisture stable ionic liquid mixture, (16.7/83.3 mole %) [Emim][Cl]/[Emim][BF_4],[15] and its chemical and electrochemical behaviour was found to be similar to that in Lewis basic $AlCl_3$/[Emim][Cl].[11] The redox couple Cu(I)/(II) was found to be quasi-reversible at platinum, glassy carbon and tungsten working electrodes. The deposition of copper from Cu(I) on platinum involved underpotential deposition, whereas an overpotential was required for the electrodeposition of copper on glassy carbon and tungsten. The diffusion coefficient of Cu(I) measured in ambient atmosphere was larger than that measured in a dry nitrogen filled glovebox, suggesting absorption of water which reduces the viscosity of ionic liquids.[19]

Copper can be electrodeposited from the trimethyl-n-hexylammonium bis(trifuoromethanesulfonyl)amide ionic liquid from the Cu(I) oxidation state,[16] and anodically dissolved with virtually 100% efficiency, though copper metal is unstable in Cu(II) solutions and is oxidised to Cu(I) while the Cu(II) solution species is reduced to Cu(I).

6.1.2.2 Present Work

As is the case with silver electrochemistry in ionic liquids, most of the literature on copper electrochemistry in ionic liquids was performed using the chloroaluminate melts. In order to understand the electrochemistry of copper in a pure chloride ionic liquid, the electrochemistry of copper, as both Cu(I) and Cu(II) in [Emim][Cl] has been studied at a platinum electrode. A typical CV of CuCl in [Emim][Cl] is shown in figure 6.13.

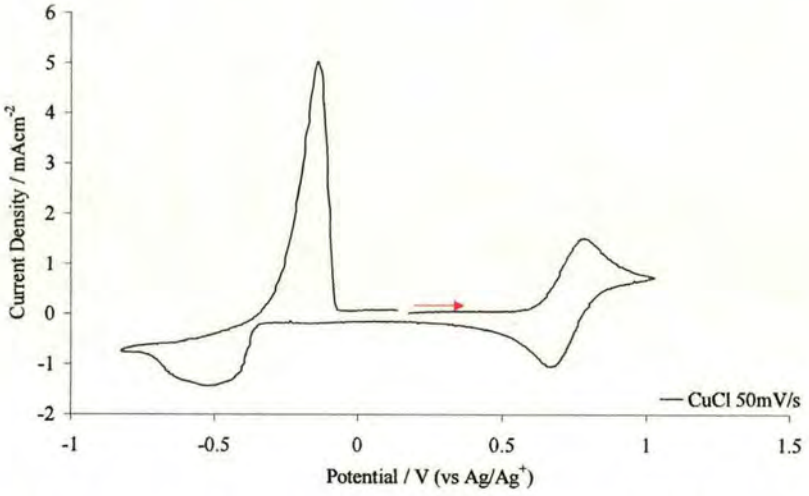

Figure 6.13: Typical CV of CuCl (0.025M) in [Emim][Cl] at a platinum electrode, $50mVs^{-1}$, 380K.

It can be seen from the CV of CuCl in [Emim][Cl], that on scanning the potential anodic from zero current (*ca* 0.25V) a redox couple is observed centred at 0.72V, corresponding to the one electron oxidation of Cu(I) to Cu(II) and the subsequent reduction of Cu(II) to Cu(I) on reversal of the potential scan. The height of the oxidation peak at 0.72V is similar to that of the reduction peak at -0.5V indicating the same number of electrons are involved in the redox reactions. The reduction peak at *ca* -0.5V is due to the electrodeposition of copper from Cu(I) on a platinum electrode, and the oxidation peak observed on reversal of the potential sweep is the subsequent oxidation of deposited copper from the electrode surface to

form a soluble Cu(I) species. It is worth noting that the reduction peak corresponding to copper deposition does not consist of one single reduction peak, but is composed of more than one peak superimposed on each other. This suggests that copper deposition on a platinum electrode shows preferential deposition at certain sites on the electrode surface which may be consistent with underpotential deposition on as observed previously[12]. Preferential deposition of copper on already deposited copper is not observed, otherwise the reduction peak observed would be one single peak as with Ag(I) (section 6.1.1.2). A CV of the Cu(I)/Cu(II) couple is shown in figure 6.14 with the peak currents and peak potentials annotated, when measuring the peak current on the reverse sweep it is important to take into account the background current resulting from the electrochemical reaction on the forward sweep.

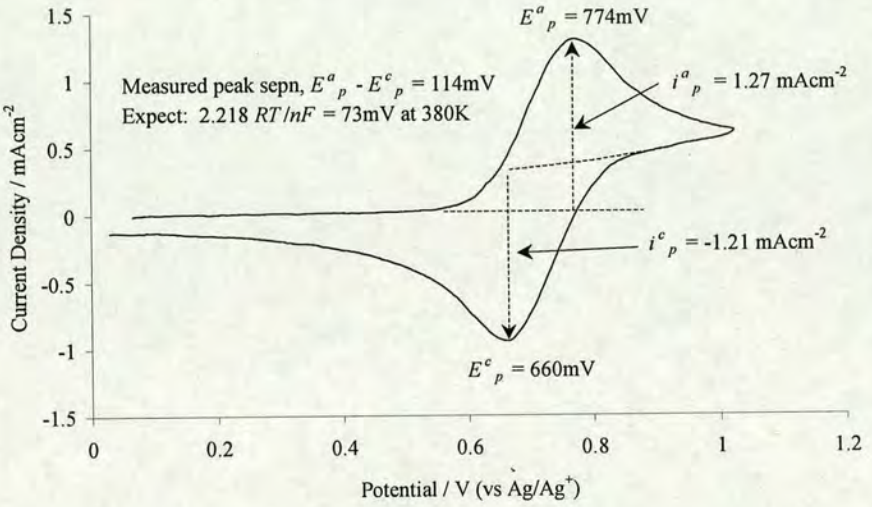

Figure 6.14: CV of Cu(I)/(II) in [Emim][Cl] at a platinum electrode, 50mVs^{-1}, 380K.

If n electrons are transferred in a reversible electrode process then the peak separation is dictated by equation (9).

$$\left|E_p^{ox} - E_p^{red}\right| = 2.218(RT/nF) \tag{9}$$

This gives rise to a theoretical peak separation of 73mV for a one electron reversible electrode process at a temperature of 380K. From figure 6.14, it can be seen that the peak separation is 114mV at 380K and a scan rate of 50mVs^{-1}, and

increases with increasing scan rate. The effect of varying scan rate on the peak potential separation is shown in figure 6.15.

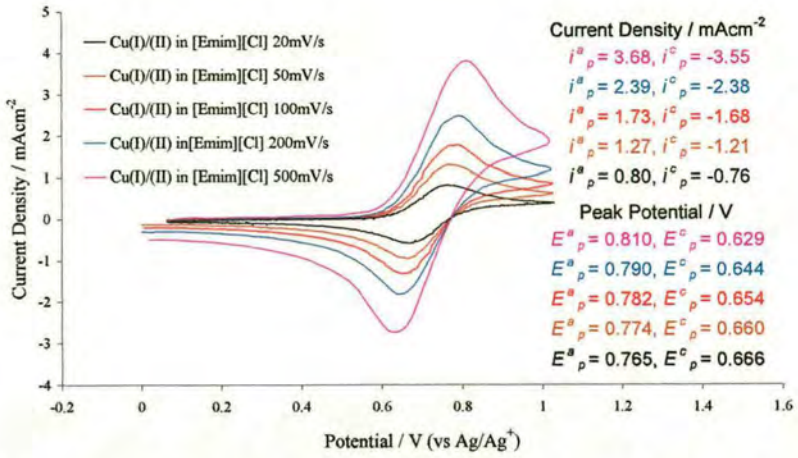

Figure 6.15: Effect of scan rate on Cu(I)/(II) redox couple in [Emim][Cl] at a Pt electrode, 380K.

For a redox reaction the peak current (i_p) should rise linearly with the square root of the scan rate ($v^{1/2}$) if the electrode reaction is controlled by diffusion of the redox species from bulk solution. The ratio of the peak oxidation and reduction currents should also be unity for a chemically reversible system unless very slow scan rates are employed. The peak current, i_p, varies linearly with the square root of the scan rate for both the forward and reverse reaction as can be seen in figure 6.16 and the ratio of the peak currents for the forward and reverse reactions is close to unity for all scan rates used. This indicates that the electrode reaction is controlled by mass transport, that is, transport of the redox species from bulk solution to the electrode surface, and the electrode reaction is chemically reversible.

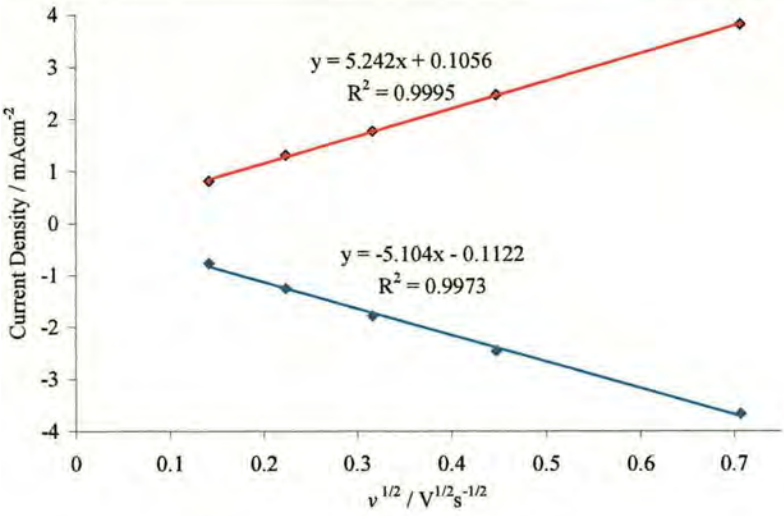

Figure 6.16: Plot of i_p vs $v^{½}$ for Cu(I) oxidation and Cu(II) reduction from CuCl in [Emim][Cl] at 380K.

As can be seen from the CVs in figure 6.15, the peak reduction and oxidation potentials move more cathodic and anodic respectively with increasing sweep rate. This behaviour suggests that the electrochemical couple Cu(I)/(II) is irreversible under the experimental conditions. However, the CVs have not been compensated for the solution resistance, and by plotting i_p vs E_p for different scan rates, the peak potential can then be estimated independent of iR effects (when i = 0A). A plot of i_p vs E_p for both the Cu(I)/(II) couple, (a), and Cu(II)/(I) couple, (b) are shown in figure 6.17.

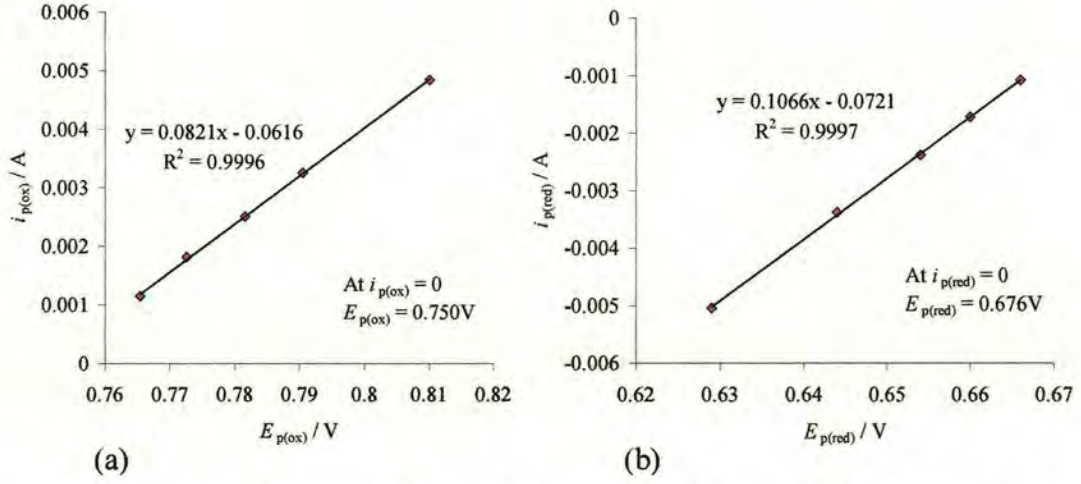

Figure 6.17: Plot of i_p vs E_p for (a) Cu(I)/(II) and (b) Cu(II)/(I) in [Emim][Cl] for varying scan rates, 20mVs^{-1}, 50mVs^{-1}, 100mVs^{-1}, 200mVs^{-1} and 500mVs^{-1}.

The values of E^a_p and E^c_p calculated from the intercept at zero current from the straight line slopes in figure 6.17 are 750 mV and 676 mV respectively, giving a peak potential separation of 74 mV. This value is within experimental error of the theoretical value for a reversible one-electron reaction of 73mV at 380K calculated from equation (9). From the slope of the linear fit of figure 6.17(a) we can estimate the solution resistance as being 12 Ω. This resistance is a reasonable value for solution resistance compared to the previously determined value for Ag(I)/Ag (section 6.1.1.2) which was estimated as a maximum resistance. The difference can be explained in terms of the difference in the positions of the W.E. and R.E. and the solution temperatures.

If we measure the peak potentials for the oxidation (E^a_p) and reduction (E^c_p) peaks and compare them to the half peak potentials (the potential at half-peak current, i_p) for the reduction ($E^c_{P/2}$) and oxidation ($E^a_{P/2}$) peaks we also get a good measure of the reversibility of the system. The relationship between E_P and $E_{P/2}$ for a chemically reversible one-electron redox reaction is outlined in equation (10)[20].

$$\left|E_p - E_{P/2}\right| = 2.2(RT/F) \qquad (10)$$

This gives a theoretical value of 72 mV at 380K, once the CVs have been compensated for *iR* effects, this gives a value for E^a_P - $E^a_{P/2}$ of 75 mV and E^c_P - $E^c_{P/2}$ of 75 mV for the *iR* corrected CV in figure 6.18,

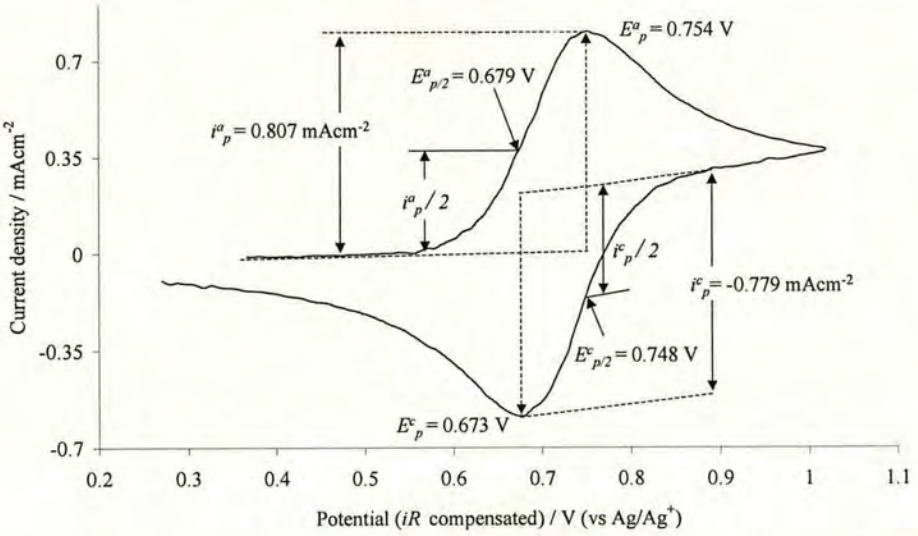

Figure 6.18: CV for the Cu(I)/(II) redox couple in [Emim][Cl] after compensation for solution resistance showing E^a_p, E^c_p, $E^a_{p/2}$, and $E^c_{p/2}$ (i^a_p/i^c_p was close to unity), 380K, 20mVs^{-1}.

We can calculate the peak current[21] for a reversible system by using the Randles-Sevcik equation, equation (11).

$$i_p = 0.4663nAFD^{1/2}v^{1/2}[A]_{bulk}(nF/RT)^{1/2} \qquad (11)$$

Where n is number of electrons, i_p is peak current (A), A as the electrode area (cm^2), D is the diffusion coefficient (cm^{2}s^{-1}), v is the scan rate (Vs^{-1}), $[A]_{bulk}$ is the bulk solution concentration (molcm^{-3}), F is Faradays constant (96485.3 Cmol^{-1}), R is the gas constant (8.31447 JK^{-1}mol^{-1}) and T is the temperature (K). In order to calculate the peak current we must first know the diffusion coefficient of the redox species, this has been experimentally determined, *vide infra,* as 9.66 x 10^{-7} cm^{2}s^{-1} at 380K for Cu(I) and this value is used in the subsequent calculations.

The peak current measured from figure 6.14 for a sweep rate of 0.05Vs^{-1} at 380K is 1.80 mA. The value for the peak current obtained from equation (11) is 1.96 mA, this would suggest the Cu(I)/(II) redox couple is not reversible in [Emim][Cl] under the experimental conditions studied. However, as has previously been stated,

these CVs have not been compensated for the solution resistance. Thus the applied scan rate will not be equal to the scan rate at the working electrode as the voltage at the working electrode will be reduced by iR. This will lead to an overestimation of the scan rate and hence theoretical overestimation of i_p. With this in mind, the agreement between theoretical and experimental i_p is reasonable, consistent with a reversible redox reaction (Also, equation (10) is not strictly valid as the v term is not constant due to the iR value not being constant).

Turning now to the Cu(I)/Cu(0) redox couple, the plating/stripping efficiency of copper on a platinum electrode from a solution of CuCl in [Emim][Cl] was estimated by calculating the charge passed during electrodeposition and the charge passed during the stripping of the deposited copper. This is shown as a plot of charge passed as a function of potential for a solution of CuCl in [Emim][Cl] in figure 6.19.

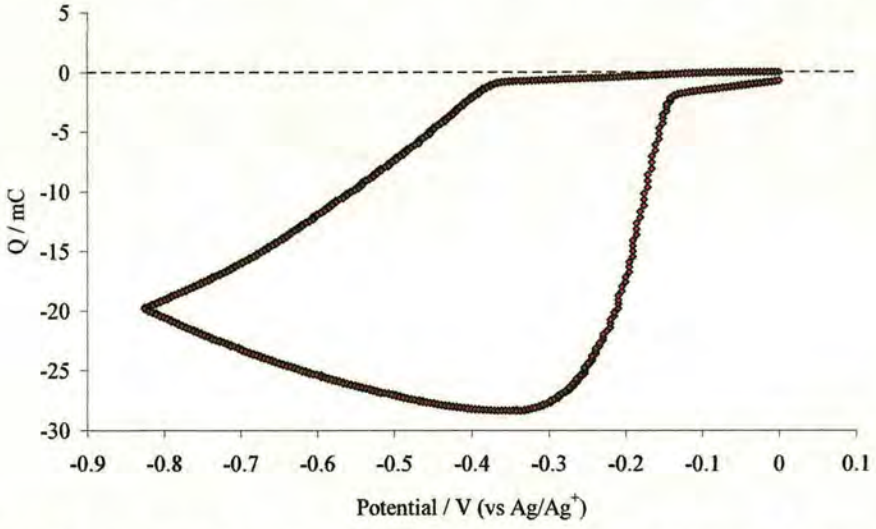

Figure 6.19: Charge as a function of potential for copper plating and stripping at a platinum electrode from CuCl in [Emim][Cl].

The plating and stripping of copper was carried out at a low scan rate, $20mVs^{-1}$, in order to minimise background currents. As can be seen from figure 6.19, plating/stripping proceeds with 100% efficiency within experimental error, indicating no competing electrochemical or chemical reactions are occurring on the time-scale of the potential scan.

The electrochemistry of Cu(II), introduced to [Emim][Cl] as $CuCl_2$, is similar to that of Cu(I) in [Emim][Cl] in that both the Cu(II)/(I) and Cu(I)/0 redox couples are observed as can be seen in figure 6.20.

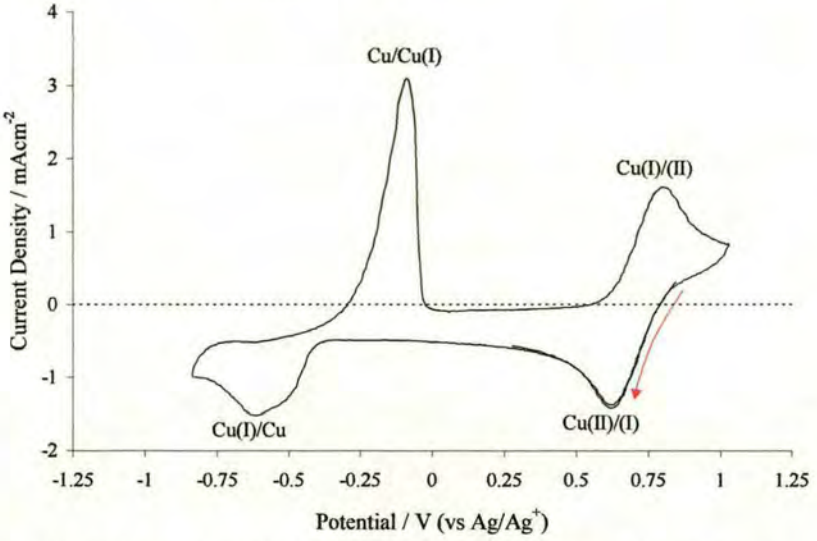

Figure 6.20: CV of $CuCl_2$ (0.049M) in [Emim][Cl] at a Pt electrode, $100mVs^{-1}$, 387K.

The CV is started more positive than the reduction of Cu(II) to Cu(I) and scanned negatively. A reduction wave at *ca.* 0.62V corresponding to Cu(II)/(I) is observed and on scanning the potential negatively, diffusion controlled currents flow as fresh Cu(II) is supplied to the electrode surface from bulk solution. On scanning further negatively a reduction peak is observed at *ca.* –0.61V which corresponds to the deposition of copper from Cu(I). Again, as with the solution of CuCl in [Emim][Cl] in figure 6.13, the reduction wave is composed of more than one reduction peak indicating preferential deposition of copper on specific sites of the platinum electrode. On reversal of the potential sweep, a peak corresponding to the stripping of copper is observed at *ca.* –0.08V. Again, small reduction currents are passed as the potential is swept positively due to the reduction of Cu(II) until an oxidation peak at *ca.* 0.80V is observed, corresponding to the re-oxidation of Cu(I) back to Cu(II).

The currents observed for the Cu(II)/(I) reduction peaks are lower than would be expected if we assume that the diffusion coefficient of Cu(II) is similar to that of

Cu(I). The peak current for Cu(I) oxidation in a 0.025M Cu(I) solution is 1.3 $mAcm^{-2}$ and the peak current for Cu(II) reduction in a 0.049M Cu(II) solution is 1.7 $mAcm^{-2}$. This would suggest either that the diffusion coefficient of Cu(II) is lower than that of Cu(I) or that there is a lower concentration of Cu(II) than expected. The most likely reason for this is due to loss of redox active material, in this case Cu(II). It is proposed that Cu(II) is reduced to Cu(I) in solution by the chloride ion, the Cu(II)/(I) couple is very close to the anodic limit of the potential window at platinum (onset of chloride oxidation, ~1V) and as the temperature is increased the oxidation of chloride moves closer in value to that of Cu(II)/(I) as can be seen in figure 6.21, when increasing anodic currents are observed at the end of the voltage sweep. This is further evidenced by the observation that oxidising currents flow when the cell potential is started at potentials more positive than required for Cu(II) reduction.

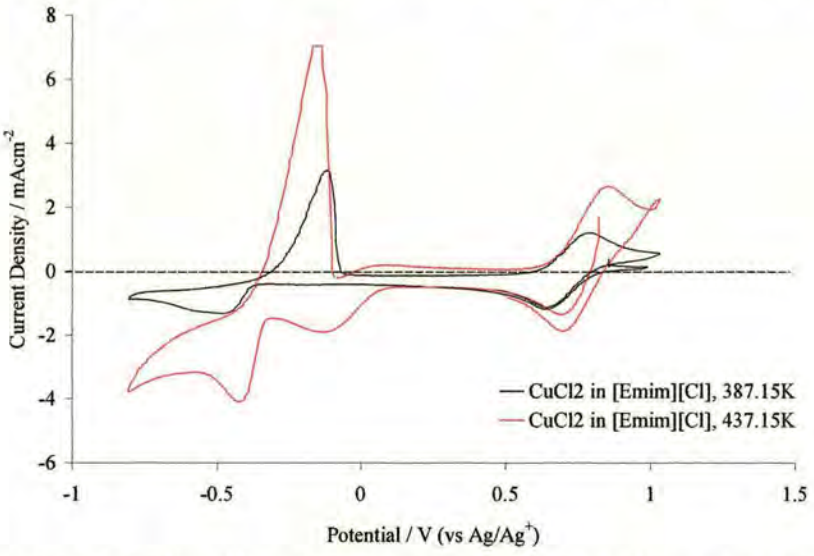

Figure 6.21: CV of Cu(II) in [Emim][Cl] at 387K and 437K, Pt electrode, $50mVs^{-1}$.

From figure 6.21, the onset of chloride oxidation can be observed just before reversal of the potential sweep direction when the CV is performed at the higher temperature of 437K. This loss of Cu(II) in chloride rich ionic liquids could explain why potentiometric titration experiments to probe the chloro-complex formation of Cu(II) in basic chloroaluminate melts were not reproducible, where as such studies on Cu(I) were reproducible.[11] The presence of the new peak at *ca.* –0.16V in figure 6.21 was also observed for CuCl in [Emim][Cl] at similar temperatures in this study, but has not been investigated fully. A possible explanation could be the

underpotential deposition of copper on platinum as has been observed previously,[12,15] with the kinetics of underpotential deposition increasing with rising temperature. The theoretical charge required for the deposition of a monolayer of copper[15] on an electrode of geometric area 1.42 cm^2 is 4.96 x 10^{-4} C. The charge passed for the reduction peak at –0.16V in figure 6.21 was calculated by integrating a plot of i(A) vs t(s), giving 1.16 x 10^{-2} C. This suggests that underpotential deposition of a monolayer of copper is not responsible for the new reduction peak at –0.16V with increasing temperature. This extra redox peak may be due to the breakdown product of chemical reaction between Cu(II) and the ionic liquid.

6.1.3 Electrochemistry of iron in [Emim][Cl]

6.1.3.1 Introduction

Electrochemical data on the redox behaviour of iron in ionic liquids is relatively sparse, though studies on Fe(II)[22,23,24] and Fe(III)[22,24,25,26] in low temperature melts have been carried out.

The stability of iron (II) and (III) in the Butylpyridinium chloroaluminate melt ($AlCl_3$/[BuPy][Cl]) with varying Lewis acidity has been studied by Osteryoung[24] *et. al.* Constant potential oxidation of an iron electrode at –0.4V (vs Al/Al(III) in (66/34 mole%) $AlCl_3$/[BuPy][Cl]) resulted in the formation of a soluble Fe(II), which underwent a further oxidation process at 0.07V to give Fe(III). By employing potentiometry of the Fe/Fe(II) system as a function of the melt composition, Fe(II) was determined to exist as the $[FeCl_4]^{2-}$ species and Fe(III) as $[FeCl_4]^-$ at all Lewis basic compositions in the melt. The Fe(II)/Fe(III) redox couple was found to be reversible in the Lewis basic (<50 mole % $AlCl_3$) melt, $FeCl_2$ was found to precipitate at the Lewis neutral composition and re-dissolved on moving to more Lewis acidic (>50 mole % $AlCl_3$) compositions. The Fe(II)/Fe(III) redox couple was irreversible in the Lewis acidic melt, the peak separation decreases and $E_{P/2}$ shifts anodically with increasing Lewis acidity of the melt, although the peak separation was always greater than in the Lewis basic melt.

Similar studies in the Lewis basic $AlCl_3$/[BuPy][Cl][22] melt also determined potentiometrically that the Fe(II) and Fe(III) species in solution were $[FeCl_4]^{2-}$ and $[FeCl_4]^-$ respectively. When Fe(III) was introduced to the Lewis acidic melt as $FeCl_3$, the Fe(III) species was observed to oxidise the melt, it was necessary to reduce Fe(III) to Fe(II) immediately after introduction of $FeCl_3$ to the melt. The equimolar mixtures of Fe(II) and Fe(III) were observed to be stable in the Lewis acidic melt, and both Fe(II) and Fe(III) chloro-complexes were found to be

exceptionally stable in the Lewis basic chloroaluminate melts. Osteryoung[26] later confirmed Fe(III) existed as the $[FeCl_4]^-$ species in Lewis basic chloroaluminate melts by examining the change in the limiting rotating-disc current of the chloride oxidation wave when $FeCl_3$ was added to a Lewis neutral $AlCl_3$/[Emim][Cl] melt containing a small excess of chloride ion added as [BuPy][Cl]. The decrease of the chloride oxidation wave corresponded quantitatively to $FeCl_3$ dissolving according to equation (11).

$$FeCl_3 + Cl^- \longrightarrow [FeCl_4]^- \qquad (11)$$

Further studies of Fe(III) in the Lewis neutral $AlCl_3$/[Emim][Cl][26] melt showed a *ca.* 1.5V anodic shift of the Fe(III)/(II) redox couple on going from a "basic neutral" to "acidic neutral" melt (The terms "basic neutral" and "acidic neutral" refer to Lewis neutral $AlCl_3$/[Emim][Cl] melts where there is a slight excess (< 100 mmol dm^{-3}) of [Emim][Cl] or $AlCl_3$ present in the melt respectively). The reduction of Fe(II) to iron was also observed at potentials *ca.* 1.5V cathodic from the Fe(III)/(II) couple in the "acidic neutral" melt. In order to obtain the electrochemistry of Fe(III) observed in a Lewis acidic melt from $[FeCl_4]^-$ in a Lewis neutral melt, it was necessary to add 4 equivalents of $AlCl_3$ to the melt, this resulted in the Fe(III) species having no "free" chloride, and was likely to be solvated by $[AlCl_4]^-$ or $[Al_2Cl_7]^-$.

Raman scattering of $FeCl_2$/[Bmim][Cl], $FeCl_3$/[Bmim][Cl] and the mixed $FeCl_2/FeCl_3$/[Bmim][Cl] melts[27] were conducted to ascertain the coordination of Fe(II) and Fe(III) in these melts. $FeCl_3$ was found to form room-temperature melts when combined with [Bmim][Cl] if the mole % of $FeCl_3$ was between 34.5 and 63.0 mole %. For the Lewis basic melts (<50 mole % $FeCl_3$), $[FeCl_4]^-$ is determined to be the principal Fe(III) species from Raman scattering, for Lewis acidic melts (>50 mole % $FeCl_3$), $[FeCl_4]^-$ and $[Fe_2Cl_7]^-$ are present in the melt with $[Fe_2Cl_7]^-$ increasing with increasing $FeCl_3$ added. $FeCl_2$ was found to form ionic liquids when combined with [Bmim][Cl] for compositions ranging from 25 mol % $FeCl_2$ to slightly less than 50 mole % $FeCl_2$. $[FeCl_4]^{2-}$ was found to be the predominant Fe(II) species in these compositions by Raman spectroscopy and *ab initio* calculations. In the mixed

oxidation state $FeCl_2/FeCl_3$/[Bmim][Cl] melt the only iron containing species observed in the Raman scattering spectra were $[FeCl_4]^-$ and $[FeCl_4]^{2-}$ for all compositions studied, which were all Lewis basic (>50 mole % [Bmim][Cl]) due to solubility problems.

The ferrocene ($Fe(Cp)_2$) and ferrocenium ($Fe(Cp)_2^+$) ion were also studied in the $AlCl_3$/[BuPy][Cl] melt as a function of melt acidity.[23] The ferrocenium cation was found to be unstable in the Lewis basic melt, this was evidenced by adding [BuPy][Cl] to a solution of $[FeCl_4][Fe(Cp)_2]$ in Lewis neutral $AlCl_3$/[BuPy][Cl], $Fe(Cp)_2$ and $[FeCl_4]^-$ were observed as the decomposition products. The $[FeCl_4]^-$ resulting from the decomposition of the ferrocenium ion underwent a slow reduction to $[FeCl_4]^{2-}$ in the basic melt. Ferrocene was unstable in the Lewis acidic melts and is oxidised in the melt to form ferrocenium, this was evidenced by reducing currents corresponding to the reduction of ferrocenium in freshly prepared ferrocene solutions in Lewis acidic $AlCl_3$/[BuPy][Cl]. The increase in ferrocenium was less than the decrease in ferrocene, suggesting side reactions, and this was confirmed to be reactions with traces of water and oxygen present in the melt as impurities. The $Fe(Cp)_2/Fe(Cp)_2^+$ couple was found to be electrochemically reversible in all accessible compositions of solvent, despite the limited stability of ferrocene and the ferrocenium ion in Lewis acidic and basic solutions respectively.

6.1.3.2 Present Work

To date, the electrochemistry of iron in ionic liquids has mainly focused on the chloroaluminate melts. In order to ascertain the electrochemical behaviour of Fe(II) and Fe(III) in a non-chloroaluminate ionic liquid the electrochemistry of iron has been performed in the pure chloride melt, [Emim][Cl]. The electrochemistry of both Fe(II) and Fe(III) in the ionic liquid [Emim][Cl] are presented. Fe(II) and Fe(III) were introduced into solution by the addition of known amounts of $FeCl_2$ and $FeCl_3$ respectively into the ionic liquid used. Cyclic voltammograms showing the effect of scan rate on the Fe(II)/(III) redox couple in [Emim][Cl] are shown in figure 6.22.

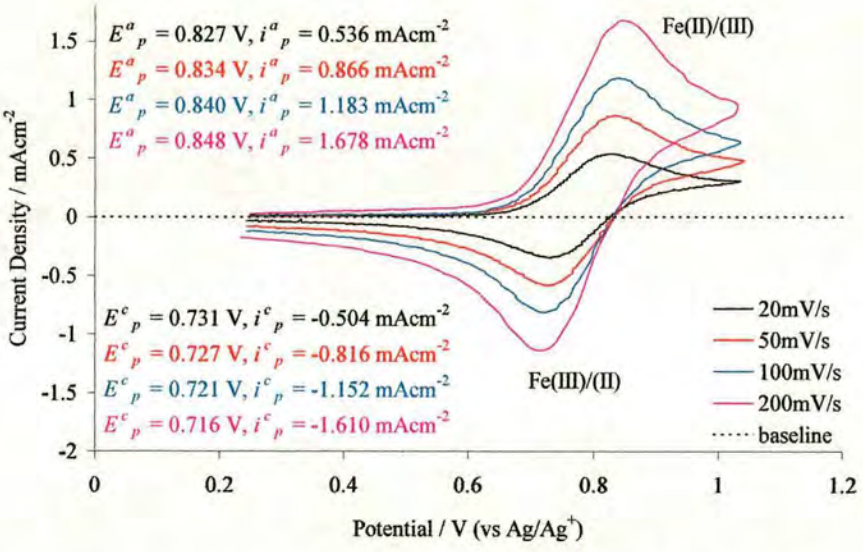

Figure 6.22: Effect of scan rate on Fe(II)/(III) redox couple of $FeCl_2$ in [Emim][Cl] at a Pt electrode, 389K, all scans started anodic from 0.25V.

As can be seen from figure 6.22, the peak potentials are dependant on the scan rate, with the oxidation potentials experiencing a positive shift and the reduction potential experiencing a negative shift with increasing scan rate. This behaviour suggests that the electrochemical couple Fe(II)/(III) is irreversible under the experimental conditions. However, the CVs have not been compensated for the solution resistance, and by plotting i_p vs E_p for different scan rates, we can then

estimate the peak potential independent of *iR* effects (when i = 0A). A plot of i_p vs E_p for both the Fe(II)/(III) redox reaction, (a), and Fe(III)/(II) redox reaction, (b) are shown in figure 6.23.

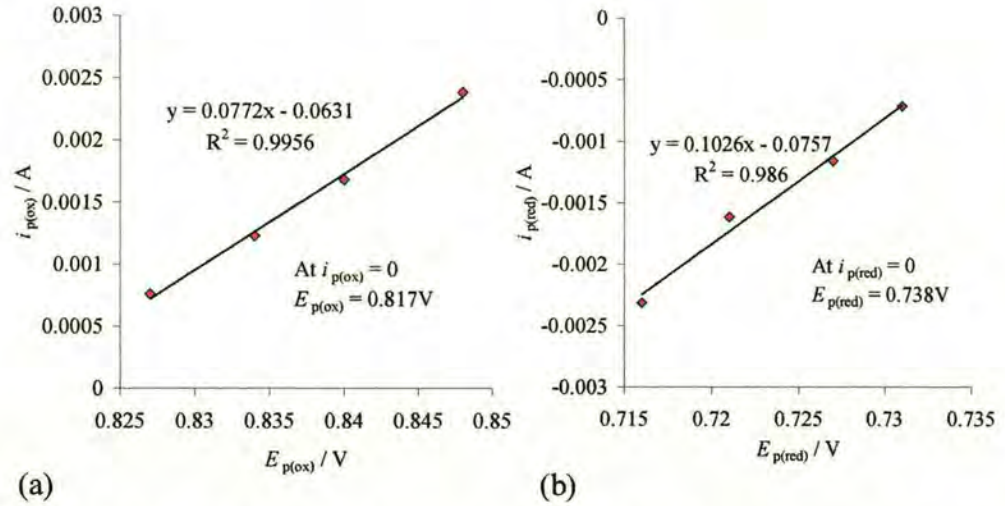

Figure 6.23: Plot of i_p vs E_p for (a) Fe(II)/(III) and (b) Fe(III)/(II) in [Emim][Cl] for varying scan rates, 20mVs^{-1}, 50mVs^{-1}, 100mVs^{-1} and 200mVs^{-1}.

The values of E^a_p and E^c_p calculated from the straight-line slopes in figure 6.23 are 817mV and 738mV respectively, giving a peak potential separation of 79 ± 10mV. This value agrees within experimental error with the theoretical value for a reversible one-electron reaction of 74mV at 389K calculated from equation (9). From the slope of the linear fit in figure 6.23(a) we can estimate the solution resistance as being 13 Ω. This resistance value is similar to that obtained for Cu(II)/(I) in [Emim][Cl], 10 Ω (section 6.1.2.2), and comparable to Ag(I)/Ag, 41 Ω (section 6.1.1.2).

For a diffusion controlled solution reaction, the peak current, i_p, must rise linearly with the square root of the scan rate, $v^{½}$, as can be seen in figure 6.24 this is the case for both the anodic and cathodic redox reactions. For a redox reaction to be chemically reversible the ratio of the peak oxidation and reduction currents should also be close to unity, and this found to be the case for all scan rates used.

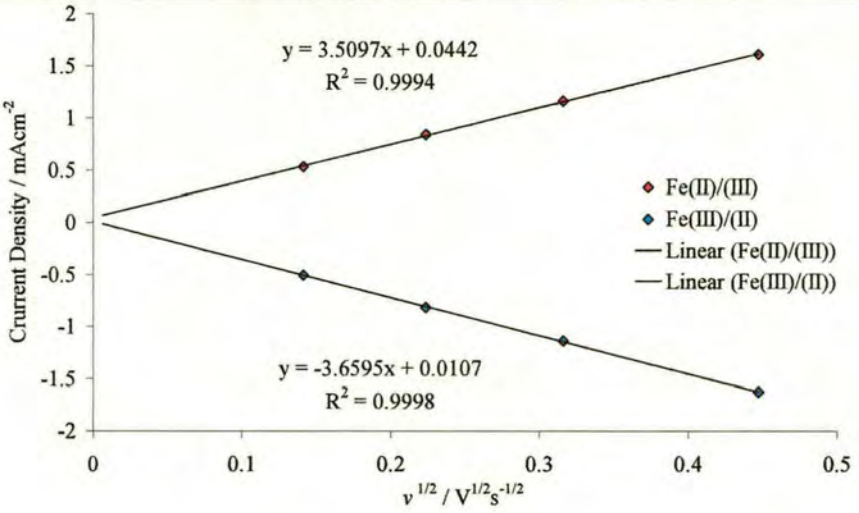

Figure 6.24: Plot of i_p vs $v^{½}$ for Fe(II) oxidation and Fe(III) reduction from a solution of $FeCl_2$ in [Emim][Cl] at 389K.

A scan of the full potential window of [Emim][Cl] shows that deposition of iron on a platinum electrode from Fe(II) in [Emim][Cl] is hindered at 389K, with only small redox peaks observable at this temperature near 0V, figure 6.25. The kinetics of Fe(II) reduction must be poor at this temperature.

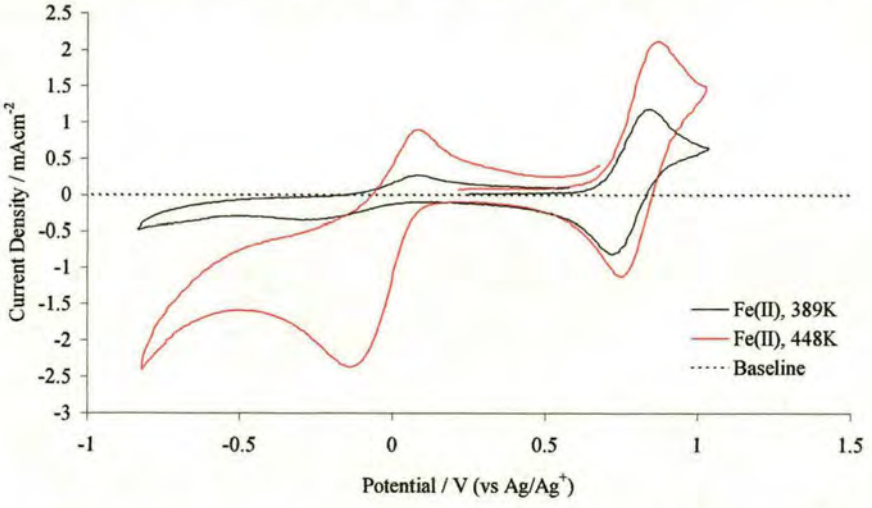

Figure 6.25: CV's of $FeCl_2$ (0.0298M) in [Emim][Cl] at a Pt electrode, (——) 389K and (——) 448K, $100mVs^{-1}$. Scans started anodically from 0.2V vs Ag/Ag^+.

In contrast however, when the temperature is increased to 448K, the reduction peaks attributable to Fe(II)/Fe near 0V become more pronounced at a platinum electrode. If we examine the CV's in figure 6.25, we can see that on scanning

positive from the starting potential, only background currents pass until an oxidation peak at *ca.* 0.87V is observed, this is attributed to the oxidation of Fe(II) to Fe(III). On reversing the potential scan a corresponding reduction wave occurs at *ca.* 0.75V, corresponding to the reduction of the electrochemically generated Fe(III) at the electrode surface to Fe(II). On continuing to scan the potential negatively a reduction peak at *ca.* -0.13V is observed, this has been ascribed to the reduction of Fe(II) to iron. On scanning the potential further negatively from the diffusion limited reduction peak of Fe(II), another reduction current begins to flow before reversal of the potential scan direction, this is the cathodic limit of the melt and corresponds to the reduction of the imidazolium cation. When the scan is reversed, an oxidation peak at *ca.* 0.09V associated with the reduction peak at *ca.* –0.13V is observed, though the charge passed on the oxidation peak is much lower than that during the reduction peak. Reversing the potential scan before excursion into the cathodic limit of the melt results in little change to the magnitude of the oxidation peak. The values of peak potential, E_p, and peak current density, i_p, for the CV's at each temperature are detailed in table 6.2.

	389K	**448K**
E^a_p **Fe(II)/(III)**	0.842 V	0.871 V
E^c_p **Fe(III)/(II)**	0.719 V	0.741 V
i^a_p **Fe(II)/(III)**	1.16 mAcm^{-2}	2.04 mAcm^{-2}
i^c_p **Fe(III)/(II)**	-1.09 mAcm^{-2}	-1.89 mAcm^{-2}
E^c_p **Fe(II)/Fe**	-0.279 V	-0.137 V
E^a_p **Fe/Fe(II)**	0.083 V	0.082 V
i^c_p **Fe(II)/Fe**	-0.25 mAcm^{-2}	-2.62 mAcm^{-2}
i^a_p **Fe/Fe(II)**	0.26 mAcm^{-2}	1.00 mAcm^{-2}

Table 6.2: E_p an i_p values from the CV's of $FeCl_2$ (0.0298M) in [Emim][Cl] at a Pt electrode, E_p values quoted w.r.t. Ag wire in 0.01M AgCl in [Emim][Cl].

From the values in table 6.2, we can see that the peak current density of Fe(II) reduction increases dramatically, by approximately 950%, when we increase the temperature to 448K, this is in comparison with an increase of 3.4% in the peak

current density for the Fe(II)/(III) redox peaks. Figure 6.26 shows a plot of charge passed versus potential for the iron plating and stripping in [Emim][Cl] at 389K and 448K.

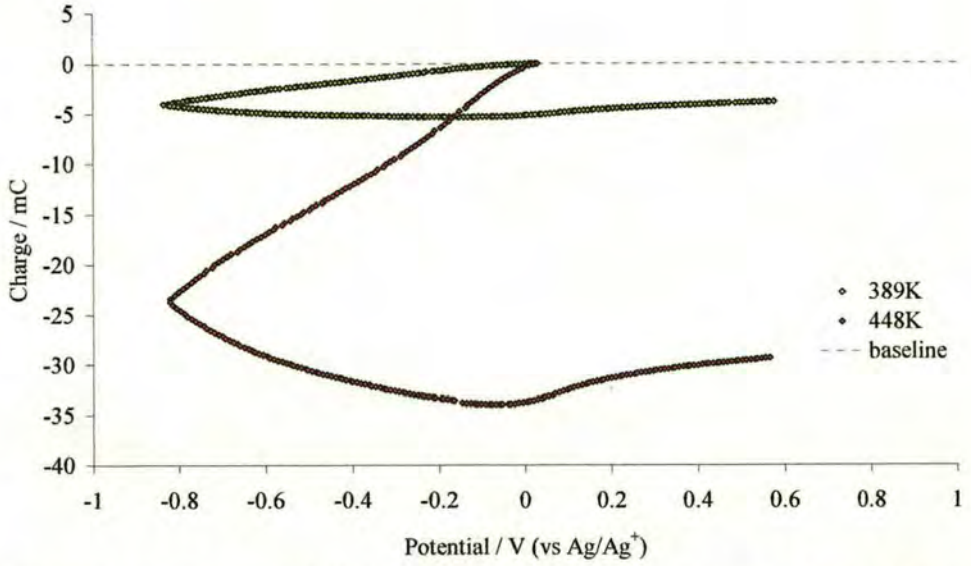

Figure 6.26: Charge passed during the plating and stripping of iron from a Pt electrode in [Emim][Cl] at389K and 448K.

It can be seen from figure 6.26 that the charge passed during plating does not return to zero when the scan is reversed, this shows that the product of Fe(II) reduction is not re-oxidised in it's entirety. The reduction peak for Fe(II) to Fe is larger than that for the peak due to Fe(II)/(III), though not twice as large. This indicates that the electrode kinetics are important in the electrochemical reduction of Fe(II) in [Emim][Cl], this is evidenced by the effect of temperature on the Fe(II) reduction peak. The small oxidation peak observed at slightly positive potentials to the Fe(II) reduction when the scan is reversed after Fe(II) reduction is observed, suggests that the reduction reaction does not result in the formation of an adherent iron deposit on the surface of the platinum electrode, and possibly results in the formation of adatoms on the electrode surface rather than a closed film. These adatoms may be reactive towards the reduction of the $[Emim]^+$ cation, eliminating the possibility of re-oxidation on the reverse scan.

The electrochemistry of Fe(III), introduced to [Emim][Cl] as $FeCl_3$, is similar to that of Fe(II) in [Emim][Cl] in that both the Fe(III)/(II) and Fe(II)/0 redox couples are observed as can be seen in figure 6.27.

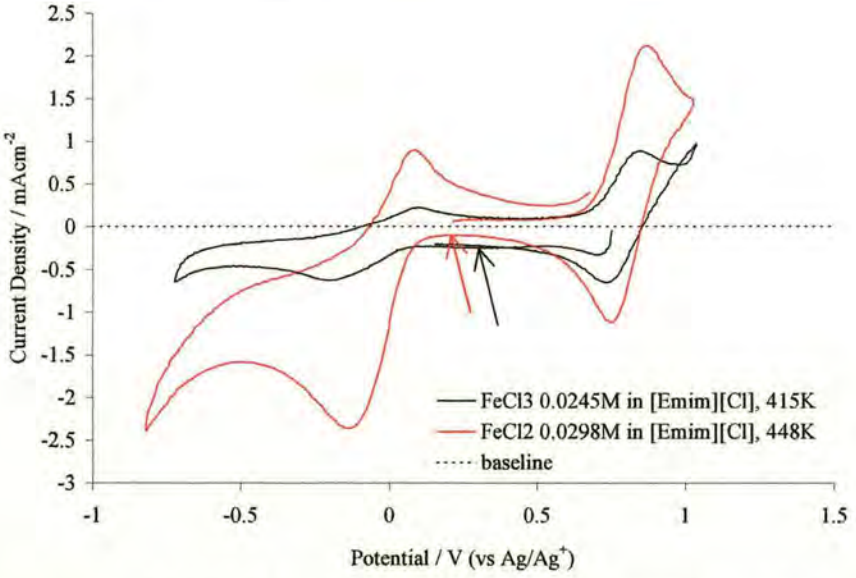

Figure 6.27: CVs of 0.0245M $FeCl_2$ (——) at 448K, $100mVs^{-1}$ and 0.0298M $FeCl_3$ (——) at 415K, $50mVs^{-1}$ in [Emim][Cl]. ⟶ marks the loss of Fe(III) – no Fe(III) present in solution

As was observed with $FeCl_2$ in [Emim][Cl], the reduction peak at roughly –0.2V increased significantly when the temperature was increased for a solution of $FeCl_3$ in [Emim][Cl]. However, as was observed with Cu(II) in [Emim][Cl] (section 6.1.2.2), Fe(III) was found to be unstable in the [Emim][Cl] ionic liquid as the temperature was increased. The instability of Fe(III) in the Lewis basic $AlCl_3$/[BuPy][Cl] has been observed previously,[22] though Fe(III) is stable in Lewis acidic chloroaluminate melts, suggesting chloride may have a role to play in the reduction of Fe(III) by the melt. At temperatures above 423 K, when the electrochemical cell was turned on near 0.5V, a potential less than the Fe(II)/(III) couple, no current corresponding to the reduction of Fe(III) in solution was observed. This suggests that Fe(III) is no longer present in solution, though Fe(III) must be stable for the timescales used in the CVs of Fe(II) in [Emim][Cl] as the ratio of the

oxidation and reduction currents in figure 6.22 are close to unity for all scan rates used.

6.1.4 Electrochemistry of zirconium in [Emim][Cl]

6.1.4.1 Introduction

Zirconium is an important metal in the nuclear fuel cycle, and is usually employed as the main constituent of the casing that holds the nuclear fuel pins together in the reactor assembly (cladding). Aqueous processing of zirconium is not permissible due to the extreme oxophilicity of the metal, as a result zirconium processing is performed in the high temperature molten salt systems where water is absent from the reaction vessel.[28] The molten salts employed most often in zirconium processing consist of one or more alkaline earth metal chloride, and zirconium can be introduced in a variety of forms such as $ZrCl_4$, $ZrCl_3$, ZrF_4 or K_2ZrF_6. Zr^{4+} or Zr^{3+} migrates to the cathode surface and is deposited as zirconium metal, indications are that zirconium is deposited as a one step process whether from the trivalent or tetravalent state. The most successful zirconium electrodeposition processes have employed the starting material in the tetravalent state.

6.1.4.2 Present Work

Due to the importance of zirconium as a material used in the nuclear fuel cycle, the electrochemistry of zirconium in an ionic liquid must be understood to determine the fate of zirconium in an electrorefining process. To date, the literature available on the study of zirconium in ionic liquids is rather limited. The only studies of zirconium in ionic liquids has concerned the use of zirconium as a catalyst for the dimerisation of 1-butene[29] or the use of ionic liquids for the isolation of zirconium clusters[30] such as $[(Zr_6B)Cl_{18}]^{5-}$ and the electrochemistry of zirconium clusters as a solute in both Lewis basic and acidic chloroaluminate melts[31]. Reported

is the electrochemistry of Zr(IV) introduced as $ZrCl_4$ in the ionic liquid [Emim][Cl], a typical CV is shown in figure 6.28.

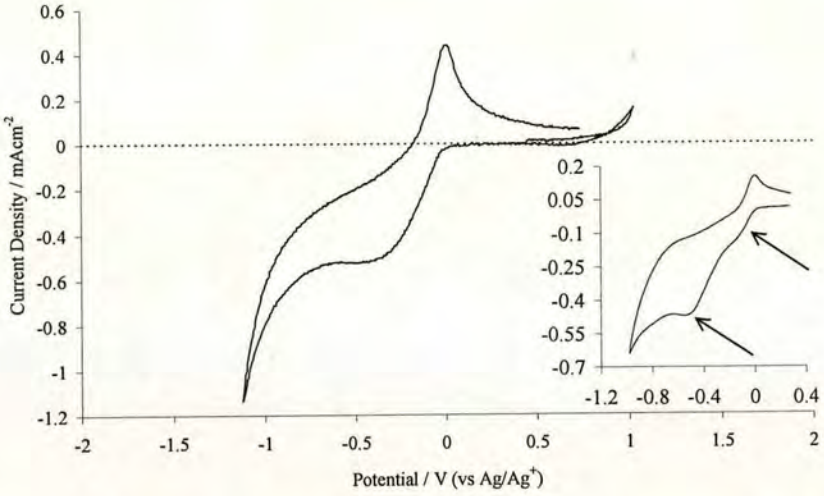

Figure 6.28: CV of $ZrCl_4$ (0.022M) in [Emim][Cl] at a platinum electrode, 50 mVs^{-1} 393K. Inset scanned at $10mVs^{-1}$ with arrows showing two reduction peaks.

As can be seen from the CV presented in figure 6.28 there is only one reduction wave within the electrochemical window (reduction limit of solvent is *ca.* -1.0 V) with an associated oxidation peak on the reverse scan. However, the reduction wave does not exhibit a well defined peak and thus there is no region of diffusion controlled current where a potential step experiment can be performed to obtain the diffusion coefficient of Zr(IV) in [Emim][Cl]. The onset of reduction for the imidazolium cation occurs negative to that of Zr(IV) reduction, though this does not seem likely to be the reason for the absence of a diffusion limited falling current due to the potential difference between the two redox reactions. Some catalytic reduction of $[Emim]^+$ by Zr(0) cannot be excluded as the reason for this lack of diffusion limited current. When the scan rate is lowered to $10mVs^{-1}$, inset figure 6.28, it becomes apparent that the reduction wave is comprised of more than one peak, suggesting that zirconium deposition occurs preferentially at various sites on the platinum surface, and not preferentially on already deposited zirconium. Alternatively, the reduction reaction may not proceed in a single step as observed in the high temperature molten salt[28], and may first undergo a reduction from Zr(IV) to

Zr(III) followed closely by a three electron reduction to Zirconium metal. It is impossible to distinguish this given the resolution of the CV data.

The oxidation wave at *ca.* 0V associated with the reduction reaction at *ca.* -0.4V has the same form as that expected for a stripping wave, though the current does not drop sharply to zero as the potential is scanned positive. This could suggest that zirconium oxidation from the surface has different thermodynamics depending on the site at which it has been deposited. If the reduction and oxidation peaks are due to Zr(IV)/Zr and Zr/Zr(IV) respectively then from the charges passed the mass of zirconium deposited is not equal to the amount of zirconium oxidised from the surface of the electrode. If we consider the possibility zirconium is deposited from Zr(IV), but reoxidised into solution as Zr(III) the charges passed still do not correspond to that expected for complete deposition/stripping of zirconium. Thus either zirconium metal is not stable in contact with Zr(IV) in the chloride ionic liquid, or any deposited zirconium is not forming an adherent film on the platinum electrode surface. A plot of charge passed versus potential highlights the incomplete plating/stripping of Zr(IV) at a platinum electrode in [Emim][Cl], figure 6.29.

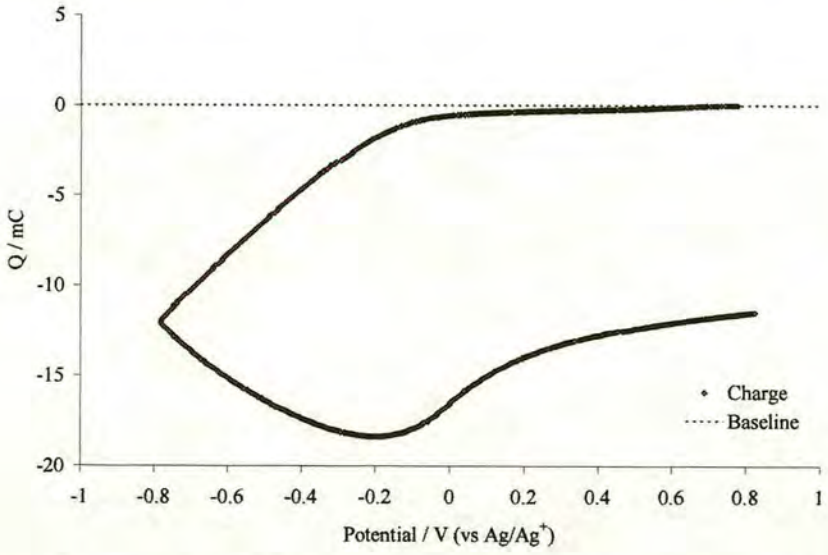

Figure 6.29: Charge passed versus potential for the deposition and stripping of Zr(IV) (0.022M) from [Emim][Cl] at a platinum electrode, 413K, $50mVs^{-1}$.

The effect of scan rate on the peak currents was investigated, CV's of $ZrCl_4$ in [Emim][Cl] at varying scan rates are shown in figure 6.30. As can be seen from figure 6.30, the scan rate has an effect on the reduction current, however the relationship is complicated since for some scan rates the reduction currents are very similar. This response of the reduction currents to the scan rate indicates that for the reduction of Zr(IV), the surface kinetics are important, rather than diffusion of Zr(IV) from bulk solution. The oxidation currents vary with scan rates also, but in a more expected way, that is the peak current densities rise linearly with the square root of the scan rate indicating a diffusion controlled process.

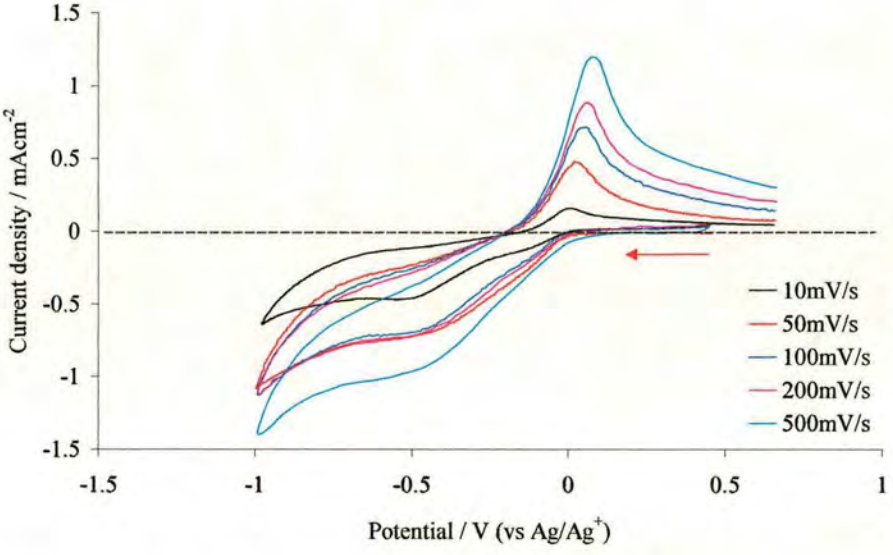

Figure 6.30: Effect of scan rate on $ZrCl_4$ (0.022M) in [Emim][Cl] at a platinum electrode, 412K.

6.1.5 Electrochemistry of uranium in [Emim][Cl]

6.1.5.1 Introduction

Uranium is the main constituent of spent nuclear fuel, usually comprising ~96% of the material, the remaining materials are the products of nuclear fission (fission products) and plutonium, which is produced through the transmutation of ^{238}U. If uranium is to be separated from the fission products and plutonium in spent nuclear fuel by an electrorefining process in ionic liquids, then the electrochemistry of uranium in the electrolyte concerned must be known.

Several research groups have studied uranium electrochemistry in ionic liquids. The first study of uranium in a room temperature melt was undertaken by *D'Olieslager et. al.* in which the electrochemistry of uranium(IV) was investigated in a Lewis acidic $AlCl_3$/[BuPy][Cl] melt[32]. The reduction of U(IV) to U(III) was found to be irreversible at a glassy carbon electrode in the 2:1 melts, and the oxidation of U(IV) to U(V) and subsequently to U(VI) were observed close to the oxidation limit of the solvent. Further investigations[33] into the electrochemistry of uranium in the Lewis acidic $AlCl_3$/[BuPy][Cl] found that in the most acidic melts U(IV) was coordinated by $[Al_2Cl_7]^-$ which was displaced by $[AlCl_4]^-$ at lower acidity.

D'Olieslager *et.al.* also studied the spectroscopy and electrochemistry of uranium in a Lewis basic $AlCl_3$/[BuPy][Cl].[34] The electrochemistry of $[UCl_6]^{2-}$ in the basic melt is rather limited, U(III) was observed to be an unstable oxidation state in the $AlCl_3$/[BuPy][Cl] melt due to its reaction with the $[BuPy]^+$ cation to produce U(IV) and the 1,1'-dibutyl-4,4'-bi-pyridinium radical cation. Further studies[35] of U(IV)/U(III) electrochemistry in the Lewis basic $AlCl_3$/[Emim][Cl] melt revealed that U(IV) could be reduced to U(III) before the onset of the melt potential window (reduction of $[Emim]^+$ is 800mV negative of $[BuPy]^+$). Potentiometric measurements for U(IV)/U(III) as a function of $[Cl]^-$ indicated both U(IV) and U(III) were present

as the hexachloro anions, $[UCl_6]^{2-}$ and $[UCl_6]^{3-}$ respectively. Pure solutions of U(III) could not be prepared by controlled electrolysis of U(IV) however. This was attributed to U(III) reacting with trace oxygen or water to produce U(IV).

In another study of uranium in ionic liquids, the uranium salts $[Emim]_2[UCl_6]$ and $[Emim]_2[UO_2Cl_4]$ were prepared, characterised by X-ray crystallography, and their electrochemistry studied[36] in the Lewis basic $AlCl_3$/[Emim][Cl] melt. Two voltammetric reduction waves were observed at a glassy carbon electrode for the $[UO_2Cl_4]^{2-}$ salt. The first reduction wave (E_p = -0.66V) was twice the size of the second reduction wave (E_p = -1.37V), and no oxidation current was observed on reversing the scan at –1.00V. The reduction wave at –1.37V exhibited an oxidation current when the scan was reversed at –1.60V with a peak potential separation close to that expected for a one electron reversible charge transfer reaction. When exhaustive electrolysis of the $[UO_2Cl_4]^{2-}$ solution was performed at an applied potential of –1.00V, it was calculated the number of electrons associated with the reduction wave at –0.66V was n = 2.1. Furthermore the electrochemistry of the resulting green solution consisted only of the second reduction wave at –1.37V. This was identical to the electrochemistry observed when $[Emim]_2[UCl_6]$ was used in the same system. The following reaction was proposed to explain these observations, equation (13).

$$[UO_2Cl_4]^{2-} + 2[AlCl_4]^- + 2e^- \longrightarrow 2\text{“}[AlOCl_2]^-\text{”} + [UCl_6]^{2-} + 2Cl^- \qquad (13)$$

Where “$[AlOCl_2]^-$” was the postulated oxide transfer product of $[AlCl_4]^-$. The transfer of the oxide to the melt is presumed to be fast as no current was observed on reversing the scan after the production of reduced $[UO_2Cl_4]^{2-}$.

Smith *et.al.*[37] observed that when the uranyl ion, $[UO_2]^{2+}$, was added to a Lewis acidic $AlCl_3$/[Emim][Cl] ionic liquid, the uranyl ion was reduced in bulk solution by a chloroaluminate species and the final stable product in solution was U(V). By using spectroscopy and electrochemistry at intervals after sample preparation, it was possible to observe the change in solution species. The proposed

mechanism for the removal of the "*-yl*" oxygen's from $[UO_2]^{2+}$ and subsequent reduction by the melt were as outlined in figure 6.28.

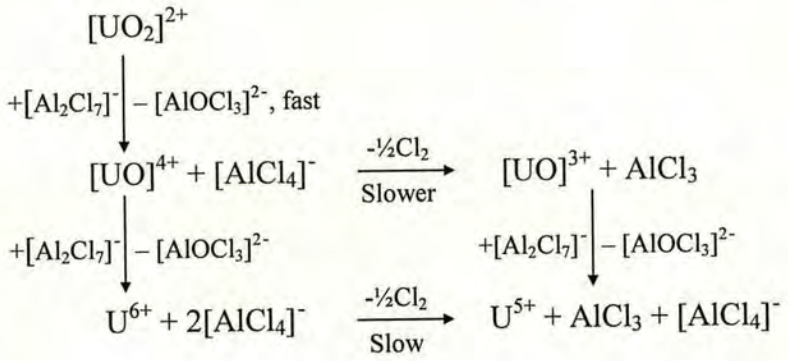

Figure 6.28: Proposed scheme for the net reduction of $[UO_2]^{2+}$ to U(V) in the Lewis acidic $AlCl_3$/[Emim][Cl] melt.

The removal of the "*-yl*" oxygen's are thought to occur rapidly due to the peak reduction current of $[UO_2]^{2+}$ diminishing rapidly with subsequent CV scans.

As part of an ongoing study at Los Alamos National Laboratory (LANL) into the feasibility of utilising ionic liquids in the nuclear fuel cycle, Smith et. al. have extended their studies to the speciation[38] of uranium with N-heterocyclic carbenes (NHC's) and also the electrochemistry[39] of uranium in recently developed non-chloroaluminate ionic liquids. Single crystal x-ray structure determination of $UO_2Cl_2(IMes)_2$ and $UO_2Cl_2(IMesCl_2)_2$ (IMes = 1,3-dimesitylimidazole-2-ylidene, $IMesCl_2$ = 1,3-dimesityl-4,5-dichloroimidazole-2-ylidene) revealed the first cases of carbene bonding to a uranyl centre[38]. The U-C bond was reported as being shortest for the $ImesCl_2$ ligands, this was attributed to the electron withdrawing effect of the chloride substituents reducing the bonding radius of the carbene lone pair. This is in stark contrast to NHC's exceptionally strong donor strength observed in low valent transition metal complexes.[40] Both U-C bonds were longer than has been observed previously in complexes of the type $UO_2Cl_2L_2$ which are observed between 2.27-2.30Å. The use of uranyl NHC's is seen as a possible route to novel separation technologies. The amount of free NHC's could be adjusted by careful control of pH in ionic liquids, allowing control of the coordination sphere of dissolved ions.

The electrochemistry of uranium in the 1-(2-methoxyethyl)-1-methyl-pyrrolidinium bis (trifluoromethanesulfonyl) imide ionic liquid,[39] [MPyr][N(Tf)$_2$], was obtained by dissolving [MPyr]$_2$[UCl$_6$] in [MPyr][N(Tf)$_2$]. The electrochemistry of uranium exhibited two redox couples, attributed to both U(IV)/(III) and U(IV)/(V) and these can be observed along with associated redox peaks on reversal of the scan. It is suggested that reversible reduction and oxidation of active metals may only be achieved if the water content is well below 20ppm. To date there has been no published data on the electrochemistry of soluble uranium species in [Emim][Cl].

6.1.5.2 Present Work

Presented below is the study of uranium, introduced as UCl_4 in the ionic liquid, 1-ethyl-3-methylimidazolium chloride, [Emim][Cl]. The cyclic voltammogram of uranium in [Emim][Cl] at a platinum electrode is shown in figure 6.31.

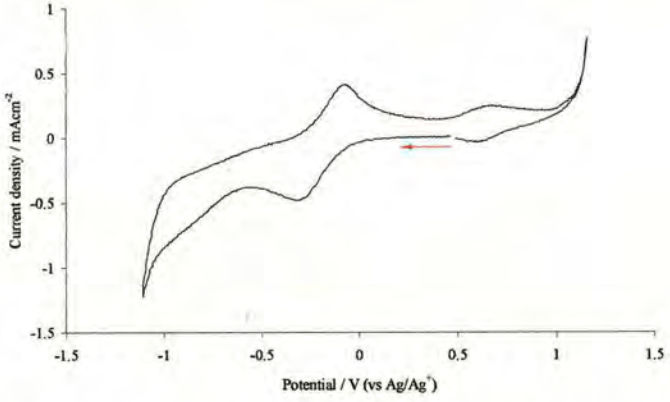

Figure 6.31: CV of UCl_4 (0.0151M) in [Emim][Cl] at a Pt electrode, 388K, 50mVs^{-1}.

Figure 6.31 shows a full scan CV of U(IV) in [Emim][Cl], the rising current at either extreme of the CV is due to the solvent limit. As can be seen, there is only one reduction peak observed on scanning negatively, followed by a linearly rising current before the onset of the solvent reduction limit. On reversing the scan, the current rises linearly until an oxidation peak is observed at ~100mV positive of the reduction peak. On scanning to potentials that are more positive a small oxidation

current is observed before the onset of the solvent oxidation limit. The responses of the peak current and peak potential to the scan rate are shown in figure 6.32.

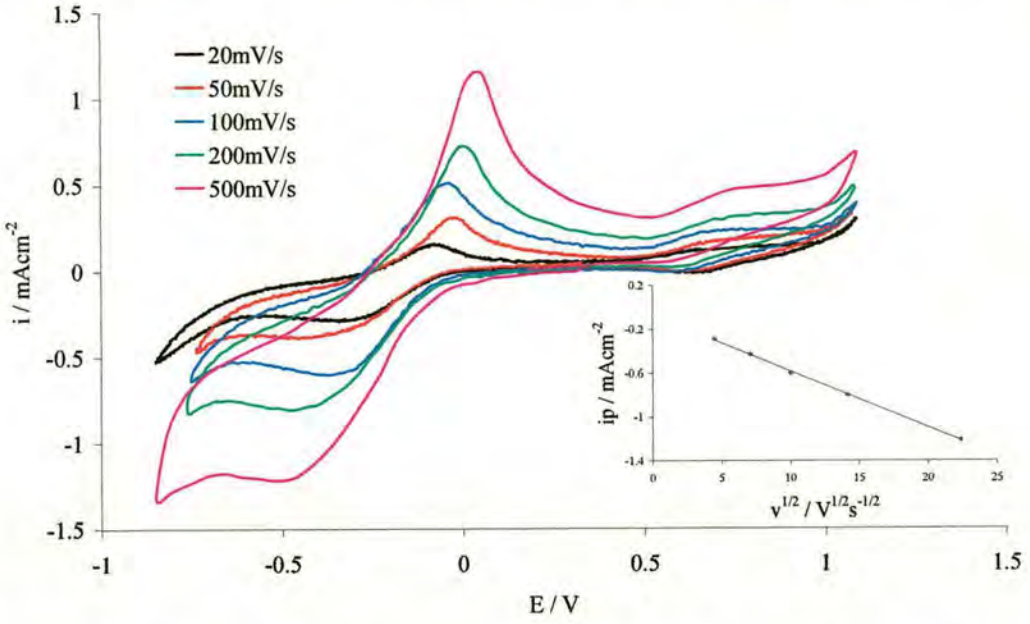

Figure 6.32: Effect of scan rate on the reduction of UCl_4 (0.0151M) in [Emim][Cl] at a Pt electrode, 388K. Inset shows peak current versus $v^{1/2}$ for the reduction peak.

As can be seen from figure 6.32, the peak currents increase with the square root of the scan rate, $v^{1/2}$, showing that the redox reactions are under diffusion control. The oxidation current close to the anodic limit also increased with $v^{1/2}$, showing that it is the oxidation of a solution species. It would be expected that UCl_4 would dissolve in [Emim][Cl] as the hexachloro species, $[UCl_6]^{2-}$, and that the U(IV)/U(III) redox couple would be observed. The oxidation peak has the appearance of a stripping peak and this would rule out the U(IV)/(III) redox couple. The oxidation current close to the oxidation limit of the melt would seem unlikely to be U(IV)/ U(V) since U(V) is observed to spontaneously reduce to U(IV) when the solvent is moved from a Lewis acidic composition to a Lewis basic composition.[41] As has been mentioned previously (section 6.1.2.1), the presence of water can prevent the observation of reversible redox peaks. In addition to this, if water is present, it could be possible that uranium oxy-chloro or hydroxide species could be formed. This gives rise to more than one uranium species in solution and could explain why the electrochemistry does not have the appearance of a single redox species. With this in mind, the

electrochemistry of UCl_4 in [Emim][Cl] was performed with baked out molecular sieves present in solution, this has been shown to lead to dry ionic liquids (section 6.2.2). Therefore this would allow us to ascertain if there was water present preventing reversible electrochemistry. The electrochemistry of UCl_4 in [Emim][Cl] with baked out molecular sieves present in solution is shown in figure 6.33.

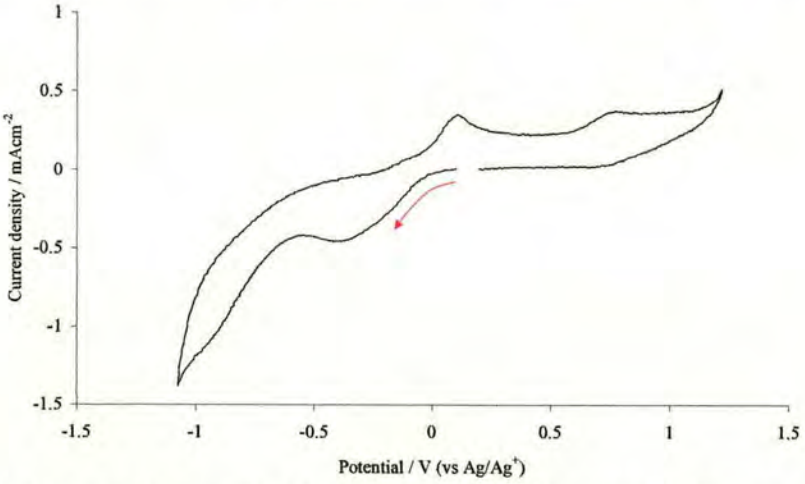

Figure 6.33: CV of UCl_4 (0.0162M) in [Emim][Cl] with dried molecular sieves, $50mVs^{-1}$, 389K.

As can be seen from figure 6.33, the CV is very similar to that without molecular sieves present, the main differences being the reduction and oxidation peaks around 0V have actually increased in separation and the reduction has become two peaks.

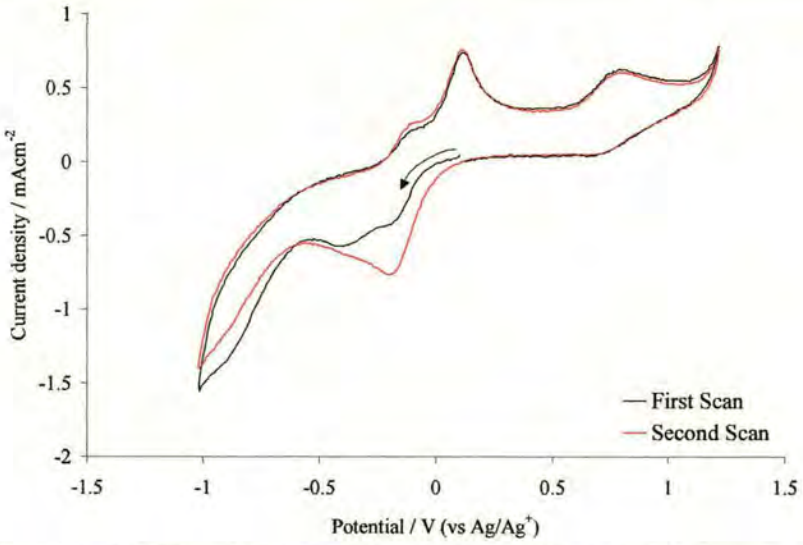

Figure 6.34: CV of UCl_4 (0.0162M) in [Emim][Cl] with dried molecular sieves, 100mVs^{-1}, 389K. (—) – first scan, (—) – second scan.

On increasing the scan rate the reduction wave starts to separate into two distinct peaks, interestingly the first reduction wave increases dramatically after an excursion into the oxidation reaction at *ca.* 0.75V, this is highlighted in figure 6.34. The second oxidation peak still has the appearance of a stripping peak as was observed without the molecular sieves. The effect of the scan rate on the reduction and oxidation peaks can be seen in figure 6.35.

As can be seen from the inset in figure 6.35, the peak current for the first reduction peak increases linearly with $v^{½}$ indicating a diffusion controlled redox process is occurring. This is observed for the other peaks too. The peak separation (118mV) between the reduction peak and the associated oxidation peak centred at roughly - 0.15V does not increase with increasing scan rate, though it is difficult to say with any certainty what the peak potential at each scan rate is precisely due to overlap of the reductions. The appearance of this peak in an ionic liquid that has been dried would suggest that it is $[UCl_6]^{2-}$ species as opposed to a uranium oxy-chloride or hydroxide species. The theoretical peak separation at 389K for a one-electron redox reaction is 74mV, indicating this is not a one-electron reversible reaction.

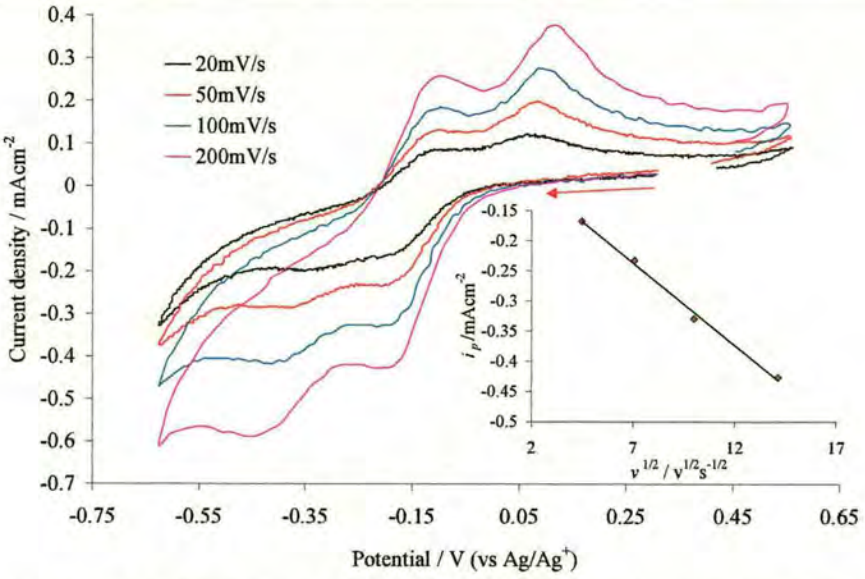

Figure 6.35: Effect of scan rate, v, on the reduction and oxidation peaks of UCl_4 (0.0162M) in [Emim][Cl] with molecular sieves, 389K. Inset shows peak current versus $v^{½}$ for the first reduction peak.

The same experiment was repeated but was operated using Schlenk techniques to ensure no water was entering the electrochemical cell. A platinum wire dipping into the uranium solution was used as a pseudo-reference electrode and the [Emim][Cl] was dried using molecular sieves before transferral to the sealed cell containing UCl_4, and further dried under reduced pressure on the Schlenk line. A CV of UCl_4 in [Emim][Cl] under these conditions is shown in figure 6.36.

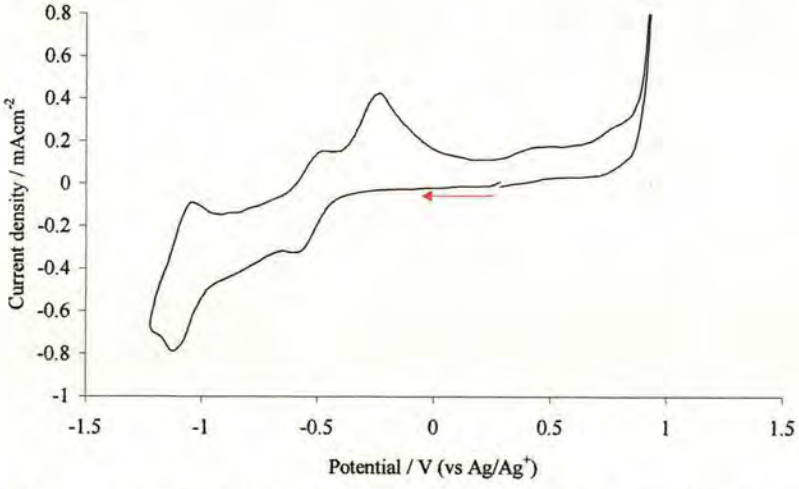

Figure 6.36: CV of UCl_4 (0.014M) in [Emim][Cl] in a sealed cell under an N_2 atmosphere, 500mVs^{-1}, 382K.

The most obvious difference between the CV recorded in the sealed cell and those not, is the appearance of distinguished peaks near the solvent reduction limit, and the disappearance of the oxidation peak near the solvent oxidation limit. The reduction peak at the most positive potentials in the CV performed in the sealed cell corresponds to the reduction peak at the most positive potentials in figure 6.34. Not all of the UCl_4 dissolved in the [Emim][Cl] in the sealed cell, this was unexpected since a lower concentration was used than in previous experiments in the argon glovebox. This suggests that ionic liquids that have moisture present dissolve UCl_4 by reaction with water to give uranium oxy-chloride species and possibly uranium hydroxide species.

Synthesising the $[UCl_6]^{2-}$ salt would be expected to increase the solubility of U(IV) in the chloride ionic liquid. For ease of use, the Tetramethylammonium salt, $[TMA]_2[UCl_6]$ was synthesised (section 4.2.2) and studied in [Emim][Cl]. A CV showing the full scan of U(IV) in [Emim][Cl] is shown in figure 6.37. The inset shows the increase of the peak current density for the reduction peak at –0.2V with increasing $[UCl_6]^{2-}$ concentration. As can be seen from the inset in figure 6.37, the peak current density for the reduction peak at –0.2V rises in a linear manner as the concentration of $[UCl_6]^{2-}$ is increased

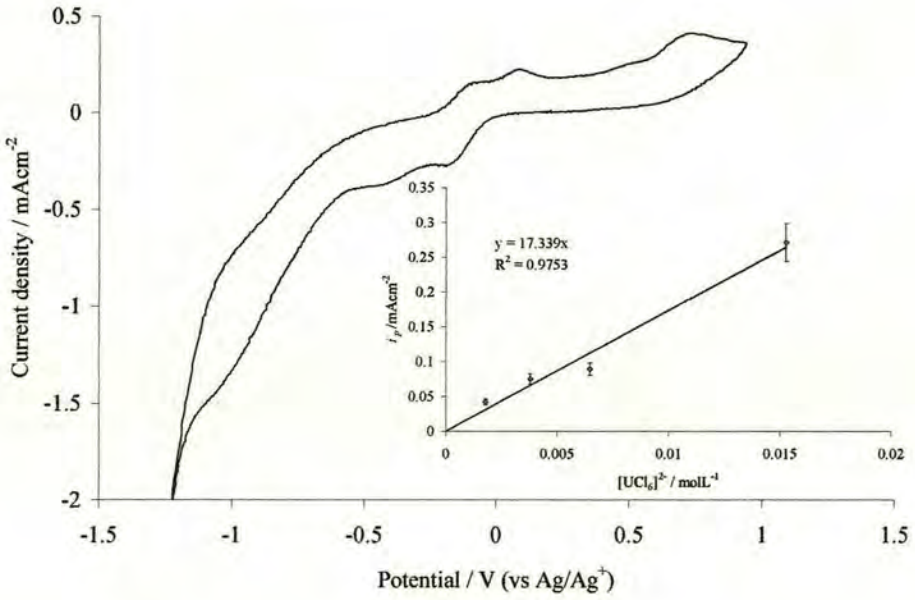

Figure 6.37: CV of $[TMA]_2[UCl_6]$ in [Emim][Cl] with the inset showing the peak current density of the reduction peak at –0.2V with increasing $[UCl_6]^{2-}$ concentration, error bars show 10% confidence limits.

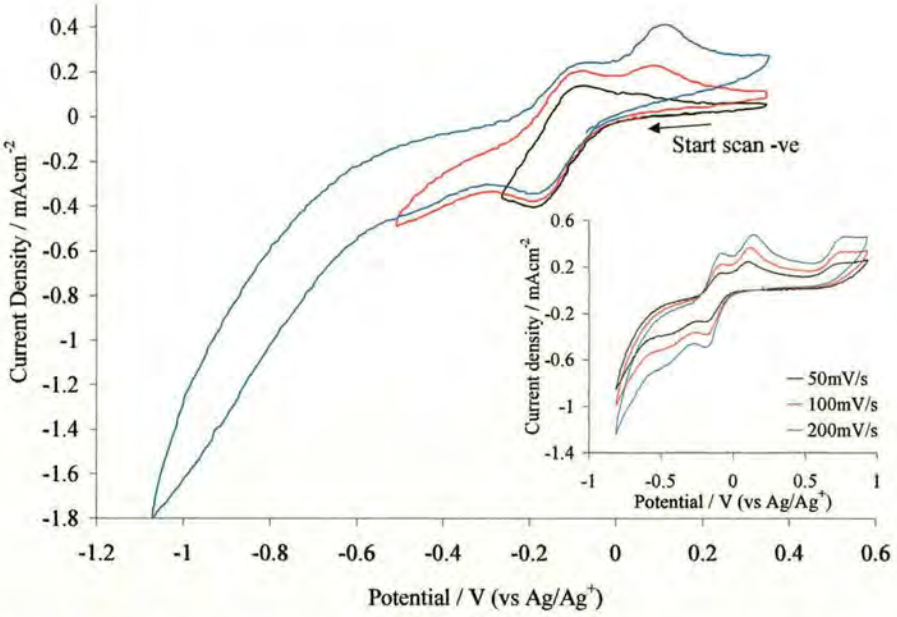

Figure 6.37: CV of $[TMA]_2[UCl_6]$ in [Emim][Cl] showing the effect of scan reversal on the oxidation peaks,100mVs^{-1}. The inset shows the effect of scan rate on the peak current densities.

The effect of the potential where the CV is reversed on the oxidation peaks is shown in figure 6.37. The reduction peak at –0.2V is associated with the oxidation peak at –0.07V and also corresponds to the first reduction peak observed in figures 6.32 and 6.34. T4he oxidation peak at 0.12V increases as the CV is reversed at more negative potentials, though it is difficult to attribute it to any reduction peak with certainty. This oxidation peak is also observed in figures 6.32 and 6.34. The peak potentials of the redox couple centred at roughly –0.1V do not change significantly with scan rate. The similarity in the CVs obtained from the addition of UCl_4 and $[TMA]_2[UCl_6]$ to [Emim][Cl] suggest that UCl_4 dissolves in the chloride ionic liquid to form the same solution species, $[UCl_6]^{2-}$. This is in consistent with the observation of the formation of the $[UCl_6]^{2-}$ (section 4.2.1) anion by EXAFS when UCl_4 was dissolved in [Hmim][Cl].

6.1.6 Electrochemistry of a Uranium electrode in Ionic Liquids.

6.1.6.1 Introduction

During the electrorefining process for spent nuclear fuel, the uranium has to be introduced into solution as a soluble species. This is carried out by applying a sufficiently oxidising potential so as to oxidise uranium into solution. In order to ascertain the feasibility of uranium oxidation into an ionic liquid, the electrochemistry of a uranium electrode was observed in ionic liquids. To date there have been no studies utilising uranium as an electrode material in ionic liquids.

6.1.6.2 Electrochemistry of a Uranium electrode in [Emim][Cl]

Since high temperature chloride melts are currently being investigated as potential solvents for pyrochemical processes to replace the currently used PUREX nuclear fuel reprocessing technology, investigation of ionic liquids based on the chloride anion was undertaken. The electrochemistry of [Emim][Cl] at a uranium electrode is shown in figure 6.38.

The most striking feature of the extremely complex CV in figure 6.38 is that the oxidation current on the reverse scan crosses over that of the oxidation current on the forward scan and crosses back when a reducing current starts to pass. This is termed a nucleation loop, and results from a change in the reactivity of the electrode, resulting in the electrode surface being more oxidising when the scan is reversed, giving a larger current at the same potential. In the case of the uranium electrode in [Emim][Cl] the nucleation loops occur at potentials of –0.43V and –0.81V. The oxidation currents between -1V and -0.5V were thought to be due to the U 0/(III) reodx couple, though no deep purple colouration corresponding to U(III) was

observed during or after electrogeneration experiments, suggesting this was not the case.

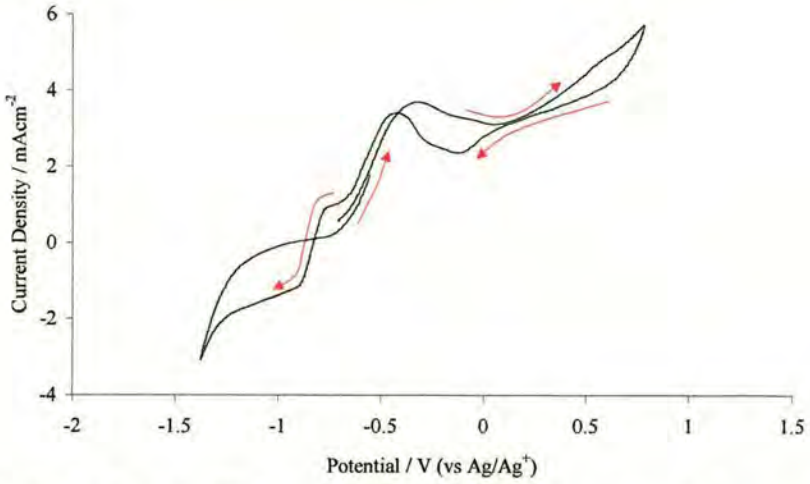

Figure 6.38: CV of [Emim][Cl] at a uranium electrode, arrow indicates direction of scan, 10mV/s, 398K

On further inspection of figure 6.38, in the oxidative dissolution region the oxidation current rises linearly with the applied potential above 0.15V with an observed resistance of *ca.* 240 Ωcm^2. This relatively high resistance suggests a migrational surface process through a resistive film, which limits the current passing through the electrode. The uranium electrode employed in this study had an oxidised surface which gave the metal a matt black appearance, the bare metal being silvery in appearance. After prolonged periods of oxidation currents being passed through the uranium electrode, pits of silvery white metallic sheen were observed on the electrode surface that had been in contact with solution. The currents passed during CV's collected after prolonged oxidation currents were generally larger than that obtained before the oxidation currents were passed. This is evidence for the dependence of the current on the nature of the electrode surface, which is most probably a reduction in the barrier properties of the oxide layer.

Due to the electrochemistry of uranium in [Emim][Cl] being dependent on the nature of the uranium oxide surface, preliminary investigations were made to determine if the nature of the electrode surface could be changed electrochemically. It is well known that halide ions, especially fluoride ions can disrupt metal oxide

surfaces by insertion of the halide ion into the oxide layer, e.g. hydrofluoric acid in steel or hydrofluoric acid in glass. With this in mind, the electrochemistry of a uranium electrode in [Emim][Cl] was studied with potassium fluoride added as a source of fluoride ions. A CV of a uranium electrode in [Emim][Cl] with KF added is shown in figure 6.39.

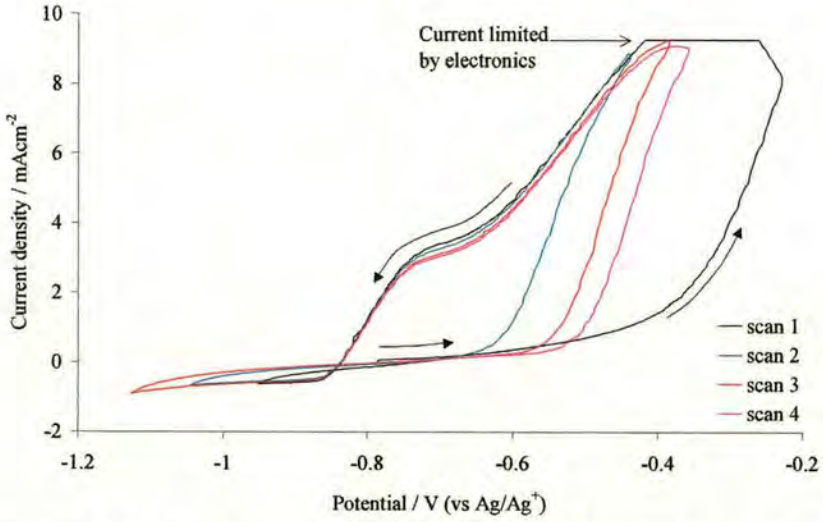

Figure 6.39: CV of a uranium electrode in [Emim][Cl] with 0.037M KF added, 20mVs^{-1}, 398K. Arrow indicates direction of scan.

As can be seen from figure 6.39, the onset of an oxidation peak occurs at around –0.6V but rises more sharply and to larger oxidation currents than those found in figure 6.38. A large nucleation loop is also seen, which is good evidence that insertion of fluoride into the lattice has compromised the oxide barrier properties and produced enhanced metal ion dissolution. The effect of the reduction current passed on the oxidation current on the subsequent scan is also highlighted in figure 6.39. When the scan is reversed at more positive potentials, the onset of oxidation currents occur at less anodic potentials. This is consistent with electrochemical reduction resulting in the ejection of F^- from the oxide and the reestablishment of the barrier oxide properties. These results suggest that the two forms of the uranium oxide surface, fluoride doped and undoped are electrochemically interchangeable.

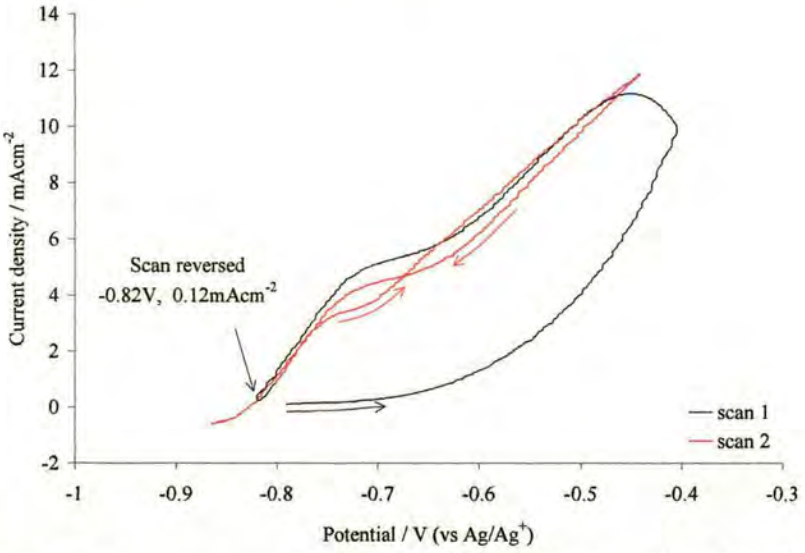

Figure 6.40: CV of a uranium electrode in [Emim][Cl] with 0.049M KF added, 10mV/s, 398K. Arrows indicate direction of scan.

The close correlation between the reduction current and the reestablishment of barrier oxide properties is clearly demonstrated in the limiting case where no reduction currents are allowed to pass. The reverse scan shows that there has been no discernible change in the reactivity of the electrode as the oxidation currents are very similar on the positive sweep as can be seen in figure 6.40.

6.1.6.2.1 Electrochemical dissolution of Uranium in [Emim][Cl]

For an electrorefining process, one possible means of introducing uranium into solution from the metallic form is by electrochemically oxidising the uranium metal into solution in the ionic liquid. This process is termed electrochemical dissolution. There is no information available in the published literature about the electrochemical dissolution of uranium metal into a room-temperature ionic liquid. The ionic liquid, [Emim][Cl], was investigated as a potential ionic liquid for the electrochemical dissolution of uranium into solution. When electrochemical dissolution experiments were performed, the counter electrode was contained in a

fritted compartment to prevent any redox products from this electrode contaminating the bulk melt. Electrochemical dissolution was performed by applying a constant potential and observing the change in current with time, the resulting data was a current that fluctuated initially, but as the electrochemical dissolution progressed, the current stabilised to a constant value. By the end of electrochemical dissolution experiments, the surface of the uranium electrode displayed areas where the oxide surface had been removed and these areas on the electrode surface had a metallic lustre. An example of the variation of current with time for an electrochemical dissolution of uranium in [Emim][Cl] at a constant potential (-0.72V) is shown in figure 6.41.

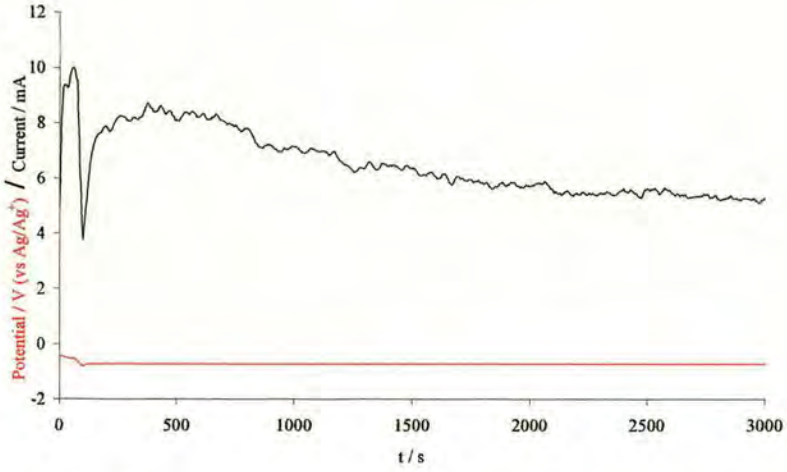

Figure 6.41: Plot of Current (——) and Potential (——) versus time for the electrochemical dissolution of uranium in [Emim][Cl] at 428K.

A series of electrochemical dissolution experiments were undertaken, and a CV of the resulting solution was recorded at a platinum electrode to determine if any redox active species were being electrochemically dissolved into solution. Figure 6.42 shows the resulting CV's from different charges

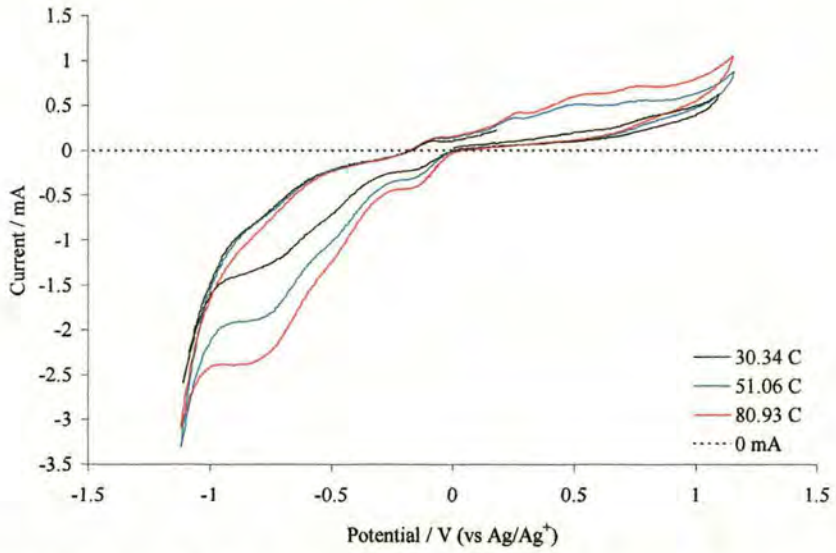

Figure 6.42: CV's at a Pt electrode after 30.34 C (——), 51.06 C (——) and 80.93 C (——) have been passed through a uranium electrode in [Emim][Cl] at 428K.

From figure 6.42, it can be seen that the redox peak currents increase with charge passed through the uranium electrode. The peak currents of the reduction waves at around -0.87V display a linear increase in peak current with charge passed, but this linear relationship does not correspond to zero current for zero charge passed. The first reduction peak on scanning negatively in figure 6.42 corresponds to the first reduction peak observed on scanning negatively in figures 6.32, 6.34 and 6.37. This indicates a soluble uranium species is being produced through the oxidative dissolution of a uranium electrode in [Emim][Cl]. This species is most likely to be a hexachloro- species as these peaks are observed in both the solutions where UCl_4 and $[UCl_6]_2^-$ (section 6.1.5.2) were added as a soluble U(IV) source. The oxidation peak associated with this reduction peak is also present in the electrogenerated solution as has also been observed in the CVs of UCl_4 and $[TMA]_2[UCl_6]$, indicating this may be due to $[UCl_6]^{2-}/[UCl_6]^{3-}$. The large reduction peak that is observed on scanning to potentials negative of the first reduction peak is broad and appears to be composed of two reduction peaks, neither of which correspond to any peaks observed in the previous CVs from soluble U(IV) species (section 6.1.5.2). Add to this the large size in comparison to the first reduction peak

6.1.6.3 Electrochemistry of a Uranium electrode in [Phos][N(Tf)$_2$]

The use of chloride ionic liquids as solvents has some advantages such as ease of preparation and co-ordinating chloride ions, but they also have a few drawbacks such as their hygroscopic nature and relatively high melting points. This can make handling chloride ionic liquids problematic especially when solutes are sensitive to moisture. In light of this, the behaviour of a uranium electrode in the tetraalkylphosphonium bis(trifluoromethanesulfonyl)imide, [Phos][N(Tf)$_2$], ionic liquid has been studied. This also gives the added advantage of increasing the cathodic stability over that of the imidazolium ionic liquid, which is of potential advantage in the study of active metals. The electrochemistry of [Phos][N(Tf)$_2$] at a uranium electrode is shown in figure 6.43.

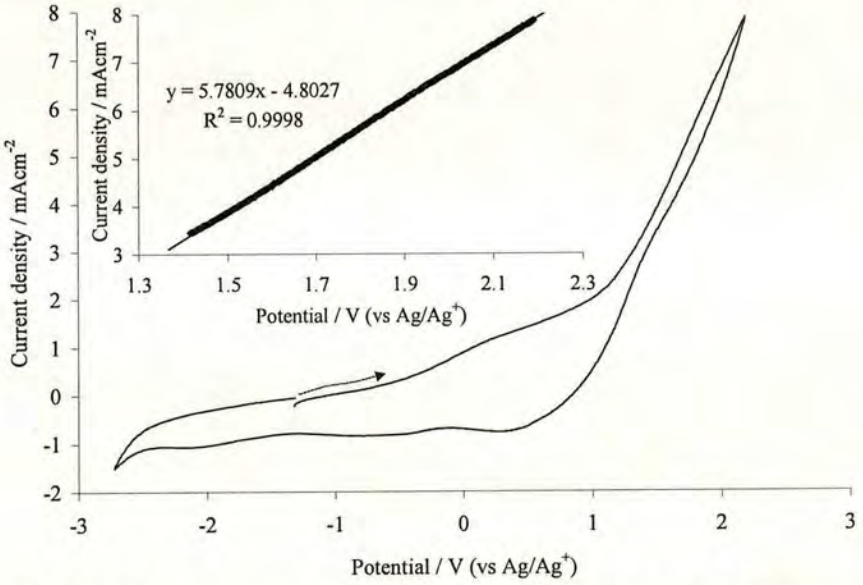

Figure 6.43: CV of a uranium electrode in [Phos][N(Tf)$_2$], 20mV/s, 383K. Arrow indicates direction of scan. Inset shows linear fit of rising oxidation current.

The main feature of the CV of uranium in [Phos][$N(Tf)_2$] ionic liquids is the oxidation current rises linearly with potentials above 1.4V as can be seen in the inset of figure 6.43. This type of electrochemical behaviour is characteristic of an electrode with an electrically resistive layer on the surface. The resistance was estimated to be around 173 Ωcm^2 and is similar to that observed for a uranium electrode in the chloride ionic liquid (section 6.1.6.2). This is, as observed in the chloride ionic liquids, most likely due to an oxide layer on the surface of the uranium electrode. Since the $[N(Tf)_2]^-$ anion is unlikely to be able to insert into the oxide layer on the electrode surface, at least not as efficiently as the smaller chloride and fluoride anions, the effect of added fluoride was studied in this ionic liquid. A CV of a uranium electrode in [Phos][$N(Tf)_2$] with added KF is shown in figure 6.44.

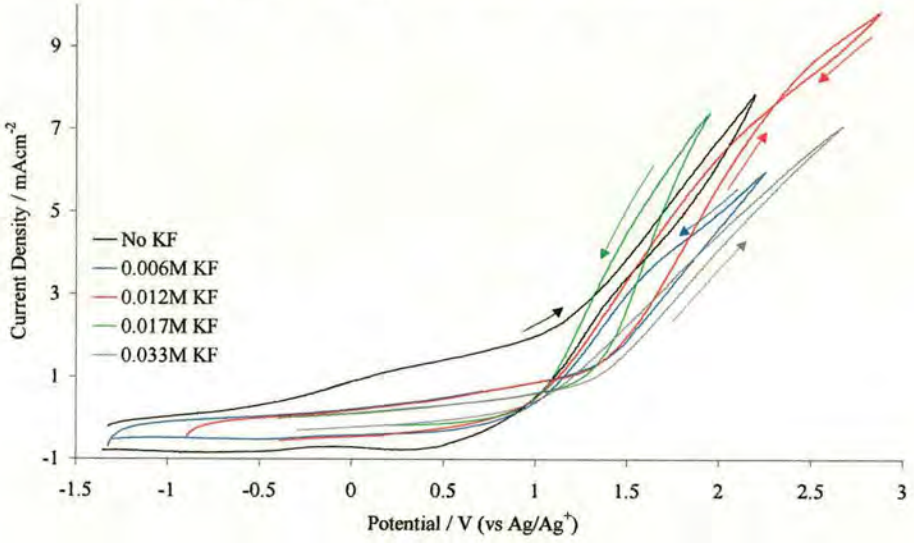

Figure 6.44: CV of a uranium electrode in [Phos][$N(Tf)_2$] with increasing concentration of KF, 20mV/s, 383K. All scans started anodically, arrows indicate direction of scan.

The effect of fluoride is again to induce nucleation loops in the CV at oxidising potentials. This is again consistent with oxidation leading to ingress of fluoride into the oxide layer, ultimately reducing the barrier oxide resistance and increasing the oxidation current. Increasing the concentration of KF can be seen to increase this effect, although not as markedly as with the chloride ionic liquids. Also, reduction of the overall capacitance of the surface film, as evidenced by the

decrease in the difference between the oxidation and reduction currents in the forward and reverse sweeps. This may be further evidence of the decrease in the barrier oxide integrity. When the concentration of KF is increased to 0.033M, the currents observed are similar to the currents observed when the KF concentration was 0.006M, rather than increasing as would be expected. A white precipitate was observed in the electrochemical cell at this concentration of KF (0.033M) suggesting the solution was saturated at this concentration. A possible explanation for the lowering of the current at this concentration is that the available electrode surface is lowered by KF precipitated on the uranium surface.

The effect of the reduction current passed and the potential of the scan reversal are shown in figure 6.45.

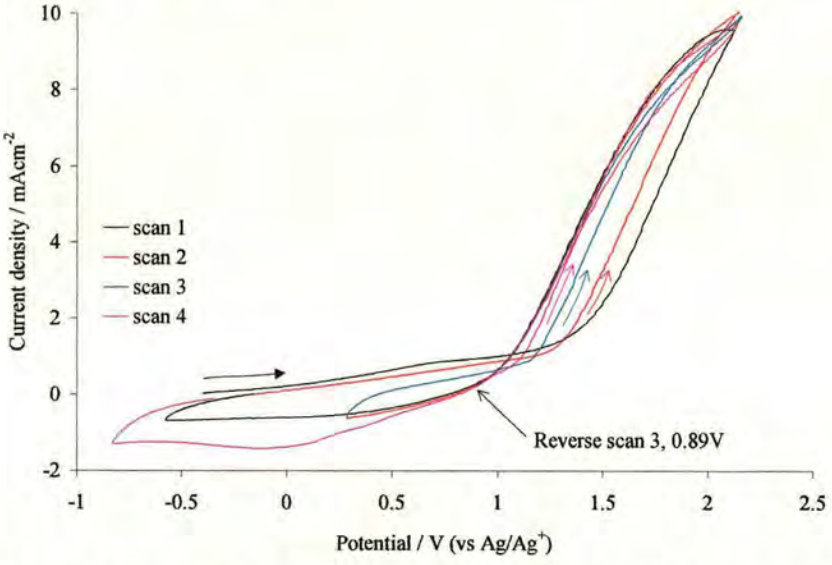

Figure 6.45: CV of a uranium electrode in [Phos][N(Tf)$_2$] with 0.017M KF, 20mV/s, 383K. Arrows indicate direction of scans.

As can be seen from figure 6.45, the potential at which the scan is reversed again influences the potential at which the onset of oxidation occurs on the subsequent scan. This is essentially identical behaviour to that found in the chloride ionic liquid (figure 6.39) and is again explained by the reduction current expelling fluoride ions from the barrier oxide layer. The current still appears to rise, essentially linearly with applied potential, indicating the electrode surface still has a resistive

found in the absence of added KF. The reduction current observed on scan 4 is greater than for any of the other scans, the previous scan was reversed before any reduction currents were passed and thus an oxidation current was passed for longer. This suggests the reduction wave is a result of the oxidation reaction, further evidencing the reversible nature of the electrode surface change. The thermodynamics of the oxidation reaction change too, with the oxidation occurring at a lower potential, indicating the electrode reaction is more facile.

6.1.6.3.1 Electrochemical dissolution of Uranium in $[N(Tf)_2]^-$ melts.

In contrast to the chloride ionic liquids which have the strongly co-ordinating chloride anion, the $[N(Tf)_2]^-$ anion is relatively non co-ordinating. This could be a disadvantage when it comes to the electrochemical dissolution of uranium in an $[N(Tf)_2]^-$ melt. In order to ascertain the feasibility of the electrogeneration of uranium as a means of introducing a soluble uranium species into an $[N(Tf)_2]^-$ melt, a uranium electrode was subjected to anodisation at constant potential in the ionic liquid [Phos][$N(Tf)_2$]. The variation of current with time for a typical uranium electrodissolution experiment is shown in figure 6.46.

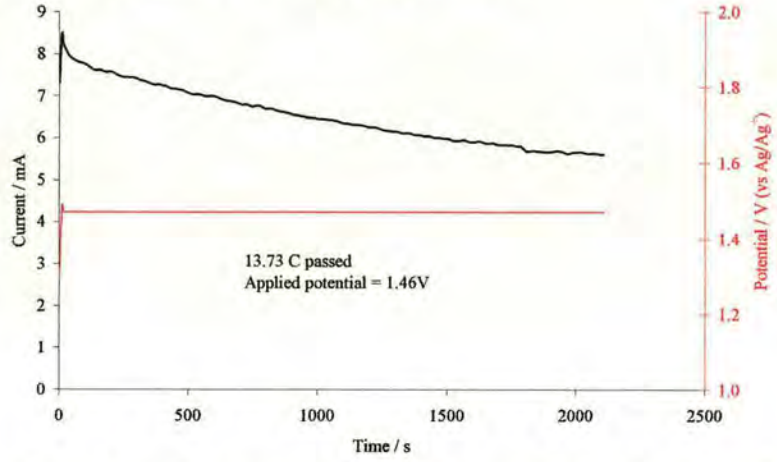

Figure 6.46: Plot of (——) Current and (——) Potential against time for a uranium electrode in [Phos][$N(Tf)_2$], 383K.

As can bee seen from the plot in figure 6.46, at a constant applied potential the current passed through the uranium working electrode decreases with time. CV's were sampled at a platinum electrode after each electrodissolution experiment to determine if any electroactive species had been produced during the electrodissolution. Figure 6.47 shows CV's collected after 13.73 C and 53.37 C have been passed through the electrochemical cell, along with a CV that was collected before any electrodissolution experiments had been performed.

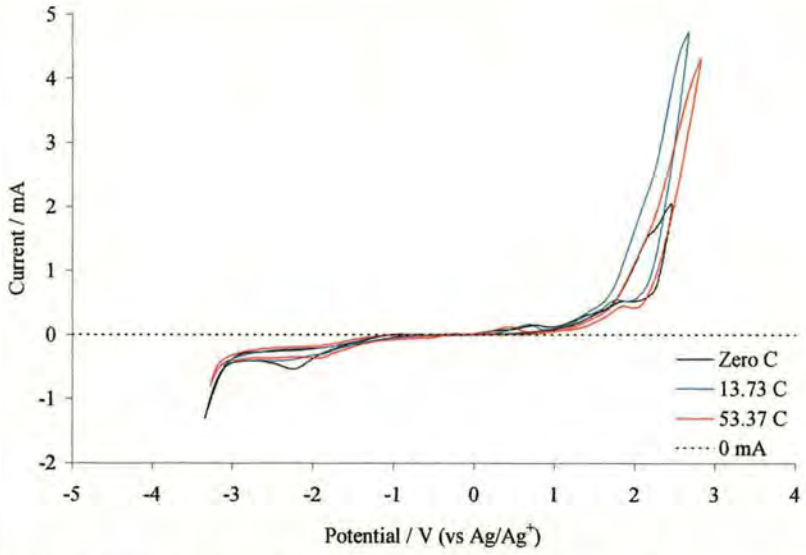

Figure 6.47: CV of $[Phos][N(Tf)_2]$ after electrodissolution of a uranium electrode at a Pt electrode after (——) 0 C, (——) 13.73 C and (——) 53.37 C. All scans started at 0V and scanned cathodically.

As can be seen from figure 6.47, the CVs collected after electrodissolution experiments have not produced any species that are electroactive within the electrochemical window of the melt. After electrodissolution experiments, the melt in the main compartment of the electrochemical cell had a dark cloudy appearance and the melt in the fritted counter electrode compartment was an orange colour.

The electrogeneration of a soluble uranium species from a uranium electrode was also attempted in the ionic liquid $[Pyr][N(Tf)_2]$ as this melt has a lower viscosity than that of the $[Phos][N(Tf)_2]$ ionic liquid due to the smaller size of the cation. The $[Pyr]^+$ cation is more stable to reduction than the $[Emim]^+$ cation but not as stable to reduction as the $[Phos]^+$ cation. A plot of current and applied potential versus time for a typical electrogeneration experiment with a uranium electrode in $[Pyr][N(Tf)_2]$ is shown in figure 6.48. As we can see from figure 6.48, once a steady current has been reached it remains at a similar value for the duration of the electrogeneration experiment at a constant applied potential.

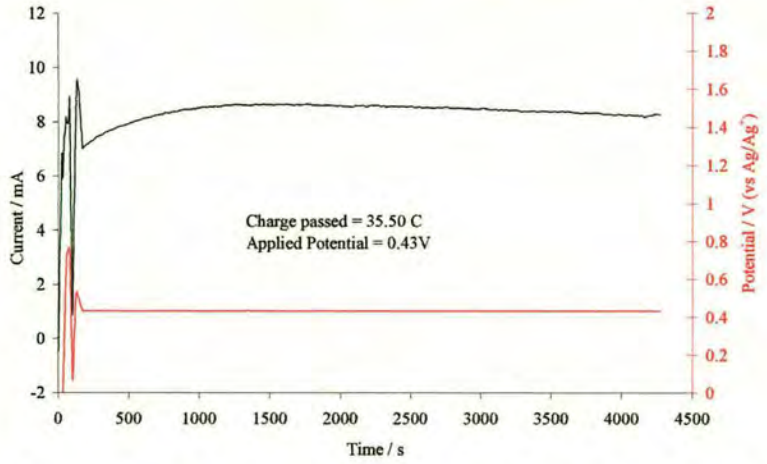

Figure 6.48: Plot of (——) Current and (——) Potential against time for a uranium electrode in [Pyr][N(Tf)$_2$], 423K.

Cyclic voltammograms of the resulting [Pyr][N(Tf)$_2$] melts after electrogeneration experiments using a uranium electrode were carried out are shown in figure 6.49.

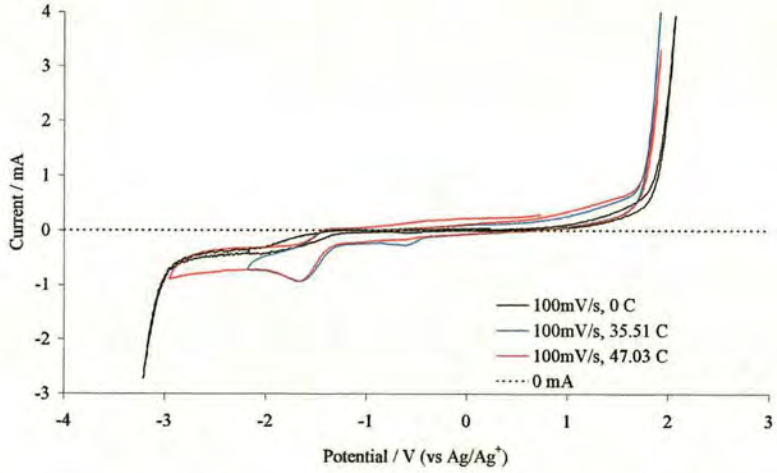

Figure 6.49: CVs of a [Pyr][N(Tf)$_2$] melt at a platinum electrode after (——) 35.51 C and (——) 47.03 C were passed through a uranium electrode. (——) is the pure melt. All scans started anodically from -1 V and performed at 423K.

As can be seen from figure 6.49, there are extra reduction peaks after electrogeneration experiments, however, these reduction peaks do not increase proportionally to the charge passed through the uranium electrode.

The electrogeneration of a soluble uranium species from a uranium electrode was also attempted in the ionic liquid [Emim][$N(Tf)_2$]. A plot of current and potential versus time for a typical electrogeneration experiment is shown in figure 6.50.

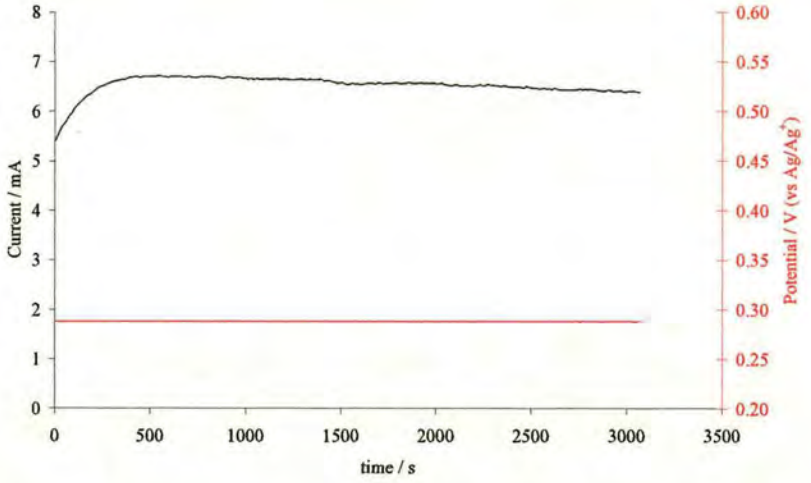

Figure 6.50: Plot of (——) Current and (——) Potential against time for a uranium electrode in [Emim][$N(Tf)_2$], 423K.

The cyclic voltammograms recorded after succesive electrogeneration experiments are shown in figure 6.51.

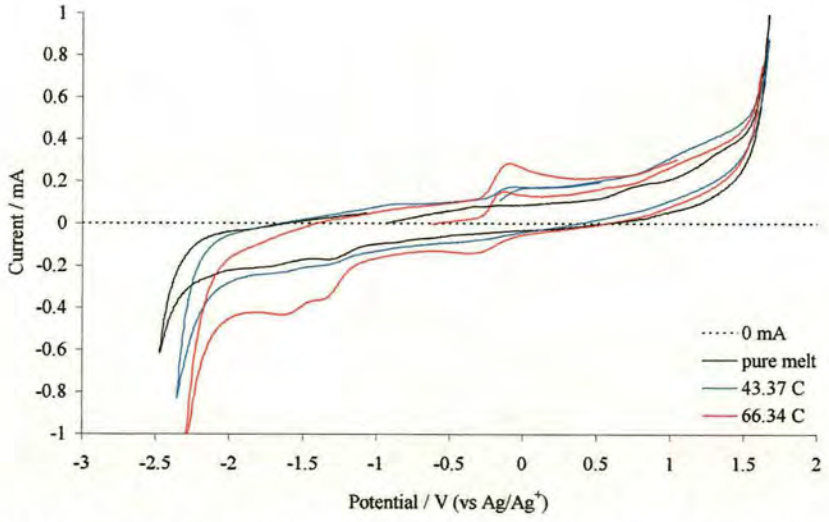

Figure 6.51: CVs of a [Emim][$N(Tf)_2$] melt at a platinum electrode after (——) 43.37 C and (——) 66.34 C were passed through a uranium electrode. (——) is the pure melt. All scans started anodically and performed at 423K.

The currents that were passed during the electrodissolution of uranium in [Phos][$N(Tf)_2$], figure 6.47, were similar to that observed for the electrodissolution of uranium in [Emim][Cl], figure 6.41. However, for the case of the [Phos][$N(Tf)_2$] melt, no electroactive species are observed after electrodissolution experiments, whereas in the chloride melt reduction peaks corresponding to an electrogenerated species are observed. Moreover, the reduction peaks observed in the chloride melt increase as the charge passed during the electrodissolution increases, this clearly does not occur in $[N(Tf)_2]^-$ melts. It is possible that a soluble uranium species is produced, but moisture within the melt could react with any solution uranium oproduced to give the insoluble UO_2. This could explain the dark cloudy appearance of the [Phos][$N(Tf)_2$] melt after electrodissolution experiments.

The analysis of the peaks produced in the $[N(Tf)_2]^-$ salts are hindered by the difficulty of producing solutions of U(IV) in $[N(Tf)_2]^-$ salts. It has been shown that uranium can be dissolved in the $[N(Tf)_2]^-$ ionic liquids by the addition of UCl_4 or $[UCl_6]^{2-}$ salts[39] to give soluble U(IV) solutions in the $[N(Tf)_2]^-$ salts. The soluble U(IV) species in these salts were still complexed by chloride in solution, this will clearly give different electrochemistry to than what would be observed for uranium species electrogenerated in $[N(Tf)_2]^-$ salts without chloride ions present.

Future work in this area would be to synthesise soluble uranium bis(trifluoromethanesulfonyl)imide salts and to compare the CVs containing these salts in a $[N(Tf)_2]^-$ melt with the CVs obtained after the electrogeneration of uranium in the $[N(Tf)_2]^-$ melts. Perhaps by adopting a similar strategy to that used by I.W. Sun and co-workers, where a mixture of [Emim][Cl]/[Emim][BF_4] was employed in which the chloride ions facilitated the dissolution of copper into the melt,[42] a mixture of $[N(Tf)_2]^-$ and chloride melts could be employed to investigate the posssible electrodissolution of uranium.

6.2 Electrochemical detection of impurities

6.2.1 Chloride ionic liquids

Electrochemistry is a very powerful tool for the determination of trace amounts of impurities, and impurities can in principle be detected at concentrations as low as pico-molar levels using conventional three electrode electrochemical cells. The CV's of [Emim][Cl] at a platinum electrode before and after recrystallisation from acetonitrile/ethyl acetate were recorded to determine if any impurities were electrochemically active within the electrochemical window of the solvent, figure 6.52.

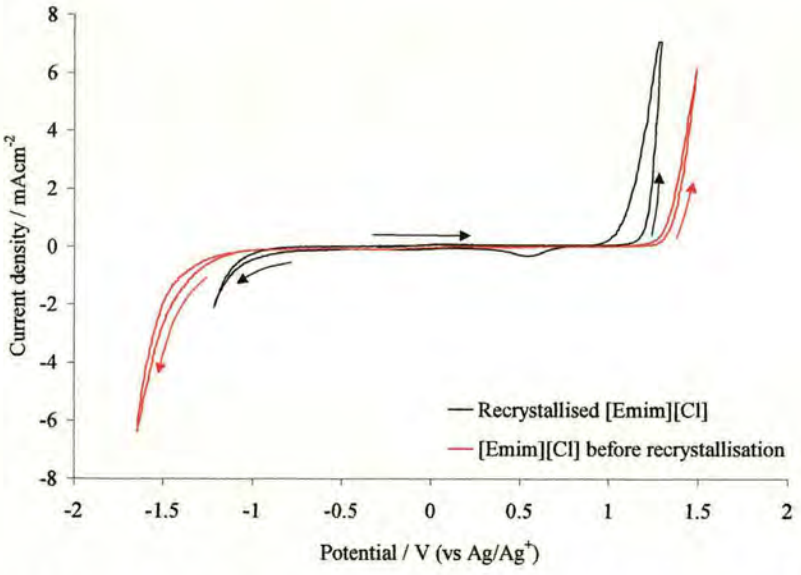

Figure 6.52: CV of [Emim][Cl] at a Pt electrode before (—) and after (—) recrystallisation, 50mV/s.

From figure 6.52 it can be seen that the electrochemical window of [Emim][Cl] is affected rather dramatically by the presence of impurities. The identity of the impurities is unknown but they are likely to be unreacted starting materials, or impurities in the starting materials carried over to the final ionic liquid

product. The electrochemical window of the [Emim][Cl] is smaller when it is recrystallised, this seems counterintuitive at first as you would expect any impurities to decrease the available electrochemical window. However, the effect that reactive impurities can have on the CV is that they can poison the surface of the electrode by forming a resistive layer. If such a resistive layer were formed on the platinum electrode surface, the voltage applied to the electrode would need to be larger than the voltage experienced at the electrode/solution interface to drive the solvent breakdown reaction, due to the resistive layer. This is shown schematically in figure 6.53.

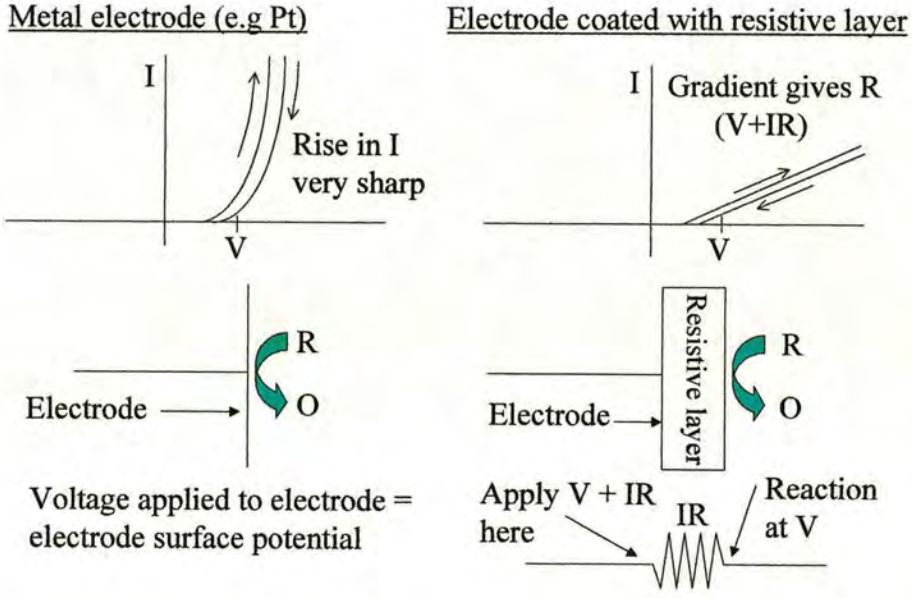

Figure 6.53: Effect of resistive film on electrode surface on CV's obtained.

If we examine figure 6.52 further, the gradients of the currents at either end of the solvent window are indeed lower for the non-crystallised [Emim][Cl] than those observed for the recrystallised [Emim][Cl]. This is good evidence of surface impurities on the platinum electrode resulting in a resistive film.

Another feature of the CV in figure 6.52 that suggests that a resistive film is present on the electrode surface is that after excursions into the solvent oxidation limit (chloride oxidation), no re-reduction of chlorine absorbed on the electrode surface is observed. This re-reduction of absorbed chlorine is clearly visible in the CV of recrystallised [Emim][Cl] in figure 6.52 and the reduction of adsorbed gases on Pt is diagnostic of a clean Pt surface. Therefore it is dangerous to look merely at the solvent window and the currents within the solvent window to assess the purity of the solvent.

The detection of water electrochemically in the ionic liquid, [Emim][Cl], is not possible. When water was added to [Emim][Cl], no extra redox peaks were observed, water therefore must not be redox active within the electrochemical window of the chloride ionic liquids.

6.2.2 Bis(trifluoromethanesulfonyl)imide ionic liquids

Even though the $[N(Tf)_2]^-$ ionic liquids are termed as 'hydrophobic' in that they form a two phase system when contacted with water, they still absorb water from the atmosphere when left in ambient conditions. Ionic liquids based on the hexafluorophosphate anion, PF_6^-, are also termed hydrophobic, but can absorb up to 12 wt.% water.[43] Concentrations of water as high as this will certainly be detectable by electrochemical methods if the redox behaviour of water lies within the potential window of the ionic liquid being studied. The $[Phos][N(Tf)_2]$ ionic liquid was chosen to test the electrochemical detection of water since it had the largest electrochemical window of the ionic liquids available. The CV of $[Phos][N(Tf)_2]$ recorded at a platinum electrode after drying on a Schlenk line and after the addition of water is shown in figure 6.54.

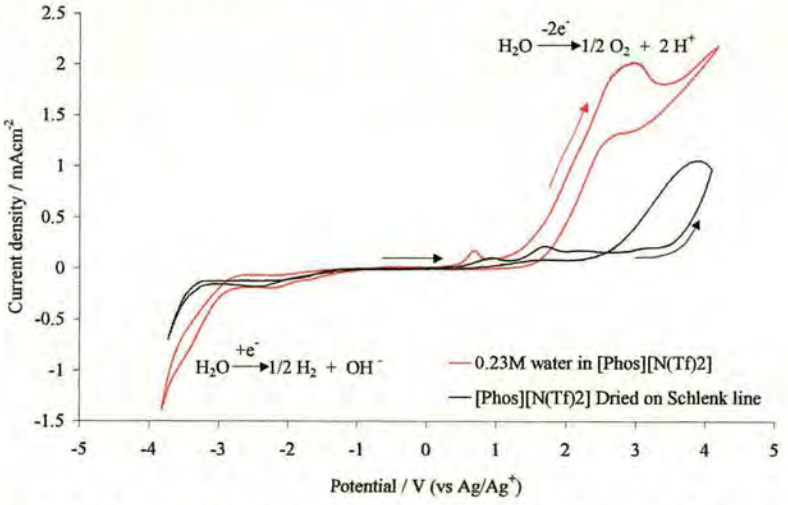

Figure 6.54: CV of $[Phos][N(Tf)_2]$ at a platinum electrode after drying on a Schlenk line (—) and with added water, 0.23M (—),50mV/s, 473K.

As can be seen from figure 6.54, the oxidation and reduction of water can be observed within the electrochemical window of the $[Phos][N(Tf)_2]$ melt and are annotated on the CV. The electrochemical window between the reduction and oxidation of water in the ionic liquid $[Phos][N(Tf)_2]$ is *ca.* 4.0V at a platinum electrode, this is in comparison to that observed in pure water with added electrolyte

which is *ca.* 1.3V.[20] This shows that water is stabilised towards reduction and oxidation in the ionic liquid due to coulombic interactions and hydrogen bonding between water and the cation and anion, this indicates that it will be hard to remove water from the system due to these strong interactions. Molecular sieves that were dried on a Schlenk line at 200°C (baked out) were added to the [Phos][$N(Tf)_2$] melt containing 0.23M H_2O, and CV's recorded at intervals to observe any change in the water oxidation peak height. The resulting CV's are shown in figure 6.55.

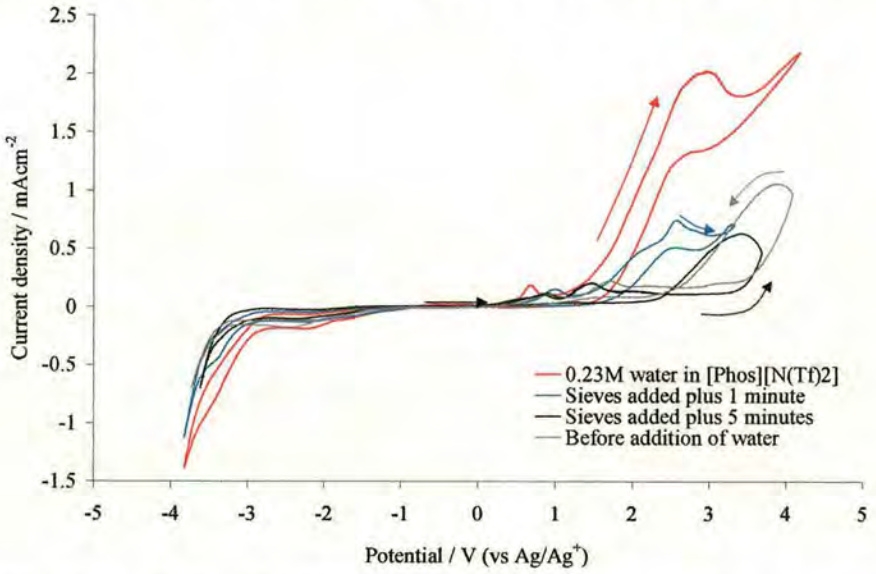

Figure 6.55: CV's of [Phos][$N(Tf)_2$] at a Pt electrode with 0.23M water (—), after addition of baked out molecular sieves plus 1 min. stirring (—), 5 min. stirring with sieves (—) and before water was added (—) for comparison.

From figure 6.55 we can see that the oxidation peak due to water diminishes with time, as does the reduction peak due to water, though this is harder to observe as it overlaps with the solvent reduction limit. After 5mins stirring with baked out molecular sieves, the oxidation and reduction peaks due to water have almost completely disappeared. The final CV is very similar to the starting CV when no water or sieves had been added. When molecular sieves are added to the $[N(Tf)_2]^-$ melts the solution turns cloudy, though this is observed when sieves are added to any solvent. No extra peaks are observed in the CVs when molecular sieves are present and the electrochemistry of the melt does not appear to be affected by the presence of molecular sieves at the temperatures and conditions used.

6.3 Conclusions

The electrochemistry of transition metal species and uranium species in ionic liquids has been performed in both the $[Cl]^-$ and $[N(Tf)_2]^-$ ionic liquids. Copper was observed to give reversible stripping and plating from [Emim][Cl], with the metal being deposited from Cu(I) in solution. The stripping/plating behaviour was shown to be almost 100% efficient from a plot of charge versus potential. Several pre-deposition waves were observed and analysis of the charge passed during these peaks showed that the charge passed was greater than that required for the underpotential deposition of a copper monolayer. The pre-deposition peaks were attributed to the deposition of copper on different sites on the platinum electrode surface. The Cu(I)/(II) redox couple was also observed from a solution of Cu(I) in [Emim][Cl], with the peak currents of the Cu(I) oxidation and Cu(II) reduction waves increasing linearly with the square root of the scan rate. The CVs were recorded without IR compensation and as such the peak separation for the Cu(I)/(II) redox couple were greater than expected for a reversible one-electron reaction at the temperatures studied. However, when the effects of the solution resistance were removed, the peak separation agreed with the theoretical value for a reversible one-electron redox reaction. When a solution of Cu(II) was prepared by the addition of $CuCl_2$ to a solution of [Emim][Cl], the stability of Cu(II) decreased as the temperature of the solution was increased, and as such it was not possible to analyse the electrochemistry of a bulk solution of Cu(II) in [Emim][Cl]. However when a CV of the bulk Cu(II) solution was compared to a CV from the bulk Cu(I) solution in [Emim][Cl], the scans obtained were very similar, with both showing the Cu(I)/(II) redox couple and the plating and stripping of copper from the platinum electrode, indicating the reaction of Cu(II) with the ionic liquid produces Cu(I).

A solution of Fe(II) in [Emim][Cl] prepared by the addition of $FeCl_2$ to [Emim][Cl] was observed to give the redox couple Fe(II)/Fe(III) on scanning positive from zero current, and when the potential was scanned negative from zero current the redox couple Fe(II)/Fe was observed although the deposition/stripping kinetics were

slow. Increasing the temperature had a positive effect on the deposition/stripping redox couple with the peak heights increasing significantly and the rate at which the current rises with potential increasing. As with Cu(I) in [Emim][Cl], the CVs were recorded without *iR* compensation and as such the peak separation for the Fe(II)/(III) redox couple were greater than expected for a reversible one-electron reaction at the temperatures studied. However, when the effects of the solution resistance were removed, the peak separation agreed with the theoretical value expected at the temperatures studied. When a solution of Fe(III) was prepared by the addition of $FeCl_3$ to a solution of [Emim][Cl], the stability of Fe(III) decreased as the temperature of the solution was increased due to reaction with the solvent, and as such it was not possible to analyse the electrochemistry of a bulk solution of Fe(III) in [Emim][Cl]. However when a CV of the bulk Fe(III) solution was compared to a CV from the bulk Fe(II) solution in [Emim][Cl], the scans obtained were very similar, with both showing the Fe(II)/(III) redox couple and the plating and stripping of iron from the platinum electrode, indicating that Fe(III) had reacted to form Fe(II).

Solutions of Zr(IV) in [Emim][Cl] prepared by the addition of $ZrCl_4$ to [Emim][Cl] displayed two overlapping reduction peaks at potentials negative of 0V and an oxidation peak positive of 0V. The reduction peaks were controlled by kinetics due to very broad nature of the peaks and the absence of diffusion limited peaks. Varying the scan rate resulted in an increase in the reduction currents, though the increase in peak size did not correspond to a linear increase in peak current with the square root of the scan rate. This is further evidence of irreversible electrode kinetics. The oxidation peak had the appearance of a stripping wave, although the current does not drop sharply to zero current after the diffusion limited peak. The oxidation peak also displayed a linear increase in peak current with the square root of the scan rate indicating diffusion from bulk solution was controlling the oxidation process. In combination, this suggests that the oxidation may the be the stripping of deposited zirconium, and the thermodynamics for stripping of the zirconium depends on the site on the electrode surface at which the zirconium was deposited.

A solution of U(IV) in [Emim][Cl] was prepared by dissolving UCl_4 in [Emim][Cl]. CVs of the resulting solution showed that the electrochemistry was complex. The CVs appear to be complicated by multiple redox active species with potentials that are overlapping, resulting in CVs that have no well-resolved peaks. Trace amounts of water[39] have been suggested as a cause for irreversible electrochemical reactions ionic liquids, with this in mind the electrochemistry of U(IV) in [Emim][Cl] was investigated with dried molecular sieves present in the ionic liquid when the electrochemistry was performed. Reversible electrochemistry was still not obtained under these conditions. When electrochemical experiments were performed with [Emim][Cl] dried with molecular sieves, then transferred to a sealed cell with UCl_4 and further dried on a Schlenk line, all the UCl_4 did not dissolve. The CV obtained under these conditions was still complex, though the oxidation wave near the solvent oxidation limit disappeared and distinguished redox peaks were observed near the reduction limit of the solvent. This would suggest the presence of water is not the issue with the reversibility of U(IV) reduction in [Emim][Cl]. Bis (tetramethylammonium) hexachlorouranate, $[TMA]_2[UCl_6]$, was used as a source of U(IV) in [Emim][Cl] to increase the solubility of the uranium species. The CVs obtained from these solutions again resulted in complex electrochemistry, with multiple redox peaks. The CVs of U(IV) performed under different conditions all had in common the reduction wave that started at roughly 0V and the oxidation wave that started at 0V, suggesting UCl_4 dissolves in [Emim][Cl] to give $[UCl_6]^{2-}$ and these peaks may correspond to $[UCl_6]^{2-}/[UCl_6]^{3-}$.

The electrochemistry of a uranium electrode in both chloride and $[N(Tf)_2]^-$ ionic liquids was studied. In the chloride ionic liquids, the uranium electrode undergoes a change on scanning to oxidising potentials, this was evidenced by the presence of a 'nucleation-loop' on reversing the potential scan and this has been attributed to the chloride ions in the ionic liquid disrupting the structure of the oxide surface. By the addition of KF, this effect was increased and a larger nucleation loop and enhanced oxidation currents were observed, indicating a greater degree of disruption of the barrier oxide layer. The oxidative electrochemistry of a uranium electrode in the $[N(Tf)_2]^-$ ionic liquids displayed a linear rise in current with potential

which is indicative of transpassive dissolution of uranium through a resistive layer on the surface of the electrode, and also a large capacitive envelope was observed in the region where no oxidative dissolution current was passed. The addition of a fluoride source to the $[N(Tf)_2]^-$ ionic liquids resulted in the observation of a nucleation loop when the uranium electrode was scanned to oxidising potentials and the oxidation currents were enhanced and the barrier resistance decreased indicating a change in the nature of the electrode surface oxide. This was attributed to the fluoride ions disrupting the barrier oxide layer, as was observed for the chloride ions in the ionic liquid [Emim][Cl] and to a greater extent for fluoride ions in the same ionic liquid. This is consistent with the resistive nature of the electrode being decreased, in addition to this effect, the capacitive envelope of the CVs were also smaller after the addition of a fluoride source, further evidence of the decrease in the resistive properties of the electrode.

The electrodissolution of uranium into [Emim][Cl], $[Emim][N(Tf)_2]$, $[Pyr][N(Tf)_2]$ and $[Phos][N(Tf)_2]$ was attempted by means of constant potential electrolysis. Of the ionic liquids tested, only electrogeneration of uranium in [Emim][Cl] resulted in the production of a soluble electrochemically active product which could be attributed to redox peaks observed in the CVs of soluble U(IV) compounds in [Emim][Cl]. The electrochemistry observed in the resulting electrogenerated solution was complex, though the redox peaks centred near 0V were consistent with those observed through the addition of UCl_4 and $[UCl_6]^{2-}$ to [Emim][Cl]. This could suggest the production of $[UCl_6]^{2-}$ as was postulated for the CVs resulting from the addition of UCl_4 and $[UCl_6]^{2-}$ to [Emim][Cl]. However, due to the complexity of the CVs resulting from the electrogeneration of uranium in [Emim][Cl], the electrogeneration appears to result in the production of more than a single soluble uranium redox species.

The electrochemical detection of impurities in ionic liquids was investigated. A CV of [Emim][Cl] received from QUILL[†] at Queens University of Belfast and a CV of the same [Emim][Cl] after two recrystallisations from acetonitrile/ethyl acetate were compared. It was observed that the purified ionic liquid displayed a smaller electrochemical window. This seems counterintuitive, and was explained by the presence of impurities forming a resistive film on the electrode surface thereby reducing the catalytic activity of Pt for the ionic liquid redox reaction. This was evidenced by the currents at the solvent limits of the impure [Emim][Cl] rising at a slower rate with potential as compared to the purified [Emim][Cl], and the observation of re-reduction of adsorbed chlorine gas on the Pt electrode after excursion into the ionic liquid oxidation limit. Addition of water to the ionic liquid [Emim][Cl] did not result in the appearance of any redox peaks within the electrochemical window of the ionic liquid, as such, electrochemical detection of water in the chloride ionic liquids was not deemed possible. However, in [Phos][$N(Tf)_2$], addition of water resulted in the presence of distinct oxidation and reduction peaks within the electrochemical window of the ionic liquid due to the oxidation and reduction of water at a Pt electrode. The potential window of water at a Pt electrode in the ionic liquid was greater than that observed in water with added electrolyte by around 2.3V, this highlights the increased electrochemical stability of water in the $[N(Tf)_2]^-$ ionic liquid. The effect would be expected to be greater in the chloride ionic liquid due to the increased coulombic and hydrogen bonding interaction between water and this melt, it is therefore unsurprising that neither the oxidation or reduction of water were detected electrochemically in this melt. After adding dried molecular sieves to the wet ionic liquid and subsequently observing the CVs obtained over time, the CVs showed a return to the "dry" ionic liquid CV, indicating that water could be removed from [Phos][$N(Tf)_2$] by the use of molecular sieves.

[†] Queens University Ionic Liquids Laboratories.

[1] T.J. Melton, J. Joyce, J.T. Maloy, J.A. Boon and J.S. Wilkes, *J. Electrochem. Soc.*, 1998, **137**, 3865-3869.

[2] F.H. Hurley and T.P. Wier, Jr. *J. Electrochem. Soc.*, 1951, **98**, 203-206.

[3] T.M. Laher and C.L. Hussey, *Inorg. Chem.*, 1983, **22** (9), 1279-1283.

[4] X.H. Xu and C.L. Hussey, *J. Electrochem. Soc.*, 1992, **139** (5), 1295-1300.

[5] F. Endres and W. Freyland, *J. Phys. Chem. B.*, 1998, **102**, 10229-10233.

[6] C.A. Zell, F. Endres and W. Freyland, *Phys. Chem. Chem. Phys.*, 1999, **1**, 697-704.

[7] Q. Zhu, C.L. Hussey and G.R. Stafford, *J. Electrochem. Soc.*, 2001,**148** (2), C88-C94.

[8] Y. Katayama, S. Dan, T. Miura and T. Kishi, *J. Electrochem. Soc.*, 2001, **148**(2), C102-C105.

[9] D.R. MacFarlane, P. Meakin, J. Sun, N. Amini and M. Forsyth, *J. Phys. Chem. B.*, 1999, **103**(20), 4164-4170

[10] P.A.Z. Suarez, C.S. Consorti, R.F. de Souza, J. Dupont and R.S. Gonçalves, *J. Braz. Chem. Soc.*, 2002, **13**, 106-109.

[11] T.M. Laher and C.L. Hussey, *Inorg. Chem.*, 1983, **22**, 3247-3251.

[12] J.J. Lee, B. Miller, X. Shi, R. Kalish and K.A. Wheeler, *J. Electrochem. Soc.*, 2001, **148**(3), C183-C190.

[13] C.L. Hussey, L.A. King and R.A. Carpio, *J. Electrochem. Soc.*, 1979, **126**(6), 1029-1034.

[14] F. Endres and A. Schweizer, *Phys. Chem. Chem. Phys.*, 2000, **2**, 5455-5462.

[15] P.Y. Chen and I.W. Sun, *Electrochimica Acta*, 1999, **45**, 441-450.

[16] K. Murase, K. Nitta, T. Hirato and Y. Awakura, J. Appl. Electrochem., 2001, **31** (10), 1089

[17] M. Elleb, J. Meullemeestre, M.-J. Schwing-Weill and F. Vierling, *Inorg. Chem.*, 1982, **21**, 1477.

[18] J.J. Lee, B. Miller, X. Shi, R. Kalish and K.A. Wheeler, *J. Electrochem. Soc.*, 2000, **147**(9), 3370-3376.

[19] K.R. Seddon, A. Stark and M. J. Torres, *Pure and Applied Chemistry.*, 2000, **72**(12), 2275-2287.

[20] A.J. Bard and L.R. Faulkner, *Electrochemical Methods, Fundamentals and Applications,* J. Wiley & sons.

[21] A.C. Fisher, 1996, *Electrode Dynamics*, Oxford Chemistry Primer, **34**, Oxford University Press.

[22] T.M. Laher and C.L. Hussey, *Inorg. Chem.*, 1982, **21**, 4079-4083.

[23] Z.J. Karpanski, C. Nanjundiah and R.A. Osteryoung, *Inorg. Chem.*, 1984, **23**, 3358-3364.

[24] C.Nanjundiah, K. Shimizu and R.A. Osteryoung, *J. Electrochem. Soc.*, 1982, **129**(11), 2474-2480.

[25] I-W. Sun, J.R. Sanders and C.L. Hussey, *J. Electrochem. Soc.*, 1989, **136**(5), 1415-1419.

[26] M. Lipsztajn and R.A. Osteryoung, *Inorg. Chem.*, 1985, **24**, 716-719.

[27] M.S. Sitze, E.R. Schreiter, E.V. Patterson and R.G. Freeman, *Inorg. Chem.*, 2001, **40**, 2298-2304.

[28] The Encyclopedia of Electrochemistry, C.A. Hampel (Ed.), 1972, Robert E. Kreiger Publishing Company, Huntington, N.Y., p 1188.

[29] X. Yang, L. Dai, Y. Shan and M. He, *Cuihua. Xuebao.*, 2003, **24**, 895-899.

[30] **(a)** Y. Tian and T. Hughbanks, *Inorg. Chem.*, 1995, **34**, 6250-6254. **(b)** S. Dong, T. Hughbanks, *Inorg. Chem.*, 2000, **39**, 1964-1968.

[31] D. Sun and T. Hughbanks, *Inorg. Chem.*, 1999, **38**, 992-997.

[32] R. De Waele, L. Heerman and W. D'Olieslager, *J. Electroanal. Chem.*, 1982, **142**, 137-146.

[33] R. De Waele, L. Heerman and W. D'Olieslager, *J. of Less-Common Metals*, 1986,122, 319-327.

[34] L. Heerman, R. De Waele and W. D'Olieslager, *J. Electroanal. Chem.*, 1985, **193**, 289-294.

[35] C.J. Anderson, M.R. Deakin, G.R. Choppin, W. D'Olieslager, L. Heerman and D.J. Pruett, *Inorg. Chem.*, 1991, **30**, 4013-4016.

[36] P.B. Hitchcock, T.J. Mohammed, K.R. Seddon and J.A. Zora, *Inorg. Chim. Acta*, 1986, **113**, L25-L26.

[37] C.J. Anderson, G.R. Choppin, D.J. Pruett, D. Costa and W Smith, *Radiochim. Acta.*, 1999, **84**, 31-36.

[38] W.J. Oldham Jr., S.M. Oldham, B.L. Scott, K.D. Abney, W.H. Smith and D.A. Costa, *Chem. Commun.*, 2001, **15**, 1348-1349.

[39] K. Abney, E. Bluhm, E. Garcia, W. Smith, M. Barr, W. Oldham, D. Costa, D. Morris and D. Tait, FY00 Yearly report, 10/06/00, LA-UR-00-5043. http://lib-www.lanl.gov/la-pubs/00393792.pdf

[40] J. Huang, H.-J. Schanz, E. D. Stevens and S. P. Nolan, *Organometallics*, 1999, **18**, 2370; T. Weskamp, F. J. Kohl, W. Hieringer, D. Gleich and W. A. Herrmann, *Angew. Chem., Int. Ed.*, 1999, **38**, 2416.

[41] S. Dai, L.M. Toth, G.R. Hayes, and J.R. Peterson, *Inorg. Chim. Acta.,* 1997, **256,** 143-145.

[42] P.-Y. Chen, I.-W. Sun, *Electrochim. Acta.*, 1999, **45**, 441-450.

[43] U. Schröder, J.D. Wadhawan, R.G. Compton, F. Marken, P.A.Z. Suarez, C.S. Consorti, R.F. de Souza and J. Dupont, *New J. Chem.*, 2000, **12**, 1009-1015.

7 Diffusion Coefficients

The measurement of diffusion coefficients of solute species in ionic liquids allows us to gain insights into the fundamentals of mass transport of redox active species in ionic liquids. When ionic species are dissolved in aqueous media and subjected to an applied electric field, it is easy for us to conceptualise the drift of ions as the movement of solvated ions separated in a sea of neutral water molecules. Models have already been proposed for the transport of species in high temperature molten salts and this is referred to as the 'hole' model[1]. In the hole model, ions move through the fused salt by the generation of a hole in the molten structure. An important question arises - do aqueous transport properties hold in ionic liquids, which not only themselves are charged but have significant coulombic interactions between the anion and cation, and also display significant hydrogen bonding interactions. In order to determine the feasibility of nuclear fuel reprocessing in ionic liquids it is necessary to determine the transport properties of radiological ions in these novel solvents. The present study examines the transport of simple, well defined systems such as silver cations in [Emim][Cl] before progressing onto the more complex systems such as U(IV) and Zr(IV) in [Emim][Cl].

7.1 Diffusion Coefficients in Ionic Liquids

Diffusion coefficients have thus far not been reported for solute species in the chloride based ionic liquids. Due to their relatively high viscosity, the mass transport of solute species may be too low for an electrotransport process to be economically feasible in a chloride ionic liquid. Early studies to determine the diffusion coefficient of U(IV) in [Hmim][Cl] by RDE suggested the diffusion coefficient was in the region of 10^{-10} cm^2s^{-1}. This value for a diffusion coefficient is prohibitively low for the design of an economically viable electrorefiner with a high enough throughput of spent fuel from the nuclear industry.[2] In order for ionic liquids to be a viable replacement for high temperature molten salts in the electrorefining step in the nuclear fuel cycle, the diffusion coefficients must approach those obtained in high

temperature molten salts, but at a much lower temperature. The maximum practical temperature at which the diffusion coefficients in ionic liquids must approach those in molten salts has been highlighted by BNFL as 473K. This is because the technology required for heating processes above 473K is more expensive and technically demanding so the possibility of performing an industrial process below 473K is both financially and practically viable. Furthermore, molten salts are highly corrosive materials, and the use of ionic liquids, which are more benign, would allow the use of cheaper materials in the manufacture of electrorefiner cells.

The diffusion coefficient of a solute species is defined as the rate at which a diffusing substance is transported between opposite faces of a unit cube of a system when there is unit concentration difference between them. For the translational diffusion of solutes, diffusion is described by Fick's First Law, equation (1),

$$J_i(x,t) = -D_i(\partial C_i(x,t)/\partial x) \tag{1}$$

Where J_i is the flux of species i of concentration C_i in direction x, and dC_i/dx is the concentration gradient. D_i is the diffusion coefficient (proportionality factor between flux and concentration gradient) of species i and has unit of cm^2s^{-1}. The minus sign ensures the species is moving from concentrated to dilute solution. Fick's second law describes the change of concentration at the centre of a volume element bounded by two planes parallel to the surface with time, equation (2).

$$\partial C_i(x,t)/\partial t = D_i(\partial^2 C_i(x,t)/\partial^2 x^2) \tag{2}$$

Self-diffusion in ionic liquids is governed by the Arrhenius equation, eqn (3).

$$D = D_o \exp(-E_d/RT) \tag{3}$$

Where D_o is the pre-exponential factor for self-diffusion (m^2s^{-1}), E_d the activation energy for self-diffusion ($Jmol^{-1}$), R the gas constant (8.31 $Jmol^{-1}K^{-1}$) and T the absolute temperature (K). Equation (3) can be rewritten as equation (4).

$$\ln D = \ln D_o - E_d / RT \quad (4)$$

The activation energy for self-diffusion of solutes in ionic liquids and D_o can be estimated from a plot of ln$D$ vs $1/T$. Once the values of D_o and E_d/R are known, an estimate of the diffusion coefficient of the solute species at 473K can be obtained.

As a result of the many electrochemical studies of transition metal complexes in ionic liquids, a large volume of data has been collected on the transport properties, namely diffusion coefficients and Stoke-Einstein products[3] of solutes in ionic liquids. As with most areas studied in the field of ionic liquid research, the vast majority of literature is from the haloaluminate ionic liquids. Diffusion coefficients for selected solute species in high temperature molten salts and ionic liquids are presented in table 7.1.

Several methods have been employed in the collection of diffusion coefficient data. The most commonly used method to probe diffusion coefficients in ionic liquids has been to use a Rotating Disc Electrode (RDE) to impose a known hydrodynamic flow of electrolyte. Other techniques used have been chronoamperometry, linear sweep voltammetry and chronopotentiometry. In this study, the technique used for the determination of the diffusion coefficient of solute species was chronoamperometry. Convection due to thermal gradients needed to be avoided, to minimise this before each measurement was taken the cell was kept at the temperature to be measured for a half hour prior to each potential step experiment. During chronoamperometric experiments, the build up of redox products at the electrode can lead to density gradients[4] which lead to convection, in order to minimise this, the current transients were generally sampled for only 10-15s.

Species	System (mole%)	T / K	Method	D_o / cm^2s^{-1}
U(III)	LiCl/KCl[5]	673	CP	5.6×10^{-6}
U(IV)	LiCl/KCl[5]	673	CP	7.3×10^{-6}
V(V)	$K_2SO_4/K_2S_2O_7$[6]	698	CA	1.5×10^{-6}
Hg(I)	$NaNO_3/KNO_3$[7]	523	RDE	1.4×10^{-6}
U(IV)	Acidic $AlCl_3$/NaCl[8]	448	DPP	2.98×10^{-6}
U(IV)	(66.7:33.3) $AlCl_3$/[BuPy][Cl][20]	308	RDE	3.65×10^{-7}
U(IV)	(66.7:33.3) $AlCl_3$/[Emim][Cl][21]	318	RDE	6.87×10^{-6}
U(III)	(44.8:55.2) $AlCl_3$/[Emim][Cl][23]	301	CA	1.61×10^{-7}
U(IV)	(44.8:55.2) $AlCl_3$/[Emim][Cl][23]	301	CA	1.85×10^{-7}
Yb(III)	(44.4:55.6) $AlCl_3$/[Emim][Cl][9]	300	RDE CA	1.99×10^{-7}
Fe(III)	(42.8:57.2) $AlCl_3$/[Emim][Cl][10]	313	RDE	2.29×10^{-7}
Fe(II)	(42.8:57.2) $AlCl_3$/[Emim][Cl][10]	313	RDE	1.36×10^{-7}
Pb(II)	(66.7:33.3) $AlCl_3$/[Emim][Cl][11]	313	CA	9.00×10^{-7}
Os(III)	(44.4:55.6) $AlCl_3$/[Emim][Cl][12]	313	CA	2.32×10^{-7}
Eu(III)	(44.4:55.6) $AlCl_3$/[Emim][Cl][13]	313	RDE CA LSV	2.03×10^{-7}
Cu(I)	(47.4:52.6) $AlCl_3$/[Emim][Cl][14]	308	CA	7.1×10^{-7}
Cu(I)	(60:40) $AlCl_3$/[Emim][Cl][15]	313	CA	3.6×10^{-7}
Cu(II)	[Emim][BF_4]/[Emim][Cl][16]	303	RDE	1.5×10^{-7}
Cu(I)	[Emim][BF_4]/[Emim][Cl][16]	303	RDE	2.3×10^{-7}
Cd(II)	[Emim][BF_4]/[Emim][Cl][17]	303	RDE	2.4×10^{-7}
Ag(I)	(55:45) $AlCl_3$/[Emim][Cl][18]	298	CA	1.50×10^{-6}
Ag(I)	(66.7:33.3) $AlCl_3$/[Emim][Cl][19]	313	RDE	1.2×10^{-6}

Table 7.1: Diffusion coefficients for selected solute species in ionic liquids and high temperature molten salts. CP = Chronopotentiometry, RDE = Rotating Disc Electrode, CA = Chronoamperometry, LSV = Linear Sweep Voltammetry, DPP = Differential Pulse Polarography.

Presented in this section is the study of the diffusion coefficients of a number of solute species in chloride and bis(trifluoromethanesulfonyl)imide, $[N(Tf)_2]^-$ based ionic liquids. The diffusion coefficient of the solute species has been measured over a range of temperatures and a plot of ln$D$ vs $1/T$ used to calculate E_d and estimate the diffusion coefficient of the solute at 473K.

7.1.1 Diffusion coefficients in [Emim][Cl]

Whilst most diffusion coefficients of solute species in ionic liquids have been collected in Lewis basic haloaluminate based ionic liquids[3], it remains to be seen if solutes in the pure chloride ionic liquids posses similar transport properties. The ionic liquid 1-ethyl-3-methylimidazolium chloride, [Emim][Cl], has been employed to investigate the diffusion coefficients of transition metal solutes at varying temperatures.

7.1.1.1 Silver in [Emim][Cl]

The potential of the working electrode was stepped to a potential that was 100mV negative of the Ag(I)/Ag peak potential in figure 6.4 (section 6.1.1.2). The current time transients were collected at a number of temperatures and analysed using the integrated Cottrell equation. A typical current time transient is shown in figure 7.1

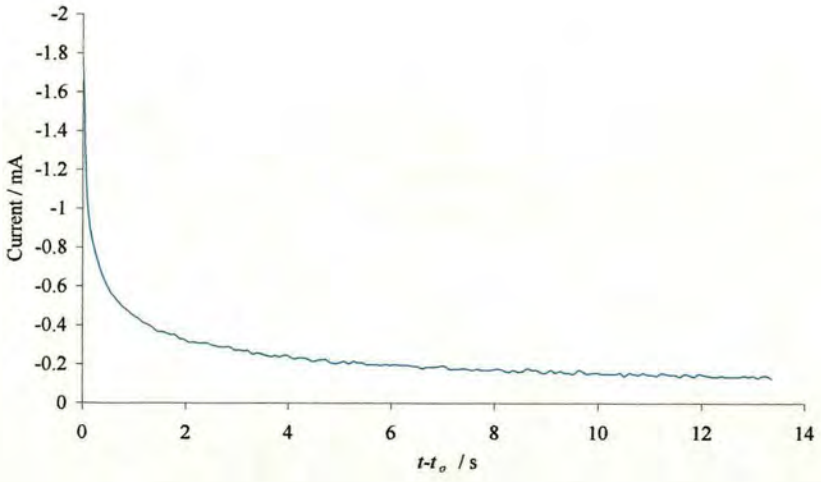

Figure 7.1 Current/time transient for 0.01M AgCl in [Emim][Cl] at a silver electrode (area = 1.38cm^2), 366K, -0.10V.

As can be seen from figure 7.1 the current decays with time, indicating that the electrode reaction is under diffusion control. By performing integrated Cottrell analysis on this current / time transient, a plot of Q vs $(t\text{-}t_o)^{1/2}$ should give a straight line which can be used to calculate the diffusion coefficient of the Ag(I) solute, figure 7.2

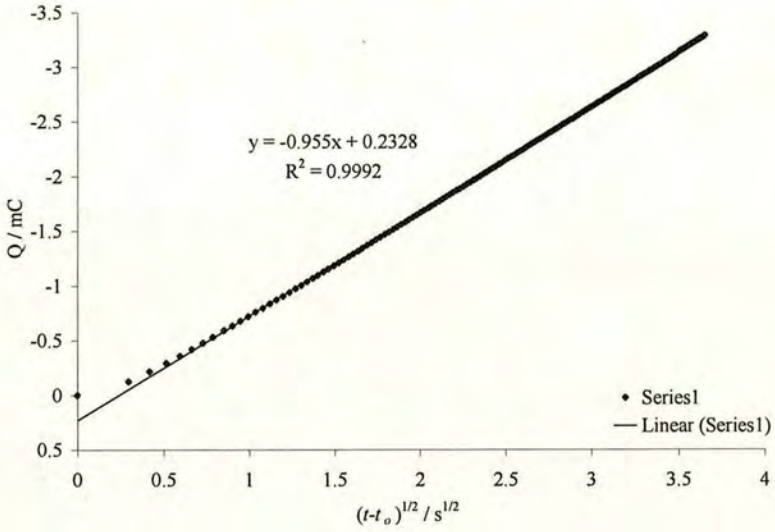

Figure 7.2 Integrated Cottrell analysis of Ag(I) reduction current time transient.

From figure 7.2 we can see that the plot of Q vs $(t\text{-}t_o)^{1/2}$ is linear, indicating that Cottrell behaviour is obeyed (see section 2.4, equation (5)). The diffusion coefficient calculated from the gradient of figure 7.2 is 2.5×10^{-7} cm^2s^{-1} at 366K.

Values of D were collected at increasing temperatures and a plot of $\ln D$ vs $1/T$ was plotted, figure 7.3.

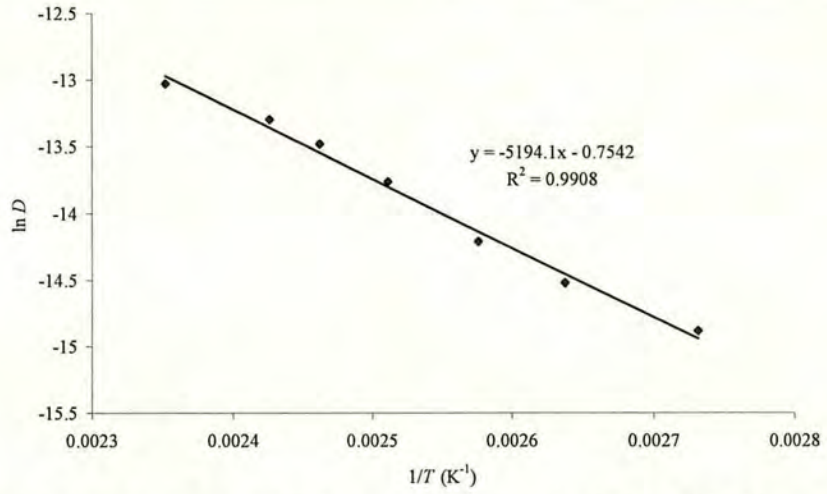

Figure 7.3: Plot of ln$D$ vs $1/T$ for Ag(I) in [Emim][Cl] with linear regression equation.

It can be seen from figure 7.3 that the plot ln$D$ vs $1/T$ is linear as would be expected from equation (4). A least squares fit of the data in figure 7.3 gives equation (5)

$$\ln D = -0.7542 - 5194.1(1/T) \qquad (5)$$

Using equation (5), the diffusion coefficient of Ag(I) in [Emim][Cl] at 473K is predicted as being 8.0 +/- 0.7 x 10^{-6}cm^{2}s^{-1} assuming the Arrhenius equation holds at these temperatures (the diffusion coefficients were not measured at 473K due to the limitations of the apparatus being used). The activation energy for the self diffusion of Ag(I) in [Emim][Cl] is calculated as being 43.2 +/- 1.9 kJmol^{-1}, and D_o as 0.470 +/- 0.035 cm^{2}s^{-1}. This value of diffusion coefficient is lower than those observed in the Lewis acidic $AlCl_3$/[Emim][Cl] melts presented in table 7.1, although it is of the same order of magnitude. The possible reasons for the lower value obtained in the [Emim][Cl] melt are the larger radius of the diffusing Ag(I) species in the chloride melt due to coordination by chloride ions. Also the chloride complex would be expected to have greater interactions with the melt through hydrogen bonding interactions with the solvent. The extent of the hydrogen bonding between $[AgCl_2]^-$ and the imidazolium cation in the crystal structure of [Emim][$AgCl_2$] has already been highlighted in section 5.1.2.

7.1.1.2 Diffusion coefficient of copper in [Emim][Cl]

Copper was introduced to the [Emim][Cl] melt as CuCl to give a solution of Cu(I) (0.025M). From cyclic voltammetry the peak potential for Cu(I)/(II) oxidation was observed as 0.78V (see section 6.1.2.2). The potential of the cell was stepped to ~100mV more positive than this potential value, to a potential where the electrochemistry is in the diffusion controlled regime and the surface concentration of Cu(I) can be assumed to be zero. A typical current time transient resulting from the potential step is shown in figure 7.4.

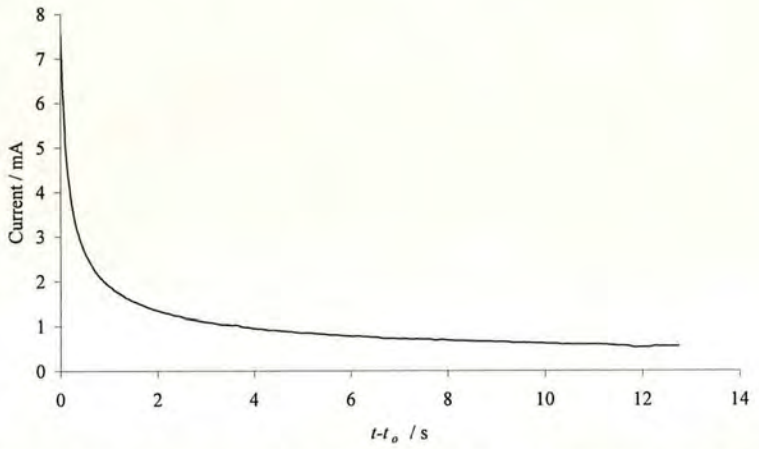

Figure 7.4: Current/time transient for potential step experiment with Cu(I), 0.025M, in [Emim][Cl] at a Pt electrode, 380K.

As can be seen from figure 7.4, the current decays with time in a manner that is consistent with Cottrell behaviour. In order to confirm this, a plot of charge versus $(t\text{-}t_o)^{1/2}$ is shown in figure 7.5.

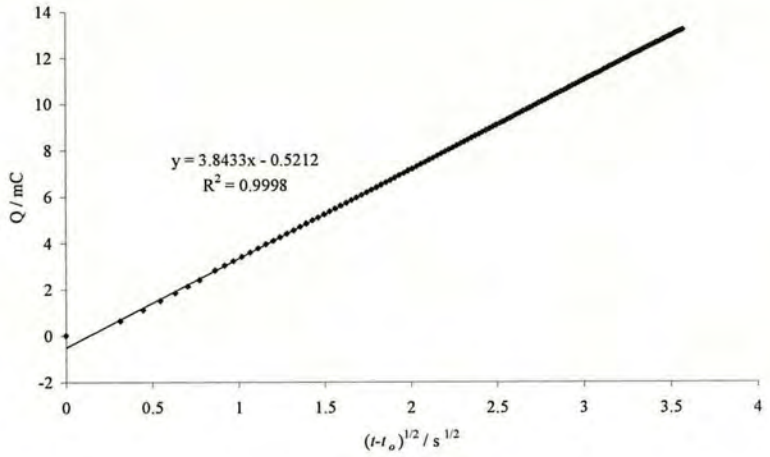

Figure 7.5: Integrated Cottrell analysis of Cu(I) (0.025M) oxidation current-time transient at a Pt electrode.

As can be seen from figure 7.5, the plot of charge vs $(t-t_o)^{1/2}$ is linear, indicating that Cottrell behaviour is observed, and that Cu(I) oxidation is proceeding under diffusion control. By collecting current/time transients at increasing temperatures, data was collected to produce a plot of ln$D$ vs $1/T$ for Cu(I) oxidation, figure 7.6.

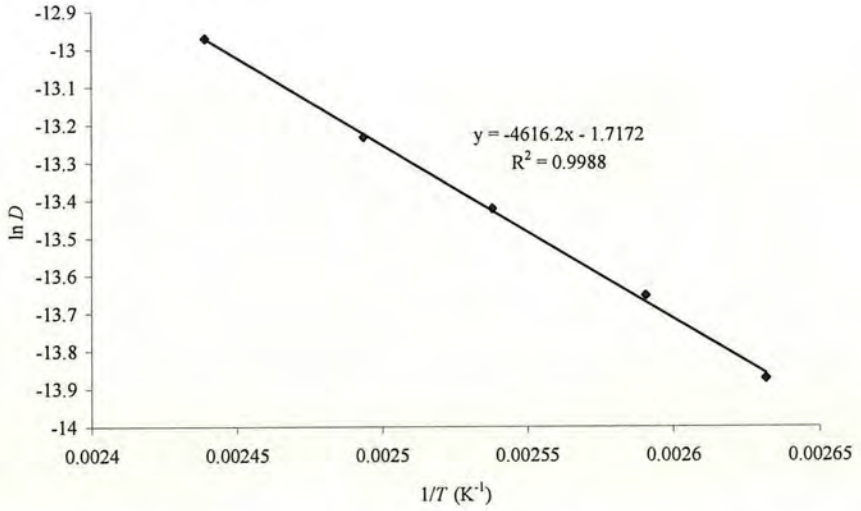

Figure 7.6: Plot of ln$D$ vs $1/T$ for Cu(I) (0.025M) in [Emim][Cl] at a Pt electrode.

As can be seen from figure 7.6, the slope of ln$D$ vs $1/T$ is linear. A least squares fit of the data in figure 7.6 gives equation (6)

$$\ln D = -1.7172 - 4616.2(1/T) \qquad (6)$$

Using equation (6), we can predict that the diffusion coefficient of Cu(I) in [Emim][Cl] will be 1.0 +/- 0.1 x 10^{-5} cm^2s^{-1} at 473K. From the gradient of the Arrhenius plot the activation energy for self diffusion of Cu(I) in [Emim][Cl] is 38.4 +/- 0.8 $kJmol^{-1}$ and from the intercept, D_o is 0.180 +/- 0.023 cm^2s^{-1}.

Attempts to obtain a linear plot of ln$D$ vs $1/T$ for Cu(II) from a solution of Cu(II) (0.049M) in [Emim][Cl] by stepping the potential to 0.57V, where the surface concentration of Cu(II) can be assumed to be zero, proved to be unsuccessful. Potential step experiments gave Cottrell behaviour, with linear responses for plots of charge passed against $(t\text{-}t_o)^{1/2}$ as can be seen in figure 7.7.

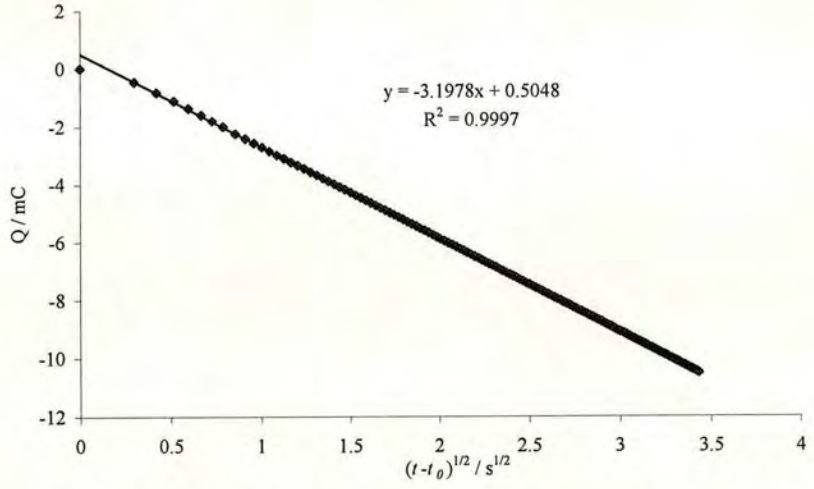

Figure 7.7: Plot of charge passed vs $(t\text{-}t_o)^{1/2}$ from a current-time transient of Cu(II) (0.049M) in [Emim][Cl].

A plot of ln$D$ vs $1/T$ for Cu(II) in [Emim][Cl] is shown in figure 7.8.

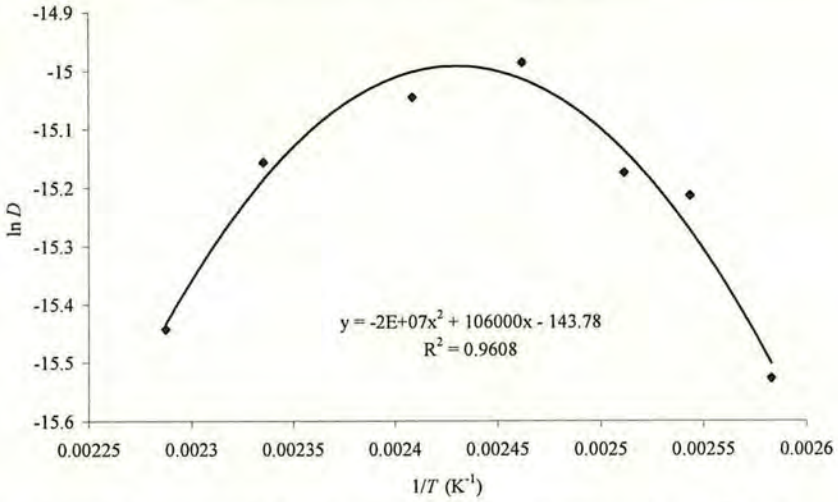

Figure 7.8: Plot of ln$D$ vs $1/T$ for Cu(II) in [Emim][Cl] with a 2nd order polynomial fit.

Although the potential step experiments result in current-time transients that are diffusion controlled, the diffusion coefficient values calculated from integrated Cottrell analysis at lower temperatures result in values that are roughly ten times smaller than that calculated for Cu(I) in [Emim][Cl]. A possible reason for this is that the actual concentration of Cu(II) is lower than that expected by the amount of $CuCl_2$ added due to Cu(II) being reduced by the solvent. This is consistent with the results presented in section 6.1.2.2. This would result in the plot of Q vs $(t\text{-}t_o)^{1/2}$ having a smaller gradient and when this gradient is used in the calculation of the diffusion coefficient the value obtained would be lower than expected.

As the temperature is increased (1/T is decreased), the diffusion coefficient calculated from the current-time transients decrease dramatically as can be seen in figure 7.8. The dramatic lowering of the diffusion coefficient values above 400K could be an indication that Cu(II) is less stable at higher temperatures. From cyclic voltammetry data, the electrochemical window (Cl^- oxidation) and the Cu(II)/Cu(I) redox peak infringe each other to a greater extent as the temperature is increased. This is consistent with the data presented section 6.1.2.2 and therefore a diffusion coefficient for Cu(II) in [Emim][Cl] can not be calculated using Cottrell analysis.

7.1.1.3 Diffusion Coefficient of iron in [Emim][Cl]

Iron was introduced to the [Emim][Cl] melt as $FeCl_2$ or $FeCl_3$ as appropriate to give a solution of Fe(II) or Fe(III). From cyclic voltammetry (section 6.1.3.2), the peak potential for Fe(II) oxidation was observed as 0.83V and the peak potential for Fe(III) reduction was 0.73V. The potential of the cell was stepped to ~100mV more positive or negative than the peak potentials for oxidation of Fe(II) and reduction of Fe(III) respectively, to a potential where the electrochemistry is in the diffusion controlled regime. A typical current-time transient resulting from the potential step is shown in figure 7.9.

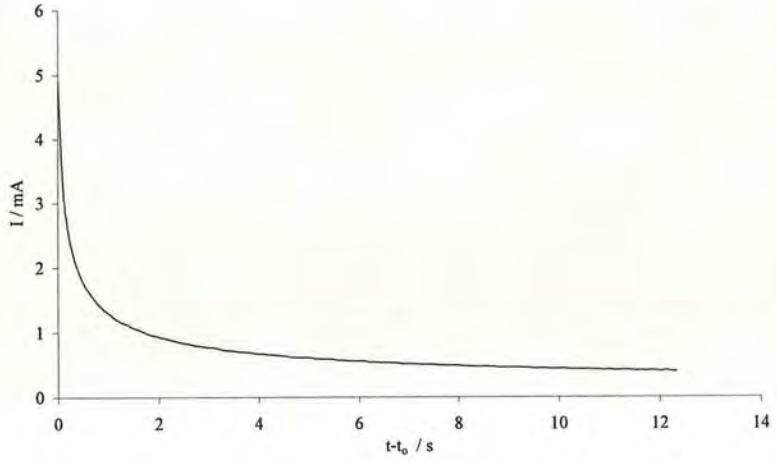

Figure 7.9: Current-time transient for Fe(II) oxidation potential step in [Emim][Cl] at 389K.

As can be seen from figure 7.9, the current decays with time in a manner that is consistent with Cottrell behaviour. In order to confirm this, a plot of charge passed during oxidation against $(t\text{-}t_o)^{1/2}$ was plotted and a linear plot was obtained, confirming Cottrell behaviour was obeyed. A plot of charge versus $(t\text{-}t_o)^{1/2}$ is shown in figure 7.10.

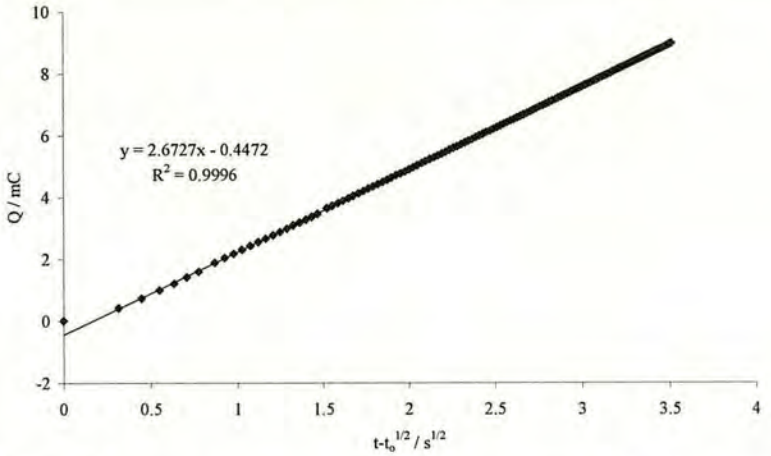

Figure 7.10: Plot of charge passed vs $(t-t_o)^{1/2}$ from a current-time transient of Fe(II) in [Emim][Cl].

As can be seen from figure 7.10, the plot of charge passed vs $(t-t_o)^{1/2}$ is linear indicating that Cottrell behaviour is observed, and the Fe(II) oxidation is proceeding under diffusion controlled conditions. By collecting current/time transients at increasing temperatures, data was collected to produce a plot of ln$D$ vs $1/T$ for Fe(II) oxidation, figure 7.11.

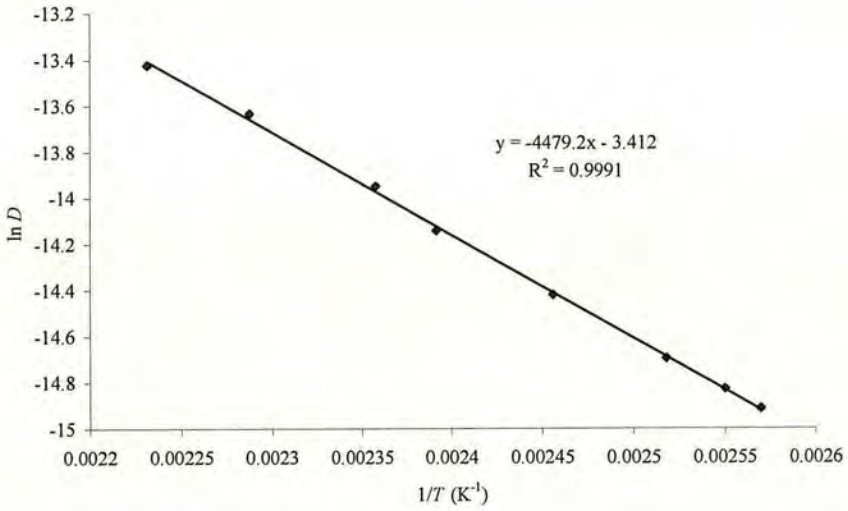

Figure 7.11: Plot of ln$D$ vs $1/T$ for Fe(II) in [Emim][Cl].

From figure 7.11, it can be seen that the variation of ln$D$ with $1/T$ was linear. A least squares fit of the data in figure 7.3 gives equation (7)

$$\ln D = -3.4120 - 4479.2(1/T) \quad (7)$$

Using equation (7),we can predict that the diffusion coefficient of Fe(II) in [Emim][Cl] will be 2.5 +/- 0.1 x 10^{-6} cm^2s^{-1} at 473K. From the gradient of the Arrhenius plot, the activation energy for the diffusion of Fe(II) in [Emim][Cl] is 37.2 +/- 0.5 $kJmol^{-1}$ and D_o is 0.033 +/- 0.001 cm^2s^{-1}.

When collecting diffusion coefficient data for Fe(III) similar problems to Cu(II) *vide ante* were encountered. Again, the current-time transients were what would be expected for a diffusion controlled redox process as can be seen in figure 7.12.

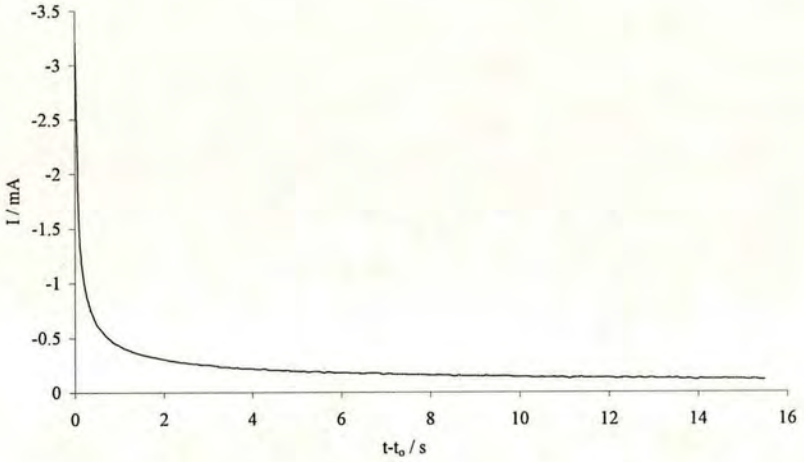

Figure 7.12: Current-time transient for Fe(III) reduction potential step in [Emim][Cl].

As with the reduction of Cu(II), the potential step reduction of Fe(III) results in a current-time transient that is limited by diffusion of Fe(III) to the electrode surface. By plotting Q vs $(t\text{-}t_o)^{1/2}$ we can ascertain if the charge passed varies with time according to the integrated Cottrell equation. A plot of Q vs $(t\text{-}t_o)^{1/2}$ is shown in figure 7.13.

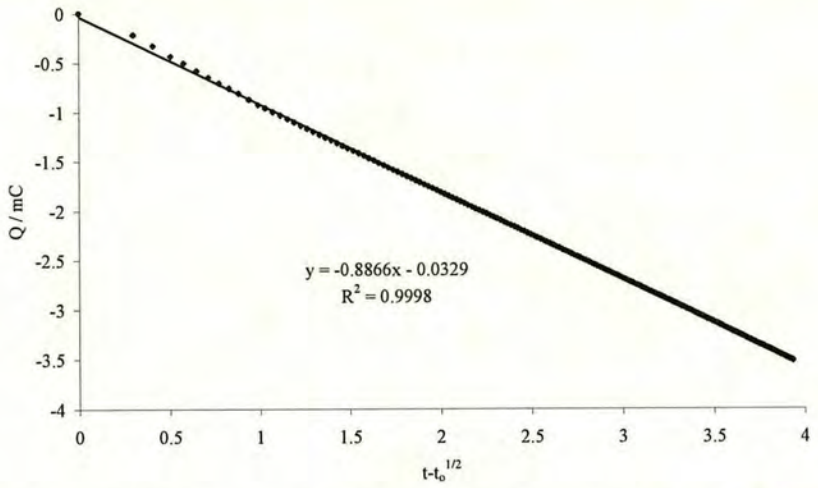

Figure 7.13: Plot of charge passed vs $(t\text{-}t_o)^{1/2}$ from a current-time transient of Fe(III) (0.025M) in [Emim][Cl] at a Pt electrode, 399K.

From figure 7.13 it can be seen that a linear plot is obtained as would be expected for a potential step experiment in which the reduction reaction is diffusion controlled. When Diffusion coefficient data was collected at higher temperatures, it was evident that similar problems that were encountered with Cu(II) *vide ante* were present. A plot of ln$D$ vs $1/T$ is presented in figure 7.14.

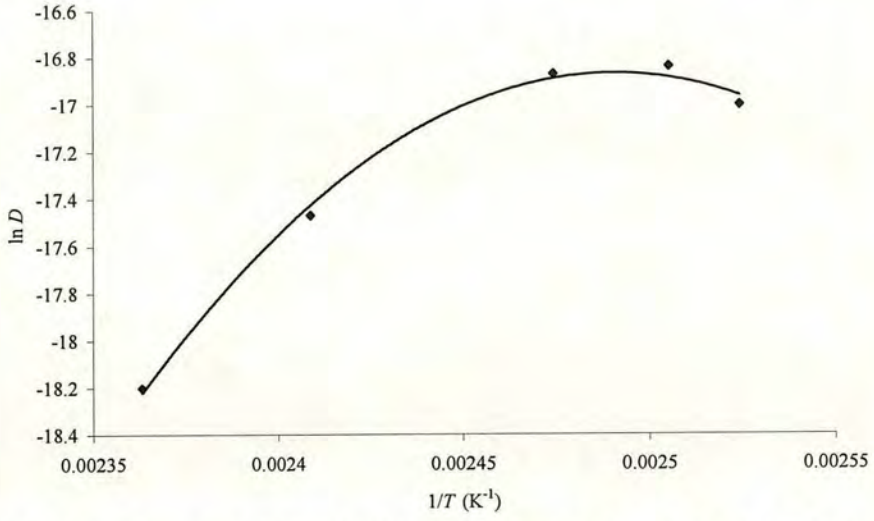

Figure 7.14: Plot of ln$D$ vs $1/T$ for Fe(III) (0.025M) in [Emim][Cl] at a Pt electrode.

As was the case with Cu(II) compared to Cu(I), the diffusion coefficients for Fe(III) were around ten times smaller than obtained for Fe(II) for temperatures up to roughly 400K. A possible reason for this could be the Fe(III) concentration is lowered by Fe(III) reacting with the solvent (Fe(III) is a strong oxidising agent). This is consistent with the cyclic voltammetry data collected for Fe(III) in [Emim][Cl] (section 6.1.3.2), the Fe(III)/(II) reduction potential was close to that of the melt chloride oxidation, as the temperature was increased these potentials became closer, suggesting this is a plausible explanation.

7.1.1.4 Diffusion Coefficient of Uranium in [Emim][Cl]

Recently, interest in the use of ionic liquids in the nuclear fuel cycle has prompted several studies of the electrochemistry and transport properties of uranium in ionic liquids. In one study[20], the diffusion coefficient of U(IV) in the Lewis acidic (66.7:33.3 mole%) $AlCl_3$/[BuPy][Cl] ionic liquid was determined to be 3.65 x 10^{-7} cm^2s^{-1} at 308K. In similar research[21], the diffusion coefficient of U(IV) in the Lewis acidic (66.7:33.3 mole%) $AlCl_3$/[Emim][Cl] ionic liquid was determined to be 6.87 x 10^{-6} cm^2s^{-1} at 318K. The diffusion coefficient would be expected to be larger in the $[Emim]^+$ ionic liquid as this was performed at a higher temperature and ionic liquids based on the $[Emim]^+$ cation generally display the lowest viscosities and highest conductivities in comparison to other cations combined with the same anion[22]. Diffusion coefficients determined in the Lewis basic $AlCl_3$/[Emim][Cl][23] ionic liquids were 1.61 x 10^{-7} cm^2s^{-1} and 1.85 x 10^{-7} cm^2s^{-1} for U(III) and U(IV) respectively at 301K. This lower diffusion coefficient in the chloride rich (Lewis basic) melt is to be expected as the chloride rich ionic liquids exhibit higher viscosities due to interactions between the cation and the chloride ion.

Attempts were made to determine the diffusion coefficient of uranium in [Emim][Cl] in order to compare the value obtained with that achievable in the high-temperature chloride based molten salt. Due to the inability to obtain CV's with a well resolved reduction peak for a solution of U(IV) in [Emim][Cl] it was not

possible to obtain any meaningful value of the diffusion coefficient. Current-time transients obtained for the reduction of solutions of U(IV) (0.01M) at a potential of –0.42V, introduced as UCl_4 in [Emim][Cl] displayed Cottrell behaviour as can be seen in figure 7.15.

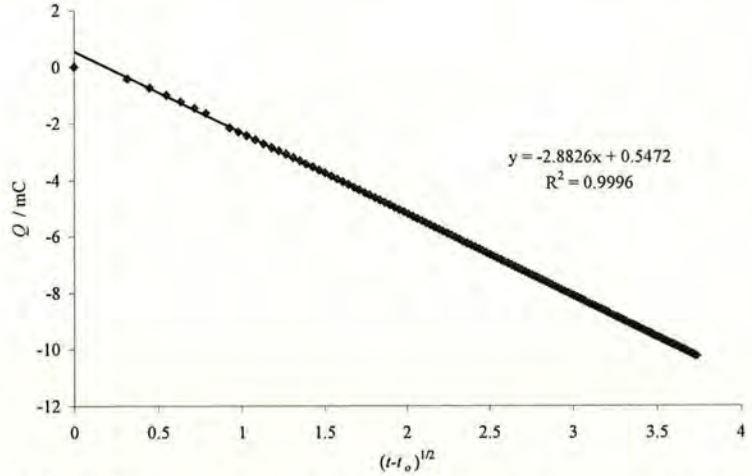

Figure 7.15: Plot of charge passed vs $(t\text{-}t_o)^{1/2}$ from a current-time transient of U(IV) (0.01M) in [Emim][Cl], Pt WE, 405K.

The diffusion coefficient obtained from the current-time transient in figure 7.15 is 3.48 x 10^{-6} cm^2s^{-1} assuming a one-electron reduction. This value is higher than would be expected in comparison to the values already obtained for Ag(I) (1.27 x $10^{-6}cm^2s^{-1}$), Cu(I) (2.01 x $10^{-6}cm^2s^{-1}$) and Fe(II) (5.19 x $10^{-7}cm^2s^{-1}$) in [Emim][Cl] at 405K. This increased value is most likely due to the 'extra' contribution to the reduction current of the overlapping reduction peaks (section 6.1.5.2). No reliable data was therefore gained for U(IV) in [Emim][Cl], though by examining the diffusion coefficients of U(IV) species in Lewis basic (chloride rich) chloroaluminate melts from the literature, it is possible to draw some conclusions as to the magnitude of the diffusion coefficient of U(IV) in [Emim][Cl]. When the diffusion coefficient of U(IV) was studied in the Lewis basic 44.8/55.2 mole % $AlCl_3$/[Emim][Cl] melt[23], its value was determined as 1.85 x 10^{-7} cm^2s^{-1} at 301K. If we compare this value to that obtained for the diffusion coefficient of Fe(II) in the 42.8/57.2 mole % $AlCl_3$/[Emim][Cl] melt[10], which was determined as 1.36 x $10^{-7}.cm^2s^{-1}$ at 313K, we can see that the diffusion coefficient values are similar when measured in similar melts.

7.1.2 Diffusion coefficients in $[N(Tf)_2]^-$ melts

As has been previously mentioned, chloride ionic liquids may have some unfavourable properties for use as a solvent in industrial processes, namely their extreme hygroscopic nature and higher melting points. In order to assess the suitability of ionic liquids based on the $[N(Tf)_2]^-$ anion the diffusion coefficient of Ag(I) in these ionic liquids has been investigated, and compared to those obtained [Emim][Cl].

7.1.2.1 Diffusion coefficient of silver in $[Emim][N(Tf)_2]$

In order to compare the diffusion coefficient of silver between [Emim][Cl] and an $[N(Tf)_2]^-$ ionic liquid, the most logical ionic liquid to use is $[Emim][N(Tf)_2]$. Ag(I) was introduced into the ionic liquid as silver trifluoroacetate and potential step experiments were carried out for the reduction of Ag(I) at increasing temperatures. A typical current-time transient resulting from the potential step is shown in figure 7.16.

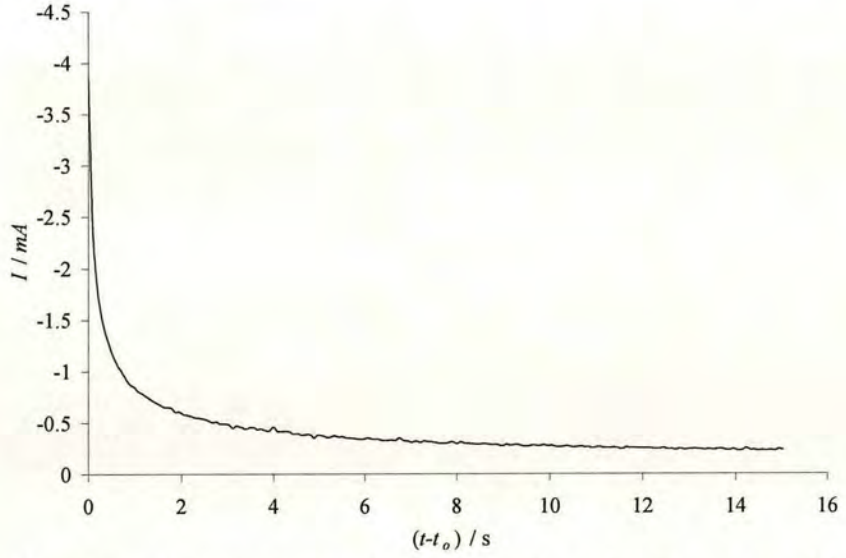

Figure 7.16: Current-time transient for Ag(I) reduction potential step in $[Emim][N(Tf)_2]$ at a silver electrode, 350K.

As was the case with Ag(I) in [Emim][Cl], the potential step experiment results in a current-time transient in which the current is controlled by diffusion of the solute species to the electrode surface. By plotting the charge passed, Q, versus $(t\text{-}t_o)^{1/2}$, a straight line plot should be obtained if Cottrell behaviour is observed, figure 7.17.

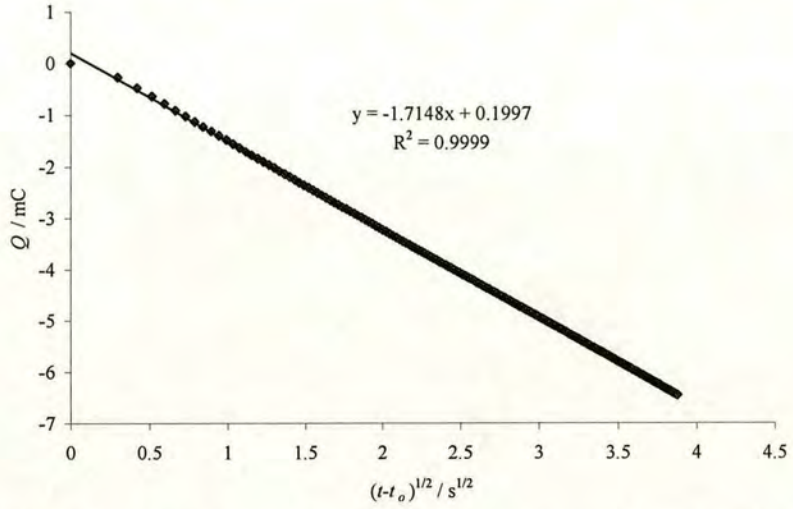

Figure 7.17: Plot of charge passed vs $(t\text{-}t_o)^{1/2}$ from a current-time transient of Ag(I) in [Emim][$N(Tf)_2$].

As can be seen from figure 7.17, the plot of charge passed vs $(t\text{-}t_o)^{1/2}$ is linear indicating that Cottrell behaviour is observed, and the reduction of Ag(I) is proceeding under diffusion controlled conditions. By collecting current-time transients at increasing temperatures, data was collected to produce a plot of ln$D$ vs $1/T$ for Ag(I) oxidation, figure 7.18.

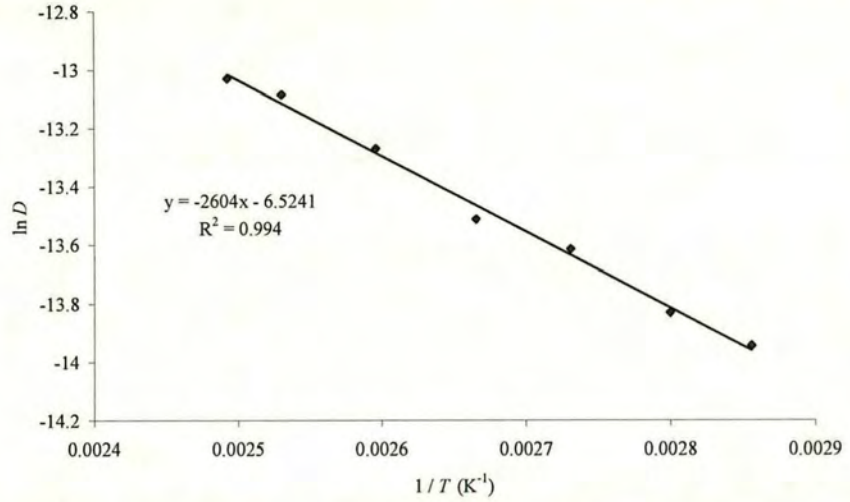

Figure 7.18: Plot of ln$D$ vs 1/T for Ag(I) in [Emim][$N(Tf)_2$] at a silver electrode.

From figure 7.18, the diffusion coefficient of Ag(I) in [Emim][$N(Tf)_2$] was found to vary linearly with the reciprocal of temperature over the temperature range of 350 to 401K. A least squares fit of the data in figure 7.18 gives equation (8)

$$\ln D = -6.5241 - 2604.0(1/T) \tag{8}$$

Using equation (8), we can predict that the diffusion coefficient of Ag(I) in [Emim][$N(Tf)_2$] will be 6.0 +/- 0.3 x 10^{-6} cm^2s^{-1} at 473K. From the linear fit of ln$D$ vs 1/T in figure 7.18, the activation energy for diffusion was calculated to be 21.7 +/- 0.8 $kJmol^{-1}$ and D_o was 1.47 +/- 0.05x 10^{-3} cm^2s^{-1}.

7.1.2.2 Diffusion coefficient of silver in [Pyr][N(Tf)$_2$]

The hydrophobic room temperature ionic liquid *N*,*N*-butyl-methyl-pyrrolidinium bis(trifluoromethanesulfonyl)imide [Pyr][N(Tf)$_2$] was used to investigate the effect of changing the cation on the diffusion coefficient of solute species. The pyrrolidinium cation was used as it afforded a more negative reduction limit when compared to the imidazolium cation, ionic liquids based on quaternary ammonium cations have been shown to allow the electrodeposition of active metals[24]. Silver was introduced into solution as Ag(I) by the addition of silver trifluoroacetate to [Pyr][N(Tf)$_2$] and potential step experiments were performed on this solution at increasing temperatures at a silver electrode. An example of a current/time transient obtained is shown in figure 7.19.

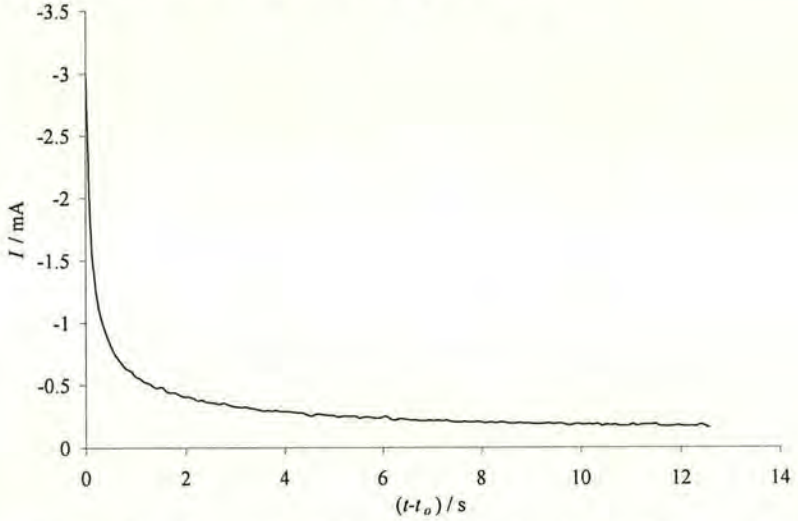

Figure 7.19: Current-time transient for Ag(I) reduction on a silver electrode in [Pyr][N(Tf)$_2$] at 345K.

As was the case with Ag(I) in [Emim][Cl] and [Emim][N(Tf)$_2$], the potential step experiment results in a current-time transient in which the current is controlled by diffusion of the solute species to the electrode surface. By plotting the charge passed, Q, versus $(t\text{-}t_o)^{1/2}$, a straight line plot should be obtained if Cottrell behaviour is observed, figure 7.20.

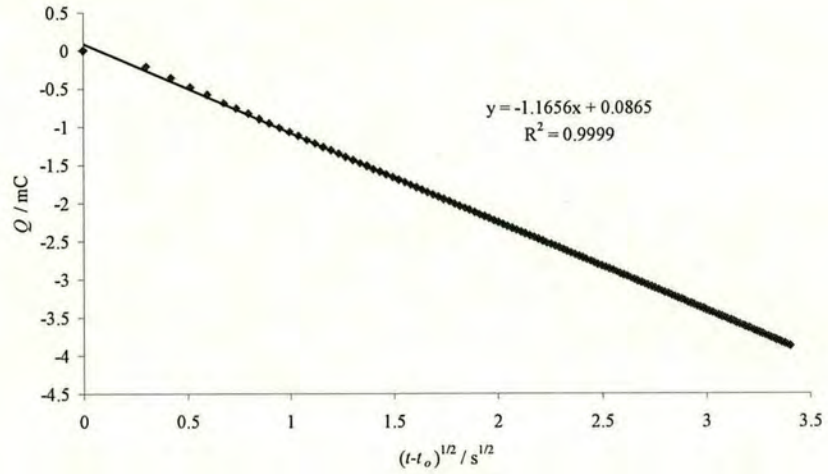

Figure 7.20: Plot of charge passed vs $(t\text{-}t_o)^{1/2}$ from a current-time transient of Ag(I) in [Pyr][N(Tf)$_2$].

As can be seen from figure 7.20, the plot of Q vs $(t\text{-}t_o)^{1/2}$ is linear indicating Cottrell behaviour is observed and the Ag(I) reduction current is controlled by diffusion of the solute species to the electrode. Current-time transients were collected at increasing temperatures and the diffusion coefficients calculated to produce a plot of ln$D$ vs 1/T, figure 7.21.

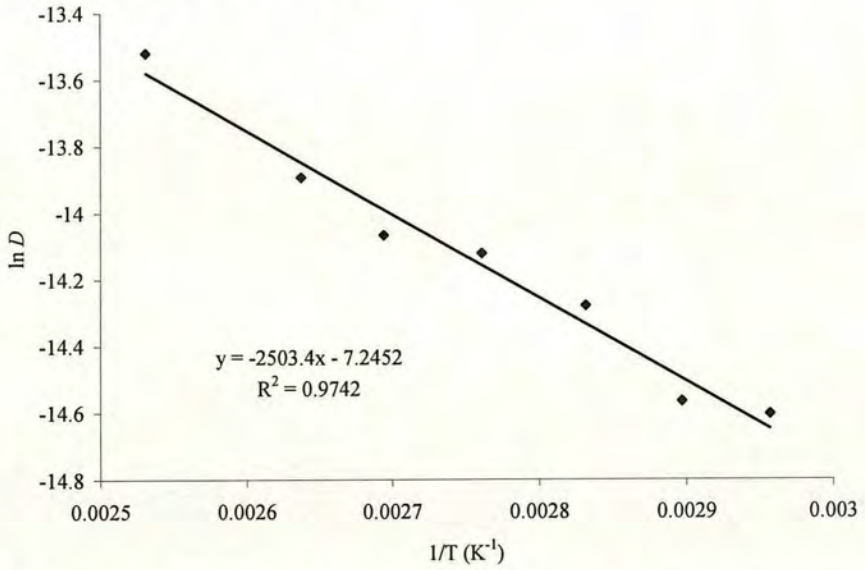

Figure 7.21: Plot of ln$D$ vs 1/T for Ag(I) in [Pyr][N(Tf)$_2$] at a silver electrode.

From figure 7.21, the diffusion coefficient of Ag(I) in [Pyr][$N(Tf)_2$] was found to vary linearly with the reciprocal of temperature over the temperature range of 338 to 395K. A least squares fit of the data in figure 7.21 gives equation (9)

$$\ln D = -7.2452 - 2503.4(1/T) \qquad (9)$$

Using equation (9), we can predict that the diffusion coefficient of Ag(I) in [Pyr][$N(Tf)_2$] will be 3.6 +/- 0.4 x 10^{-6} cm^2s^{-1} at 473K. From the linear fit of ln$D$ vs 1/T in figure 7.21, the activation energy for diffusion was calculated to be 20.8 +/- 1.5 $kJmol^{-1}$ and D_o was 7.14 +/- 0.50x 10^{-4} cm^2s^{-1}.

7.2 Conclusions

A summary of the diffusion coefficients calculated for various solute species in the $[Cl]^-$ and $[N(Tf)_2]^-$ salts along with activation energies of self diffusion are shown in table 7.2.

Species	System	T / K	D_o / cm^2s^{-1}	D / cm^2s^{-1}	E_d / $KJmol^{-1}$
Ag(I)	[Emim][Cl]	473#	0.470 +/- 0.035	8.0 +/- 0.7 x 10^{-6}	43.2 +/- 1.9
Cu(I)	[Emim][Cl]	473#	0.180 +/- 0.023	1.0 +/- 0.1 x 10^{-5}	38.4 +/- 0.8
Fe(II)	[Emim][Cl]	473#	0.033 +/- 0.001	2.5 +/- 0.1 x 10^{-6}	37.2 +/- 0.5
Ag(I)	[Emim][$N(Tf)_2$]	473#	1.47 +/- 0.05 x 10^{-3}	6.0 +/- 0.3 x 10^{-6}	21.7 +/- 0.8
Ag(I)	[Pyr][$N(Tf)_2$]	473#	7.14 +/- 0.50 x 10^{-4}	3.6 +/- 0.4 x 10^{-6}	20.8 +/- 1.5

Table 7.2: Diffusion coefficients of solutes in $[Cl]^-$ and $[N(Tf)_2]^-$ ionic liquids determined by chronoamperometry. #extrapolated from Arrhenius plot.

From table 7.2, it is of note that the activation energies for diffusion are comparable for all the solutes in the chloride melts, and likewise for Ag(I) in the $[N(Tf)_2]^-$ salts. The activation energies for diffusion are higher for the chloride salts as would be expected with the greater anion-cation interactions through greater electrostatic interactions and a greater degree of hydrogen bonding, which leads to a greater viscosity. The plots of lnD vs 1/T obey Arrhenius behaviour for all the ionic liquids studied over the temperature range measured; a plot of the diffusion coefficient of U(III) in a NaCl/KCl molten salt has been included in the plot for comparison with the ionic liquids[25], figure 7.22. As the activation energy is derived from the gradient of the linear plots in figure 7.22, it is evident that the chloride ionic liquids have very similar gradients and thus similar activation energies to diffusion. The activation energy for self diffusion of U(III) in NaCl/KCl[25] is 37.2 +/- 1.9 $kJmol^{-1}$, which is comparable to that observed for solutes in [Emim][Cl]. This may be indicative that the diffusion activation involves the movement of the chloride ions surrounding the cation in each case. This would be consistent with the model proposed by Bockris[1] to explain the diffusional transport of ions in molten salts. This

model proposes that even though a metal cation dissolved in a molten salt can be though of as a complex ion (e.g. four chloride ions in a $[FeCl_4]^-$ complex), a certain number of ligands participate in the random walk of the ion (i.e. the Fe3+ ion in the $[FeCl_4]^-$ complex). Of the solutes in the chloride ionic liquids, Cu(I) had the highest diffusion coefficients; this was expected as it will have the smallest ionic radius of the solutes studied.

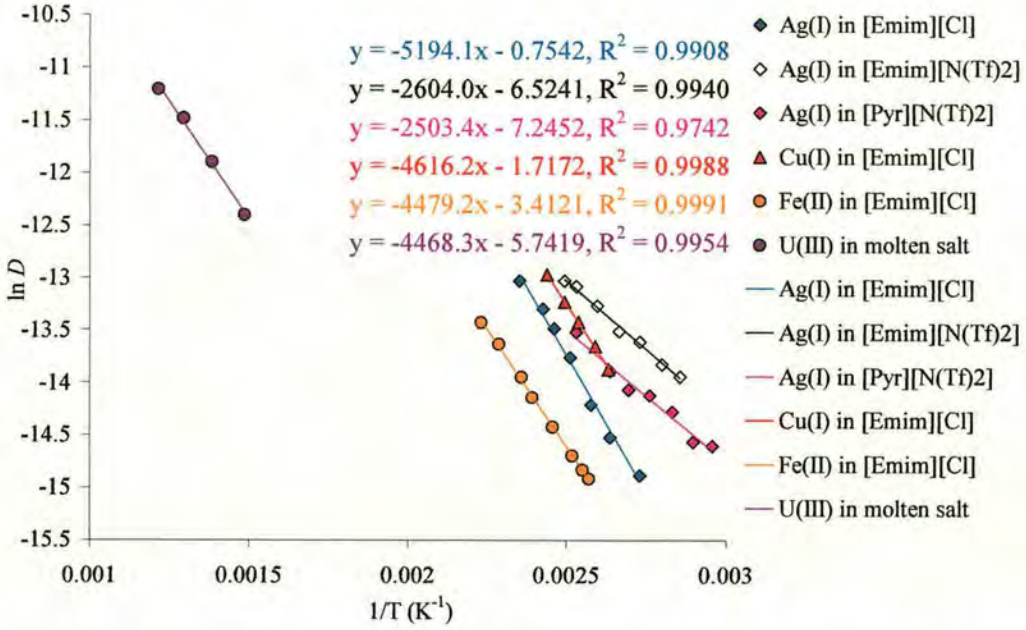

Figure 7.22: Plot of ln*D* vs 1/T for all ionic liquids with U(IV) in NaCl/KCl for comparison.

Thus neglecting any solvation or coordination differences, Cu(I) would be expected to have a higher diffusion coefficient of the solute species studied, and does. It is expected that U(IV) would have diffusion coefficients of the same order of magnitude as the solute species investigated in this study due to comparisons with diffusion coefficient studies performed in both the Lewis acidic and Lewis basic chloroaluminate melts (table 7.1) in which U(III) had a similar diffusion coefficient to that of Fe(II) in similar melts. The diffusion coefficient of U(III) in NaCl/KCl have diffusion coefficient values around 4 x 10^{-5} cm^2s^{-1} at their operating temperatures, roughly 1000K. Thus the transport properties of solute species in the chloride based ionic liquids at 473K are expected to be within an order of magnitude of the transport properties of those observed in high temperature molten salts

currently used in the nuclear fuel cycle. The transport of electroactive material in ionic liquids is therefore not seen to be the limiting factor in the application of ionic liquids for nuclear fuel reprocessing. Though this study has involved electrochemical investigations of uranium species in ionic liquids, at no point has the electrodeposition of uranium been observed at potentials positive of the imidazolium cation reduction. In this respect, the high temperature molten salts hold a significant advantage over ionic liquids in that the cathodic stability of the alkali earth cations is greater than that observed for imidazolium based ionic liquids.

Of the $[N(Tf)_2]^-$ salts, Ag(I) has similar activation energies to diffusion in both the $[Emim]^+$ and $[Pyr]^+$ melts, this is, as with the chloride ionic liquids, consistent with the model of diffusional transport of ions in molten salt proposed by Bockris[1]. The diffusion coefficient for Ag(I) is higher for the $[Emim][N(Tf)_2]$ salt at the same temperature, most likely due to its lower viscosity. Both the $[N(Tf)_2]^-$ salts are expected to have diffusion coefficients within one order of magnitude of those observed in the high temperature molten salts used at present. The more favourable transport properties of the $[Emim][N(Tf)_2]$ salt are somewhat redundant as the deposition of active metals is not observed before the reduction of the imidazolium cation, thus the solvent is unsuitable for an electrorefining process involving uranium electrodeposition. The $[Pyr][N(Tf)_2]$ melts show promise for use in an electrorefining process for nuclear fuel reprocessing in terms of a combination of reasonable transport properties and an increased cathodic stability compared to the imidazolium melts. Though it must be noted, uranium electrodeposition has not been observed from any room temperature ionic liquids. The most successful step toward the electrodeposition of uranium or plutonium in an ionic liquid has been the electrodeposition of the highly active Europium and Lithium. These metals were deposited at a glassy carbon electrode from the ionic liquid $[Me_4P][N(Tf)_2]$[24(b)] (Where $[Me_4P]^+$ is the tetramethyl-phosphonium cation).

[1] J.O'M. Bockris and A.K.N. Reddy, *Modern Electrochemistry 1 - Ionics*, Second Edition, Plenum Press, New York, 1998.

[2] Communicated at engineering meeting at BNFL.

[3] C.L. Hussey, I-W. Sun, S.K.D. Strubinger and P.A. Barnard., *J. Electrochem. Soc.*, 1990, **137**, 2515-2516.

[4] A.J. Bard and L.R. Faulkner, *Electrochemical Methods, fundamentals and applications.*, John Wiley & Sons, Inc., 1980.

[5] M. Kanno and S. Yamagami, *Denki Kagaku*, 1975, **43**, 131-137.

[6] M.S. Murthy, K. Rajamani and P. Subramanian, *Chemical Engineering Science.*, 1975, **30**, 1529-1533.

[7] H.S. Swofford Jr. and J.Dietz, *Anal. Chem.*1972, **44**, 2232-2235.

[8] F. Meuris, L. Heerman and W. D'Olieslager, *J. Electrochem. Soc.*, 1980, **127**, 1294 -1299.

[9] W-J Gau and I-W Sun, *J. Electrochem. Soc.*, 1996, **143**, 170-174.

[10] C. Nanjundiah, K. Shimizu and R.A. Osteryoung, *J. Electrochemical. Soc.*, 1982, **129**, 2474-2480.

[11] C.L. Hussey and X. Xu, *J. Electrochemical. Soc.*, 1991, **138**, 1886-1890.

[12] I-W. Sun, E.H. Ward and C.L. Hussey, *J. Electrochemical. Soc.*, 1988, **135**, 3035-3038.

[13] W-J. Gau and I-W. Sun, *J. Electrochem. Soc.*, 1996, **143**, 914 -919.

[14] J-J. Lee, B. Miller, X. Shi, R. Kalish and K.A. Wheeler. *J. Electrochem. Soc.*, 2001, **148**, C183-C190.

[15] B.J. Tierney, W.R. Pitner, J.A. Mitchell, C.L. Hussey and G.R. Stafford, *J. Electrochem. Soc.*, 1998, **145**, 3110-3116.

[16] P-Y. Chen and I-W. Sun, *Electrochimica Acta.*, 1999, **45**, 441-450.

[17] P-Y. Chen and I-W. Sun, *Electrochimica Acta.*, 2000, **45**, 3163-3170.

[18] F. Endres and W. Freyland, *J. Phys. Chem. B.*, 1998, **102**, 10229-10233.

[19] X-H. Xu and C.L. Hussey, *J. Electrochem. Soc.*, 1992, **139**, 1295-1300.

[20] R. De Waele, L. Heerman and W. D'Olieslager, *J. Electroanal. Chem.*, 1982, **142**, 137-146.

[21] K.G. Ray, Thesis submitted to University of Mississippi, 1985.

[22] D.R. MacFarlane, P. Meakin, J. Sun, N. Amini and M. Forsyth, *J. Phys. Chem. B.*, 1999, **103**, 4164-4170.

[23] C.J. Anderson, M.R. Deakin, G.R. Choppin, W. D'Olieslager, L. Heerman and D.J. Pruett, *Inorg. Chem.*, 1991, **30**, 4013-4016.

[24] **(a)** W.J. Oldham, D.A. Costa and W.H. Smith, *Los Alamos National Laboratories Internal Report*, **LA-UR-01-2279**, 2001. http://lib-www.lanl.gov/la-pubs/00818127.pdf. **(b)** A.I. Bhatt, I. May, V.A. Volkovich, M.E. Hetherington, B. Lewin, R.C. Thied and N. Ertok, *J. Chem. Soc., Dalton. Trans.*, 2002, 4532-4533.

[25] Data provided by BNFL

8 Conclusions and Further Work

A structural analysis of imidazolium salts has been undertaken. Single crystal X-ray crystallography has been performed on both [Emim][Cl] and [Emim][$AgCl_2$] and powder X-ray diffraction has been performed on [Emim][$AgCl_2$]. Raman scattering experiments have been performed on [Emim][$CuCl_2$] and [Emim][$AgCl_2$] to try and ascertain the reason for the large difference in the melting points of the two ionic liquids.

Both structures display significant degrees of hydrogen bonding and close-contacts between the imidazolium hydrogens and the anions and both structures were calculated with a degree of disorder in one imidazolium unit yielding a better fit with the experimental data. The shortest contacts between the hydrogens on the imidazolium unit and Cl^- in [Emim][Cl] occur between H2 and Cl^- as expected, with the shortest of these contacts occurring between H2D and Cl(3). The hydrogen bonding with the [Emim][Cl] structure is dominated by the interactions between the hydrogens on the imidazolium ring and the chloride anion, however, the hydrogen bonding between the hydrogen atoms on the alkyl chains is also significant and cannot be ignored. In contrast to the [Emim][Cl] crystal structure, the structure of [Emim][$AgCl_2$] in the crystal phase shows the shortest contacts between the imidazolium cation and the anion occurs at the H1 position on the methyl group not to the H2 position of the imidazolium ring. This is unexpected and is presumably due to the increased number of close contacts between the anion and the cation causing this structure to be adopted in the crystal phase. The infinite polymeric $[AgCl_2]^-$ anion adopts a helical structure in the crystal phase, this has not previously been observed in the literature for silver halide salts of the type [Cation][AgX_2] (where X = halide), and [Emim][$AgCl_2$] represents the first such example of a helical silver halide chain. The helical nature of the anion arises from the interactions between the cation and itself with the close contacts between the asymmetric cation and the anion. The number of close contacts to the chlorides of the anion are

different, with four close contacts to Cl(12) and 6 close contacts to Cl(21), this leads to the weakening of the Ag-Cl(21) bonds relative to the Ag-Cl(12) bonds and results in the helical motif adopted by the $[AgCl_2]^-$ anion. The ionic liquid [Emim][Cl] shows promise as a solvent for the recrystallisation of AgCl due to the high solubility of AgCl in [Emim][Cl], dissolving up to 50 mole %. This could prove an attractive alternative to the current method of recrystallising AgCl, which involves recrystallising AgCl from molten silver chloride.

In order to improve upon the crystal structure of both [Emim][Cl] and $[Emim][AgCl_2]$, neutron diffraction experiments could be performed to better locate the hydrogen atoms on the imidazolium cation. Hydrogen atoms are poorly located in X-ray crystallography experiments due to their poor scattering factor, this is because X-rays are scattered by electron density and hydrogen atoms have very low electron densities. The location of hydrogen atoms will be particularly problematic for the case of the $[Emim][AgCl_2]$ crystal due to the presence of a heavy atom, Ag, which has a high scattering factor due to its high electron density. Neutron diffraction experiments do not suffer from the problem of locating hydrogen atoms since neutrons are scattered by the nuclei of atoms and so it is generally a better technique for studying the structure of the crystal phase for crystals containing hydrogen atoms. The major problem with neutron diffraction experiments are most laboratories do not have their own nuclear reactors and therefore do not have ready access to the high flux of neutrons required for diffraction experiments.

Electrochemical measurements of various solute transition metal and uranium species have been performed in $[Cl]^-$ and $[N(Tf)_2]^-$ ionic liquids. The Cu(I)/Cu(II) and Fe(II)/(III) redox couples display Nernstian behaviour in the chloride ionic liquids. The electrodeposition of copper from [Emim][Cl], and silver from [Emim][Cl], $[Emim][N(Tf)_2]$ and $[Pyr][N(Tf)_2]$ was observed at a platinum electrode. Future work could involve the use of these ionic liquids to perform the electrotransport of these metals and determine their potential applicability to purification of these metals by electrotransport.

The electrochemistry of zirconium and uranium was complex in the ionic liquids studied, displaying kinetic limited peaks and multiple overlapping peaks. Further electrochemical investigation into these metals in the ionic liquids used is required to gain a better understanding of the complex chemistry that is occurring in these melts. The electrochemistry of electrogenerated uranium solutions in [Emim][Cl] resulted in multiple overlapping peaks as was observed through the addition of soluble uranium species. Though comparison between the added U(IV) complexes and electrogenerated U complexes suggested that $[UCl_6]^{2-}$ was a possible product from uranium electrogeneration in [Emim][Cl]. No such comparisons could be made with the electrogeneration of uranium in the $[N(Tf)_2]^-$ salts since no $[N(Tf)_2]^-$ salts of uranium were available for addition to the triflimide melts to provide CVs of known uranium compounds. The synthesis of such uranium salts would allow for a better understanding of uranium in the $[N(Tf)_2]^-$ ionic liquids.

The ionic liquids studied displayed favourable diffusional transport properties when compared to those observed in the high temperature molten salts. Though an order of magnitude less than observed in molten salts, the transport of ions through solution would not appear to be a limiting step for the electrorefining of metals. For the electrorefining of highly active metals, the ionic liquids studied would appear to be unsuitable due to the limited potential window with which is available to deposit the active metals, namely the cathodic limit. The investigation of ionic liquids with greater cathodic stability, and suitable anions for the solubilisation and transport of metal ions is required to optimise the use of ionic liquids in electrorefining processes.

Appendix

1 X-ray Crystallography

A1. 1-ethyl-3-methylimidazolium chloride, [Emim][Cl].

Table A1. Crystal data, solution and refinement for 1-ethyl-3-methylimidazolium chloride.

Empirical formula	$C_6 H_{11} Cl N_2$
Formula weight	146.62
Wavelength	0.71073 Å
Temperature	190(2) K
Crystal system	Orthorhombic
Space group	P212121
Unit cell dimensions	a = 10.0953(13) Å $\alpha = 90$ °. b = 11.0593(15) Å $\beta = 90$ °. c = 28.587(4) Å $\gamma = 90$ °.
Volume	3191.6(7) $Å^3$
Number of reflections for cell	5466 (2 < theta < 25.5 deg.)
Z	16
Density (calculated)	1.221 gcm^{-3}
Absorption coefficient	0.398 mm^{-1}
F(000)	1248
Crystal description	Colourless needle
Crystal size	0.66 x 0.20 x 0.20 mm
Instrument	CCD area detector
Theta range for data collection	1.42 to 26.39°.
Index ranges	-12<=h<=8, -12<=k<=13, -35<=l<=35
Reflections collected	14587
Independent reflections	6497 [R(int) = 0.0296]

Scan type	Phi and omega scans
Absorption correction	Sadabs (T_{min} = 0.682, T_{max} =1)
Solution	Direct (SHELXS-97 (Sheldrick, 1990))
Refinement type	Full-matrix least-squares on F^2
Program used for refinement	SHELXL-97
Hydrogen atom placement	Calc
Hydrogen atom treatment	Riding
Data / restraints / parameters	6497 / 0 / 347
Goodness-of-fit on F^2	0.990
Conventional R [F>4sigma(F)]	R1 = 0.0420 [5488 data]
Weighted R (F^2 and all data)	wR2 = 0.0953
Absolute structure parameter	0.00(5)
Extinction coefficient	0.0014(3)
Final maximum delta / sigma	0.034
Weighting scheme	Calc $w = 1/[\s^2(Fo^2)+(0.0518P)^2+0.0000P]$ where $P = (Fo^2+2Fc^2)/3$
Largest diff. peak and hole	0.235 and -0.226 e.$Å^{-3}$

Table A2: Bond Lengths for 1-ethyl-3-methylimidazolium chloride, esd's in brackets

Bond	Length / Å	Bond	Length / Å
N(1A)-C(2A)	1.326(3)	C(6B)-C(7B)	1.487(6)
N(1A)-C(5A)	1.371(3)	C(7BB)-C(6BB)	1.42(3)
N(1A)-C(6A)	1.475(3)	N(1C)-C(2C)	1.318(3)
C(1A)-N(3A)	1.472(3)	N(1C)-C(5C)	1.361(3)
C(2A)-N(3A)	1.324(3)	N(1C)-C(6C)	1.477(3)
N(3A)-C(4A)	1.372(3)	C(1C)-N(3C)	1.474(3)
C(4A)-C(5A)	1.340(3)	C(2C)-N(3C)	1.310(3)
C(6A)-C(7A)	1.511(4)	N(3C)-C(4C)	1.368(3)
C(1B)-N(3B)	1.463(3)	C(4C)-C(5C)	1.343(4)
N(1B)-C(2B)	1.317(4)	C(6C)-C(7C)	1.485(4)

N(1B)-C(5B)	1.391(4)	N(1D)-C(2D)	1.316(3)
N(1B)-C(6B)	1.468(4)	N(1D)-C(5D)	1.370(3)
C(2B)-N(3B)	1.334(4)	N(1D)-C(6D)	1.480(4)
N(1BB)-C(2BB)	1.327(17)	C(1D)-N(3D)	1.468(3)
N(1BB)-C(5B)	1.496(12)	C(2D)-N(3D)	1.311(3)
N(1BB)-C(6BB)	1.51(2)	N(3D)-C(4D)	1.358(3)
C(2BB)-N(3B)	1.384(15)	C(4D)-C(5D)	1.349(4)
N(3B)-C(4B)	1.370(3)	C(6D)-C(7D)	1.470(5)
C(4B)-C(5B)	1.340(4)		

Table A3: Bond Angles for 1-ethyl-3-methylimidazolium chloride, esd's in brackets.

Atoms	Angle / °	Atoms	Angle / °
C(2A)-N(1A)-C(5A)	108.2(2)	C(4B)-C(5B)-N(1B)	107.0(3)
C(2A)-N(1A)-C(6A)	125.6(2)	C(4B)-C(5B)-N(1BB)	102.7(5)
C(5A)-N(1A)-C(6A)	126.2(2)	N(1B)-C(5B)-N(1BB)	32.1(5)
N(3A)-C(2A)-N(1A)	108.8(2)	N(1B)-C(6B)-C(7B)	112.2(4)
C(2A)-N(3A)-C(4A)	108.3(2)	C(7BB)-C(6BB)-N(1BB)	109.1(18)
C(2A)-N(3A)-C(1A)	125.3(2)	C(2C)-N(1C)-C(5C)	108.2(2)
C(4A)-N(3A)-C(1A)	126.3(2)	C(2C)-N(1C)-C(6C)	126.1(2)
C(5A)-C(4A)-N(3A)	107.2(2)	C(5C)-N(1C)-C(6C)	125.7(2)
C(4A)-C(5A)-N(1A)	107.4(2)	N(3C)-C(2C)-N(1C)	109.3(2)
N(1A)-C(6A)-C(7A)	110.9(2)	C(2C)-N(3C)-C(4C)	108.4(2)
C(2B)-N(1B)-C(5B)	107.7(3)	C(2C)-N(3C)-C(1C)	125.9(2)
C(2B)-N(1B)-C(6B)	125.3(3)	C(4C)-N(3C)-C(1C)	125.7(2)
C(5B)-N(1B)-C(6B)	126.9(3)	C(5C)-C(4C)-N(3C)	106.8(2)
N(1B)-C(2B)-N(3B)	109.5(3)	C(4C)-C(5C)-N(1C)	107.3(2)
C(2BB)-N(1BB)-C(5B)	106.7(10)	N(1C)-C(6C)-C(7C)	111.2(2)
C(2BB)-N(1BB)-C(6BB)	127.1(12)	C(2D)-N(1D)-C(5D)	108.4(2)
C(5B)-N(1BB)-C(6BB)	124.4(10)	C(2D)-N(1D)-C(6D)	125.0(3)
N(1BB)-C(2BB)-N(3B)	107.3(11)	C(5D)-N(1D)-C(6D)	126.6(3)
C(2B)-N(3B)-C(4B)	107.8(2)	N(3D)-C(2D)-N(1D)	108.9(2)

C(2B)-N(3B)-C(2BB)	26.1(6)	C(2D)-N(3D)-C(4D)	109.2(2)
C(4B)-N(3B)-C(2BB)	108.5(7)	C(2D)-N(3D)-C(1D)	125.8(3)
C(2B)-N(3B)-C(1B)	126.6(2)	C(4D)-N(3D)-C(1D)	125.0(3)
C(4B)-N(3B)-C(1B)	125.3(2)	C(5D)-C(4D)-N(3D)	106.8(2)
C(2BB)-N(3B)-C(1B)	122.3(6)	C(4D)-C(5D)-N(1D)	106.7(2)
C(5B)-C(4B)-N(3B)	107.6(2)	C(7D)-C(6D)-N(1D)	111.7(3)

A2. 1-ethyl-3-methylimidazolium dichloroargentate.

Table A4. Crystal data, solution and refinement for 1-ethyl-3-methylimidazolium dichloroargentate.

Empirical formula	$C_6 H_{11} Ag Cl_2 N_2$
Formula weight	289.94
Wavelength	0.71073 Å
Temperature	150(2) K
Crystal system	Monoclinic
Space group	C2/c
Unit cell dimensions	a = 15.4284(10) Å α = 90° b = 10.9030(10) Å β = 103.872(2)° c = 17.3246(12) Å γ = 90°
Volume	2829.3(4) $Å^3$
Number of reflections for cell	5454 (2.3 < theta < 28.7°)
Z	12
Density (calculated)	2.042 g/cm^3
Absorption coefficient	2.643 mm^{-1}
F(000)	1704
Crystal description	Colourless Block
Crystal size	0.54 x 0.42 x 0.40 mm
Theta range for data collection	2.42 to 28.82°
Index ranges	-20<=h<=20, -14<=k<=14, -22<=l<=23

Reflections collected	11668
Independent reflections	3454 [R(int) = 0.0316]
Scan type	Phi and omega scans
Absorption correction	Semi-empirical from equivalents (Tmin= 0.88807, Tmax=1)
Solution	direct (SHELXS-97 (Sheldrick, 1990))
Refinement type	Full-matrix least-squares on F^2
Program used for refinement	SHELXL-97
Hydrogen atom placement	Geom
Hydrogen atom treatment	Mixed
Data / restraints / parameters	3454 / 0 / 145
Goodness-of-fit on F^2	1.441
Conventional R [F>4sigma(F)]	R1 = 0.0373 [3373 data]
Weighted R (F^2 and all data)	wR2 = 0.0964
Extinction coefficient	0.0054(2)
	0.001
Weighting scheme	Calc w=1/[\s^2^(Fo^2^)+(0.0161P)^2^+16.8568P] where P=(Fo^2^+2Fc^2^)/3
Largest diff. Peak and hole	0.766 and -0.830 $e.A^{-3}$

Table A5: Bond Lengths for 1-ethyl-3-methylimidazolium dichloroargentate, esd's in brackets

Bond	Length / Å	Bond	Length / Å
N(1A)-C(2A)	1.324(5)	C(7B)-H(7B1)	0.9800
N(1A)-C(5A)	1.378(6)	C(7B)-H(7B2)	0.9800
N(1A)-C(6A)	1.473(6)	C(7B)-H(7B3)	0.9800
C(6A)-C(7A)	1.499(8)	C(2B)-N(3B)	1.324(11)
C(6A)-H(6A1)	0.9900	C(2B)-H(2B)	0.9500
C(6A)-H(6A2)	0.9900	N(3B)-C(4B)	1.392(10)

C(7A)-H(7A1)	0.9800	N(3B)-C(1B)	1.482(14)
C(7A)-H(7A2)	0.9800	C(1B)-H(1B1)	0.9800
C(7A)-H(7A3)	0.9800	C(1B)-H(1B2)	0.9800
C(2A)-N(3A)	1.327(5)	C(1B)-H(1B3)	0.9800
C(2A)-H(2A)	0.9500	C(4B)-C(4B)#1	1.354(11)
N(3A)-C(4A)	1.377(5)	C(4B)-N(1B)#1	1.379(10)
N(3A)-C(1A)	1.465(5)	C(4B)-H(4B)	0.9500
C(1A)-H(1A1)	0.9800	Ag(1)-Cl(12)	2.5889(11)
C(1A)-H(1A2)	0.9800	Ag(1)-Cl(11)#2	2.5985(12)
C(1A)-H(1A3)	0.9800	Ag(1)-Cl(11)	2.6006(12)
C(4A)-C(5A)	1.356(7)	Ag(1)-Cl(21)	2.6720(10)
C(4A)-H(4A)	0.9500	Ag(1)-Ag(2)	3.0306(4)
C(5A)-H(5A)	0.9500	Ag(1)-Ag(1)#2	3.1900(7)
N(1B)-C(2B)	1.321(12)	Ag(2)-Cl(12)#1	2.5603(10)
N(1B)-C(4B)#1	1.379(10)	Ag(2)-Cl(12)	2.5603(10)
N(1B)-C(6B)	1.488(12)	Ag(2)-Cl(21)#1	2.6246(10)
C(6B)-C(7B)	1.498(13)	Ag(2)-Cl(21)	2.6246(10)
C(6B)-H(6B1)	0.9900	Ag(2)-Ag(1)#1	3.0306(4)
C(6B)-H(6B2)	0.9900	Cl(11)-Ag(1)#2	2.5985(12)

Table A6: Bond Angles for 1-ethyl-3-methylimidazolium dichloroargentate, esd's in brackets.

Atoms	Angle / °	Atoms	Angle / °
C(2A)-N(1A)-C(5A)	109.0(4)	N(3B)-C(2B)-H(2B)	125.6
C(2A)-N(1A)-C(6A)	126.0(4)	C(2B)-N(3B)-C(4B)	102.9(7)
C(5A)-N(1A)-C(6A)	125.1(4)	C(2B)-N(3B)-C(1B)	126.3(8)
N(1A)-C(6A)-C(7A)	111.5(4)	C(4B)-N(3B)-C(1B)	130.6(8)
N(1A)-C(6A)-H(6A1)	109.3	N(3B)-C(1B)-H(1B1)	109.5
C(7A)-C(6A)-H(6A1)	109.3	N(3B)-C(1B)-H(1B2)	109.5
N(1A)-C(6A)-H(6A2)	109.3	H(1B1)-C(1B)-H(1B2)	109.5
C(7A)-C(6A)-H(6A2)	109.3	N(3B)-C(1B)-H(1B3)	109.5

H(6A1)-C(6A)-H(6A2)	108.0	H(1B1)-C(1B)-H(1B3)	109.5
C(6A)-C(7A)-H(7A1)	109.5	H(1B2)-C(1B)-H(1B3)	109.5
C(6A)-C(7A)-H(7A2)	109.5	C(4B)#1-C(4B)-N(1B)#1	98.1(4)
H(7A1)-C(7A)-H(7A2)	109.5	C(4B)#1-C(4B)-N(3B)	115.5(5)
C(6A)-C(7A)-H(7A3)	109.5	N(1B)#1-C(4B)-N(3B)	20.1(4)
H(7A1)-C(7A)-H(7A3)	109.5	C(4B)#1-C(4B)-H(4B)	122.3
H(7A2)-C(7A)-H(7A3)	109.5	N(1B)#1-C(4B)-H(4B)	138.3
N(1A)-C(2A)-N(3A)	108.2(4)	N(3B)-C(4B)-H(4B)	122.3
N(1A)-C(2A)-H(2A)	125.9	Cl(12)-Ag(1)-Cl(11)#2	115.32(4)
N(3A)-C(2A)-H(2A)	125.9	Cl(12)-Ag(1)-Cl(11)	113.94(4)
C(2A)-N(3A)-C(4A)	109.4(4)	Cl(11)#2-Ag(1)-Cl(11)	104.30(3)
C(2A)-N(3A)-C(1A)	126.1(4)	Cl(12)-Ag(1)-Cl(21)	103.01(3)
C(4A)-N(3A)-C(1A)	124.6(4)	Cl(11)#2-Ag(1)-Cl(21)	110.11(4)
N(3A)-C(1A)-H(1A1)	109.5	Cl(11)-Ag(1)-Cl(21)	110.24(4)
N(3A)-C(1A)-H(1A2)	109.5	Cl(12)-Ag(1)-Ag(2)	53.51(2)
H(1A1)-C(1A)-H(1A2)	109.5	Cl(11)#2-Ag(1)-Ag(2)	147.24(3)
N(3A)-C(1A)-H(1A3)	109.5	Cl(11)-Ag(1)-Ag(2)	108.22(3)
H(1A1)-C(1A)-H(1A3)	109.5	Cl(21)-Ag(1)-Ag(2)	54.37(2)
H(1A2)-C(1A)-H(1A3)	109.5	Cl(12)-Ag(1)-Ag(1)#2	132.78(3)
C(5A)-C(4A)-N(3A)	106.4(4)	Cl(11)#2-Ag(1)-Ag(1)#2	52.18(3)
C(5A)-C(4A)-H(4A)	126.8	Cl(11)-Ag(1)-Ag(1)#2	52.12(3)
N(3A)-C(4A)-H(4A)	126.8	Cl(21)-Ag(1)-Ag(1)#2	124.21(3)
C(4A)-C(5A)-N(1A)	107.1(4)	Ag(2)-Ag(1)-Ag(1)#2	160.03(2)
C(4A)-C(5A)-H(5A)	126.5	Cl(12)#1-Ag(2)-Cl(12)	113.56(5)
N(1A)-C(5A)-H(5A)	126.5	Cl(12)#1-Ag(2)-Cl(21)#1	105.15(3)
C(2B)-N(1B)-C(4B)#1	114.6(7)	Cl(12)-Ag(2)-Cl(21)#1	109.88(3)
C(2B)-N(1B)-C(6B)	125.6(8)	Cl(12)#1-Ag(2)-Cl(21)	109.88(3)
C(4B)#1-N(1B)-C(6B)	119.7(8)	Cl(12)-Ag(2)-Cl(21)	105.15(3)
N(1B)-C(6B)-C(7B)	112.4(8)	Cl(21)#1-Ag(2)-Cl(21)	113.43(5)
N(1B)-C(6B)-H(6B1)	109.1	Cl(12)#1-Ag(2)-Ag(1)#1	54.38(2)
C(7B)-C(6B)-H(6B1)	109.1	Cl(12)-Ag(2)-Ag(1)#1	107.80(3)
N(1B)-C(6B)-H(6B2)	109.1	Cl(21)#1-Ag(2)-Ag(1)#1	55.84(2)

C(7B)-C(6B)-H(6B2)	109.1	Cl(21)-Ag(2)-Ag(1)#1	147.02(2)
H(6B1)-C(6B)-H(6B2)	107.9	Cl(12)#1-Ag(2)-Ag(1)	107.80(3)
C(6B)-C(7B)-H(7B1)	109.5	Cl(12)-Ag(2)-Ag(1)	54.38(2)
C(6B)-C(7B)-H(7B2)	109.5	Cl(21)#1-Ag(2)-Ag(1)	147.02(2)
H(7B1)-C(7B)-H(7B2)	109.5	Cl(21)-Ag(2)-Ag(1)	55.84(2)
C(6B)-C(7B)-H(7B3)	109.5	Ag(1)#1-Ag(2)-Ag(1)	150.74(2)
H(7B1)-C(7B)-H(7B3)	109.5	Ag(1)#2-Cl(11)-Ag(1)	75.70(3)
H(7B2)-C(7B)-H(7B3)	109.5	Ag(2)-Cl(12)-Ag(1)	72.11(3)
N(1B)-C(2B)-N(3B)	108.8(7)	Ag(2)-Cl(21)-Ag(1)	69.80(3)
N(1B)-C(2B)-H(2B)	125.6		

2. Conferences and Lecture Courses Attended

Date	**Conference / Course**
Jan 2000	"Ionic liquids Week", Queens University of Belfast, Belfast
May 2000	EXAFS Training Course, Daresbury Laboratory, U.K.
11-13th September 2000	Concepts of Chemical Engineering for Chemists, UCL (Organised by RSC, Industrial Affairs Division) , London
1-5th April 2001	The American Chemical Society Conference, San Diego, California
12-14th December 2001	XAS Training Course for Beginners, Daresbury Laboratory, U.K.
17th December 2001	Molten Salts Discussion Group, RSC, Burlington House, London
2002	The University of Edinburgh Inorganic Section Meeting, Firbush Field Centre.

Additionally, I attended nearly all of the Inorganic, Physical and Materials section meetings, as well as six monthly meetings at BNFL.

3. Publications

Contributed papers:

A structural and electrochemical investigation of 1-alkyl-3-methylimidazolium salts of the Nitratodioxouranate(VI) anions $[\{UO_2(NO_3)_2\}_2(\mu 4\text{-}C_2O_4)]^{2-}$, $[UO_2(NO_3)_3]^-$, and $[UO_2(NO_3)_4]_2^-$.
A.E. Bradley,C. Hardacre, M. Nieuwenhuyzen, W.R. Pitner, D. Sanders, K.R. Seddon, R.C. Thied, *Inorg. Chem.*, 2004, **43(8)**, 2503 - 2514.

A cell for the in situ study of electrocrystallization.
A. Parkin, S.F. Johnstone, A.R. Mount, S. Parsons, C.R. Pulham, D. Sanders, *Journal of Applied Crystallography*, 2004, **37(2)**, 312 - 318.

An investigation of the radiochemical stability of ionic liquids.
D. Allen, G. Baston, A.E. Bradley, T. Gorman, A. Haile, I. Hamblett, J.E. Hatter, M.J.F. Healey, B. Hodgson, R. Lewin, K. Lovell, B. Newton, W.R. Pitner, D.W. Rooney, D. Sanders, K.R. Seddon, H.E. Sims, R.C. Thied, *Green Chemistry*, 2002, **4(2)**, 152 - 158.